Robotic Assistant Systems for Otolaryngology-Head and Neck Surgery

By

Kevin C. Olds

A dissertation submitted to The Johns Hopkins School of Medicine in conformity with the requirements for

the degree of Doctor of Philosophy

Baltimore, Maryland

March, 2015

Abstract

Recently, there has been a significant movement in otolaryngology-head and neck surgery (OHNS) toward minimally invasive techniques, particularly those utilizing natural orifices. However, while these techniques can reduce the risk of complications encountered with classic open approaches such as scarring, infection, and damage to healthy tissue in order to access the surgical site, there remain significant challenges in both visualization and manipulation, including poor sensory feedback, reduced visibility, limited working area, and decreased precision due to long instruments. This work presents two robotic assistance systems which help to overcome different aspects of these challenges.

The first is the Robotic Endo-Laryngeal Flexible (Robo-ELF) Scope, which assists surgeons in manipulating flexible endoscopes. Flexible endoscopes can provide superior visualization compared to microscopes or rigid endoscopes by allowing views not constrained by line-of-sight. However, they are seldom used in the operating room due to the difficulty in precisely manually manipulating and stabilizing them for long periods of time. The Robo-ELF Scope enables stable, precise robotic manipulation for flexible scopes and frees the surgeon's hands to operate bimanually. The Robo-ELF Scope has been demonstrated and evaluated in human cadavers and is moving toward a human subjects study.

The second is the Robotic Ear Nose and Throat Microsurgery System (REMS), which assists surgeons in manipulating rigid instruments and endoscopes. There are two main types of challenges involved in manipulating rigid instruments: reduced precision from hand tremor amplified by long instruments, and difficulty navigating through complex anatomy surrounded by sensitive structures. The REMS enables precise manipulation by allowing the surgeon to hold the surgical instrument while filtering unwanted movement such as hand tremor. The REMS also enables augmented navigation by calculating the position of the instrument with high accuracy, and combining this information with registered preoperative imaging data to enforce virtual safety barriers around sensitive anatomy. The REMS has been demonstrated and evaluated in user studies with synthetic phantoms and human cadavers.

Advisor:

Russell H. Taylor PhD, Professor

Department of Computer Science, The Johns Hopkins University

Readers:

Peter Kazanzides PhD, Research Professor

Department of Computer Science, The Johns Hopkins University

Iulian Iordachita PhD, Associate Research Professor

Department of Mechanical Engineering, The Johns Hopkins University

Jeffery Siewerdsen PhD, Professor

Department of Biomedical Engineering, The Johns Hopkins University School of Medicine

Masaru Ishii MD PhD, Associate Professor of Otolaryngology-Head and Neck Surgery

Department of Otolaryngology-Head and Neck Surgery, The Johns Hopkins University School of Medicine

Jeremy Richmon MD, Associate Professor of Otolaryngology-Head and Neck Surgery

Department of Otolaryngology-Head and Neck Surgery, The Johns Hopkins University School of Medicine

Acknowledgements

Contents

List of Tables

List of Figures

Chapter 1   Introduction

Otolaryngology-Head and Neck Surgery (OHNS) is the study and treatment of conditions of the ear, nose, throat, head, and neck. For many OHNS conditions, surgical approaches are the preferred method of treatment, however traditional open surgical methods can have many drawbacks, such as damage to surrounding tissues, bleeding, infection, and scarring. Because of this, there has been a recent movement in OHNS toward minimally invasive techniques, particularly those utilizing natural orifices. While these techniques can reduce the risk of complications encountered with classic open approaches, there remain significant challenges in both visualization of anatomy and manipulation of surgical instruments, including poor sensory feedback, reduced visibility, limited working area, and decreased precision due to long instruments [1]. Though robotic surgical systems have been successful in addressing surgical challenges such as these in some areas, there is currently no general robotic solution for OHNS.

This dissertation presents the design, development, and validation of two robotic systems for OHNS, the Robotic Endo-Laryngeal Flexible (Robo-ELF) Scope, and the Robotic ENT Microsurgery System (REMS). The Robo-ELF Scope is a novel robotic system to address the challenges of manipulating flexible endoscopes in OHNS (Figure 1.1).
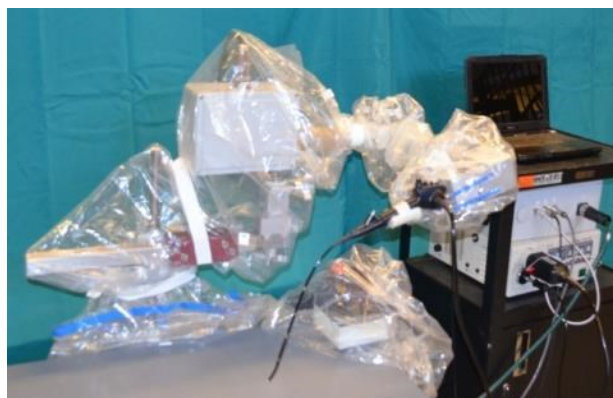
Figure 1.1: Robo-ELF Scope Overview

The Robo-ELF Scope is intended to be a proof of concept system capable of being used in human clinical studies that validate the concept of using a simple robot to control flexible endoscopes, initially in laryngeal surgery. It has been through several design iterations and was validated successfully in two

cadaver studies evaluating its performance compared to rigid endoscopes and ease of use. It has also received a non-significant risk determination from the FDA for use in human subjects.

The REMS is a novel robotic system to address the precision and navigation challenges of OHNS. The REMS is intended to be an engineering prototype to validate the feasibility of using cooperatively controlled robots in a variety of OHNS procedures. The REMS has been successfully validated in precision manipulation tasks using phantoms based on laryngeal surgery, as well as a sinus surgery task using phantoms and cadavers.
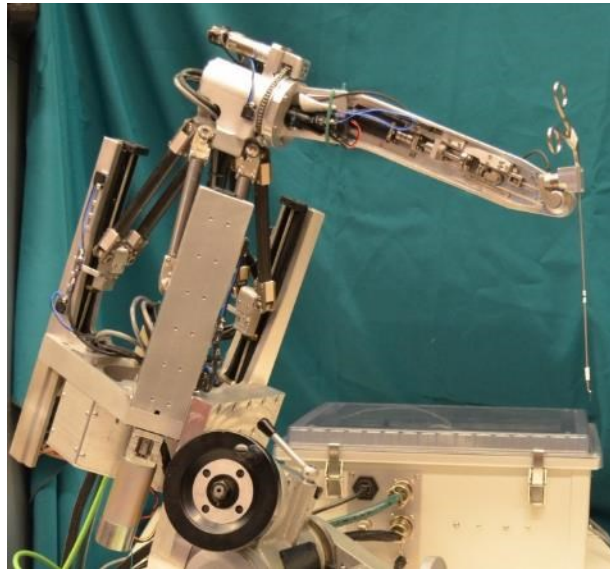
Figure 1.2: REMS Overview

1.1 Thesis Statement

Simple, general purpose robotic assistant systems can improve surgical performance in OHNS, as well is in other disciplines, by enhancing surgeons' visualization, precision, and navigation.

Thesis arguments:

- Though complex surgical systems have been shown to improve surgical performance in many areas including laparoscopic and orthopedic surgery, no similarly general purpose system exists for OHNS.

- Many OHNS procedures share similar challenges that are feasible to address with simple yet highly general robotic systems.

- Robotic flexible endoscope manipulation can improve visualization of anatomy over conventional rigid endoscopes, as well as enable two-handed operation which is not feasible with current flexible endoscopes.

- Cooperatively controlled robotic assistance can improve precision and navigation in different areas of OHNS, including laryngeal and sinus surgery.

1.2 OHNS Overview

OHNS is both a medical and surgical specialty, and can be split into several subspecialties, including pediatrics, laryngeal, allergy, sleep, sinus, facial plastics, oncology, and otology. OHNS practitioners can be specialists, focusing on one area, or generalists, who practice several or all categories to some degree. Since OHNS is such a broad field, a good way to understand the challenge of OHNS is to examine representative examples from ear, nose, and upper aerodigestive tract surgery.

1.3 Ear Surgery

1.3.1 Anatomical Overview

The human ear is traditionally thought of in three main sections, the outer ear, middle ear, and inner ear (See Figure 1.3). The outer ear contains the pinna, which is important for sound localization and directing sound into the ear, and the ear canal, which conducts sound into the middle ear. The middle ear consists of the tympanic membrane, or ear drum, which vibrates in response to air pressure fluctuations from sound waves, and the ossicles, or middle ear bones, which conduct sound into the inner ear. The ossicles, starting from the ear drum, are the malleus, incus, and stapes bones. The stapes bone connects to the membrane covering the oval window which leads into the cochlea. The inner ear consists of the cochlea and semicircular canals of the vestibular system. The cochlea transduces the sound vibrations conducted into it by the ossicles into neural signals which the brain perceives as sound.
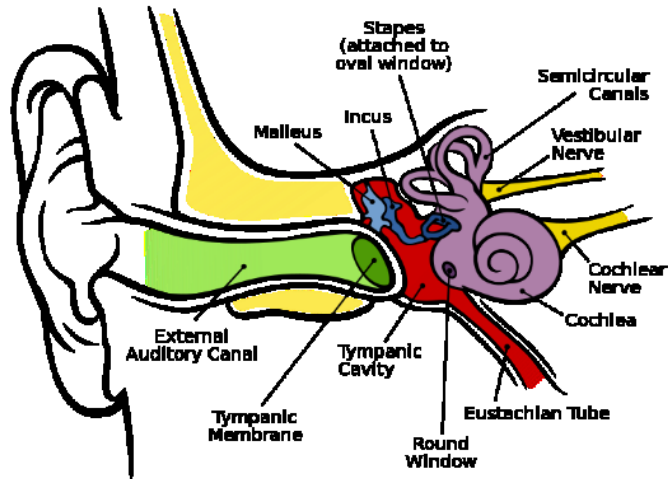
Figure 1.3 Anatomy of the auditory system

(Image credit Brockmann 2015 [2])

In the cochlea, sound vibrations enter through the oval window, and pass through the vestibular canal, around the apex of the cochlea, through the tympanic canal, and out the round window (see Figure 1.4). While these sound vibrations are passing through the cochlea, they cause the basilar membrane to vibrate in different locations depending on the frequency of the sound. Higher frequencies cause the basilar membrane to vibrate near the base of the cochlea (near the oval and round windows) and lower frequencies near the apex of the cochlea. These vibrations in the basilar membrane are detected by specialized hair cells in the organ of Corti on the basilar membrane (see Figure 1.5). These hair cells transduce vibrations into neural signals and are connected to the cochlear nerve which carries these signals to the brain.
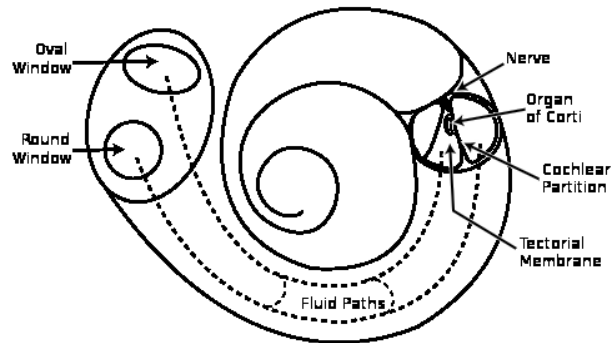
Figure 1.4: Anatomy of the cochlea

(Image credit www.wikipedia.org)
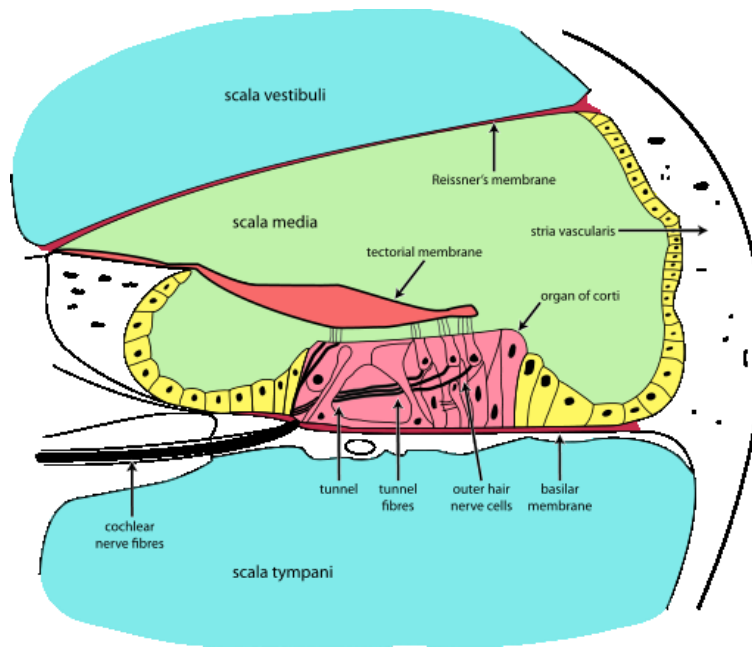
Figure 1.5: Cross-sectional view of the cochlea.

(Image credit: www.wikipedia.org)

1.3.2 Ear Surgery Introduction

One of the most common reasons a patient would require surgery in the middle or inner ear is hearing loss. There are two main types of hearing loss, conductive and sensorineural. In conductive hearing loss, some type of pathology is preventing sound vibrations from properly conducting through the ear drum –> ossicle –> oval window chain. One common cause of conductive hearing loss is fixation of the stapes to the cochlea, which can be caused by otosclerosis, abnormal mineralization of the junction between the stapes and the oval window, or congenital malformation of the stapes bone. Though otosclerosis can be identified in 10% of the population histologically, about 1% of the population exhibit noticeable hearing loss. As access to care and diagnostic and treatment methods have improved, the number of years of noticeable hearing loss and the average age of the patients before treatment have decreased over the last 50 years. Though conductive hearing loss from otosclerosis can be treated with hearing aids, surgery is often required for severe cases. One common surgical treatment for otosclerosis is stapedotomy, which involves removing the affected ossicles, ablating a hole in the stapes footplate, and inserting a prosthesis to restore

sound conduction into the cochlea. Stapedotomy is used as a case study for middle ear surgery because it is a good example of middle ear surgery done through the ear canal.

In sensorineural hearing loss, sound may be conducted into the cochlea properly, but the vibrations are not properly transduced into neural signals. One common cause of this is damage to the hair cells in the cochlea resulting from pharmaceuticals, disease, exposure to excessively loud sound, congenital conditions, or old age. This type of hearing loss can be treated with hearing aids in mild cases, but for severe cases a cochlear implant is the primary treatment option. About 324,000 people worldwide, and 96,000 people in the US have received cochlear implants as of 2012 [3]. Access in developing countries is limited due to the high cost of the devices. Cochlear implant surgery involves drilling through the mastoid bone and inserting an electrode array into the cochlea. Cochlear implant surgery is used as a second example of ear surgery because it is representative of surgeries that involve drilling through the mastoid bone to access the desired anatomy, and also involves significant surgical challenges (See 1.3.4).

1.3.3 Stapedotomy

Conductive hearing loss resulting from stapes fixation can be treated though surgical intervention. Most commonly, this means performing a stapedotomy, which involves removing the stapes bone except for the footplate (now fixed over the oval window), drilling a hole through the stapes footplate, and inserting a prosthesis which connects to the incus and conducts sound through the hole in the stapes footplate directly through the oval window into the cochlea (see Figure 1.6). This procedure is done routinely with a high success rate, though it presents some significant manipulation challenges for surgeons.

Figure 1.6: Steps of stapedotomy

1) Remove the stapes leaving the footplate. 2) Use a laser or drill to make a hole in the footplate. 3) Insert a prosthetic stapes and clamp it onto the incus. Sometimes a vein graft is used to seal the prosthesis as in 3). (Image Credit: http://www.nyogmd.com/hearing-balance-center/steps-of-stapedotomy-surgery/)

One aspect of stapedotomy that can be challenging is the small scale of all the anatomy. The stapes footplate typically is not larger than 2x3 mm, and the prosthesis is typically about 0.5 mm in diameter. In addition, the entire surgery takes place through the ear canal, which is only 7 mm in diameter at a depth of around 5 cm, creating significant space constraints. This requires surgeons to use specialized forceps designed for working through small channels (see Figure 1.7). Though these forceps are not exceptionally long compared to other types of ENT forceps, they can still amplify hand tremor, which can be significant when working on a sub-millimeter scale. This can be especially problematic when attempting to clamp the prosthesis onto the incus (for some types of prostheses), since applying the larger force needed for clamping further exacerbates hand tremor. Hand tremor can also make it difficult to create the correct size and shape hole in the stapes footplate for the prosthesis. Another potential challenge is avoiding sensitive anatomy while operating. For example, sometimes the facial nerve can protrude very close to the stapes footplate, and in these cases, it is critical that the facial nerve is not damaged during the course of the surgery. When using a laser to make the hole in the stapes footplate, another potential complication can occur when the laser hits the fluid in the cochlea directly when the laser shoots through a hole that was already made. This can cause an acoustic shockwave in the cochlea which can damage the hair cells and affect hearing outcomes.

Figure 1.7: Otology forceps.

1.3.4 Cochlear Implant Surgery

Sensorineural hearing loss resulting from damage to cochlear hair cells can be treated surgically with a cochlear implant. A cochlear implant consists a small array of electrodes that is inserted into the cochlea through the round window or through a cochleostomy (artificially created hole in the cochlea), and a microphone with digital signal processing electronics that transduce sound vibrations into electrical signals (see Figure 1.8). The electrical signals from the electrode array directly stimulate the auditory nerve inside the cochlea, bypassing the faulty hair cells and restoring hearing.
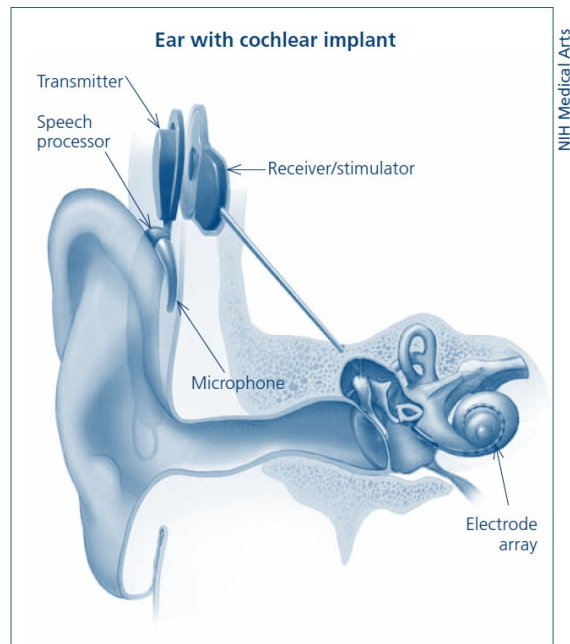
Figure 1.8: Cochlear implant.

(Image credit www.nidcd.nih.gov)

The first step in cochlear implant surgery is to drill through the mastoid bone to create the cavity for the electronics and access the cochlea (Figure 1.9). This can be challenging because the facial nerve runs very close to this area, so it is important to avoid damaging the facial nerve while drilling. This can be quite difficult since the facial nerve is not easily visible until the bone over it has been drilled away. The next step is preparing a cochleostomy, a hole drilled into the cochlea or through the round window. These operations can also be very difficult due to the fragility and small scale of the anatomy.
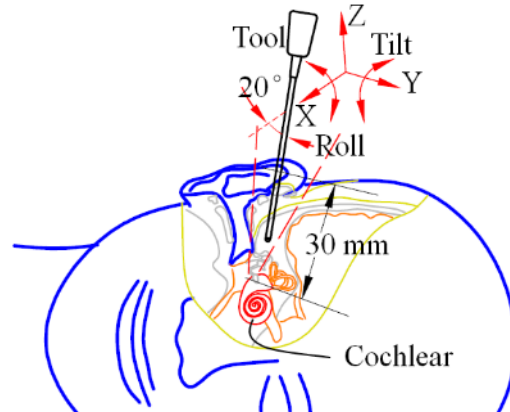
Figure 1.9: Drilling to access the cochlea.

1.4   Sinus Surgery

1.4.1 Anatomical Overview

The paranasal sinuses are a collection of complex interconnected passages that fill the spaces around the eyes, ears, nose, mouth, and throat (see Figure 1.10). There are four main sinuses, the frontal, sphenoid, maxillary, and ethmoid (see Figure 1.11). They are composed of air-filled sacks in bone and lined with respiratory epithelium. Though there is still some debate, it is suspected that the evolutionary purpose of the sinuses is to lighten the weight of the head, while also providing "crumple zones" during trauma.

Nose and Nasal Cavities

Frontal sinus

Superior nasal concha

Sphenoid sinus

Middle nasal concha

Middle meatus

Uncinate process

Inferior nasal choncha

Nasopharynx

External naris

Maxillary ostium

Bulla ethmoidalis
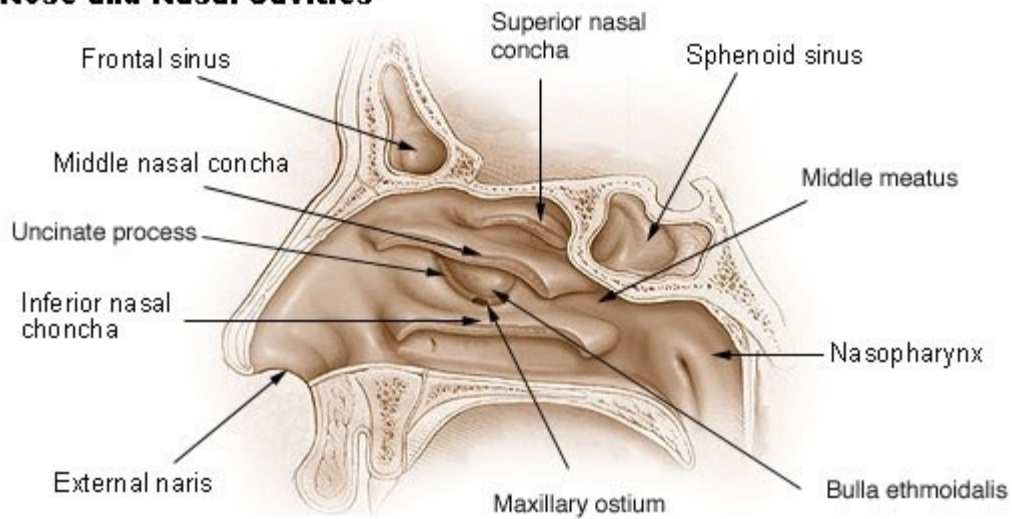
Figure 1.10: Anatomy of the sinuses

(Image credit http://training.seer.cancer.gov)

Frontal sinus

Sphenoid sinus

Ethmoid air cells

Maxillary sinus

Frontal sinus

Sphenoid sinus

Ethmoid air cells

Maxillary sinus

Lateral

Anterior
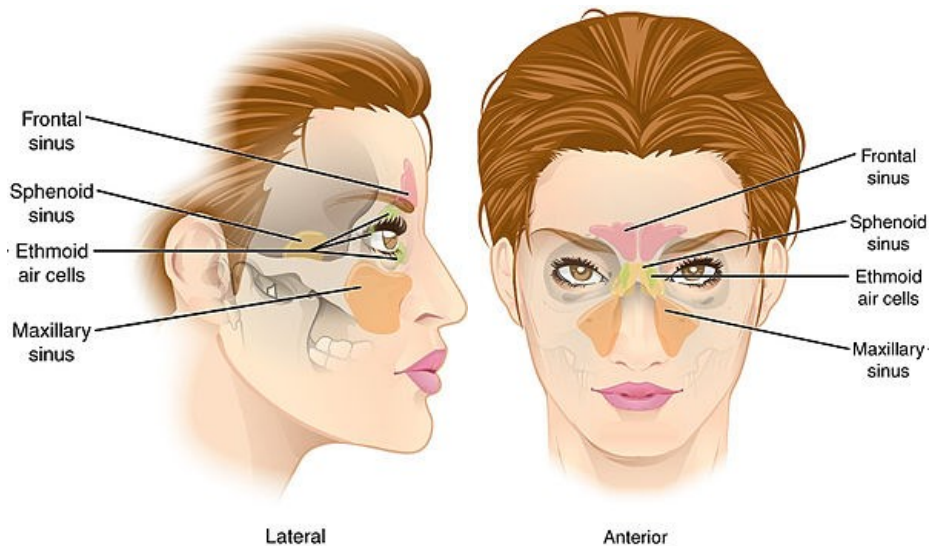
Figure 1.11: The four main sinuses.

(Image credit www.wikipedia.org)

1.4.2 Sinus Surgery Introduction

There are two main reasons sinus surgeries are performed. The first is to treat pathologies in the sinus, such as polyps, infection (bacterial and fungal), and some types of cancer. The second is to use the sinuses to access other anatomical areas that are difficult to reach by other means, such as the pituitary gland near

the base of the brain behind the sphenoid sinus. The most common reason to perform sinus surgery is chronic or recurrent sinusitis, which results when the sinuses do not drain properly and become infected and inflamed. Sinusitis is extremely common, with over 90% of adults reporting symptoms at least once in their lives. In most cases, e.g. a common cold, the infection passes in a few weeks or less. However, in some cases it persists, and in the case of bacterial sinusitis may require treatment with antibiotics. Antibiotic treatment can be complicated by patient allergies to certain antibiotics, and also by the rising number of antibiotic resistant infections. In cases where sinusitis either does not clear up in response to antibiotics (chronic sinusitis) or where it keeps coming back after treatment (recurrent sinusitis) surgery may be required to either remove the infected tissue, or open the sinus outflow tracts so that they drain more effectively. Chronic sinusitis is very common, affecting approximately 12.5% of the US population [4], making endoscopic sinus surgery one of the most frequently performed surgical procedures in OHNS, with about 250,000 ambulatory (out-patient) surgeries performed per year [5].

Traditionally, surgery in the sinuses was performed "open" by entering through an incision in the face, such as through the cheek or under the upper lip. However, this approach has many drawbacks, including scarring, infection, and damage to healthy tissue. As new technologies have emerged, including endoscopes, microscopes, and specialized instruments, minimally invasive techniques have become more prevalent. Currently most sinus surgeries are performed endoscopically using a rigid endoscope and long instruments inserted through the nose (Figure 1.12).
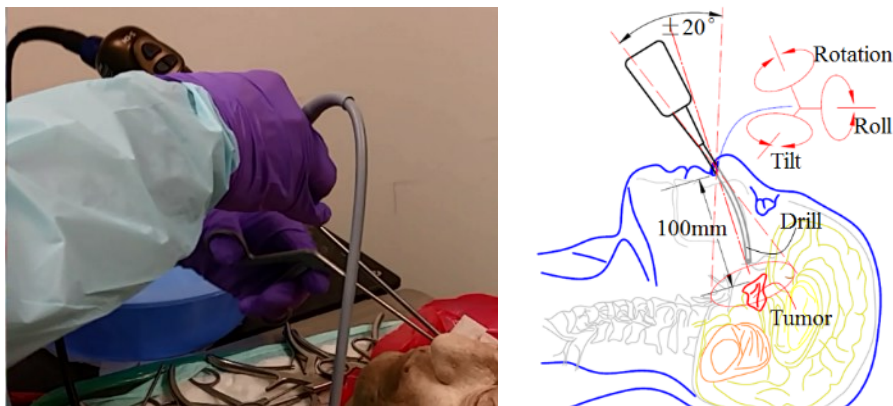
Figure 1.12: Endoscopic Sinus Surgery

This endoscopic approach has also enabled treatments that use the sinuses to access otherwise difficult to reach anatomy, such as the pituitary gland (see Figure 1.13). The pituitary gland is an endocrine

gland that controls the levels of several different hormones. Pituitary pathologies such as tumors can affect hormone levels and produce dramatic anatomical effects such as gigantism. The primary method of treating these conditions is surgical removal of the pathology from the pituitary gland.
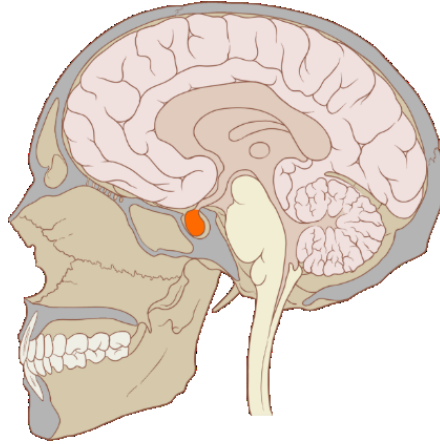
Figure 1.13: Pituitary gland shown in orange.

(Image credit www.wikipedia.org)

1.4.3 Endoscopic Sinus Surgery

Endoscopic sinus surgery, such as for the treatment of chronic sinusitis, presents many surgical challenges. The objective is typically to remove infected tissue, or open the passages in the sinus to allow for proper drainage. While many simpler cases are often done with endoscopic visual feedback alone, image guidance is often used for more difficult cases. The typical workflow for image guided sinus surgery involves acquiring a pre-operative CT scan, fixing the patient's head in place with a strap or Mayfield clamp, and registering an optical tracker to the CT image. This allows the surgeon to insert a tracked probe into the sinuses through the nose to check the correspondence between endoscopic views and CT locations. Surgeries are typically done with the endoscope in one hand, and an operative instrument (drill, suction, tissue shaver, clippers, etc.) in the other. The surgeon typically uses the tracked probe to navigate to a target area in the CT, and checks the correspondence in the endoscopic image, which is displayed on a second monitor. Once the location is confirmed, the tracked probe is removed, and an operative instrument is inserted. The most commonly used instruments include suction, clippers of many different sizes and orientations for removing bone walls, drills, and tissue shavers. The bone walls being removed can vary from as thin and delicate as an eggshell, to solid, hard structures several millimeters thick, requiring a wide

range of operating forces. In addition to these challenges, it is also desirable to prevent instrument shafts from pressing against the sinuses, since this can result in tissue damage and bleeding, which can further obstruct the endoscopic view.

Though repeatedly removing operative instruments to check CT position with the tracked probe is suboptimal, it is done because the anatomy of the sinuses is complex and highly variable, and many critical structures (brain, eye orbit) are closely adjacent to the sinuses. In addition to this, the sinuses are often inflamed during surgery, sometimes making it difficult to spot anatomical landmarks or even determine where the bony structures of the sinus are behind the tissue. In addition to frequent operative instrument changes, the rigid endoscopes that are commonly used can only show views at a fixed angle relative to the endoscope tip. If a different angle is needed, a different scope needs to be inserted with the correct viewing angle. The scope tips also frequently get dirty due to dripping blood and other fluids and need to be removed and cleaned, resulting in frequent endoscope insertion and removal as well.

1.4.4 Endonasal Skull Base Surgery

Endonasal skull base surgery involves using the nose and sinuses to access otherwise hard to reach anatomical structures such as the pituitary gland. Typically in pituitary surgery, and OHNS surgeon and neurosurgeon work together, with the OHNS surgeon performing sinus surgery to gain access to the pituitary gland through the sphenoid sinus, and the neurosurgeon then taking over and removing the pituitary pathology. This adds some additional challenges including removing the thin, delicate bone wall over the pituitary gland without damaging it, difficulty visualizing the pituitary pathology, and long operation times. For the second half of the surgery, which can take up to several hours, the OHNS surgeon is often acting as a scope holder to allow the neurosurgeon to operate bimanually. Though mechanical scope holders exist, they are often not used because they can be difficult to repeatedly set up and take down as the scope needs to be removed, cleaned, and reinserted.

1.5 Upper Aerodigestive Tract Surgery

1.5.1 Anatomical Overview

The upper aerodigestive tract can be subdivided into four main areas, the pharynx, larynx, trachea, and esophagus (See Figure 1.14). The epiglottis is a flap of cartilage which acts as a valve between the larynx and the pharynx. When swallowing, the epiglottis closes to prevent food from going into the airway.
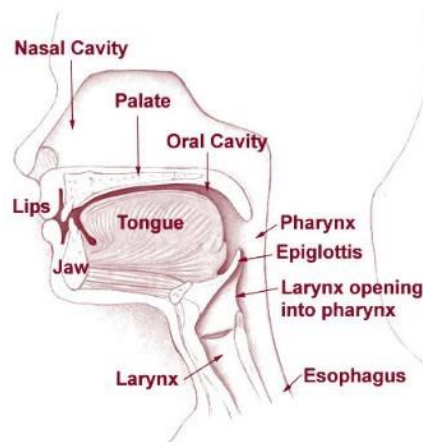
Figure 1.14: Anatomy of the upper aerodigestive tract.

(Image credit http://training.seer.cancer.gov/head-neck/anatomy/overview.html)

The glottis (colloquially called the voice cords) is located inside the larynx (See Figure 1.15). The glottis opens when breathing and closes when speaking. Each vocal fold consists of three layers of tissue: the epithelium is a thin layer of tissue which covers the surface of the vocal fold and helps provide lubrication, the lamina propria lies under the epithelium and consists of elastic tissue which vibrates when speaking, and the muscularis lies under the lamina propria and provides the muscle control over whether the vocal folds are abducted (open) or adducted (closed). When the vocal folds are pressed together and air is forced between them, the epithelium and lamina propria vibrate, producing sound.
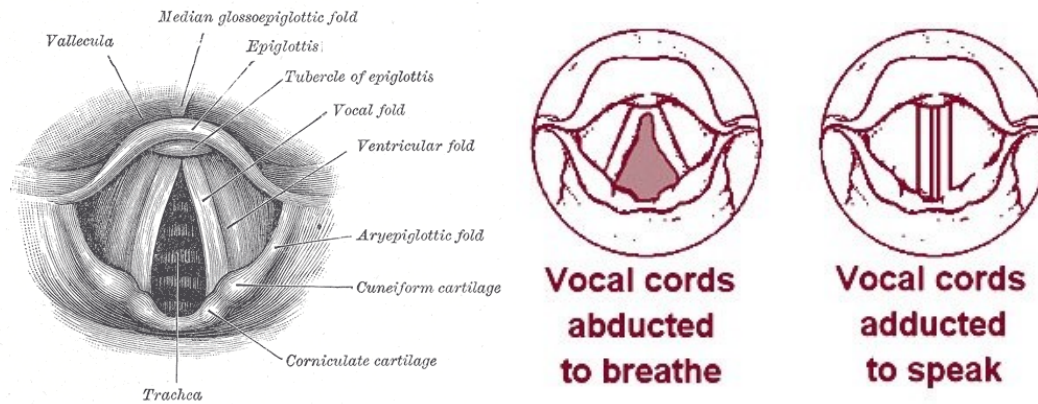
Figure 1.15: Anatomy of the glottis

(Image credit Gray's Anatomy of the Human Body, 20th Edition)

1.5.2 Upper Aerodigestive Tract Surgery Introduction

Since this is a very broad topic, the analysis here will be restricted to two different examples of pathologies and corresponding surgical procedures to give a rough overview. The first set of pathologies includes cysts, nodules, polyps, and tumors of the vocal folds. Nodules are generally formed through vocal abuse (e.g. repeated loud talking or singing) and can be thought of as calluses on the vocal cords. Polyps can also be formed by vocal abuse, and can be thought of as blisters on the vocal cords. Cysts can be formed by vocal abuse or arise spontaneously, and can be thought of as fluid-filled sacs deeper in the vocal cords. Papillomas are most often caused by the human papilloma virus (HPV), but can also result from other causes, and typically consist of small wart-like growths on the surface of the vocal cord. All of these pathologies can significantly affect the voice quality of the patient, particularly if the growth is large. Benign growths are typically treated with a combination of voice therapy and surgical treatment (microlaryngeal phonosurgery).

The second example pathology is laryngeal cancer. The biggest risk factors for laryngeal cancer are heavy smoking and heavy chronic alcohol consumption. Laryngeal cancer typically starts in the glottis, and is detected through symptoms of voice hoarseness, soreness, and lumps in the throat. In more moderate cases, the cancer can be treated surgically through a transoral approach. In more severe cases, an open approach involving an incision in the neck may be required. In very severe cases, a total laryngectomy may be performed, and significant reconstructive surgery may be required.

1.5.3 Microlaryngeal Phonosurgery

In microlaryngeal phonosurgery, the patient is anesthetized, intubated, and suspended with a laryngoscope (Figure 1.16) that both allows line of sight access to the glottis, and immobilizes the patient during the surgery.

Figure 1.16: Airway phantom suspended with a laryngoscope.

The vocal folds are visualized using a surgical microscope with a 400 mm focal length lens. Depending on the pathology, different types of instruments are used, including long shafted instruments (forceps, scissors, and blades) and laser ablation instruments.
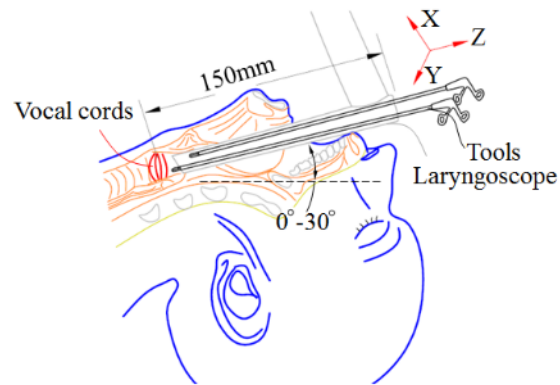
Figure 1.17: Microlaryngeal Phonosurgery

One typical surgical maneuver for removing certain types of pathology involves making a precise incision into the outer layer of the vocal fold and retracting a flap of tissue to expose the pathology below. This maneuver presents several significant challenges. Since the instruments can be up to 25 cm long, hand tremor is amplified by the long lever arm, making precise instrument movements difficult. It can also be very challenging to hold the flap still without tearing it while removing the pathology. Finally, since the

pathology abnormally stretched the outer layers of the vocal cord, the flap must be trimmed down once the pathology is removed, which requires very precise manipulation.

1.5.4 Laryngeal Cancer Surgery

For early stages of laryngeal cancer, the pathologies can often be removed via a trans-oral approach or treated with radiation. This approach typically uses rigid endoscopes with straight or angled tips, and long laryngeal instruments. One of the difficulties of this approach is that the anatomy of the throat can often prevent rigid endoscopes from achieving a satisfactory view. Though flexible endoscopes (Figure 1.18) are often used in the clinic and for diagnostics, they are rarely used in surgery due to the difficulty in manually manipulating and stabilizing them for long periods of time.

Figure 1.18: Flexible endoscope

In more severe cases of laryngeal cancer, an open approach involving a large incision in the neck may be required. These cases can require that large amounts of tissue be removed, depending on the size of the tumor.

1.6 Other Potential Applications

Though not necessarily directly related to OHNS, there are several other surgical areas that share many features in common with it and could potentially benefit from any solutions developed for OHNS. These are summarized below, though these areas are not the focus of this work.

1.6.1 Neurosurgery

Several different areas in neurosurgery share similar characteristics to some areas of OHNS, including similar precision requirements, the need to operate in a narrow confined space, and the need for accurate surgical navigation. One example is craniotomy, where a section of the skull is removed in order to access the brain. This involves both precise bone drilling, as well as delicate tissue manipulation in a constrained workspace. Another example is pedicle screw placement in spine surgery. Placing a screw down the pedicle of a vertebra requires both high precision and accuracy. If the screw breaks through the pedicle into the spinal canal, significant complications can result. For a final example, peripheral nerve suturing is done when nerves need to be reattached. This is often done in reconstructive surgery where either a transplant or nerve graft is being reattached, or where a laceration is being repaired. Nerve suturing requires high precision not only in placing the sutures, but also in properly aligning the ends of the nerves.

1.6.2 Plastic and Reconstructive Surgery

Plastic and reconstructive surgery has significant overlap with OHNS and neurosurgery, particularly in suturing for reconstructive surgery and facial surgery. Whether repairing damage or transplanting tissue, reconstructive surgery frequently involves suturing small nerves and blood vessels, as well as precise suturing of other tissues such as skin. Recent advances in reconstructive surgery have made more and more elaborate transplants possible, including complete hand and face transplants. In these advanced transplants, the ability to quickly and precisely suture many small nerves and blood vessels is often a limiting factor.

1.6.3 Biopsy/Ablation

As cancer treatment moves more toward minimally invasive techniques, precise insertion of needles and probes for biopsy and ablation has become a significant clinical problem. A typical biopsy/ablation scenario involves inserting needles/probes through the skin into a target area in an organ such as the lungs or liver. This is often done under ultrasound, x-ray, CT, or MRI guidance. However, hand insertion is error prone and may require many x-ray images, resulting in long procedure times and undesirable x-ray doses for patients.

1.7   Summary of Surgical Challenges

The surgical challenges discussed above can be categorized into three basic categories: visualization, navigation, and precision.

- Navigation
  - Avoiding sensitive anatomy
    - Carotid artery, optic nerve, etc. in sinus surgery
  - Knowing where you are and finding where you want to be
    - Locating anatomical targets in the sinuses
    - Finding biopsy/ablation targets
- Precision
  - Precise instrument movements
    - Suturing
      - Reattaching nerves
      - Reattaching blood vessels
    - Tissue manipulation
      - Flaps in microlaryngeal phonosurgery
    - Drilling bone
    - Creating a precise fenestration in stapedotomy
- Visualization
  - Holding visualization stable for long periods of time
    - Rigid endoscopes in sinus surgery and otology
    - Flexible endoscopes in throat cancer surgery
  - Precise adjustment of visualization
    - Rigid endoscopes in sinus surgery and otology
    - Flexible endoscopes in throat cancer surgery
  - Line of sight constraints
    - Flexible endoscopes in throat cancer surgery

1.8 Prior Work

1.8.1 Conventional Solutions to Surgical Challenges

1.8.1.1 Visualization Solutions

Conventional approaches to improving visualization have generally focused on augmenting endoscopes to provide better control. The most common approach is passive endoscope holders. Since flexible endoscopes are generally used mostly in the clinic for diagnostic purposes, there are not many examples of passive holders for flexible endoscopes. However, there is a wide variety of passive holders available for rigid endoscopes. Rigid endoscope holders are typically mechanical arms that use friction to lock in place, although holders with more elaborate and expensive pneumatic and electromagnetic locking mechanisms have been developed. Though these holders can be effective for holding a scope in place for long periods of time, they suffer from some significant drawbacks. In many surgeries, particularly sinus surgery, the endoscope has to be withdrawn frequently to clean the tip to keep a good view. Many endoscope holders make this difficult and time consuming since they require two hands to use, and can be difficult and time consuming to set up and adjust precisely. An even more serious effect of this is that it can be very difficult to remove the scope quickly in an emergency situation. This can also make it difficult to use these holders in surgeries where there is a risk of the patient moving, since a sudden movement of the patient could result in the endoscope getting caught between the patient and the holder before it can be removed, and injuring the patient.

1.8.1.2 Navigation Solutions

Surgical navigation solutions can be grouped into two broad categories; image guidance and tracking systems. Image guidance involves using an imaging modality (CT, x-ray, MRI, ultrasound, etc.) during the procedure to provide feedback. However, this feedback is often not real-time due to constraints of the imaging modality and procedure, such as space constraints inside a scanner, x-ray dose, and material incompatibilities (e.g. metal in an MRI scanner). In these cases, the guidance can only be intermittent.

Image guidance can also have other drawbacks, such as slowing the procedure down to get images and difficulty interpreting images quickly.

There are two main types of surgical tracking systems, optical and electromagnetic. Optical tracking systems typically use either passive reflective markers or active LEDs with a stereo infrared camera to determine the position and orientation of surgical instruments with respect to patient anatomy. Though optical trackers can have sub-millimeter accuracy, they also have some significant drawbacks, particularly line of sight constraints, which can interfere in how operations are performed. These systems also typically require a significant amount of time and effort to register the patient to the system. Though optical tracking systems work well technically, there is significant doubt how much real benefit they provide in terms of surgical outcomes, since they only provide intermittent guidance, rather than always-on navigation with mechanical assistance.

Electromagnetic (EM) tracking systems use active electromagnetic coils in a base unit to create a time varying electromagnetic field, which is received by coils attached to a surgical instrument. Unlike optical tracking systems, EM tracking systems have no line of sight constraints, however they are sensitive to distortions in the EM field near the operating area. This places restrictions on the use of metals or magnetic materials, which can be a significant drawback since stainless steel is the primary material used for surgical instruments and equipment.

Though all of these navigation methods provide some degree of knowledge about where surgical instruments are relative to anatomy, they are not capable of actively protecting sensitive anatomy from unintentional or mistaken surgical instrument motion. All of this added information can also significantly increase the cognitive load on the surgeon, or even worse, if not set up and used properly, provide false or misleading information.

1.8.1.3 Precision Solutions

The primary conventional approaches to improving surgical precision are through ergonomics and training. Surgeons who perform surgical procedures requiring high precision are specifically trained in techniques to stabilize instruments and reduce the effects of hand tremor. Though the ergonomics of instruments, arm and hand rests, OR chairs, etc. are also optimized to improve surgical precision, in

practice many surgeons face poor ergonomic conditions. Additionally, training and ergonomics can only go so far. As surgery advances toward micro-scale and minimally invasive procedures, fundamental limits are being reached that training and ergonomics cannot overcome. It is already the case that not everyone who wants to be a surgeon in a high precision field can do so because of limitations in manual precision. On the other side of the spectrum, many older highly skilled surgeons can no longer operate simply because of physiologic hand tremor.

Another approach to improving precision, particularly in fields involving drilling/cutting bones involves using cutting guides. Cutting guides can allow surgeons to produce precise cuts and holes that would not be feasible without them. With modern 3d printing technology, cutting guides can even be custom designed for specific patients. However, cutting guides also have their drawbacks. They can be laborious and time consuming to design and produce, and cannot be used in all circumstances. They tend to be used for larger-scale modification of bones where there is ample space.

A more recent approach to improving both precision and access for minimally invasive procedures has been to modify conventional instruments to enable them to function in novel ways. One example of this is a family of SerpENT flexible instruments from ENTrigue Surgical Inc. (San Antonio, Texas). These instruments resemble those used for sinus surgery, but have the added ability to flex around corners while remaining rigid through purely mechanical means (Figure 1.19). Though this allows for improved access to certain anatomical areas in endoscopic sinus surgery, it does not significantly improve surgical precision since the instruments are manipulated similarly to conventional ones. These instruments are also more complex to control than conventional ones because of the added degrees of freedom.

Figure 1.19: SerpENT surgical instrument.

(Image Credit: http://www.entriguesurgical.com/)

Other examples of enhanced surgical instruments are multi-lumen flexible surgical endoscope systems like the Olympus Endo-Samurai. The Endo Samurai uses a large flexible endoscope with multiple lumens as a base, through which several endoscopic instruments can be inserted and individually mechanically controlled using joysticks on the back of the device. Though this system can potentially improve both access and precision in certain minimally invasive procedures, it is too large for most OHNS procedures.

Semi-robotic systems have also been developed for control of surgical lasers in laryngeal surgery. These systems mount a laser fiber on the microscope which can be controlled using a joystick. Though this can improve precision over hand-held laser fibers, it also presents additional challenges. Since the laser is attached to the microscope, any movement of the microscope relative to the patient can reduce the precision. Also, the beam is passing through a substantial distance in open air, which introduces more safety issues than a conventional laser probe which is held with the end closer to the tissue [6].

1.8.2 Robotic Solutions to Surgical Challenges

1.8.2.1 Robotics Terminology

- Active: An active device is capable of moving under its own power (i.e. powered motors).

- Passive: A passive device is not capable of moving under its own power, and will usually contain no motors.

- Master: The robot that the user is interacting with.

- Slave: The robot that is interacting with the patient.

- Teleoperation: Under the teleoperation paradigm, the user does not interact with the slave robot directly, but instead interacts with a master robot which passes commands to the slave robot.

- Cooperative control: Under the cooperative control paradigm, the master and slave are the same robot, and the user controls it through direct interaction.

1.8.2.2 Commercial Medical Robotics Systems

Robotic systems can mitigate surgical challenges in many ways, including increased precision, motion scaling, and tremor reduction, as well as more sophisticated features such as virtual fixtures to protect sensitive anatomy, enhanced data collection for surgical evaluation, and a "brake pedal" for surgeons in training [7]. Many commercially available robotic systems have been developed to address surgical challenges in a variety of areas. Minimally invasive laparoscopic surgery is the most well developed area, with the da Vinci Surgical System from Intuitive Surgical Inc. (Sunnyvale, CA) as the most successful example.

The da Vinci was preceded by the AESOP rigid endoscope holding robot and the ZEUS robotic surgical system from Computer Motion Inc. (subsequently merged with Intuitive Surgical Inc.). These systems were designed to improve visualization and ergonomics in laparoscopic surgery. Though originally also marketed primarily to solve visualization and manipulation challenges in minimally invasive laparoscopic surgery, the da Vinci system is currently the most widely used surgical robotic system, and has recently been gaining use in trans-oral surgery [8]. The current da Vinci Si System uses a teleoperation paradigm in which the surgeon sits at a master console away from the patient, and controls the slave robot which does the operation with robotic instruments inserted into the patient through several trocars much like in traditional laparoscopic surgery. This presents many advantages in laparoscopic surgery in which surgeon ergonomics can be poor. However, the separate master and slave robots add to the cost and footprint of the system, making it impractical for many operations. Additionally, since it was not designed for head and neck surgery, working in tight spaces can be difficult, and the added bulk can obstruct critical areas in emergencies [9].

Many other surgical systems for minimally invasive robotically assisted laparoscopic surgery similar to the da Vinci Si are also in various stages of development, including the Telelap AFL-X from SOFAR (Milan, Italy) [10], Surgenius BETA from Surgica Robotica (Verona, Italy) , and Raven Surgical Robotic System from Applied Dexterity (Seattle, WA) [11]. These systems all use the same basic multiple entry port, teleoperated, master-slave paradigm as the da Vinci Si. More recently, a new generation of minimally invasive surgical robots has been under development, best exemplified by the da Vinci Sp, SPORT Surgical

System from Titan Medical (Toronto, Canada), and numerous other research systems. Similar to the da Vinci Si, these systems also use a master-slave teleoperation paradigm, however they can function through only a single entry port. Though these changes make the systems less bulky and avoid tool collisions, the resulting systems are still optimized for abdominal surgery, and are too bulky to be used in OHNS except possibly for limited trans-oral applications. A major disadvantage of these complex teleoperated systems, particularly the da Vinci, is their high cost, with a da Vinci Si costing in the neighborhood of $2 million, making it the most costly medical robot sold commercially.

Orthopedic surgery is another area which has been well developed, with several commercially available robotic systems, however, the approaches taken by different robotic systems are more diverse than in laparoscopic surgery. The most successful orthopedic surgical robot is the RIO from MAKO Surgical Corp. (acquired by Stryker Corp. Kalamazoo, MI) [12], which focuses primarily on knee and hip replacements. Unlike the da Vinci, the RIO is not a teleoperated master-slave system, and instead uses a cooperative control paradigm where the surgeon directly hand-guides the robot. The surgeon pre-plans the shape of the cuts that need to be made in the bone based on CT images, then, intra-operatively registers the robot to the patient. The surgeon can then hand guide the robot to make the required cuts, with the robot enforcing a virtual fixture which keeps the cuts within the original plan. Though the RIO has been successful in orthopedics, it is unlikely it will find much application in OHNS due to its size.

Other orthopedics robots include the TCAT from Think Surgical (Freemont, CA), based on the previous ROBODOC from Curexo (Freemont, CA) [13], which also focuses on knee and hip replacements. The ROBODOC uses a similar approach to the RIO, in that it uses pre-operative planning with CT data, and can be hand-guided, but differs in that the cutting procedure is completely autonomous. Other approaches in orthopedic surgery include the APEX from Global Orthopedic Technology (Baulkham Hills, Australia), which uses a specially made tracking system to help surgeons in quickly aligning cutting guides for implants, and the Navio PFS surgical system from Blue Belt Technologies Inc. (Plymouth, MN) [14] which uses an optical tracker to automatically control the insertion/retraction of a hand-held drill.

Orthopedic spine surgery has also a successful commercial system, the Mazor Robotics Renaissance (Orlando, FL) [15]. The Renaissance is a small hexapod robot that attaches to a frame which mounts on the patient's spine. The system is registered to the patient using fluoroscopy images. The robot then positions a

tool guide which the surgeon can use to insert tools according to the preoperative plan. The Renaissance system is unique compared to the previous robots in that it is small and mounts directly onto the patient, reducing the consequences of patient movement during the operation. The downside of this arrangement is that the Renaissance is not very versatile, and is limited to a small number of procedures due to its small range of motion.

Several commercial robotic systems have also been developed for neurosurgery, particularly stereotactic brain surgery. The ROSA from Medtech (Montpellier, France) [16] and the Neuromate from Renishaw (Gloucestershire, UK) [17] are both large, stiff robotic arms which hold guides to allow precise insertion into the brain. Though large, stiff systems like these may work for brain surgery, it is unlikely they would be useful for most OHNS applications due to their bulk, cost, and lack of agility. In addition to holding instruments for brain surgery, robots have also been develop to enable precise manipulation of the operating microscope. The Surgiscope from ISIS (Saint Martin d'Hères, France) [18] is a large, ceiling mounted robot that enables precise positioning of an operating microscope, endoscope, or biopsy needles. Due to its large size and mass, the Surgiscope is mostly used simply for holding things still, rather than operating dynamically. Because of this, it is unlikely to have much use in many OHNS applications.

Robotic cardiac surgery has largely focused on robotic control of catheter systems. The Niobe from Stereotaxis (St. Louis, MO) [19], Sensei from Hansen Medical (Mountain View, CA) [20], and Amigo from Catheter Robotics (Mount Olive, NJ) [21] are all catheter based robotic systems for cardiac ablation. These systems work by providing precise robotic control over a catheter which is inserted into the patient's vein and guided to the desired location in the heart. Systems like this could potentially be useful for other applications which involve accessing ablation sites through the vascular system, such as cancer treatment, but they are unlikely to be of use in most OHNS applications.

Robotic flexible endoscope systems have also been developed in several different areas. The Invendoscope from Invendo Medical (Kissing, Germany) [22] is a robotic flexible endoscope system for colonoscopy. The system consists of a custom robotic endoscope with a steerable tip, and a flexible sheath that covers the endoscope shaft to reduce friction between it and the intestine wall. The portion of the Invendoscope which enters the patient is also disposable, enhancing hygiene, and eliminating the need for time consuming reprocessing which accompanies many endoscopic systems. However, since the

26

Invendoscope was developed for colonoscopy, it is unlikely it would find any applications in OHNS due to its size. The Flex system from Medrobotics (Raynham, MA) [23] is also a robotic endoscope, but it is unique in that it is largely targeted at OHNS applications. The Flex consists of both an endoscope for visualization, and ports for endoscopic instruments to be inserted. It is small enough to be used in some laryngeal applications, though it is unlikely it could be used in otology or sinus applications due to its size.

1.8.2.3 Commercial Non-Medical Robotics Systems

Some commercial robotic systems not originally designed for medical use have also been adapted to perform surgical tasks. The most notable of these is the Light Weight Robot (LWR) from KUKA (Augsburg, Germany). The LWR was primarily designed as a general purpose robotic platform for use in environments where human interaction is required, e.g. helping human workers on an assembly line [24]. It has also been used in medical applications such as manipulating endoscopes in minimally invasive surgery [25], controlling an ultrasound probe [26], and stereotactic applications like laser ablation of bone [27]. The LWR has many of the advantages of traditional industrial robots, such as speed, accuracy, stiffness, and large work volume. It also has many advantages over typical industrial robots, such as being relatively light weight, small, and compliant. This makes the robot well suited to teleoperation or autonomous tasks requiring large motions. However, the LWR is not well suited to head and neck surgery tasks which would be better performed with the cooperative control paradigm. The LWR has very complex kinematics, which could make it difficult to control when extensively guiding it by hand. Also, even though it is small and light for an industrial robot, it is still over 20 kg, much of which moves with the robot, which can result in substantial inertia. Its bulk is also evenly distributed across the arm, rather than concentrated away from the operating area, which can result in unnecessary obstruction of the surgical field. Though the LWR is a 7 degree of freedom arm, only 5 active degrees of freedom are needed for many surgical tasks when cooperative control is used [28], meaning the cost, size, mass, and complexity of the LWR are larger than necessary because of the extra motors and sensors for unneeded degrees of freedom. Finally, microsurgery with long instruments requires very high rotary precision in order to produce smooth motions under large magnification, and the LWR lacks the precision to do this.

1.8.2.4 Research Medical Robotics Systems for OHNS

In addition to the preceding commercial and non-medical systems, many surgical robotics systems are being developed and are still in the research phase. Since the number of research systems is orders of magnitude larger than commercial and pre-commercial systems [29] [30] [31], only select examples highly relevant to OHNS will be discussed here. As discussed above, the trend in commercial surgical robotics is that robots which do fine manipulation such as the da Vinci are teleoperated, whereas larger robots that do heavier applications like orthopedic bone drilling such as the RIO are cooperatively controlled. In spite of this, a series of research robotic systems developed at Johns Hopkins University have successfully used cooperative control to do very fine manipulation. The cooperative control paradigm overcomes many of the drawbacks of teleoperated systems, eliminating the large and costly master robots used in teleoperation, and giving the surgeon more direct access to the patient with less impact on established surgical protocols. In cooperatively controlled robots, the surgeon holds the surgical tool along with the robot. The robot senses the surgeon's intent through a force sensor, which is used to drive the robot accordingly [28]. However, since the robot is actually in control of the tool, the surgeon's input can be filtered or scaled to achieve better precision and eliminate hand tremor. Three generations of cooperatively controlled "steady hand" robots, including the Steady-Hand robot [28], Eye Robot 1 [32], and Eye Robot 2 [33], have been developed to verify the new control paradigm and study its performance in retinal microsurgery. These systems, however, were not optimized for head and neck surgery or use in the OR, and present several limitations including limited range of motion, bulky envelope, and large overall mass, preventing their direct application to head and neck surgeries.

Other research robotic systems have been developed specifically for OHNS, though they tend to focus on only one specific application, e.g. laryngeal surgery [34], [35] or otology [36], [37]. These systems also generally use the teleoperation paradigm, and present many of the same challenges as other teleoperated systems. Most, though not all, of these systems also require costly disposable customized instruments, which are not always economically feasible. Several groups have also reported development of robotic actuation for the tip of flexible endoscopes. Reilink *et al.* [38] combine computer vision techniques with robotic tip actuation for a hand-manipulated colonoscope. Although this assists in controlling the view and

28

advancing the endoscope, it still requires manual manipulation of the scope itself. Similarly, Eckl *et al.* [39] partially actuate a flexible endoscope for diagnostic use in the nasal cavity. This approach uses a two degree-of-freedom hand-held manipulator which controls scope rotation and tip angle, but not translation, which is left for the surgeon to control manually. This system is small and simple, but since the scope is not completely robotically controlled, its benefits during surgery are reduced. At the other extreme, a number of groups (e.g., [40], [41], [42], [43], [44]) have reported development of very sophisticated robotic systems for natural orifice surgery, providing bimanual telemanipulation of robotic arms and cameras at the end of flexible endoscopes. These systems, which are in various stages of development, tend to be complex and expensive compared to typical endoscopes. Finally, Children's National Medical Center has begun development of a robotic system for full manipulation of flexible endoscopes, however nothing has been published about this system except for a patent [45].

1.8.2.5 Prior Work Conclusions

Since development, regulatory, and training costs associated with medical robots are typically high, it is desirable for such systems to be as multi-purpose as possible. As the most prominent example, the da Vinci has been adopted for many minimally invasive laparoscopic procedures, most commonly prostatectomies and hysterectomies. The da Vinci has also been generalized to procedures far beyond the intent of its original design, including trans-oral surgery. This generalizability has been one of the main contributors to the da Vinci's success, however, neither flexible endoscope manipulation, nor instrument manipulation have been solved generally in head and neck surgery. Although the da Vinci has been reported for endolaryngeal surgery in select patents with favorable anatomy [46], [47] there is currently no robotic device available for general head and neck procedures [48].

1.9 Summary of Dissertation Contributions

1.9.1 Flexible Endoscope Manipulation

- Requirements and specifications for a robotic system to manipulate a flexible laryngeal endoscope [49].

- Design and implementation of a novel mechanical design for flexible endoscope manipulation [49], [50], [51].

- Cadaver study demonstrating effectiveness of the Robo-ELF Scope [52].

- Clinical version of the Robo-ELF Scope [53].

- Cadaver study demonstrating ease of use of the Robo-ELF Scope [54].

- FDA and IRB approved version of Robo-ELF Scope with human subjects study design.

1.9.2 Robotic ENT Microsurgery System Design and Development

- Requirements and specifications for instrument manipulation in OHNS [55].

- A novel design concept and mechanical design for a microsurgery robot for general purpose OHNS [55], [56].

- A novel design optimization method for specification-based design of parallel robots [57].

- A functional prototype demonstrating the feasibility of the design concept and mechanical design, and the validity of the design optimization [58].

1.9.3 Robotic ENT Microsurgery System Validation

- Calibration of REMS and validation that it meets technical requirements [59].

- Study demonstrating improved surgical precision using REMS compared to manual operation in two phantom models of microlaryngeal phonosurgery [59].

- Demonstration of feasibility of robotic microlaryngeal phonosurgery in a human cadaver.

- Demonstration of feasibility of REMS for microvascular suturing in an ex-vivo chicken model.

- Demonstration of feasibility of navigation in sinus surgery using REMS in human cadaver.

1.10 Summary of Relevant Publications

- K. Olds, "Global Indices for Kinematic and Force Transmission Performance in Parallel Robots" IEEE Transactions on Robotics, 2015 (in Press).

- K. Olds, P. Chalasani, P. Lopez, I. Iordachita, L. Akst, R. H. Taylor, "Preliminary Evaluation of a New Microsurgical Robotic System for Head and Neck Surgery" IEEE International Conference on Intelligent Robotics and Systems (IROS) 2014.

- C. He, K. Olds, I. Iordachita, R. H. Taylor, "A New ENT Microsurgery Robot: Error Analysis and Implementation" IEEE International Conference on Robotics and Automation (ICRA) May 2013.

- C. He, K. Olds, L. M. Akst, W. W. Chien, M. Ishii, I. Iordachita, and R. H. Taylor, "Evaluation, Optimization, and Verification of the Wrist Mechanism of a New Cooperatively Controlled Bimanual ENT Microsurgery Robot," In Proceedings of ASME International Mechanical Engineering Congress & Exposition, IMECE2012, Houston, Texas, USA, Nov. 2012.

- X. He, D. Roppenecker, D. Gierlach, M. Balicki, K. Olds, P. Gehlbach, J. Handa, R. Taylor, I. Iordachita, "Toward Clinically Applicable Steady-Hand Eye Robot for Vitreoretinal Surgery" In Proceedings of ASME International Mechanical Engineering Congress & Exposition, IMECE2012, Houston, Texas, USA, Nov. 2012.

- K. Olds, L. Akst, R. H. Taylor, J. Richmon, "Assessment of the Robotic Endolaryngeal Flexible (Robo-ELF) Scope by Novice Users" 8th International Conference on Head and Neck Cancer. July 2012.

- K. Olds, A. Hillel, J. Kriss, A. Nair, H. Kim, E. Cha, M. Curry, L. Akst, R. Yung, J. Richmon, RH. Taylor, "A Robotic Assistant for Trans-Oral Surgery: The Robotic Endo-Laryngeal Flexible (Robo-ELF) Scope" Journal of Robotic Surgery. Dec. 2011.

- K. Olds, A. Hillel, E. Cha, M. Curry, L. Akst, RH. Taylor, J. Richmon, "Robotic Endolaryngeal Flexible (Robo-ELF) Scope: A Preclinical Feasibility Study" The Laryngoscope, vol 121, issue 11. Oct. 2011.

- K. Olds, A. Hillel, E. Cha, M. Curry, L. Akst, J. Richmon, RH. Taylor, "A Robotic Assistant for Trans-Oral Surgery: The Robotic Endo-Laryngeal Flexible (Robo-ELF) Scope" Hamlyn Symposium on Medical Robotics. June 2011.

1.11 Chapter Summary

This chapter has presented background and motivation for this work, including an overview of OHNS as a whole with representative sample procedures, a summary of surgical challenges in OHNS, an overview of solutions to OHNS challenges, including conventional solutions, and both commercial and research robotic solutions, a summary of the proposed new solutions, and an outline of the contributions of this thesis.

Chapter 2   Robo-ELF Scope

The main goal of the Robo-ELF Scope project was to develop a simple robot to aid in flexible endoscope manipulation that could be easily translated to human procedures. My contributions include the requirements, hardware design, fabrication, documentation, and validation. Though I participated in some of the software design and debugging, most of the software work was done by other students including Elizabeth Cha, Jon Kriss, Tae Soo Kim, Steve Park, and Marcin Balicki, and is not discussed in detail here. Most of the clinical work and protocol design was done by Dr. Jeremy Richmon.

2.1   Analysis of Requirements

There are two main types of flexible endoscopes used in OHNS, fiber scopes Figure 2.1, which use a bundle of optical fibers to optically transmit images from the scope tip to an external camera which attaches to the back of the scope, and distal-chip scopes (Figure 2.2), which have an imaging sensor integrated into the scope tip and digitally transmit images to a video processor and don't require an external camera. Fiberoptic scopes are an older technology, and though they are generally cheaper, they are gradually being phased out in favor of distal-chip scopes due to the superior video quality they offer. Distal chip scopes also tend to be more durable, since the fibers in fiber scopes are prone to breaking when the scope is bent. Both types of scopes use a similar configuration of a handle with a thumb lever for manipulating the scope tip.
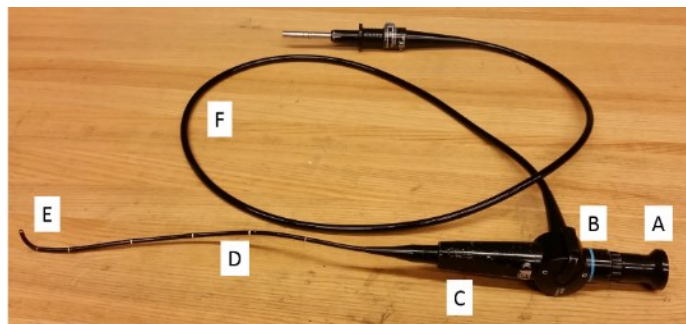
Figure 2.1: Fiber scope.

A) Camera port B) Thumb lever C) Handle D) Scope shaft E) Flexible tip F) Light pipe.
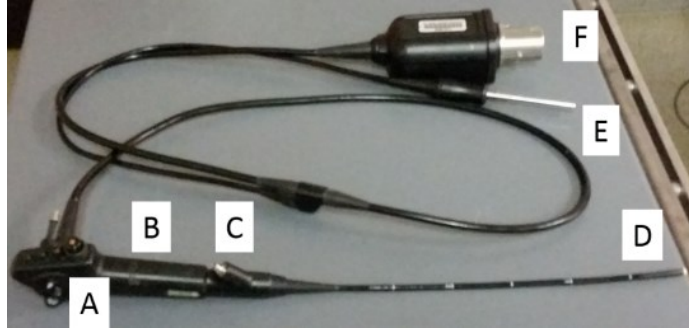
Figure 2.2: Kay-PENTAX VNL-1570STK distal-chip scope.

A) Thumb lever B) Handle C) Working channel D) Flexible tip E) Light pipe F) Video output

Flexible endoscopes in OHNS are typically used either through the nose or through the mouth. This restricts the useful degrees of freedom when controlling the scope to insertion/extraction, axial rotation about the scope shaft, and flexion/extension of the scope tip. A design concept prototype robot was built which combined a custom adapter that manipulates the thumb lever, with the LARS surgical robot that controlled the insertion/extraction and axial rotation (Figure 2.3). The user interface for the concept prototype consisted of a SpaceNavigator 3D mouse (3DConnexion, Rochester, MI) with its z-axis translation mapped to insertion/extraction, z-axis rotation mapped to axial rotation, and x-axis rotation mapped to tip extension/flexion. The custom scope adapter consisted of an Arduino microcontroller and a model airplane servo. Rather than trying to manipulate the scope's thumb handle directly, it was simpler to replace the handle with a 4-bar linkage mechanism which connected to the servo.
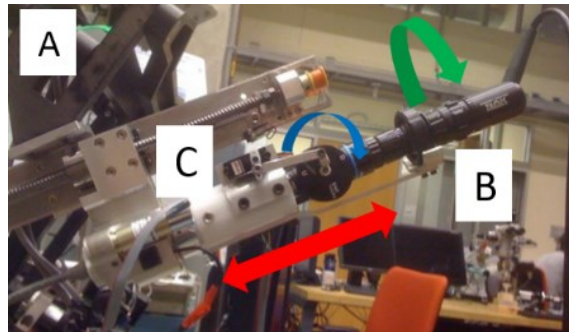
Figure 2.3: Robo-ELF Scope Concept Prototype

A) LARS robot B) Fiberoptic scope and camera C) Endoscope adapter. Insertion/extraction is shown in red, axial rotation in green, and scope tip flexion/extension in blue.

The validation experiment consisted of setting up the concept prototype with a rubber airway phantom and having clinical collaborators attempt to visualize anatomical targets around the vocal cords, Figure 2.4. Though it was determined the three degrees of freedom the system offered were sufficient to control the scope, there were also several issues. First, the servo motor was being controlled with an 8-bit PWM signal, so the position resolution was too coarse, and resulted in jerky movements. Second, though the linkage mechanism worked well, the cable mechanism in the scope itself which controlled the tip had substantial backlash and hysteresis. However, it was determined that much, though not all, of this was the result of the scope being old and no longer maintained. Third, it was difficult to control the system using the 3D mouse, since it has no way of separating degrees of freedom. This means that if the desired motion is a pure tip flex, it is difficult to perform a pure x-axis rotation without also producing motion in all other degrees of freedom.
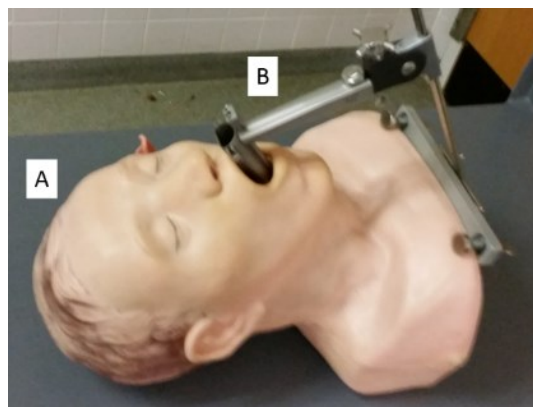
Figure 2.4: Airway phantom setup.

A) Airway phantom B) Laryngoscope.

Based on this experiment and extensive discussion with clinical collaborators and Clinical Engineering Services (CES), a list of requirements for a robotic scope manipulation system was developed, including both requirements for the active degrees of freedom (Table 2.1) as well as other general requirements (Table 2.2).

Table 2.1: Requirements for active degrees of freedom.

Requirement	Insertion/ Extraction	Axial Rotation	Tip Flexion/ Extension
Maximum Speed	25 mm/sec	90 deg/sec	90 deg/sec
Minimum Force/Torque	N/A	N/A	340 mNm
Minimum Range of Motion	100 mm	180 deg	180 deg
Resolution	0.1 mm	.23 deg	.23 deg

The resolution requirements were derived based on a lever arm of the scope tip of 25 mm.

$$25 \; mm * \Delta\theta = 0.1 \; mm$$

$$\Delta\theta = \frac{0.1 \; mm}{25 \; mm} \approx .004 \; rad \approx .23 \; deg$$

Table 2.2: Other requirements.

Requirement	Implementation
Sufficient passive adjustability of scope	x, y, z, and scope elevation angle
Cleanable with high level disinfectant	Enclosures/seals compatible with cleaning agents
Water-tight	All robot enclosures sealed
Material safety	
Allergens	No latex on robot exterior
Toxins	No lead or cadmium on robot exterior
Size	Minimum bulk around the patient
Redundant sensing	Two position sensors for each active joint
Mechanical durability	Robot must withstand being bumped in the OR
Mechanical safety	
Pinch Points	No pinch points
Stability	Robot must not fall while in use
Quick Removal	Robot must be removable to give access to the patient in less than 10 seconds
Electrical safety	
Chassis grounding	Chassis is well grounded (R < 0.1 ohms)
Power supply	Medical grade isolated power supply
Short circuit protection	3 A fuse on power to prevent short circuits
Emergency stop	Emergency stop button to shut off power to motors
Voltage	Robot voltages under 12 V
Current	Robot currents under 1 A

2.2 Robo-ELF Scope First Iteration

Based on the results from the concept prototype and the requirements list, a clinical quality prototype was developed. The first step was to finalize which endoscope would be used with the robot. Purchasing an endoscope for the project was not feasible because of the cost (~$30,000). At the time, the Johns Hopkins

Department of OHNS had an available demo model Kay-PENTAX VNL-1570STK distal-chip flexible laryngoscope (Pentax Corp., Golden, CO), so this was used for this project (Figure 2.2).

2.2.1 Design

Since keeping bulk away from the operative field is one of the main requirements, the initial mechanical design focused on keeping most of the actuators in an enclosure near the bedside away from the patient. The actuators would all be in this enclosure, and the motion for the axial rotation and scope tip flexion would be transmitted to enclosures near the scope using Bowden cables. In order to verify if this design was feasible, a simple mock-up was rapidly built using tape, foam core, and PVC pipe (Figure 2.5). After consultation with clinical collaborators, it was determined that this form factor was acceptable. The overall block diagram of the whole Robo-ELF Scope system is show in Figure 2.6. The system consists of the robot, an electronics enclosure, and a PC.
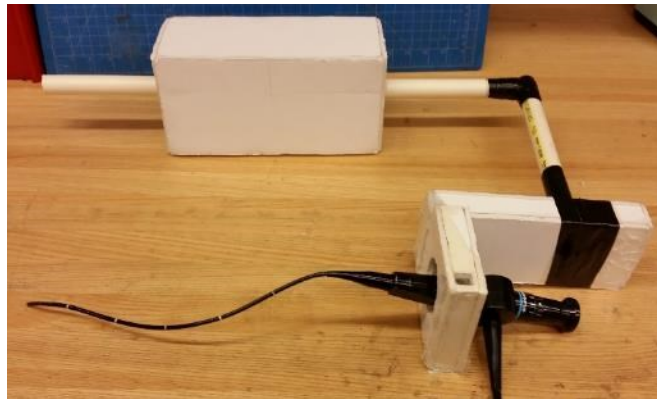
Figure 2.5: Robo-ELF Scope foam core prototype.
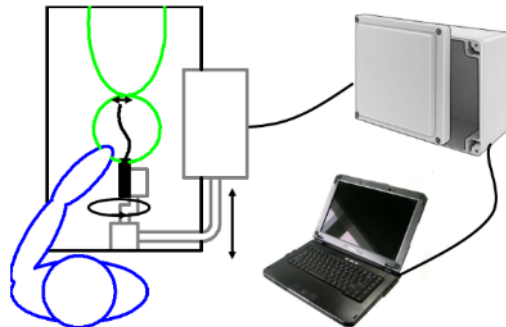
Figure 2.6: Robo-ELF Scope system block diagram.

Since being water-tight, durable, resistant to cleaners, and not exposing patients to allergens or toxins were all requirements, the next step was to determine suitable enclosures for the robot's components. Two main approaches were considered; purchasing existing enclosures meeting these requirements and modifying them, and manufacturing custom enclosures. After experimenting with several plastic, fiberglass, and cast aluminum stock enclosures, it was determined that a NEMA fiberglass enclosure rated for wash-down resistance was suitable for the main enclosure. It was determined that the remaining enclosures would be custom machined from aluminum in order to ensure durability and make manufacturing easier. The overview of the first prototype is shown in Figure 2.7.
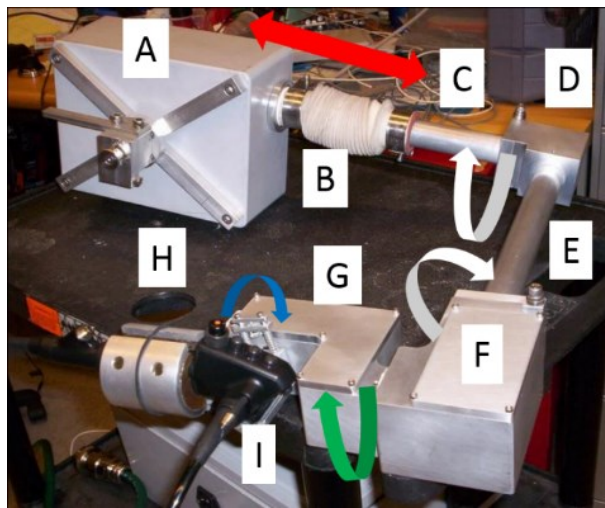
Figure 2.7: Robo-ELF Scope first clinical prototype.

A) Main enclosure B) Bellows seal C) First arm shaft D) Elbow joint with passive DOF E) Second arm shaft F) Axial rotation enclosure with passive DOF G) Scope holder enclosure H) Scope holder I) Scope lever manipulator. Insertion/extraction is shown in red, axial rotation in green, and scope tip flexion in blue.

The main enclosure contains all of the components for implementing the insertion/extraction DOF, including a linear bearing and guide rail, lead screw, belt drive, and DC servo motor with planetary gearhead (Micromo Micro Motion Solutions, Clearwater, FL) (Figure 2.8). 12 V DC servo motors with planetary gearheads and integrated magnetic encoders were used for every DOF in the Robo-ELF Scope for their compactness and simplicity to operate and control compared to stepper motors. The insertion/extraction DOF works by the motor turning the lead screw via the timing belt. The lead screw connects to a lead nut on the linear bearing carriage, which causes it to translate through a range of about 100 mm. The carriage connects to the robot arm's hollow shaft which leads to the rest of the arm. The joint

between the shaft and the main enclosure is sealed using a mounting flange and an medical grade rubber bellows, allowing the shaft to translate in and out of the main enclosure while maintaining a water-tight seal. The lid on the main enclosure is sealed with an O-ring seal on the lid. The lid attaches to the enclosure by four screws. Electrical signals and power enter the main enclosure via a water tight electrical connector.

The main enclosure also contained the motors for the axial rotation and scope tip flexion/extension DOFs. The axial rotation DOF consisted of a motor mounted on the linear bearing carriage with a pulley for actuating two Bowden cables (a pull-pull cable system). The Bowden cables ran out through the hollow arm shaft to the axial rotation enclosure. The scope tip flexion DOF consisted of a motor with a lever connected to a single Bowden cable (a push-pull cable system) which runs out to the scope lever manipulator in the scope holder enclosure.
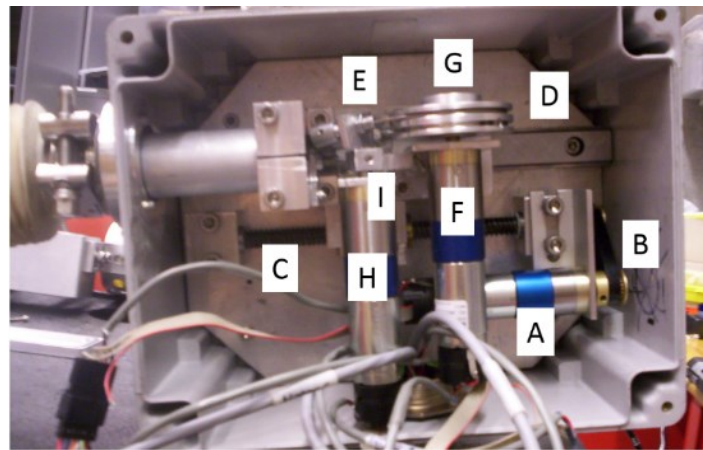
Figure 2.8: Robo-ELF Scope main enclosure.

A) Motor B) Timing belt and pulleys C) lead screw D) Linear bearing guide rail E) Linear bearing carriage F) Axial rotation motor G) Pulley for axial rotation cables H) Scope tip flexion motor I) Scope tip flexion lever

The robot arm's shaft emerges from the main enclosure and threads into the elbow joint. This joint allows the robot arm to swing away from the patient in case of emergency (Figure 2.9). The arm is held stationary by a shaft collar. Inside the elbow joint, an O-ring seals around the shaft to ensure the whole system remains watertight. On the distal side of the elbow joint, another hollow shaft emerges to connect to the rotation stage enclosure. This shaft is threaded and O-ring sealed in a similar way, but is fixed by a set screw rather than a shaft collar, since it is not adjustable by the operator. The other end of the shaft

forms the robot's "wrist joint" where it connects to the axial rotation enclosure through a similar threaded, O-ring sealed shaft collar clamped design, providing the capability to adjust the angle of the scope.
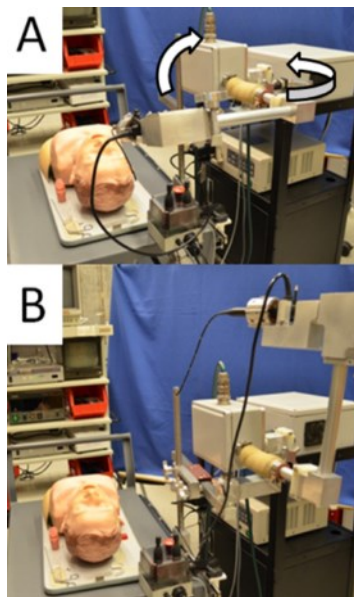
Figure 2.9: Elbow joint demonstration

A) To raise the arm, rotate the handle on the shaft collar and lift the arm B) In seconds the scope is out of the way.

The axial rotation enclosure is custom-made of aluminum with an O-ring sealed bolt-on cover. As discussed above, the power for the axial rotation DOF is transmitted from the motor in the main enclosure via Bowden cables. Support for the rotational motion is provided by two sealed bearings pressed into the rotation stage enclosure, through which a hollow stainless steel shaft is pressed. This hollow shaft threads into the scope holder enclosure, providing access to its interior, and is sealed with an O-ring. A second pulley is mounted onto this hollow shaft, providing the attachment points for the Bowden cables (Figure 2.10).

Figure 2.10: Robo-ELF Scope axial rotation enclosure.

The scope holder enclosure uses a similar design to the rotation stage enclosure, using aluminum with an O-ring sealed bolt-on cover. The scope holder enclosure supports the scope lever manipulator, which actuates the lever on the scope controlling tip flexion, as well as the scope gripper. The scope handle manipulator is spring-loaded to compensate for variations in scope positioning, such as if the rotation axis of the scope handle is not aligned with the axis of rotation of the manipulator, and uses medical grade plastic sleeve bearings to guide the spring mechanism. The Bowden cable from the motor in the main enclosure connects to the shaft from the scope hand manipulator, which is supported in the enclosure wall by a sealed ball bearing. The scope gripper consists of an aluminum frame with a urethane rubber insert, to prevent marring of the scope handle. The gripper is held shut with an elastic (Figure 2.11).
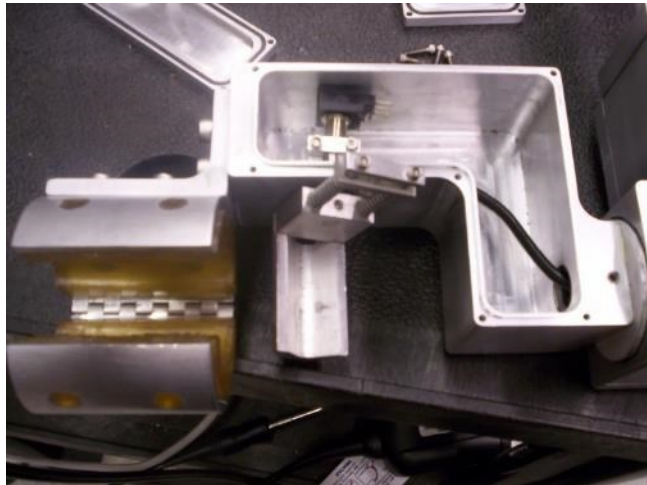
Figure 2.11: Robo-ELF Scope scope holder enclosure.

In order to support the robot and provide additional passive DOFs, the robot was designed to mount onto a Chung retractor (Figure 2.12), which is a standard large, stiff bedrail-mounted retractor already used

in the OR. The Chung retractor provides x, y, and z translation, as well as 2 DOFs of rotation, and can be locked in place after adjustment.

Figure 2.12: Chung retractor.

The electronics enclosure (Figure 2.13) contains the other electrical components that could not be incorporated into the main enclosure due to space constraints. These include a power supply, motor controller, emergency stop, and fans. The enclosure itself is from the same series of wash-down rated NEMA fiberglass enclosures as the main enclosure, but in a larger size. Since the electronics enclosure does not require surgeon interaction during surgery, it is only intended to resist incidental splashes and wipe-down cleaning. All of the signals entering and leaving the electronics enclosure pass through splash resistant connectors, except for the AC power input, which is on the back of the unit.

Power enters the enclosure through a standard hospital grade AC three prong plug. The plug connects to the enclosure through a power module which includes an on-off switch and a 2.5A fuse. The power is then connected to a linear isolated AC/DC converter with +12V and -12V outputs. A 12V cooling fan maintains air circulation through two air filters on opposite sides of the enclosure for cooling. The motors are controlled with a Galil model DMC 40x3 motor controller (Galil Motion Control Inc., Rocklin, CA) with four 1A, 20W linear amplifiers. Linear amplifiers were chosen over PWM because of their simplicity, low noise, low cost, and the low power needs of the system. The Galil controller has independent power inputs for controller electronics and motor power. The electronic power input is powered directly from the AC/DC converter, but the motor power input is in series with a manual emergency stop button. This ensures that the user can cut the power to the motors even if the Galil is not functioning properly. Earth ground is connected to the chassis of the AC/DC converter and Galil controller. Earth ground also passes

through a Souriau waterproof connector into the robot's main enclosure, where it connects to the robot chassis.

Figure 2.13: Robo-ELF Scope electronics enclosure.

The user controls the Robo-ELF Scope via a 3d mouse which interface with the PC via USB (Figure 2.14). The 3d mouse is capable of 6 DOF control, but since the Robo-ELF Scope only has 3 active DOFs, these were mapped directly to the three most intuitive mouse DOFs. The Robo-ELF Scope system was originally developed on a desktop PC, but was later moved to a laptop to save space and enable easier setup and takedown.
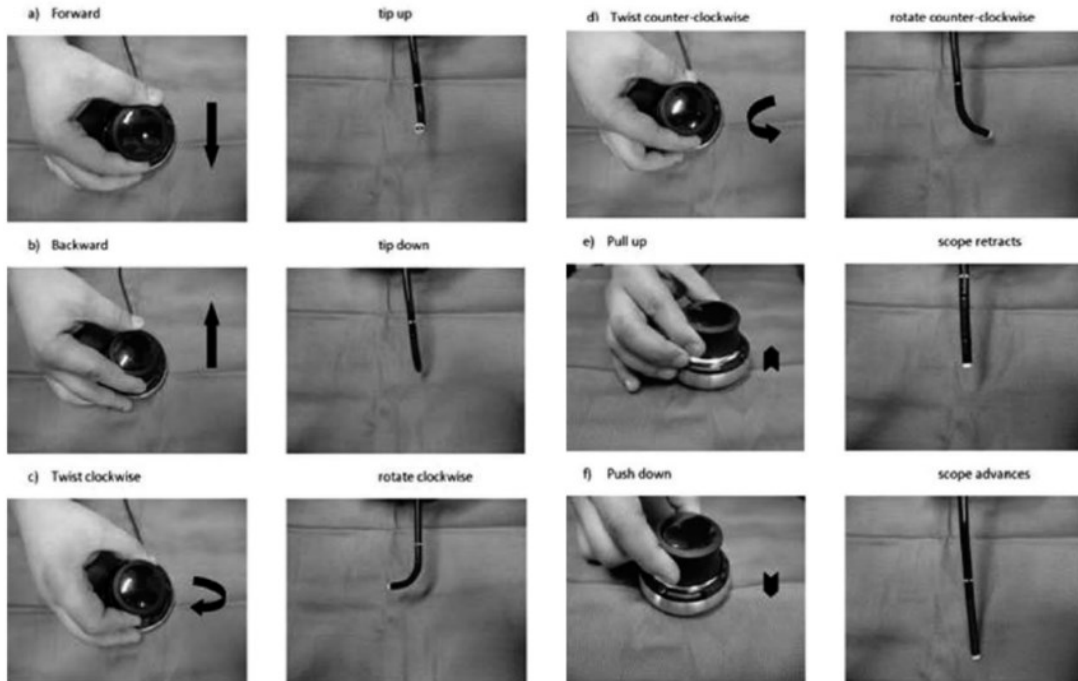
Figure 2.14: 3d mouse control of a flexible endoscope [52].

The software was written in C++ using the CISST libraries developed at JHU. Though I participated in the design and debugging of the software, the detailed design and implementation was done by Elizabeth Cha and Jon Kriss. The software block diagram (Figure 2.15) includes several tasks running on the PC: the robot task, which contains most of the control code, the space mouse task, which contains the interface to the space mouse and passes data to the robot task, and the GUI task, which had not been implemented yet. The control of the robot consisted of simply linearly mapping the values of the corresponding 3d mouse DOFs and robot DOFs with a gain. The Galil motor controller was running in velocity mode, so these values were translated into encoder counts/second and passed to it.

At this time only basic software safety features were implemented, including a basic heartbeat loop on the Galil to check if the PC had crashed. In the event of a PC crash, the system would stop all motion. However, there was no provision to stop the system if the Galil itself crashed other than the manual emergency stop button.
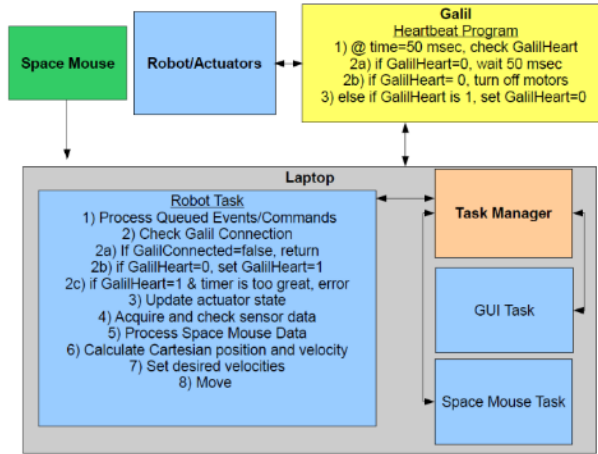
Figure 2.15: Software block diagram.

In order for development to move quickly, the goal was to get the most basic system possible running, then iterate and optimize the components, rather than trying to optimize anything before the system was running. Because of this, the first system test was carried out before many features were implemented, including: potentiometers and limit switches for the joints, a GUI, sophisticated control code, and full heartbeat code. The system was tested by having clinical collaborators try to visualize anatomical targets in a rubber airway phantom, similar to the test of the previous prototype (Figure 2.16), as well as a basic technical evaluation.

Figure 2.16: Robo-ELF Scope prototype 1 evaluation.

As part of the technical evaluation, the robot was evaluated for grounding and water resistance. In order to verify water resistance, the robot was submerged in a tub of water and left overnight. The next day, all of the enclosures were opened to check for any leakage. No leakage was found. The grounding test was

performed by clinical engineering services. It was concluded that ground resistance and leakage current were both within the acceptable range for a medical device.

The functional evaluation in the airway phantom yielded many useful results:

- When the robot was mounted on the Chung retractor, it was immediately apparent that it was not rigid enough to support the robot and maintain stable visualization.

- The robot was difficult to control using the 3d mouse. The mouse did not re-center precisely, which created a tradeoff between either a large deadband or drift when the mouse was released.

- Both fast motion and very slow motion are required to effectively use a scope so the small range of motion of the mouse made this difficult.

- The issues with separating the degrees of freedom of the mouse encountered before were even more apparent due to the higher resolution of the new robot.

- The Bowden cables added significant friction to the axial rotation DOF, which resulted in the motor being too weak to control it responsively.

- Tensioning the cables in the axial rotation DOF was also difficult because the bicycle brake cables that were used were too thick and stiff.

- The push-pull cable mechanism for manipulating the scope thumb lever created significant backlash.

- Needing a wrench to adjust the passive DOFs of the robot was too time consuming.

- The rubber band used to hold the scope gripper was not stiff enough, and was also too difficult to quickly take off and put on.

- A GUI is needed to understand the state of the robot, such as when limit switches are hit.

Based on the results of this evaluation, a series of revisions were made to the robot. Figure 2.17 shows the revised prototype. The robot was clamped onto a cart temporarily since building a support arm stiff enough with the required degrees of freedom would take significant time. The adjustment screws to lock the passive degrees of freedom were replaced with knobs to enable easy operation with no tools. The rubber band used to hold the scope gripper shut was also replaced by a stainless steel latch, enabling quick insertion and removal of the scope.

Figure 2.17: Revised prototype.

Significant changes were made to the main enclosure, including removing the motor and cable system for the scope flexion DOF, putting a new compact motor directly into the scope holder enclosure, upgrading the motor for the axial rotation DOF to one with more torque, adding a screw-driven mechanical tensioning system for the cables for the axial rotation DOF, and adding a linear slide potentiometer and limit switches to the insertion/extraction DOF. The cables for the axial rotation DOF were changed from bicycle brake cable to aircraft grade plastic coated cable, which significantly reduced friction (Figure 2.18).
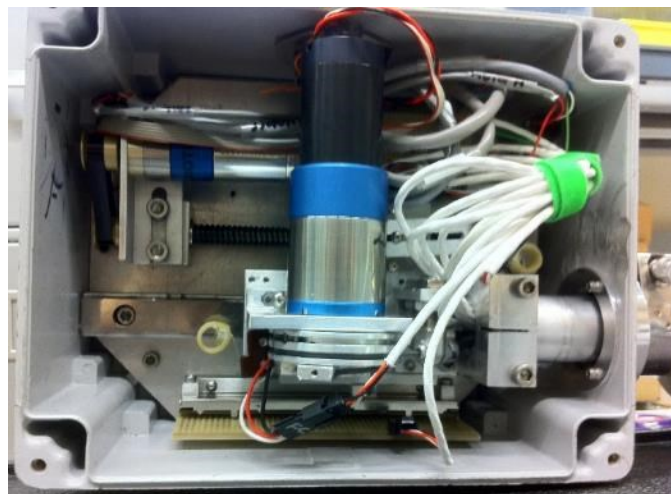
Figure 2.18: Revised main enclosure.

The axial rotation enclosure was upgraded to include a potentiometer and limit switches (Figure 2.19). The rotary potentiometer is mounted coaxially with the pulley, providing redundant sensing for added safety. Two limit switches are mounted along the face of the pulley, allowing adjustable stops mounted to

the pulley to actuate them when the joint reaches the limit of its approximately 270 degree range of motion. A mechanical stop is mounted between the limit switches to ensure that the joint cannot overreach its intended range.

Figure 2.19: Revised axial rotation enclosure.

The scope holder enclosure was significantly revised to include the motor for actuating the scope flexion DOF. The motor is mounted inside, and connects to the scope handle manipulator shaft via a four bar linkage. Adjustable stops are mounted on the linkage bar, which activate limit switches mounted adjacent to the bar when the manipulator reaches the end of its range of motion. A potentiometer is also mounted directly to the scope handle manipulator shaft to improve safety through redundant sensing (

Figure 2.20).
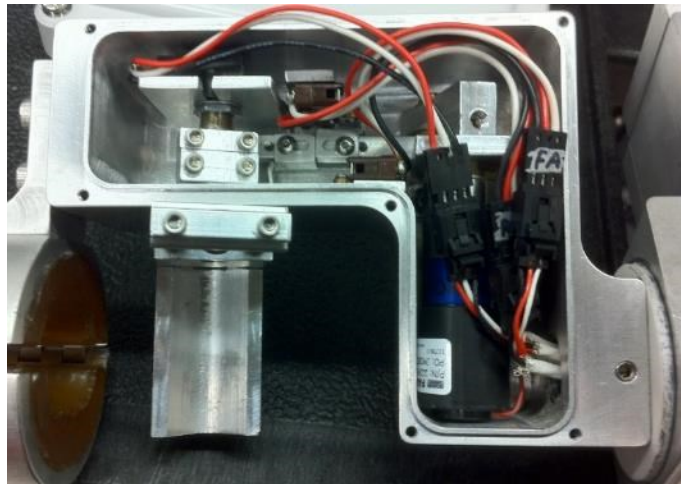
Figure 2.20: Revised scope holder enclosure.

The electronics enclosure was also revised, including a safety cover over the power supply, and an additional circuit board and wiring to handle the potentiometer and limit switch signals. The Galil supports both A/D conversion and digital I/O, in addition to motor and encoder channels, so it was used to interface all signals between the PC and the rest of the robot. The analog potentiometer signals from the robot's joints are buffered and low pass filtered on an analog signal conditioning board before entering the Galil's A/D ports. Power for all of the peripheral electronics (potentiometers, signal conditioning board, limit switches) is provided by the Galil's 5V and 3.3V outputs (Figure 2.21).

Figure 2.21: Revised electronics enclosure.

The software was revised in several ways, including a homing routine, additional safety features, improved control software, and a basic GUI. The homing routine runs on startup, and involves the robot running from its startup position to the forward limit switch, then back to the reverse limit switch. The robot then goes to the home position, which is half way in between the limit switches. The safety of the system was improved by checking both the potentiometer and encoder values to ensure that the position estimate from both agree (Figure 2.22). The control software for the space mouse was improved by using non-linear gains for the 3d mouse inputs that provide a wider range of output values given its small range of motion, as well as fine tuning its deadband to prevent drift. The GUI allows for visualization of basic robot state data such as limits switches and Galil connection state, as well as allowing the user to control the robot directly using the GUI (Figure 2.23).
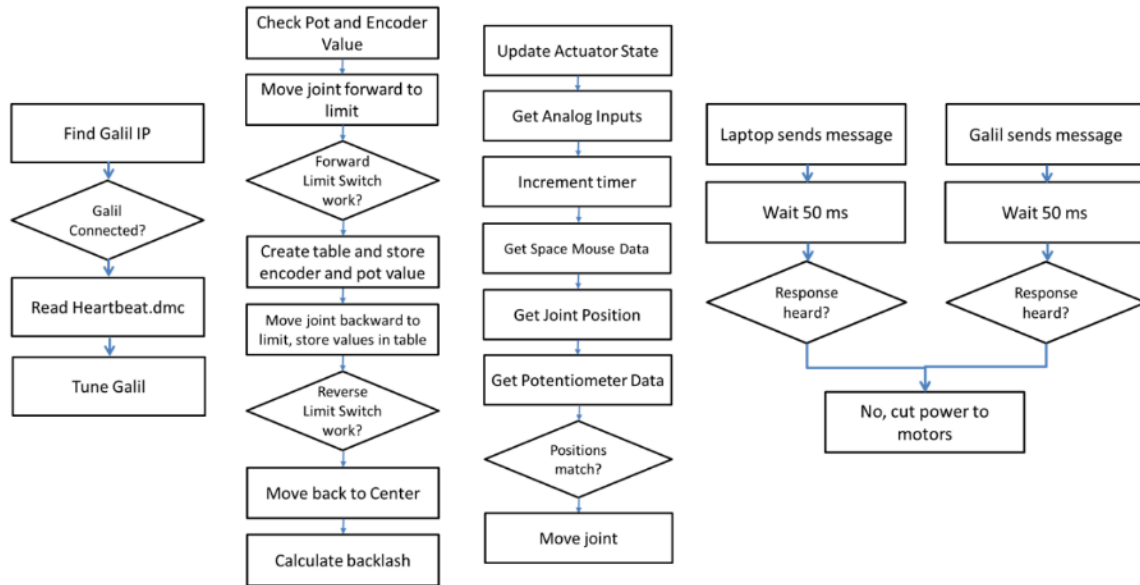
Figure 2.22: Software flow chart.
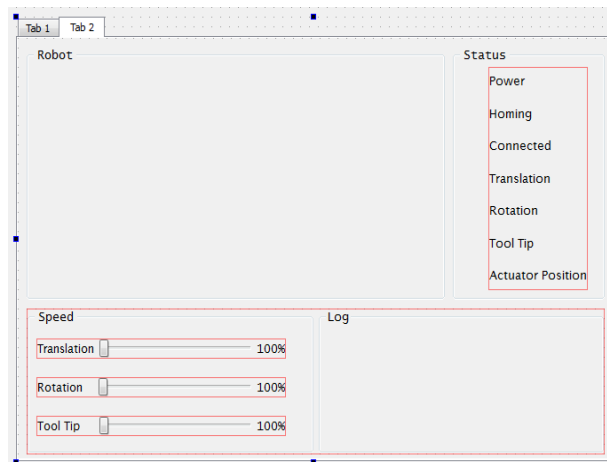
Figure 2.23: GUI overview.

2.2.2 Validation

2.2.2.1 Methods

In order to understand how the system would perform in a more realistic situation, an evaluation was conducted using human cadavers. Two fresh human cadavers were obtained from the University of Maryland State Anatomy Board after approval by the Johns Hopkins Hospital Minimally Invasive Surgical Training Center. Both were male with full dentition. Each cadaver was suspended with a Steiner laryngoscope to afford visualization of the endolarynx. Standard microlaryngoscopy was performed

initially using 0-, 30- and 70-degree rigid scopes. Representative photographs were taken of the endolarynx with each scope. The Robo-ELF was then mounted to the bedside and advanced through the scope (Figure 2.24).

Figure 2.24: Experimental setup for cadaver study.

The evaluation consisted of three tasks:

Task 1: To demonstrate comparable if not superior field of vision with the Robo-ELF scope. After the Robo-ELF was positioned, the 3D mouse was used to manipulate the scope in order to obtain the same endoscopic views afforded by the rigid scopes. The entire field of vision navigated by the Robo-ELF was then compared to that of the rigid scopes.

Task 2: To achieve optimal visualization of normally challenging anatomical areas with precise biopsy sampling. With one hand controlling the joystick and the other manipulating a laryngoscopic biopsy forceps, attempted biopsies were taken of the subglottis, anterior commissure and ventricle.

Task 3: To demonstrate the ability to perform two-handed microlaryngoscopic procedures with the Robo-ELF in a fixed position. The Robo-ELF was driven to an optimal position above the vocal cords and left in position such that two-handed microlaryngeal surgery could be performed.

Photo and video documentation of the above tasks were reviewed by the surgeon participants to compare the effectiveness of the Robo-ELF to the traditional rigid scopes.

2.2.2.2 Results

The Robo-ELF was easily positioned through the Steiner laryngoscope and movement in all three active degrees-of-freedom was smooth, consistent, and reproducible. The speed of robotic movement was reliably translated by the amount of force placed on the joystick. No erratic or sudden movement was present. The Robo-ELF provided a wider field of vision than that of the three rigid endoscopes. The flexible tip was capable of driving around the arytenoids into the piriform sinuses and through the vocal cords into the subglottis thereby overcoming limitations of line-of-sight. The distal chip scope provided a high resolution image and navigating the scope was intuitive with virtually no learning curve. The scope is controlled by a single hand joystick allowing instrument manipulation with the other hand. Visualization of the intended biopsy sites was successful in both cadavers. However, in the first cadaver the larynx was anteriorly positioned and despite a clear view of the subglottis and anterior commissure with the Robo-ELF in a flexed position, the straight laryngoscopic forceps were unable to reach these areas. Finally, it was established that after positioning the Robo-ELF above the vocal cords there was still ample room to use two instruments to perform bimanual endolaryngeal surgery.

2.3   Robo-ELF Scope Second Iteration

2.3.1 Design

Based on the results of the first study and the previously known issues with the system, several additional revisions were made to improve the user experience of the Robo-ELF make it usable in a human study. First, a passive support arm system was developed to enable easy and safe positioning of the Robo-ELF Scope. The passive arm allows the robot to mount directly onto the bed rail, rather than needing to be mounted on a separate cart as in the first experiment, which took up too much space and was difficult to maneuver. The passive arm has 6 DOFs shown in Figure 2.25.
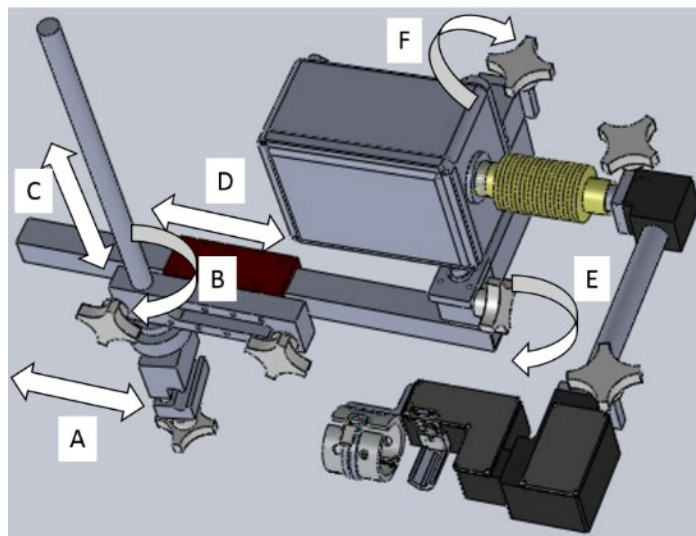
Figure 2.25: Passive arm dofs.

A) Sliding along bed rail B) rotation about support shaft C) height D) extending arm length E) horizontal rotation F) vertical rotation.

Though the 3D mouse worked for the purpose of the previous study, it has several flaws.

- Because of its sensitivity and small range of motion, it is very easy to bump it accidentally and produce unwanted robot motions.

- It has no way of mounting onto the bed, so is prone to falling off.

- It does not meet electrical or mechanical standards for being in the OR, meaning that no electrical safety information is known about it, and it is certainly not designed to handle wet environments. For the previous experiments, it had to be kept in a plastic bag while in use.

- Since it is rotationally symmetric, it is not easy to tell the directions of the x-y axes without careful examination.

- It has no redundancy to ensure that the system can tell when it is functioning properly.

- Even with fine tuning, it can still be difficult to move one degree of freedom in isolation.

In order to resolve these issues, a custom joystick system was developed. The custom joystick was designed to be very robust so it could be used in the OR in a human study (Figure 2.26). The joystick consists of a support arm which allows it to attach onto the bed rail, a NEMA splashdown resistant enclosure, and two wash-down resistant joysticks. In order to be maximally robust, binary joysticks were used, so each DOF is either fully on or off at any given time. A four position joystick is used to control the

tip flexion and axial rotation DOFs, and a two position joystick is used to control the insertion-extraction DOF. The joysticks themselves are watertight sealed industrial control joysticks which pass through the top of the enclosure.
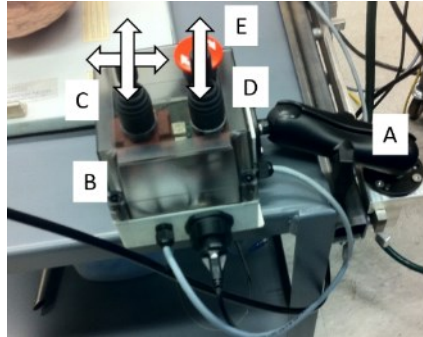
Figure 2.26: Joystick System.

A) Support arm B) Enclosure C) 4 position joystick D) 2 position joystick E) Emergency stop button.

Each joystick position controls two independent SPST switches, switching between 3.3V and ground, resulting in twelve independent signals. The 3.3V, ground, and joystick signals pass through a sealed cable gland and terminate at the Galil controller extended IO port. The Galil controller reads these signals and passes the information to the PC via Ethernet. The system is configured so that the robot will not move unless exactly one joystick position is on. Figure 2.27 demonstrates the mapping between the joystick axes and the robot degrees of freedom.

The joystick enclosure also contains a USB controlled electromechanical relay which is in series with a watertight harsh environment manual emergency stop button. The relay connects to the PC through a watertight USB connector. If the PC robot control software detects a fault in the system, then it can directly cut the motor power to the Galil controller. The surgeon can also directly cut power manually using the emergency stop button, which is also integrated into the joystick enclosure.
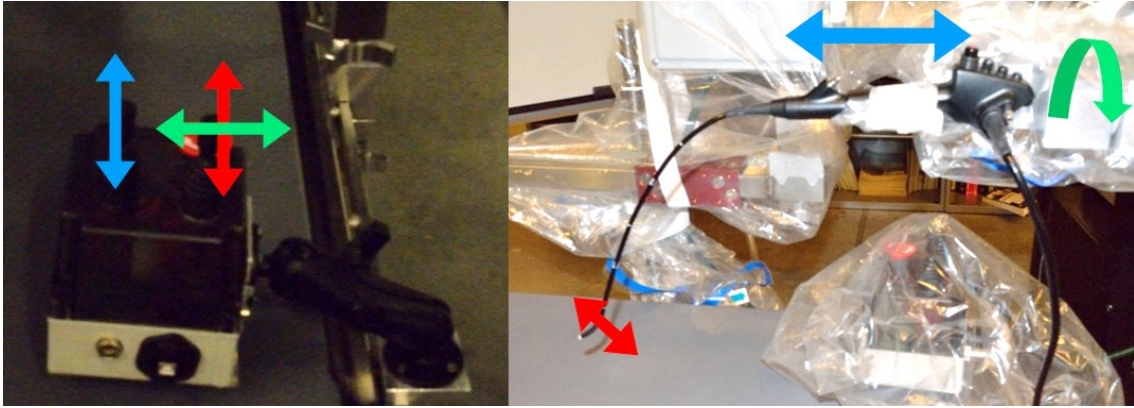
Figure 2.27: Correspondence between robot and joystick DOFs.

The joysticks should be operated as on-off switches in that once they move far enough past a threshold position, the robot will begin to move. Once the joystick is past this threshold, moving it further will have no additional effect. Because of the on-off nature of the joysticks, the best way to move the robot a small distance is to tap the joystick quickly. Also, once the joystick passes the threshold, the speed of the robot ramps up over the course of one second, so initially the robot will move slowly, enabling very precise independent control of each robot DOF.

The software was also upgraded to include additional safety checks, including a safety relay allowing the PC to shut off the motors in case of a Galil controller malfunction, re-settable calibration files to ensure the encoder and potentiometer values remain within a threshold or each other during operation, and safety checking for the joystick.

Figure 2.28 shows the completed second iteration of the Robo-ELF Scope. The components of the system not mounted to the bed rail, including the PC, electronics enclosure, and scope enclosure were all stored on a small cart. Also, in order to prevent the passive elbow joint of the robot from falling too suddenly when it is unlocked, an adjustable friction collar was added so that the joint will not move under its own weight.
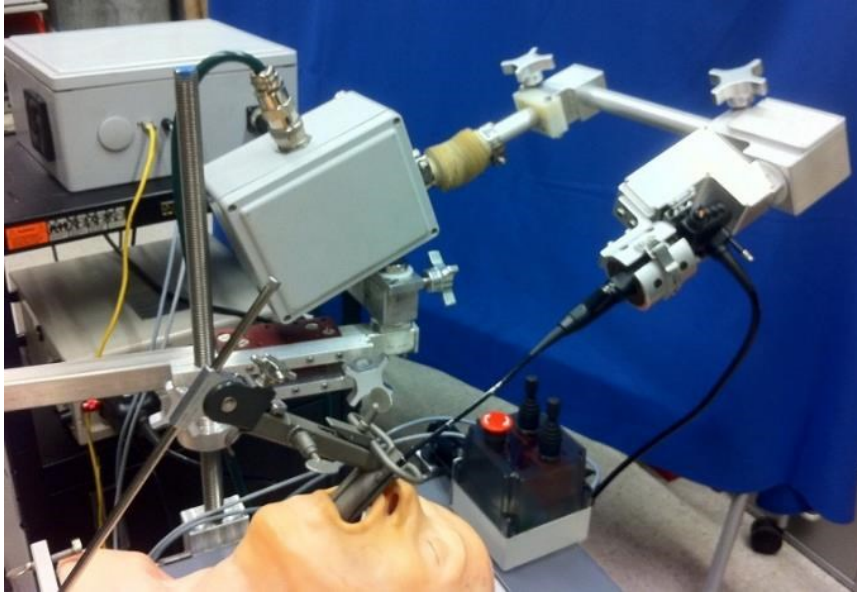
Figure 2.28: Robo-ELF Scope second iteration.

2.3.2 Validation

The system was first technically validated using the rubber airway phantom to ensure that the joystick control and safety features were all functioning properly.
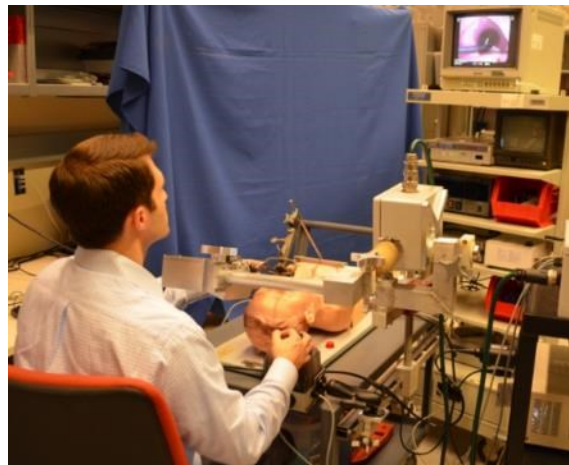
Figure 2.29: Robo-ELF Scope second iteration technical evaluation.

2.3.2.1 Methods

This improved version of the Robo-ELF Scope was then evaluated in one human cadaver to determine learning curve and ease of use. One fresh human cadaver with full dentition was suspended with a Steiner laryngoscope to afford direct visualization of the arytenoids but not of the anterior commissure, thereby

creating the view commensurate with an anteriorly displaced larynx. Seven otolaryngology residents naïve to the Robo-ELF were individually given a thirty second tutorial. This included instructions on docking and undocking the robot and how to control the joystick. They were then allowed approximately thirty seconds to familiarize themselves with the joystick controls (Figure 2.30). They were instructed to view all anatomic subsites of the larynx and advance into the subglottis until the carina was visualized. No time limit was given and assistance was provided if there were questions. At the end of the exercise each participant filled out a de-identified survey regarding the ease of use of the Robo-ELF.

Figure 2.30: Experimental setup.

2.3.2.2   Results

All residents completed the exercise in under five minutes. The survey results demonstrated that each item was scored as easy to very easy with the exception of visualization of the piriform sinus, which was neutral (Figure 2.31). This study has shown that residents with no prior experience with the Robo-ELF can learn to use it to view common anatomical sites of interest effectively within minutes.
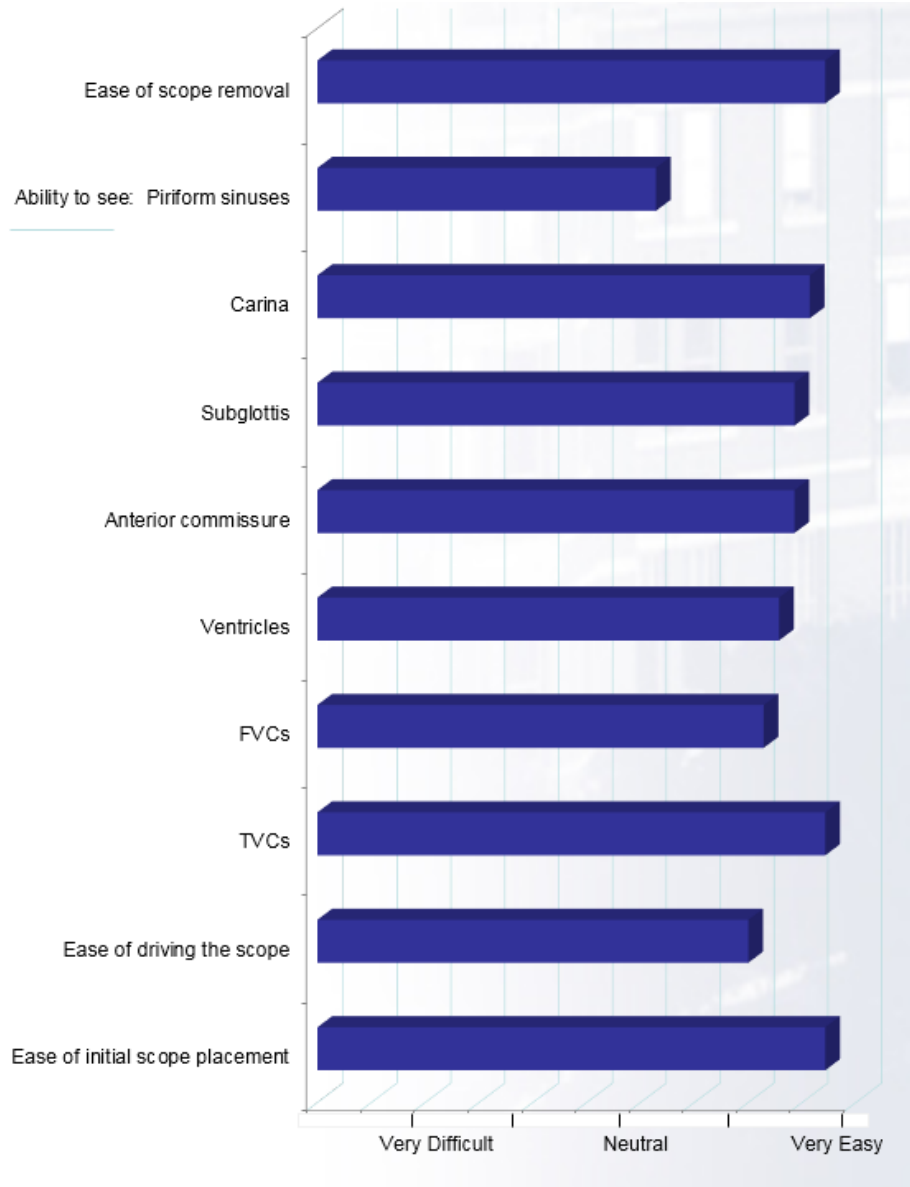
Figure 2.31: Resident assessment of ease of using the Robo-ELF for the first time.

2.3.3 Human Subjects Study

Based on these results, it was determined that the Robo-ELF Scope was ready to be validated in the OR with a human subjects study. A Johns Hopkins Institutional Review Board (IRB) protocol was then drafted and submitted to evaluate the performance of the Robo-ELF in 20 human subjects. The primary objective of this protocol was to demonstrate comparable if not superior field of vision with the Robo-ELF scope over standard rigid endoscopes in 20 human subjects. The secondary objectives are to achieve full

visualization of normally challenging anatomical areas to allow precise biopsy sampling, and to drive the Robo-ELF to a desired position and leave it in a fixed position in order to demonstrate the ability to perform two-handed endoscopic procedures. Photo and video documentation of the above tasks would be de-identified and reviewed by two blinded laryngologists to compare the effectiveness of the Robo-ELF Scope to the traditional rigid scopes. The laryngologists would be presented with all photos obtained from each patient and asked to rate the quality of each endoscopic image and the completeness of the overall endoscopic exam. Data would be recorded on Likert scales.

After this protocol had been submitted, the IRB responded that it had concerns that it did not have much experience with approving human studies for research robotic systems, and required that the system be reviewed by the Food and Drug Administration (FDA) to determine if it posed a significant risk. In response to this, a submission to the FDA was prepared which summarized the planned study and the Robo-ELF Scope system. The FDA responded with a list of concerns that would need to be addressed in order for the study to be considered non-significant risk (NSR). These concerns included requests for clarifications about the system and the protocol, some protocol changes, improved documentation including additional testing, and some changes to the Robo-ELF Scope system.

- Requested protocol changes included:
    - Exclusion of patients with active infections
- Requested documentation items included:
    - Risk assessment
    - User manual with step-by-step instructions for use
    - Photographs and diagrams of how the system will be set up and used in the OR
    - More detailed technical description
    - FDA clearance information for the endoscope
    - Detailed description of hardware and software safety checks
- Requested testing:
    - Verification of cleaning
- Requested system changes included:

o Covering the system with a disposable waterproof drape for reduced risk of cross-contamination

2.4 Robo-ELF Scope Clinical Prototype

2.4.1 Second FDA Submission

In response to the FDA concerns, a Failure Modes Effects Analysis (FMEA) was conducted (Table 2.1). The FMEA guided the development of both technical changes and documentation. It was determined that the main risk associated with the study was actually transmission of infections between patients. In order to mitigate this risk, it was determined that the Robo-ELF Scope and joystick would both have to be covered with water-tight plastic drapes during use, and detailed use and cleaning instructions would have to be created.

Another significant risk demonstrated by the FMEA was improper use and maintenance of the robot. In order to mitigate this, a full user manual and maintenance manual were created, as well as detailed software documentation. In order to verify that all of these mitigation strategies worked as expected, a test plan based on the FMEA was also implemented (Table 2.4). All of these documents were reviewed and approved at design review meetings.

Table 2.3: FMEA of the Robo-ELF Scope System

Severity Scale:
1 No harm to patient or operator and minimal disturbance to procedure
2 Minimal harm/chance of harm to patient or operator (very minor injury or disturbance to procedure)
3 Moderate harm/ chance of harm to patient or operator (minor injury or disturbance to procedure)
4 Serious harm/chance of harm to patient or operator (serious injury or significant disturbance of procedure)
5 Severe harm/chance of harm to patient or operator (life threatening or procedure failure)

Occurrence scale:
1 Extremely unlikely (should not occur during trials)
2 Minimal chance of occurrence (may occur once during whole set of trials)
3 Moderate chance of occurrence (may occur once in 10 procedures)
4 Likely chance of occurrence (may occur once in every 2-3 procedures)
5 Certain occurrence for each procedure

Detection scale:
1 Detection certain (fault will always be detected)
2 Detection probable (fault is likely to be detected)
3 Detection possible (fault has approximatley 50% chance of being detected)
4 Detection unlikely (fault will probably be undetected)
5 Detection impossible (fault will never be detected)

Item/ Function	Potential Failure Mode	Potential Effects of Failure	S	Potential Cause(s)	How Failure is Detected	O	Current Controls	D	RPN (SxOxD)	Recommended Actions
RoboELF	Unsanitary draping/undraping procedure	Spread of contamination between patients	4	Unsanitary draping/undraping procedure	Observation of torn drape or improper drape coverage, Observation of potentially contaminating splatter on robot	2	Draping and cleaning procedure; disposable parts	1	8	Follow proper draping and cleaning procedures
	Physical Injury to Patient or Operator	Robot falls on patient or operator	4	Incorrect Installation: Improper attachment to bedrail	Check stability in setup procedure	1	Check robot stability during setup; large margin for error in bedrail attachment system	1	4	Tighten joints as specified in manual; verify stability during setup
			2	Incorrect Installation: Improper tightening of joint collars	Check tightening of joint collars in setup procedure	2	Check robot stability during setup; all joints that could move due to gravity have friction collars to prevent unintended motion	1	4	Tighten joints as specified in manual; verify stability during setup
			3	Incorrect maintenance: Improper tightening of friction collars	Check tightening of friction collars during setup and maintenance procedures	1	Proper maintenance and checks during setup	1	3	Tighten friction collars according to maintenance specification
		Robot becomes electrified	3	Broken wire due to fatigue or improper assembly	Check robot grounding during maintenance, Fuse on robot electronics will trip if fault occurs in use. Circuit breaker on power strip as well.	1	Proper maintenance and electrical fuse on robot, proper grounding during manufacturing	1	3	Stop. Move the robot out of the way. Remove the endoscope from the robot. Continue surgery manually without the robot.
	Robot Becomes Unresponsive(Active). Possible uncontrolled motion, Robot could drive itself or endoscope into patient or operator	Computer could not accurately determine robot position	2	Simultaneous failure of potentiometer and encoder, preventing cross-checking	Detected by motor controller motion error	1	Galil Overcurrent check	2	4	Stop. Move the robot out of the way. Remove the endoscope from the robot. Continue surgery manually without the robot.
			2	Encoder or potentiometer failure due to manufacture defect, fatigue or faulty system wiring	Detected by cross checking between encoders and potentiometers	1	Cross checking between encoders and potentiometers; the controller stops the robot and informs the user of the error.	1	2	Stop. Move the robot out of the way. Remove the endoscope from the robot. Continue surgery manually without the robot.

Item	Potential Failure Mode	Potential Cause	Detection Method	Current Control	Rating	Recommended Action
		2 Loss of Ethernet Connection because of physical break or software error	Detected by Watchdog Timer	1 Watchdog Timer	1	2 Attempt to reinitialize system. If reinitializes successfully, then resume. If not able to reinitialize, then stop. Move the robot out of the way. Remove the endoscope from the robot. Continue surgery manually without the robot.
	Motor could move without a user command	2 Motor malfunction due to manufacture defect, fatigue or faulty wiring	Detected by motor controller motion error or cross checking between encoders and potentiometers	2 Galil Overcurrent check, Cross checking between encoders and potentiometers	1	4 Stop. Move the robot out of the way. Remove the endoscope from the robot. Continue surgery manually without the robot.
		2 Joystick malfunction due to manufacture defect, fatigue or faulty wiring	Detected by checking for inconsistent joystick commands or user observation of uncommanded motion	2 Emergency stop button, checks for inconsistent joystick commands	1	4 Stop. Move the robot out of the way. Remove the endoscope from the robot. Continue surgery manually without the robot.
Robot Becomes Unresponsive(Non-Active), No possible motion	PC unexpectedly becomes disabled	1 Internal Software error	Watchdog timer on Galil will stop system	1 Watchdog Timer	1	1 Stop. Move the robot out of the way. Remove the endoscope from the robot. Continue surgery manually without the robot.
		1 Power surge damages computer	Surge protector on power strip	1 Surge protector	1	1 Stop. Move the robot out of the way. Remove the endoscope from the robot. Continue surgery manually without the robot.
Scope damage	Scope cord not slack enough and becomes caught on something	3 Incorrect installation	Check range of motion of robot before procedure	1 Detailed setup instructions	1	3 Correct training for setup and surgeon
Robot damage	Robot runs into/tries to move past physical limits	2 Limit switch failure due to fatigue or manufacture defect	Detected by motor controller motion error	2 Galil Overcurrent check, Soft limits act as backup	1	4 Stop. Move the robot out of the way. Remove the endoscope from the robot. Continue surgery manually without the robot.
	Object blocking arm or internal jam in arm	3 Obstacles in range of motion, internal mechanical problem	Motor controller motion error	1 Follow setup instructions	1	3 Stop. Move the robot out of the way. Remove the endoscope from the robot. Continue surgery manually without the robot.

Table 2.4: Test plan based on the FMEA

Failure Mode	Test Method	Expected Results	Error Message	Actual Results	Date	Testers
Draping/Cleaning						
Water gets into motor controller enclosure and causes damage to controller	Pour water on all parts of robot to test seal	No water should get through seals	NA	No water penetrated seals	3/7/2013	Jonathan Kriss, Kevin Olds
Inadequate draping/undraping procedure	Spray drape with paint before removal	No paint should get through drape.	NA	No paint penetrated drape	1/30/2013	Jonathan Kriss, Kevin Olds
Drape tears	Attempt to tear drape during normal operations, adjust handles, scope, etc.	Drape should not tear during normal operation	NA	The drape did not tear under normal working conditions	1/30/2013	Jonathan Kriss, Kevin Olds
Joint/Arm Mechanical Failure						
Passive arm joint clamp becomes loose	Loosen joint clamp	Friction Collar should stop motion.	NA	Friction Collars(Properly tightened) stop motion as expected	1/10/2013	Jonathan Kriss, Kevin Olds
Friction collars not tightened correctly	Loosen collars	Loose joint will be clearly noticable while trying to make adjustments during setup.	NA	Joints are able to fall is joint is loosened. Add check in set up instructions to verify tight enough friction collars	1/10/2013	Jonathan Kriss, Kevin Olds
Incorrect Attachment to bedrail	Loosen attachment to bedrail	Robot should be unstable but not fall	NA	Robot is slightly unstable but not in danger of falling in any way, as expected.	1/10/2013	Jonathan Kriss, Kevin Olds
Object blocking arm or internal jam in arm	Block joint with immovable object, do not damage robot.	Galil current/torque limits stop robot.	Error! Motor Error Detected!	Galil error stops motion and turns off motors, as expected	1/10/2013	Jonathan Kriss, Kevin Olds
Motor failure due to broken wire or short	Disconnect power from a motor during motion.	Robot will not move on that axis.	None	Motion Stops, no error, as expected	1/10/2013	Jonathan Kriss, Kevin Olds
Mechanical break between the motor and joint	Loosen pot attachment during operation then command motion.	PC pot/encoder check will fail and stop motion. Estop activated.	System Error! Encoder Failure	Axis A: Encoder Failure Error, as expected. Axis B: Encoder Failure Error, as expected. Axis C: Encoder Failure Error, as expected.	1/10/2013	Jonathan Kriss, Kevin Olds
Switch/Joystick Failure						
Broken wire, short causes robot to become electrified	Test that case is properly grounded(Using multimeter)	All metal parts of the case should be electrically grounded.	NA	Case is properly earth-grounded.	1/10/2013	Jonathan Kriss, Kevin Olds
Limit switch mechanically fails during operation	Disconnect each limit switch in turn during operation	Software limits/physical limits stop motion. No apparent change in behavior	None	Software limits stop all axes, as expected.	1/10/2013	Jonathan Kriss, Kevin Olds
Limit switch mechanically fails before operation begins	Remove each limit switch in turn before operation	Physical limits should stop robot during calibration. Galil Motion Error should stop calibration	Calibration Fail	Motor Error during calibration, as expected	1/22/2013	Jonathan Kriss, Kevin Olds
Joystick mechanical failure: joystick cannot change switch settings	Remove switch assembly.	Robot should not respond to commands. Program should throw an error.	Joystick Error	Joystick Error, as expected.	1/10/2013	Jonathan Kriss, Kevin Olds
Joystick double switch failure	Simulate single switch failure(short switch)	Robot should not respond to commands. Program should throw an error.	Joystick Error	Joystick Error, as expected.	1/10/2013	Jonathan Kriss, Kevin Olds

Potentiometer/Encoder Failure

Failure Mode	Test Method	Expected Results	Error Message	Actual Results	Date	Testers
Pot has electrical or mechanical failure before operation begins	Disconnect wires from each pot in turn before operation	Calibration will fail or runtime checks will fail. Estop activated	Calibration Failed	Calibration Failed, as expected	1/22/2013	Jonathan Kriss, Kevin Olds
Pot has electrical or mechanical failure during operation	Disconnect wires from each pot in turn during operation	Runtime checks will fail immediately. Estop activated	Encoder Error	Encoder Error, as expected	1/22/2013	Jonathan Kriss, Kevin Olds
Encoder has electrical or mechanical failure before operation begins	Disconnect each encoder in turn before operation	Calibration will fail or runtime checks will fail. Estop activated	Calibration Failed OR Encoder Error	Calibration Failed, as expected	1/22/2013	Jonathan Kriss, Kevin Olds
Encoder has electrical or mechanical failure during operation	Disconnect each encoder in turn during operation	Runtime checks will fail immediately. Estop activated	Encoder Error	Encoder Error, as expected	1/22/2013	Jonathan Kriss, Kevin Olds
Both encoder and pot have electrical or mechanical failure	Disconnect several combination of pots/encoders(same, different axes) during and before operation	Calibration will fail or runtime checks will fail. Estop activated	Calibration Failed OR Encoder Error	Calibration Failed, as expected	1/22/2013	Jonathan Kriss, Kevin Olds

Communication Failure

Failure Mode	Test Method	Expected Results	Error Message	Actual Results	Date	Testers
Estop gets disconnected from PC	Unplug USB cord before/during run.	Before: Program should give error on startup. During: Program should stop. Power will be disconnected from motors.	System Error! Estop Connection Failed	Estop Connection Error, as expected	1/10/2013	Jonathan Kriss, Kevin Olds
Ethernet failure: motor controller loses communication with PC	Disconnect ethernet cable during different operation states (Initialization, Calibration, Runtime)	Init: Should see error during startup. Calibration: Robot should complete last issued move command then stop. Runtime: Watchdog timer should stop robot from PC. Estop activated	Connection Error! Check Connections and Restart System	Robot stops and an error is thrown as expected	1/10/2013	Jonathan Kriss, Kevin Olds
Galil Controller crashes or loses power	Turn off Galil during operation.	Watchdog timer should stop robot from PC. Estop activated	Connection Error! Check Connections and Restart System	Connection Error, Estop, as expected.	1/10/2013	Jonathan Kriss, Kevin Olds
Computer crash due to power surge or other failure	Kill PC program process during different operation states.	Watchdog timer should stop robot from Galil.	NA	Galil enters Abort mode and stops all motion, as expected	1/10/2013	Jonathan Kriss, Kevin Olds

In terms of technical challenges, draping the system presented two main challenges, first, in order for the drape to completely cover the robot but not the scope, the scope gripper would need to be changed, and second, a drape fitting the robot would need to be purchased or fabricated. It was determined that fabricating a drape for the Robo-ELF Scope was not feasible because of the costs and certifications involved. However, since the Robo-ELF Scope was not designed to be draped, it is an odd shape and the likelihood of finding a commercial solution was not high. In spite of this, it was discovered that the camera drapes for the da Vinci robot (Surgical Camera Arm Drape Ref: 420022 Ver: -02) fit the system perfectly, so this was the solution that was chosen. The joystick enclosure is a simple shape, so a commercial drape was readily available (Preferred Surgical Produces Band Bag with Tape 30"x30" Ref: BB-05).

With the drapes selected, the next step was to modify the scope gripper mechanism to be compatible with the drape. It was determined that having any holes in the drape or having any non-disposable part of the robot outside the drape would unacceptably complicate the cleaning process, so a new scope holder was 3d printed which would sit entirely inside the drape (Figure 2.32). After the robot was draped, the scope was simply taped onto the scope gripper on the outside of the drape with latex free surgical tape (Figure 2.33). Though this solution has some disadvantages, such as making it difficult to hold the scope very tightly, it significantly simplifies the draping and cleaning process of the system. The new scope gripper also includes a guard to prevent the scope lever manipulator from tearing the drape.

Figure 2.32: New scope gripper.

Figure 2.33: Scope mounted in new scope gripper.

The new draping method was evaluated by setting up the robot and joystick fully draped, then spraying it down with red latex spray paint. While the paint was still wet, the drapes were removed according to the instructions in the user manual. The robot was then inspected for any signs of paint, and none were found, demonstrating the effectiveness of the draping procedure.

In response to these FDA concerns, the system, documentation, and protocol were all amended and resubmitted to the FDA, resulting in the final clinical version of the Robo-ELF Scope (Figure 2.34). The FDA submission included:

- Cover Letter

    o Summarizing the submission

- Response to Concerns

    o Detailed responses to the concerns the FDA had to the previous submission

- IRB Protocol

    o Detailed IRB protocol outlining the experimental procedure

- Technical Description

    o Overview of the Robo-ELF Scope system

- Software Description

    o Detailed documentation of the Robo-ELF Scope software

- User Manual

    o Detailed description of setup, takedown, cleaning, and proper use procedures

- Failure Mode Effects Analysis (FMEA)

    o Detailed analysis of potential failure modes and their effects on the system, patient, and user

- Test Plan

  o A series of detailed tests carried out to verify that the mitigation strategies for the failure modes were working as expected.

- Maintenance Manual and Checklist

  o Instructions in how to properly maintain the Robo-ELF Scope system

- Publications

  o All publications related to the Robo-ELF Scope

- Meeting Attendance

  o Record of design review meetings

- FDA Readme

  o Overview of the contents of the submission
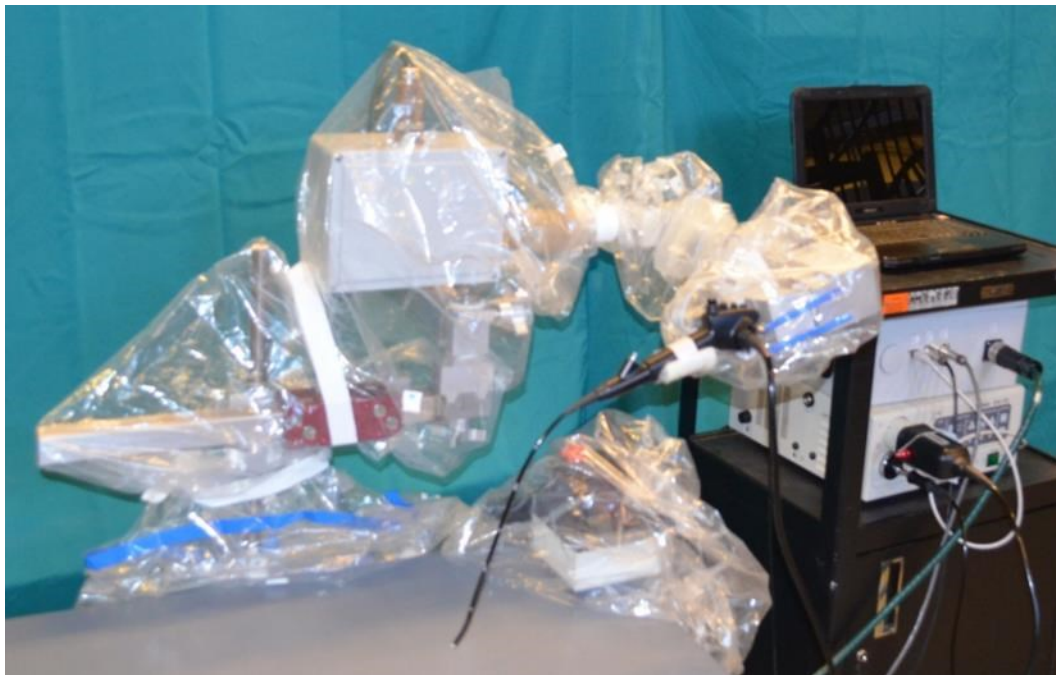
Figure 2.34: Clinical prototype.

2.4.2 Final FDA, CES, Perioperative Services, and IRB Submission

The second FDA submission was rejected due to clerical issues involving the formatting of the submission, but after these were resolved the final submission was accepted. The FDA concluded that the Robo-ELF Scope for the submitted protocol was non-significant risk, and the study was approved. The

67

system was then reviewed by Johns Hopkins Clinical Engineering Services for electrical grounding and was approved. Finally, the protocol was reviewed by Johns Hopkins Hospital Perioperative Services which objected to the scope being used since it is not compatible with the hospital's reprocessing equipment. To fix this issue, the IRB protocol was changed to use the Olympus ENF V2 flexible endoscope which is routinely used in the Johns Hopkins Outpatient Center. A new scope gripper was printed to fit the different shape of the scope handle, but the change did not create any new issues for the robot. The final IRB protocol with these changes was approved. The final FDA submission and IRB protocol can be found at [60].

2.5 Conclusions and Future Work

2.5.1 Chapter Summary

This chapter presented the design and development of the Robo-ELF Scope system for robotic flexible endoscope manipulation, particularly targeting endolaryngeal surgery. First, basic requirements were determined through analysis of the target surgical procedures, and evaluated using a basic concept prototype. Based on these requirements, a design concept for a clinically usable prototype was developed. The first prototype of the Robo-ELF Scope was then built and evaluated in a phantom, validating the concept while also pointing out improvements that would improve the system. After making revisions based on the phantom test results, the Robo-ELF Scope was evaluated in a human cadaver to determine if it could provide superior views compared to the state of the art. This cadaver validation showed that the Robo-ELF Scope could provide superior visualization compared to the state of the art, while also elucidating other areas for improvement before conducting a clinical study. Based on these results, the Robo-ELF Scope was revised again to make it clinically usable. Afterward, a second cadaver validation was performed which demonstrated not only that key anatomical targets can be visualized, but also that novice users can do so with only a few minutes of training.

Based on these results, a submission to the Johns Hopkins IRB was prepared to perform a human study involving using the Robo-ELF Scope for laryngeal endoscopy in 20 patients, and comparing the results to those obtained using the standard of care with rigid scopes. After several iterations of IRB and

FDA feedback, the final system and protocol were approved, and the system is now ready to begin the clinical study.

2.5.2 Conclusions

Though the process has been challenging, it is clear from these results that the concept of a robotic flexible endoscope manipulator is feasible. This will be the first time that a fully robotically controlled unmodified flexible clinical endoscope will be used clinically. In addition to the gains for this specific project, this endeavor has blazed a trail from concept to engineering to clinical use which can be used in future projects. The knowledge of how to get robotic clinical studies through the IRB, FDA, CES, and perioperative services will be invaluable to future projects. Additionally, the contacts made between the LCSR, the department of OHNS, and the hospital staff, will greatly enhance the future capability of Johns Hopkins as a whole to transition robotic technologies from research into clinical use.

2.5.3 Future Work

Once the clinical study is complete, the next step in bringing the Robo-ELF Scope into large scale clinical use is to build a second prototype designed for production and clinical use. This would likely involve significant emphasis on miniaturization of the current design, as well as significant cost engineering, refinement of ergonomics, and robust safety features. The regulatory process would likely be to get an IDE, perform a study, then apply for 510(k) clearance.

Another direction for future work is the development of advanced features. These could include improved control methods, such as touchscreen or motion control interfaces, and also advanced visualization methods such as robot-assisted 3d reconstruction from monoscopic endoscope images. With these more advanced control and visualization features, it may become possible to use the Robo-ELF Scope to perform robotically aided biopsy and ablation using fiberoptic lasers through the working channel of the endoscope. Other potential advanced features could include using additive manufacturing techniques to make parts of the Robo-ELF Scope disposable while reducing costs and reprocessing work.

2.6 Contributions

- Requirements and specifications for a robotic system to manipulate a flexible laryngeal endoscope [49].

- Design and implementation of a novel mechanical design for flexible endoscope manipulation [49], [50], [51].

- Cadaver study demonstrating effectiveness of the Robo-ELF Scope [52].

- Clinical version of the Robo-ELF Scope [53].

- Cadaver study demonstrating ease of use of the Robo-ELF Scope [54].

- FDA and IRB approved version of Robo-ELF Scope with human subjects study design.

Chapter 3   REMS Design and Development

The primary motivation for the REMS is to develop a general robotic system that is capable of addressing a broad set of surgical challenges, particularly those encountered in OHNS. My contributions include the analysis of requirements, high-level hardware design of the whole system, detailed design, optimization, and fabrication for the electronics, delta mechanism, tool holders, and passive support arm. I designed most of the kinematics and control software at a high level in MATLAB, and though I worked on debugging, the implementation in C++ was mostly done by other students including Preetham Chalasani, (then an MS student in CS), and Marcin Balicki (a CS postdoc). Some of the mechanical design, analysis, and fabrication for the rotary arm was also done by Alex He (a vising PhD student) under my supervision.

3.1   Analysis of Requirements

In order for the REMS to be practically useful, it must both address the surgical challenges discussed in the introduction (1.7), as well as meet other basic design requirements for use in the OR. Though this thesis only covers the development of an initial engineering prototype to demonstrate feasibility, this work is intended to lead toward a practical system for human use, so many of the requirements for the design have this in mind.

Table 3.1: REMS Requirements

Requirement	Value/Description
Degrees of freedom	To be generally useful, at least five active degrees of freedom are required, 3 translational and two rotational. The 3rd rotational degree of freedom (about the instrument shaft) can be passive for many applications, but it is desirable for it to be active for others.
Velocity	

Translation	At least 100mm/s for coarse movements.
Rotation	At least 60 degrees per second for coarse movements.
Force	At least 5 N load capacity for hand force + gravity.
Resolution	At least 0.025 mm minimum incremental movement at the tip of a 100 mm long instrument shaft.
Accuracy	At most 1 mm error (no load, after calibration) in positioning the tip of a 100 mm long instrument.
Stiffness	No more than 1 mm deflection at the tip of a 100 mm long instrument with 5 N load on instrument handle.
Size	
Overall	Must not obstruct access to the patient.
Near surgical field	Must not obstruct either visualization of the surgical field or
Weight	
Active range of motion	Must be capable of operating in deep (up to 100 mm), constrained spaces, as well as covering the area of a head (approx. 125 mm diameter cylinder).
Translation	125 mm diameter cylinder 125 mm in depth.
Rotation	+/- 60 degrees for positioning, +/- 20 degrees for operating.
Reach	Must be able to reach 300 mm over the bed (typical surgical bed is 250 mm from edge to center)
Passive adjustability	Must be able to passively adjust the position of the center of the workspace by +/- 150 mm in any direction.
Easy tool change	Must be able to insert and remove instruments in less than 5 seconds.
Easy to switch between robot and manual	Must be able to move the system from the surgical field and remove the instrument in less than 10 seconds.

3.2 Notation

This section summarizes the notation used.

Table 3.2: Basic Mathematical Notation

Name	Notation	Description
Matrix	X	Bold, italic, upper case
Vector	x	Bolt, italic, lower case
Constant	c	Italic, lower case
Non-index subscript	x_a	Lower case
Index subscript	x_a	Italic, lower case

Rotation matrices are represented as $R_i(\theta)$ which is a rotation matrix for a rotation of θ radians about the i axis where, for example, $i = x, y, z$.

Homogeneous coordinate transforms are represented as $[R, \quad t]$, which represents translation by $t = \begin{bmatrix} x \\ y \\ z \end{bmatrix}$ followed by rotation by R. This is equivalent to: $[R, \quad t] = \begin{bmatrix} R & t \\ 0\ 0\ 0 & 1 \end{bmatrix}$. In the special case of no rotation, $R = I$ where I is the 3x3 identity matrix.

3.3 Prior Work

Based on these requirements, the approach taken by the JHU Steady Hand family of robots [61], [32], [33], [62], seems the most promising as an inspiration for the design of the REMS. The cooperative control method has many advantages over teleoperation in general and in OHNS applications specifically. Since cooperative control requires no master robot, the system can be smaller, simpler, and cheaper. Also, since the surgeon can hold surgical instruments normally with robotic assistance, this approach is generally more intuitive than teleoperation and requires fewer changes to surgical procedures, requiring less training to become familiar. The cooperative control approach is also more flexible than teleoperation, since it is much easier to use different surgical instruments and keep some of their degrees of freedom manually controlled. The steady hand robots have also demonstrated that it is generally easier to bring a cooperatively controlled robot in and out of the surgical field as needed and change instruments quickly than with a teleoperated

system like the da Vinci. Cooperatively controlled robots have the added benefit of keeping the surgeon at the bedside, scrubbed and "in the game", as opposed to sitting at a non-sterile master console across the room.

The main reason for using the steady hand robots rather than other cooperative systems like the MAKO RIO, ROBODOC, etc. is that the general specifications (range of motion, precision, speed, size, etc.) of the steady hand robots are much closer to the requirements for OHNS than these other systems. Since 10+ prior years of work has been done with the steady hand robots, it is important to analyze each iteration and learn from the strengths and weaknesses of each system and how well each applies to OHNS.

3.3.1 Background

Before examining each steady hand system, it is important to understand the key concepts of cooperative control as well as the basic design principles of medical robotics.

3.3.1.1 Cooperative Control

Cooperative control is a form of admittance control. In admittance control, the force on the robot is the input, and the speed of the robot is the output, with the speed proportional to the force being applied. The force is typically sensed using dedicated force sensors.

$$\dot{x} = c_{admittance}f \qquad (3.1)$$

Admittance control is often contrasted with impedance control, where the speed of the robot is the input, and the force the robot applies is the output (typically with the direction reversed) with the force proportional to the speed that it is moving. The speed is typically detected using the encoders on the robot's motors.

$$f = -c_{impedance}\dot{x} \qquad (3.2)$$

The main advantage of admittance control over impedance control is that admittance control tends to be more transparent because the robot can respond to very small forces. In an impedance controlled robot, the user has to back-drive the robot in order for it to move, which requires a highly optimized low-inertia, low-

friction design in order to be feasible. This contrasts with admittance controlled robots which can be very stiff and not back-drivable yet still very responsive [63].

3.3.1.2   Remote Center of Motion (RCM)

Many types of surgical procedures require operating with instruments passing through an insertion point which should remain stationary. The goal is for the instrument to rotate about the insertion point as though there were a rotary joint at the insertion point. The insertion point is the center of motion for the instrument. However, putting a rotary joint at the insertion point is generally not feasible, since it would be in contact with the patient. To solve this problem, various hardware and software solutions can be used to force the instrument to rotate about the insertion point even though all of the joints of the system are remote from the insertion point. This is a remote center of motion. There are two main ways to implement a RCM, hardware and software. In a software RCM, the RCM constraint is entirely virtual and relies on the robot's control software to ensure that the instrument is constrained at the insertion point. In a hardware RCM, the robot's joints are configured in a way such that the instrument is mechanically constrained to pass through the insertion point.

3.3.1.3   Resolving Forces

One issue often encountered with admittance controlled robots is that the force sensor(s) resolve forces at the location where the force sensors are, rather than where the user's hand is. This can lead to highly unintuitive behavior since humans are generally used to objects responding to their hand force where the force is being applied. To resolve this problem, the place where the forces are resolved can be transformed in software to produce more intuitive behavior. This approach can also be used to create a pseudo-RCM behavior by placing force resolution point at the RCM point. The mathematics of transforming the force resolution point are covered in (3.5.7).

3.3.2 Original Steady Hand Robot

The original steady head robot (Figure 3.1) was developed for general microsurgery and evaluated for use in stapedotomy, an OHNS application, as well as retinal surgery [61]. The system had 7 degrees of

freedom, 3 Cartesian stages providing overall translation, a roll joint providing one rotational DoF, a chain-drive RCM mechanism providing a second rotary DoF, an insertion stage providing an axial translation along the instrument shaft, and a rotational DoF for rotation of the instrument about its axis. It had a workspace of about 100 mm x 100 mm x 100 mm with a top speed of ~40 mm/s and .0025 mm resolution.
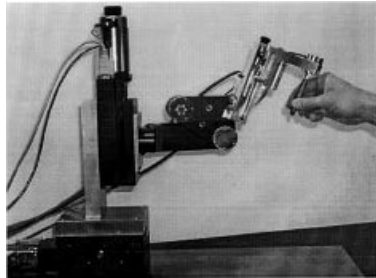
Figure 3.1: Original steady hand robot.

Though this system pioneered cooperative control for microsurgical tasks and was a functional research platform, it presented several significant limitations which would need to be overcome in order for it to be a practical system for OHNS.

- 40 mm/s is too slow. Many OHNS surgeries require instruments to be inserted and removed many times over the course of an operation. If these motions are limited to 40 mm/s, then it will significantly slow the operation down.

- A 100 mm cube is too small a workspace for many OHNS procedures. Though many surgeries can be performed within 100 mm, this requires precisely aligning the workspace of the robot with the surgical area at the beginning of the operation, which is often difficult and impractical.

- .0025 mm resolution is unnecessarily high for most OHNS applications. Specialty areas like retinal surgery may require this level of precision, but this is not typical for OHNS. This high level of precision is not in itself a problem, but the extra weight and cost of the system components to achieve this are unnecessary.

- The chain drive RCM is bulky and complex, and it is difficult to tune for optimal performance.

3.3.3 Eye Robot 1.0

The JHU Eye Robot 1 (ER1) was designed to address many of the issues with the Steady Hand system while specializing in ophthalmic surgery [32]. ER1 use a similar translation stage system, but

replaces the bulky chain RCM with a very compact 2 DoF rotary arm. The new rotary arm did not have a mechanical RCM, and the system relied instead on a software RCM.
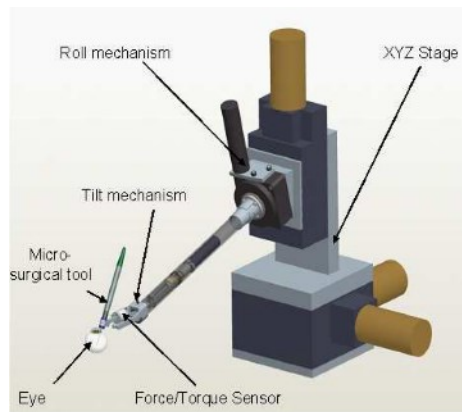
Figure 3.2: JHU Eye Robot 1

Though the ER1 design was very compact, it also had some significant drawbacks.

- The issues relating to the workspace and speed remained from before, but now the limitations of the roll and tilt rotations was more severe (+/- 30 degrees). Though many operations can be performed with a +/-30 degree envelope, this does not account for the sometimes significant motions required to align the robot with the operating field.

- Another major drawback was that the virtual RCM required the linear stages to be active in order to enforce the constraint. Their slow speed and acceleration combined with the sometimes high rotational velocities required resulted in sluggish performance.

3.3.4 Eye Robot 2.0

The JHU Eye Robot 2 (ER2) was created to address the issues with ER1 and to further refine the system for retinal surgery [33]. ER2 used a 5-bar linkage mechanical RCM which provided hardware RCM functionality without the bulk of the previous chain drive mechanism. It also incorporated higher-quality ball-screw linear stages for less friction and better performance.
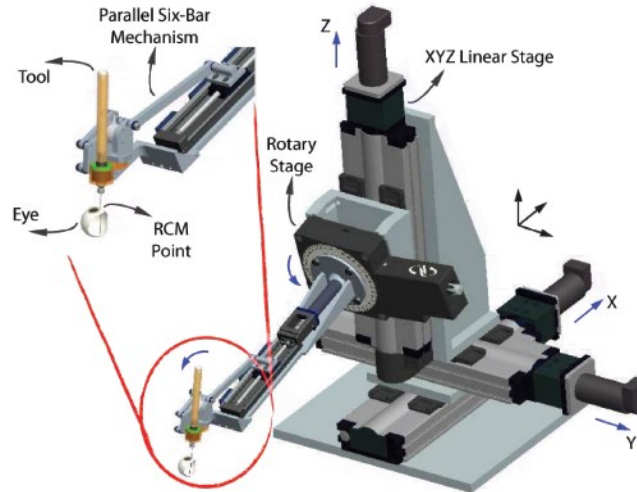
Figure 3.3: JHU Eye Robot 2.

Though many of the issues relating to the RCM were fixed compared to ER1, ER2 still had some significant drawbacks:

- The new linear stages were even bigger and heavier than ER1's, and ER2's motors were not powerful enough to accelerate this extra mass to provide the required agility.

- The total mass of the system was over 25 kg.

- The footprint is much larger than ER1.

- Like all previous designs, there was no easy way to adjust the orientation of the robot, making it difficult to align with the surgical field.

3.3.5 Eye Robot 2.1

JHU Eye Robot 2.1 (ER2.1) was developed to overcome some of the drawbacks encountered with ER2 [62]. The main changes were some electronics and cable management improvements, as well as significantly more powerful motors and an upgraded RCM mechanism.
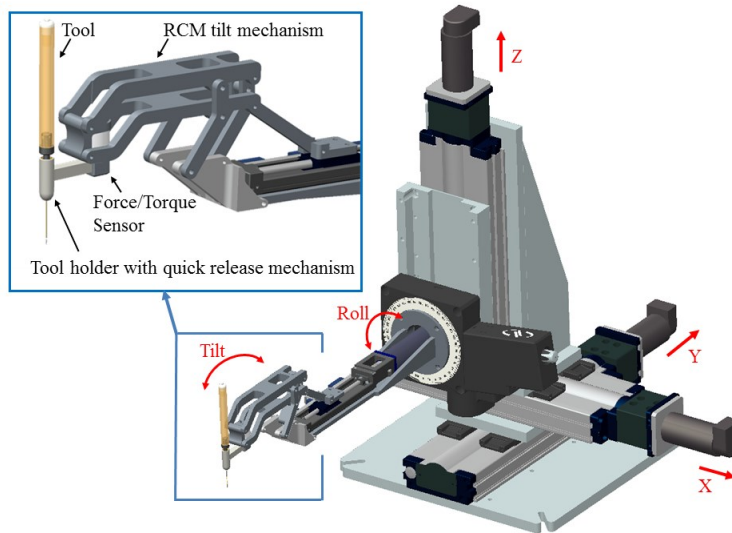
Figure 3.4: JHU Eye Robot 2.1.

Though these improvements did improve the dynamic performance of the system. The size, weight, and passive adjustment problems were still present. Even though the motors were now powerful enough to achieve significant accelerations, the significant reaction mass of the system made it difficult to use since it was capable of shaking even very sturdy tables that it was used on. Also, the range of motion (100 mm cube) was still too small for most OHNS applications.

3.3.6 Conclusions

In conclusion, the JHU steady hand series of robots provide significant insights in the challenges of using cooperatively controlled robots for microsurgical tasks. It is also important to remember that most of these systems were specifically designed with ophthalmic applications in mind, so it should be no surprise that they do not meet all of the requirements for OHNS "out of the box". In spite of this, the steady hand approach is the most likely to succeed in providing a practical platform for general OHNS. The main unresolved issues to use a system like this for OHNS include:

- Excessive weight and footprint

- Bulky RCM mechanisms

- Insufficient range of motion (particularly translational)

- Insufficient passive adjustability

- Insufficient agility

3.4 Design Concept

Most of the issues with the eye robot systems are related to the RCM and to the translation stages. Since most OHNS applications require much less rotary motion during operation (+/- 20 degrees) vs ophthalmic applications (+/- 45 degrees) a virtual RCM is probably sufficient. However, the virtual RCM puts even more range of motion demands on the already insufficient translation stages. The weight and size of the translation stages are a serious design concern, since as the stages get bigger and heavier for more power, the bottom stage has to carry more weight, requiring it to be even bigger and more powerful. One way to break this positive feedback loop is to use a different mechanism to provide translation which does not require the translation stages to carry each other. The most straightforward way to achieve this would be to use a parallel mechanism to provide these degrees of freedom. The two most popular parallel mechanisms capable of providing these degrees of freedom are the Stewart Platform, and the Delta Robot (Figure 3.5). The Stewart platform, also known as a hexapod because of its six legs, uses linear actuators with universal joints at each end to control all 6 degrees of freedom of a mobile platform. The delta robot, in contrast, uses three rotary arms connected to three parallelogram linkages to provide three translational degrees of freedom. Each parallelogram adds an orientation constraint on the mobile platform, with all three fully constraining it to remain parallel to the base, allowing only three degrees of freedom of translation.
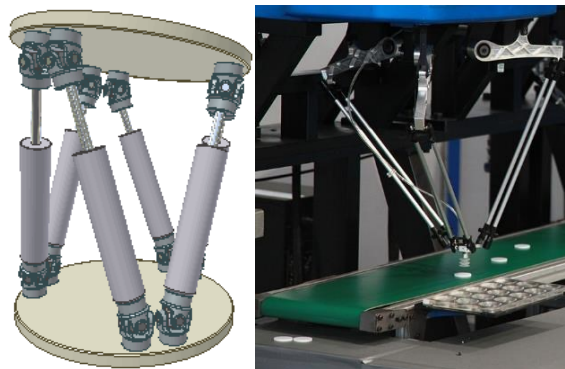
Figure 3.5: Left: Stewart Platform Right: Delta Robot.

(Image Credit: Wikipedia)

Historically the Stewart platform has been the more popular of the two for medical applications, while the delta robot has been used mostly for large-scale overhead industrial pick and place applications. As of this writing, I am aware of only one previous delta robot used for medical applications; the SurgiScope, which, like commercial delta robots, was a large, overhead system for holding surgical microscopes and other instruments. The Stewart platform has many drawbacks for this surgical OHNS application, including:

- It is a 6 DoF mechanism, while only 3 are required.

- Its range of motion is typically small compared to size.

- It requires 6 typically expensive actuators to get good performance.

The typical rotary version of the delta robot also has several drawbacks, including:

- Uncontained swinging arms making it dangerous to stand near.

- Typical systems are designed for high-speed pick and place and do not have the stiffness required for surgical applications.

However, the original patent [64] for the delta robot contains another variant which until very recently was almost never used commercially or in research, the linear delta robot. Rather than using swinging rotary arms to provide actuation, it instead uses linear actuators. This improves stiffness and also eliminates the dangerous swinging arms, making it the ideal candidate for this surgical application. Crucially, all variants of the delta robot have all of their motors located on the base, allowing the mobile platform to be very light and agile. One drawback of the linear delta robot is that since it is used so infrequently, there are no suitable commercially available systems, and also limited literature on its analysis.

With the problematic Cartesian stages replaced by a linear delta robot, the steady hand concept becomes much more viable for OHNS, and it becomes reasonable to rely on a virtual RCM, which eliminates the bulk and complexity of a hardware RCM. Based on these findings, a design concept for the REMS was developed (Figure 3.6).
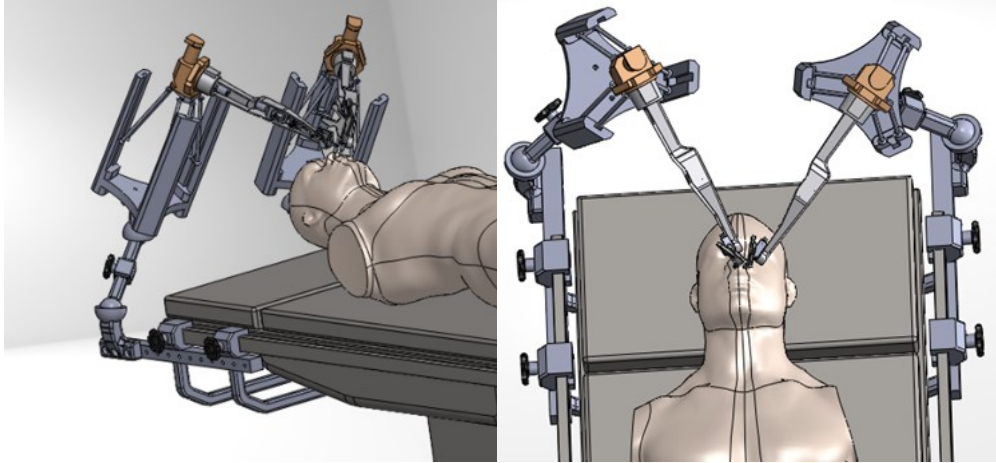
Figure 3.6: REMS Concept

One of the key features of this concept is how easily the compact, light-weight robot modules can be reconfigured for different surgery types (Figure 3.7).
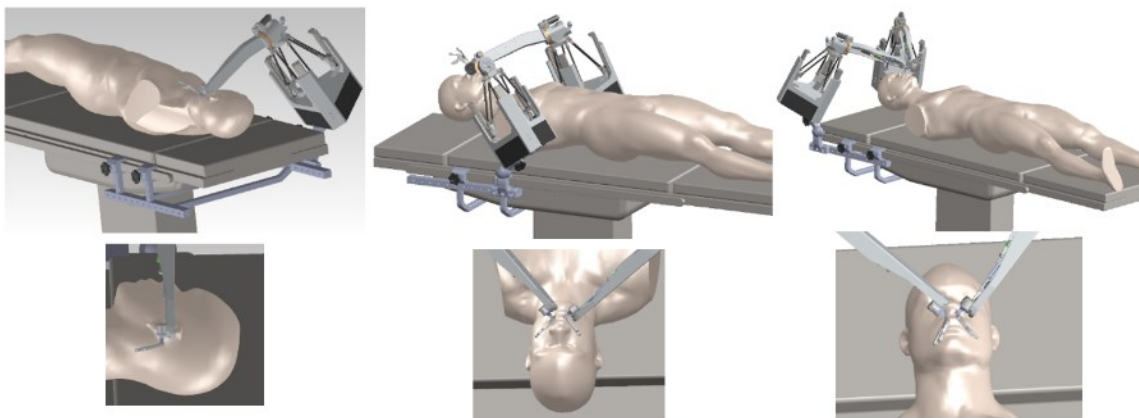
Figure 3.7: REMS configurations.

Left: Otology. Middle: Laryngology. Right: Sinus.

3.5 Kinematics

Now that the basic REMS concept has been established, the next step is to derive its kinematics, which are essential for optimizing the design.

3.5.1 Frames and Parameters

The three main coordinate frames of importance for the kinematics of the REMS are the base frame F_b located at the center of the base of the REMS (see Figure 3.8), the delta frame F_d located in the center of the mobile platform of the delta mechanism, and the tool tip frame F_t located at the tip of the tool shaft. The active degrees of freedom include z_1, z_2, and z_3, the positions of each of the delta linear actuators, θ_r, the rotation of the roll joint, and θ_t, the rotation of the tilt joint. The kinematic parameters of the REMS include r_b, the radius of the base, p_l, the length of the delta parallelograms, p_w, the width of the delta parallelograms, r_d, the radius of the mobile platform, h_r, the distance from the mobile platform to the axis of rotation of the roll joint, h_a, the distance from the axis of rotation of the roll joint to the arm, l_a, the length of the arm from the roll joint to the tilt joint, l_t, the distance from the tilt axis to the tool axis, h_t, the length of the tool from the tilt joint to the tool tip, and l_h, the length of the tool handle. The joint space of the robot consists of $(z_1, z_2, z_3, \theta_r, \theta_t)$, and the workspace consists of $(x_t, y_t, z_t, \theta_r, \theta_t)$. Note that, similar to the JHU Steady Hand systems, the workspace and joint space orientations are defined with the same roll and tilt angles.

Since the REMS consists of a parallel linear delta mechanism serially coupled to a serial rotary joint arm mechanism, it is helpful to decompose the kinematics of the REMS into these two parts for analysis. The difficulty is that since the delta mechanism is parallel, inverse kinematics are simpler and should be done before forward kinematics, but the rotary arm is serial, so forward kinematics are simpler and should be done before inverse. Therefore the forward and inverse kinematics of each component are computed independently and combined at the end.
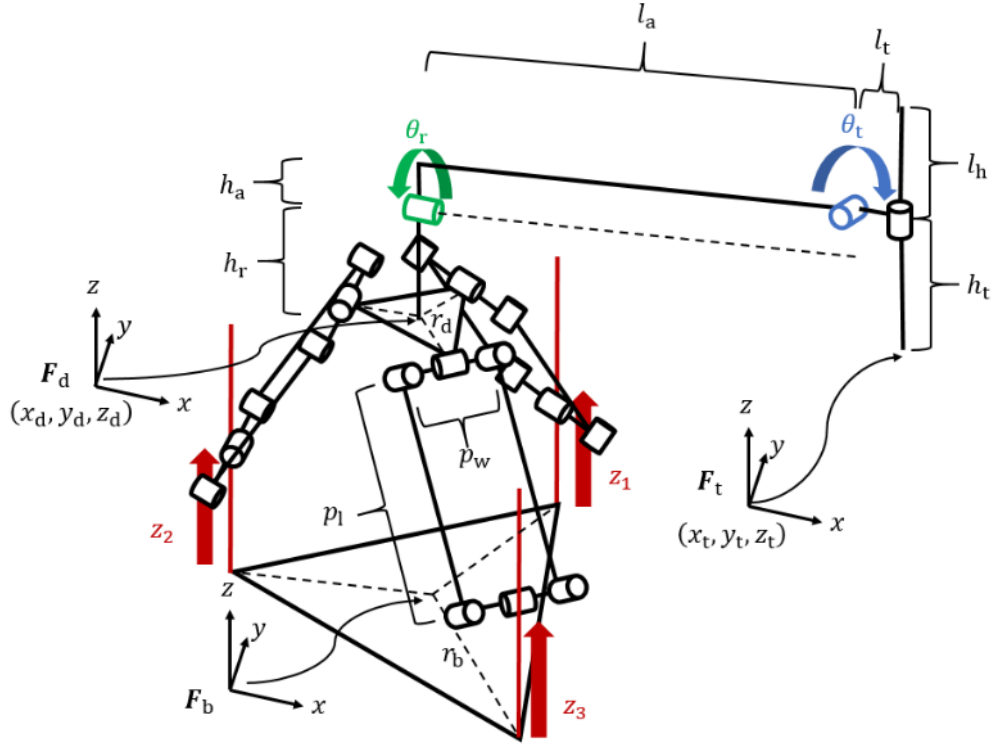
Figure 3.8: REMS kinematic diagram.

3.5.2 Delta Inverse Kinematics

Since the linear delta mechanism is a parallel mechanism, the inverse kinematics are simpler to compute and will be done first. The inverse kinematics k_{di} can be expressed as:

$$k_{di}(x_d, y_d, z_d) = (z_1, z_2, z_3) \tag{3.3}$$

The arrangement of the linear actuators on the base (Figure 3.9) is given by:

$$x_i = (r_b - r_d)\cos(\theta_{bi})$$

$$y_i = (r_b - r_d)\sin(\theta_{bi}) \tag{3.4}$$

$$\theta_{bi} = (2i - 1)\frac{\pi}{3}, i = 1, 2, 3$$

In these formulas, $(r_b - r_d)$ is used instead of just r_b because only the difference between the base radius and the mobile platform radius affects the kinematics of the robot.

84
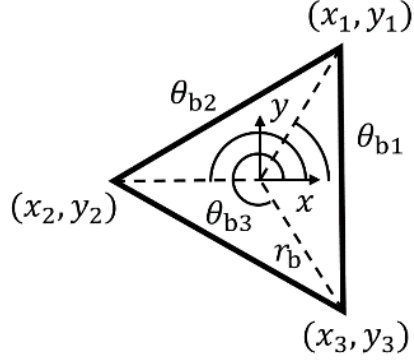
Figure 3.9: Arrangement of the delta linear actuators.

Given (x_d, y_d, z_d), the position of the delta mobile platform with respect to $\boldsymbol{F}_b$, the positions of the delta linear actuators can be computed as follows:

$$z_i = z_d - \sqrt{p_l^2 - (x_d - x_i)^2 - (y_d - y_i)^2} \tag{3.5}$$

3.5.3 Delta Forward Kinematics

Though the linear delta mechanism is a parallel mechanism, a relatively simple though somewhat tedious analytical formula for the forward kinematics exists. The forward kinematics can be expressed as:

$$k_{df}(z_1, z_2, z_3) = (x_d, y_d, z_d) \tag{3.6}$$

Starting with the positions of the linear actuators (x_i, y_i, z_i), compute:

$$w_i = x_i^2 + y_i^2 + z_i^2 \tag{3.7}$$

Then compute:

$$
\begin{aligned}
x_{3,2} &= x_3 - x_2 \\
x_{2,1} &= x_2 - x_1 \\
y_{3,2} &= y_3 - y_2 \\
y_{2,1} &= y_2 - y_1 \\
z_{3,2} &= z_3 - z_2 \\
z_{2,1} &= z_2 - z_1 \\
w_{3,2} &= w_3 - w_2 \\
w_{2,1} &= w_2 - w_1
\end{aligned} \tag{3.8}
$$

85

$$x_{3,2,2,1} = \frac{x_{3,2}}{x_{2,1}}$$

$$y_{3,2,2,1} = \frac{y_{3,2}}{y_{2,1}}$$

Now that these base terms have been computed, we can compute:

$$a_1 = -\frac{z_{3,2} - z_{2,1}y_{3,2,2,1}}{x_{3,2} - x_{2,1}y_{3,2,2,1}}$$

$$b_1 = -\frac{w_{3,2} - w_{2,1}y_{3,2,2,1}}{2(x_{3,2} - x_{2,1}y_{3,2,2,1})}$$

$$a_2 = -\frac{z_{3,2} - z_{2,1}x_{3,2,2,1}}{y_{3,2} - y_{2,1}x_{3,2,2,1}}$$

$$b_2 = -\frac{w_{3,2} - w_{2,1}x_{3,2,2,1}}{2(y_{3,2} - y_{2,1}x_{3,2,2,1})}$$

(3.9)

From these, we can compute:

$$a = a_1^2 + a_2^2 + 1$$

$$b = 2(a_1(b_1 - x_1) + a_2(b_2 - y_1) - z_1)$$

$$c = (b_1 - x_1)^2 + (b_2 - y_1)^2 + z_1^2 - p_l^2$$

(3.10)

This solution is using a quadratic formula, so if at this point in the calculation the following condition is true, then the solution is not feasible and some kind of error has occurred.

$$b^2 - 4ac < 0 \rightarrow error$$

(3.11)

Otherwise, we can compute the position of the delta mobile platform as:

$$z_d = \frac{-b + \sqrt{b^2 - 4ac}}{2a}$$

$$x_d = z_d a_1 + b_1$$

$$y_d = z_d a_2 + b_2$$

(3.12)

3.5.4 Rotary Arm Forward Kinematics

Since the rotary arm mechanism is serial, computing the forward kinematics is relatively simple using homogenous coordinate transforms. The forward kinematics can be expressed as:

$$k_{rf}(x_\mathrm{d}, y_\mathrm{d}, z_\mathrm{d}, \theta_\mathrm{r}, \theta_\mathrm{t}) = (x_\mathrm{t}, y_\mathrm{t}, z_\mathrm{t}, \theta_\mathrm{r}, \theta_\mathrm{t}) \tag{3.13}$$

The computation can be done using homogeneous transforms as:

$$\boldsymbol{t}_\mathrm{t} = \left[\boldsymbol{I}, \begin{bmatrix} x_\mathrm{d} \\ y_\mathrm{d} \\ z_\mathrm{d} \end{bmatrix} \right] \cdot \left[\boldsymbol{R}_x(\theta_\mathrm{r}), \begin{bmatrix} 0 \\ 0 \\ h_\mathrm{r} \end{bmatrix} \right] \cdot \left[\boldsymbol{R}_y(\theta_\mathrm{t}), \begin{bmatrix} l_\mathrm{a} \\ 0 \\ h_\mathrm{a} \end{bmatrix} \right] \cdot \begin{bmatrix} l_\mathrm{t} \\ 0 \\ -h_\mathrm{t} \end{bmatrix} \tag{3.14}$$

The angles $\theta_\mathrm{r}, \theta_\mathrm{t}$ are unchanged, and $\boldsymbol{t}_\mathrm{t} = \begin{bmatrix} x_\mathrm{t} \\ y_\mathrm{t} \\ z_\mathrm{t} \end{bmatrix}$.

3.5.5 Rotary Arm Inverse Kinematics

Since $\theta_\mathrm{r}, \theta_\mathrm{t}$ are unchanged by forward and inverse kinematics, inverse kinematics of the rotary arm can be obtained by simply computing the translation component of the forward kinematics and negating it. The inverse kinematics can be expressed as:

$$k_{ri}(x_\mathrm{t}, y_\mathrm{t}, z_\mathrm{t}, \theta_\mathrm{r}, \theta_\mathrm{t}) = (x_\mathrm{d}, y_\mathrm{d}, z_\mathrm{d}, \theta_\mathrm{r}, \theta_\mathrm{t}) \tag{3.15}$$

Next, from the forward kinematics formula, we can compute:

$$\boldsymbol{t}_\mathrm{d} = \boldsymbol{t}_\mathrm{t} - \left[\boldsymbol{R}_x(\theta_\mathrm{r}), \begin{bmatrix} 0 \\ 0 \\ h_\mathrm{r} \end{bmatrix} \right] \cdot \left[\boldsymbol{R}_y(\theta_\mathrm{t}), \begin{bmatrix} l_\mathrm{a} \\ 0 \\ h_\mathrm{a} \end{bmatrix} \right] \cdot \begin{bmatrix} l_\mathrm{t} \\ 0 \\ -h_\mathrm{t} \end{bmatrix} \tag{3.16}$$

The angles $\theta_\mathrm{r}, \theta_\mathrm{t}$ are unchanged, and $\boldsymbol{t}_\mathrm{d} = \begin{bmatrix} x_\mathrm{d} \\ y_\mathrm{d} \\ z_\mathrm{d} \end{bmatrix}$.

3.5.6 Complete Kinematics

Now that the forward and inverse kinematics of the delta and rotary arm mechanisms are known, they can be combined to form the complete forward and inverse kinematics of the robot.

The forward kinematics can be expressed as:

$$k_\mathrm{f}(z_1, z_2, z_3, \theta_\mathrm{r}, \theta_\mathrm{t}) = (x_\mathrm{t}, y_\mathrm{t}, z_\mathrm{t}, \theta_\mathrm{r}, \theta_\mathrm{t}) \tag{3.17}$$

Given $(z_1, z_2, z_3, \theta_r, \theta_t)$, compute $k_{df}(z_1, z_2, z_3) = (x_d, y_d, z_d)$, and use this to compute $k_{rf}(x_d, y_d, z_d, \theta_r, \theta_t) = (x_t, y_t, z_t, \theta_r, \theta_t)$.

The inverse kinematics can be expressed as:

$$k_i(x_t, y_t, z_t, \theta_r, \theta_t) = (z_1, z_2, z_3, \theta_r, \theta_t) \tag{3.18}$$

Given $(x_t, y_t, z_t, \theta_r, \theta_t)$, compute $k_{ri}(x_t, y_t, z_t, \theta_r, \theta_t) = (x_d, y_d, z_d, \theta_r, \theta_t)$, and use (x_d, y_d, z_d) to compute $k_{di}(x_d, y_d, z_d) = (z_1, z_2, z_3)$.

3.5.7 Frame Transformations

In addition to the kinematics, the force transformation from the raw force/torque sensor values to the robot frame must also be computed. This can be broken down into two transformations, the transformation from the raw force/torque values to the frame where the forces/torques are resolved, $T_{raw \to res}$ and the transformation from the resolution frame to the robot frame, $T_{res \to robot}$. $T_{raw \to res}$ will be computed first.

If f is the raw force and τ is the raw torque applied to the force/torque sensor, then a 6x1 wrench w_{raw} can be formed as:

$$w_{raw} = \begin{bmatrix} f \\ \tau \end{bmatrix} \tag{3.19}$$

w_{raw} can be transformed into the frame where the forces and torques should be resolved using a screw transform.

$$w_{res} = T_{raw \to res} w_{raw} \tag{3.20}$$

$T_{raw \to res}$ is computed using the screw transform formula as:

$$T_{raw \to res} = \begin{bmatrix} R & 0 \\ [r]_x R & R \end{bmatrix} \tag{3.21}$$

Where R is the rotation matrix from the raw frame to the resolution frame, and $[r]_x$ is the cross product matrix for r, the translation from the raw frame to the resolution frame. The value of r depends on where the force is being resolved, which depends on the control mode being used. w_{res} can then be split back apart into the force and torque components.

$$w_{\text{res}} = \begin{bmatrix} f_{\text{res}} \\ \tau_{\text{res}} \end{bmatrix} \tag{3.22}$$

Now that f_{res} and τ_{res} are resolved in the desired frame, they must be transformed into the robot frame so that they can be used for control. $T_{\text{res}\rightarrow\text{robot}}$ is closely related to the forward kinematics. Since we are only interested in orienting and not translating the force frame, we can use the forward kinematics formula with the translations set to zero.

$$T_{\text{res}\rightarrow\text{robot}} = \begin{bmatrix} R_x(\theta_r), & \begin{bmatrix} 0 \\ 0 \\ 0 \end{bmatrix} \end{bmatrix} \cdot \begin{bmatrix} R_y(\theta_t), & \begin{bmatrix} 0 \\ 0 \\ 0 \end{bmatrix} \end{bmatrix} = \begin{bmatrix} R_x(\theta_r)R_y(\theta_t), & \begin{bmatrix} 0 \\ 0 \\ 0 \end{bmatrix} \end{bmatrix} \tag{3.23}$$

Now we can compute f_{robot} and τ_{robot}, the resolved forces and torques in the robot frame, as follows:

$$f_{\text{robot}} = T_{\text{res}\rightarrow\text{robot}}f_{\text{res}}$$
$$\tau_{\text{robot}} = T_{\text{res}\rightarrow\text{robot}}\tau_{\text{res}} \tag{3.24}$$

3.5.8 Jacobians

Since the inverse kinematics formula for the delta mechanism is simple, symbolically differentiating it to find the inverse Jacobian is simple. However, the forward kinematics formula for the delta mechanism is more complex, making symbolic differentiation difficult. Because of this, it is computationally simpler to symbolically calculate the inverse Jacobian, then invert it to attain the forward Jacobian. Therefore the inverse Jacobian will be computed first. Since the REMS can be decomposed into translational (delta mechanism) and rotational (rotary arm) components, the Jacobian can also be decomposed in this way to ease computation. The inverse Jacobian J^{-1} can be decomposed as:

$$\begin{bmatrix} \dot{z} \\ \dot{\theta} \end{bmatrix} = \begin{bmatrix} J_1^{-1} & J_2^{-1} \\ J_3^{-1} & J_4^{-1} \end{bmatrix} \begin{bmatrix} \dot{x} \\ \dot{\theta} \end{bmatrix} \tag{3.25}$$

Where:

$$\dot{z} = \begin{bmatrix} \dot{z}_1 \\ \dot{z}_2 \\ \dot{z}_3 \end{bmatrix}, \dot{\theta} = \begin{bmatrix} \dot{\theta}_r \\ \dot{\theta}_t \end{bmatrix}, \dot{x} = \begin{bmatrix} \dot{x}_t \\ \dot{y}_t \\ \dot{z}_t \end{bmatrix} \tag{3.26}$$

J_1^{-1} is simply the inverse Jacobian of the linear delta mechanism, which is given by [65]:

$$J_1^{-1} = \begin{bmatrix} (x_d - x_1/(z_d - \theta_{b1}) & (y_d - y_1/(z_d - \theta_{b1}) & 1 \\ (x_d - x_2/(z_d - \theta_{b2}) & (y_d - y_2/(z_d - \theta_{b2}) & 1 \\ (x_d - x_3/(z_d - \theta_{b3}) & (y_d - y_3/(z_d - \theta_{b3}) & 1 \end{bmatrix}, \tag{3.27}$$

J_3^{-1} is all zeros since $\boldsymbol{\theta}$ is independent of $\boldsymbol{x}$.

$$J_3^{-1} = \begin{bmatrix} 0 & 0 & 0 \\ 0 & 0 & 0 \end{bmatrix} \qquad (3.28)$$

J_4^{-1} is the identity since it is the derivative of $\boldsymbol{\theta}$ with respect to $\boldsymbol{\theta}$.

$$J_4^{-1} = \begin{bmatrix} 1 & 0 \\ 0 & 1 \end{bmatrix} \qquad (3.29)$$

J_2^{-1} is more complex since it involves both rotational and translational components, however J_2^{-1} can be further decomposed as follows:

$$J_2^{-1} = \frac{\partial \boldsymbol{z}}{\partial \boldsymbol{\theta}} = \frac{\partial \boldsymbol{z}}{\partial \boldsymbol{x}_d} \frac{\partial \boldsymbol{x}_d}{\partial \boldsymbol{\theta}} \qquad (3.30)$$

Where $\boldsymbol{x}_d = \begin{bmatrix} x_d \\ y_d \\ z_d \end{bmatrix}$.

$\frac{\partial \boldsymbol{z}}{\partial \boldsymbol{x}_d}$ is simply the inverse Jacobian of the delta mechanism again, which is equal to J_1^{-1}.

$\frac{\partial \boldsymbol{x}_d}{\partial \boldsymbol{\theta}}$ is the Jacobian of the inverse kinematics of the rotary arm, which can be computed symbolically.

$$\frac{\partial \boldsymbol{x}_d}{\partial \boldsymbol{\theta}} = \frac{\partial \left(\boldsymbol{x} - \left[\boldsymbol{R}_x(\theta_r), \begin{bmatrix} 0 \\ 0 \\ h_r \end{bmatrix} \right] \cdot \left[\boldsymbol{R}_y(\theta_t), \begin{bmatrix} l_a \\ 0 \\ h_a \end{bmatrix} \right] \cdot \begin{bmatrix} l_t \\ 0 \\ -h_t \end{bmatrix} \right)}{\partial \boldsymbol{\theta}} \qquad (3.31)$$

$$= - \begin{bmatrix} 0 & a \\ \cos(\theta_r)c & \sin(\theta_r)b \\ -\sin(\theta_r)c & -\cos(\theta_r)b \end{bmatrix}$$

Where:

$$a = -(h_t \cos(\theta_t) + l_t \sin(\theta_t))$$

$$b = l_t \cos(\theta_t) - h_t \sin(\theta_t) \qquad (3.32)$$

$$c = h_a + a$$

Now we can put J^{-1} back together from its components:

$$J^{-1} = \begin{bmatrix} J_1^{-1} & J_1^{-1} \dfrac{\partial \boldsymbol{x}_d}{\partial \boldsymbol{\theta}} \\ \boldsymbol{0}_{2x3} & \boldsymbol{I}_{2x2} \end{bmatrix} \qquad (3.33)$$

To compute the forward Jacobian J, simply invert J^{-1}.

3.6 Delta Kinematic Optimization

Now that the kinematics of the REMS are understood, the next step is to optimize the kinematic parameters, staring with the delta mechanism. The most mechanically constrained part of the design is the mobile platform with parameters r_d, the radius of the mobile platform, and p_w, the width of the delta parallelograms. Since compactness is one of the design objectives, it is desirable for both parameters to be as small as possible. However, stiffness is also an objective, and stiffness improves with larger r_d and p_w. The goal then is to choose the smallest possible values of r_d and p_w which meet stiffness requirements. Some work has been done on modeling stiffness of delta robots [66], but this work has been shown to be accurate only if detailed stiffness models exist for all bearings, joints, and structural members, which is not feasible in the initial design stage. Therefore, r_d and p_w where chosen based on experience to achieve maximum compactness with acceptable stiffness while still being inexpensively manufacturable. The final values were chosen as $r_d = 29.5\ mm$ and $p_w = 54\ mm$.

For safety and simplicity, the motion of the mobile platform is constrained to remain within the linear actuators. This means that the range of motion of the linear delta mechanism is largely determined by the difference between r_d, the radius of the mobile platform, and r_b, the radius of the base, and r_d is known, r_b can be chosen to meet the range of motion requirement. The desired range of motion is a diameter of 125 mm, so the required value of r_b can be computed as:

$$r_b - r_d = \frac{125\ mm}{2} \tag{3.34}$$

This results in a minimum value of r_b of 92 mm. However, due to mechanical clearance constraints, a final value of $r_b = 95.3$ was used.

The final kinematic parameter of the delta mechanism is p_l, the length of the delta parallelograms. Intuitively, if p_l is very long, then the robot becomes more agile in the x and y directions, but not in the z direction. Conversely, if p_l is very short, then the robot becomes very slow in the x and y directions, with z direction performance unchanged. The most important part of any optimization problem is to properly define the objective function to capture the desired properties of the system. In the case of the REMS, the most important kinematic property for the delta mechanism is to deliver even performance across the

workspace so that motion feels natural and even to the user. If the performance varies wildly across the workspace, then the robot will behave unpredictably, making it useless for surgery. Therefore there must be an optimal value of p_l where performance in the x, y, and z directions are as isotropic as possible.

The typical way to approach an optimization problem like this is to use a performance index to quantify the desired property of the system, and then optimize the system parameters to maximize/minimize the index. Many papers can be found in the literature taking this approach, even some for linear delta robots [65]. The difficulty with these papers is that they all use the same family of performance indices which have been shown to make unrealistic assumptions about how real robots work [67]. These indices are so pervasive that for almost 30 years that the majority of optimization papers use them almost without question in spite of their seemingly obvious flaws. Because of this, there are few viable alternatives. Since it was clear that these indices were unsuitable for the design of the REMS, it was unclear how to proceed. Therefore I created my own performance indices which were directly based on the physical specifications of the REMS. It then became apparent that these indices could be broadly applied to many optimization problems in robotics. This section discusses the background of the field and flaws in the conventional indices, as well as the development, and validation of novel indices.

3.7 Performance Indices for Parallel Robots

3.7.1 Performance indices background and motivation

Optimal design is one of the most important problems in robotics, and a large body of literature has been devoted to it. One of the main approaches to this problem is to find objective functions, or indices, to quantify design performance. Since the properties of a mechanical design can vary dramatically between different configurations, a common approach has been to linearize the kinematics by computing the Jacobian at a given configuration, and then using the Jacobian to compute performance indices. Arguably the most popular and influential of these Jacobian-based indices have been the inverse condition number [68], and manipulability [69]. These indices are popular because they are both simple to compute and provide intuitive insight into the properties of different designs. However, since their development, cases in which these indices fail to capture the full complexity of a robot's kinematics have been found. Most

notable among these are robots with redundancy/non-square Jacobians, and robots that mix rotational and translational degrees of freedom. Much work has been devoted to solving these issues, including [70, 71, 72, 73, 74, 75, 76, 77, 78] and many others. Even more significantly, a growing body of research has debated the accuracy, consistency, and usefulness of these indices when applied to practical design problems. A comprehensive overview of this work is given in [67]. This work has shown that even in the ideal case of non-redundant robots with square Jacobians without mixed degrees of freedom, manipulability and the inverse condition number fail to consistently and accurately capture key aspects of kinematic performance. Partially in response to this new work, other types of performance indices have recently been developed, such as [79, 80, 81], which use screw theory to develop kinematic and force transmission indices. Though this approach solves many of the problems normally present in traditional indices and has many uses, it is also substantially more complex and application specific, lacking the intuitive simplicity of the conventional indices.

Another important and related area of optimal design is error propagation and accuracy analysis. Much work has been devoted to these areas as well [82, 83, 84, 85] and [79], and though this area is related to performance indices, it is often treated independently. As discussed in [84], there are many sources of error in a typical robot, including manufacturing errors, backlash, and compliance; however these can be minimized through careful design and calibration. The main remaining source of error in most properly designed and calibrated robots is "active joint errors", or errors in the joint angles [83]. Thus quantifying the relationship of joint errors to end effector errors is crucial to optimal robot design.

The indices discussed above have primarily been local and only evaluate performance in one configuration. Another body of literature has emerged to develop indices of global performance over a desired workspace [86, 87]. These indices typically involve numerically integrating a Jacobian-based index over the workspace of the robot to compute its average value. Since these typically use conventional Jacobian-based indices as a subroutine, they inherit the same problems as discussed above. In addition, most practical robot design problems are more concerned with worst case performance than average performance, making global indices based on average values only an approximate solution.

The goal of this work is to describe the limitations of the inverse condition number and manipulability when applied to optimal design problems based on common key specifications, develop novel indices

which address these limitations, and demonstrate the utility of these new indices in with an optimal design and evaluation case study.

3.7.2 Specification based design

When evaluating the kinematics of a robot, several key specifications are almost invariably involved, particularly:

- The magnitude of the worst-case (slowest) end effector velocity v_{wc}, given bounded joint speeds, v_j

- The magnitude of the worst-case (largest) end effector positioning error e_{wc}, given bounded joint errors, e_j

- The magnitude of the worst-case (smallest) end effector force f_{wc}, given bounded joint forces (or torques), f_j

Since small position errors are analogous to velocities, e_{wc} is closely related to the maximum possible end effector velocity given bounded joint speeds, demonstrating a useful connection between kinematic performance and error analysis, two subjects which are often treated separately. Here v_{wc}, e_{wc}, and f_{wc} are all defined for a specific configuration, but will be extended to the entire workspace in a later section.

Performance indices such as the inverse condition number [68] and manipulability [69] have been used to optimize and evaluate the design of robots since the 1980s, but as shown in [67], they have some significant drawbacks when applied to practical design problems. In order to demonstrate how these indices actually relate to the above specifications, they must first be analyzed in terms of how they use the Jacobian matrix.

The Jacobian of a robot is defined as:

$$\dot{x} = J\dot{\theta} \tag{3.35}$$

Where $\dot{x}$ is the end effector velocity, $\dot{\theta}$ is the vector of joint speeds, and J is the Jacobian matrix. For the rest of this paper, it is assumed that J is square and full rank, and $\dot{x}$ and $\dot{\theta}$ do not combine rotational and translational degrees of freedom. Enhancing performance indices to include these cases has been extensively covered in the literature, so these issues will not be discussed here. Since the goal is to develop

indices for parallel robots, it is assumed hereafter that all of the joints are equivalent to each other, though this constraining assumption could be relaxed.

3.7.3 Inadequacy of conventional indices

3.7.3.1 Manipulability

Manipulability is defined as:

$$m = \sqrt{|JJ^{\mathrm{T}}|} = \prod_{i=1}^{n} \sigma_i \tag{3.36}$$

Where σ_i represents the ith singular value of J. If any $\sigma_i = 0$, then $m = 0$, indicating that the robot cannot instantaneously move in some direction [69]. m is also proportional to the volume of the manipulability ellipsoid (Figure 3.10), meaning that m is intuitively characterizing the total volume of the velocity space the robot can instantaneously move in. Manipulability has historically been used to characterize proximity to singular or isotropic configurations, and efficiency of velocity and force transmission [88]. However, if some σ_i is small, meaning that the robot cannot move effectively in one direction, m can be improved by increasing some other σ_j. In this case, m has improved, but worst-case performance has not, demonstrating that m is not directly related to any of the key physical design specifications described previously, and thus should not be used to evaluate or optimize designs based on worst-case specifications.
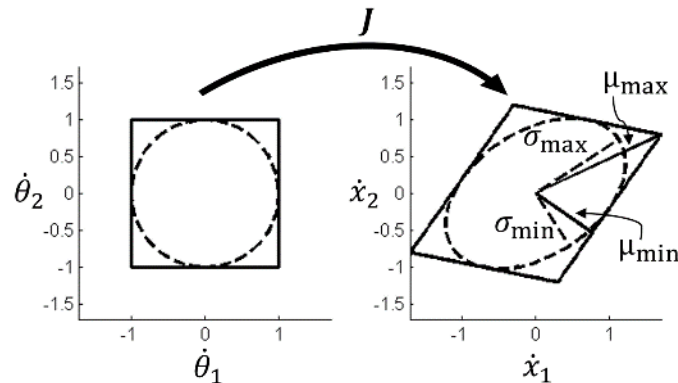
Figure 3.10: Manipulability ellipsoid and polytope.

95

Left: unit 2-norm and infinity-norm bounds on joint speeds. Right: corresponding manipulability ellipsoid and polytope for Jacobian $\mathbf{J}$. σ_{min} and σ_{max} are the smallest and largest singular values of $\mathbf{J}$, corresponding to the lengths of the principal axes of the manipulability ellipsoid. μ_{min} and μ_{max} are the smallest and largest velocities of the manipulability polytope.

3.7.3.2   Inverse Condition Number

The condition number attempts to bound the relative error of the end effector given the relative error of the joint angles:

$$\frac{\|\Delta x\|}{\|x\|} \leq \kappa \frac{\|\Delta \theta\|}{\|\theta\|} \tag{3.37}$$

Where the condition number κ is defined as:

$$\kappa = \|J\|_2 \|J^{-1}\|_2 \tag{3.38}$$

The inverse condition number κ^{-1} is then given by:

$$\kappa^{-1} = \frac{1}{\|J\|_2 \|J^{-1}\|_2} = \frac{\sigma_{min}}{\sigma_{max}} \tag{3.39}$$

Where σ_{min} and σ_{max} are the smallest and largest singular values of J. The definitions of the maximum and minimum singular values of a matrix can be used to gain further physical intuition into σ_{min} and σ_{max} as follows:

$$\begin{aligned} \sigma_{min} &= \min_{\|\dot{\theta}\|_2=1} \|J\dot{\theta}\|_2 = \min_{\|\dot{\theta}\|_2=1} \|\dot{x}\|_2 \\ \sigma_{max} &= \max_{\|\dot{\theta}\|_2=1} \|J\dot{\theta}\|_2 = \max_{\|\dot{\theta}\|_2=1} \|\dot{x}\|_2 \end{aligned} \tag{3.40}$$

Given a unit (2-norm) vector of joint speeds, σ_{min} and σ_{max} are the minimum and maximum possible end effector velocities, which correspond to the principal axes of the manipulability ellipsoid in Figure 3.10. If the robot can instantaneously move equally well in every direction, then $\sigma_{min} = \sigma_{max}$ and $\kappa^{-1} = 1$, showing that the robot is isotropic in this configuration. If there is some direction in which the robot cannot instantaneously move, then at least one $\sigma_i = 0$, so $\sigma_{min} = 0$, $\sigma_{max} \neq 0$ and $\kappa^{-1} = 0$, revealing a singularity.

Similar to manipulability, κ^{-1} has historically been used characterize proximity to singular or isotropic configurations, and to quantify the isotropy in a given configuration. However, as shown in [67], the condition number is implicitly using the same norm to measure the magnitude of both the vector of joint speeds and the end effector velocity. While the 2-norm is usually appropriate for end effector velocities, joint speed limits are normally independent of each other in physical robots, so the proper choice of norm for the vector of joint speeds is actually the infinity-norm.

This manifests strikingly when attempting to measure the isotropy of a very simple robot consisting of two orthogonal Cartesian stages. As shown in [67], the Jacobian for this robot is just the identity matrix, so the inverse condition number is:

$$\kappa^{-1} = \frac{1}{1} = 1 \tag{3.41}$$

This leads to the conclusion that the robot is completely isotropic, however, if the more realistic infinity-norm is used when choosing a unit length vector of joint speeds, the minimum possible end effector velocity is 1 (one of the joints is at full speed and the other is off), but the maximum possible end effector velocity is $\sqrt{2}$ (both joints are at full speed with the end effector moving at a 45 degree angle to the actuators). Even in this trivial example, κ^{-1} does not correspond to any of the previous key physical design specifications, making it of limited use in practical specification-based design.

3.7.4 New performance indices

The inverse condition number and manipulability indices presented two main limitations when applied to design problems based on worst-case specifications. The first is not using the proper norm for joint vs. end effector velocities. The second is not directly corresponding to any physical performance specification of the robot, which are typically worst-case. These limitations can be remedied by writing out the desired specifications precisely while using the proper norms. For continuity, v_{wc} and e_{wc} will be dealt with first, and f_{wc} will be covered in a later section.

97

3.7.4.1 Worst-Case Velocity Index

Our goal is to create an index which intuitively quantifies v_{wc}. However, v_{wc} is dependent on the magnitude of the vector of joint speeds v_j. Therefore, to remove this dependence, the worst-case velocity index μ_{min} is defined as:

$$\mu_{min} = \frac{v_{wc}}{v_j} \tag{3.42}$$

Accounting for the independent bounds on the joint speeds, the worst case end effector velocity of the robot can then be expressed as the minimum possible magnitude end effector velocity given a unit infinity norm vector of joint speeds:

$$\mu_{min} = \min_{\|\dot{\theta}\|_\infty = 1} \|\dot{x}\|_2 = \min_{\|\dot{\theta}\|_\infty = 1} \|J\dot{\theta}\|_2 \tag{3.43}$$

If the robot is not capable of moving in any one direction, the magnitude of the end effector velocity in that direction will be 0, resulting in $\mu_{min} = 0$. However, since μ_{min} is the worst case velocity, improving performance in other directions has no effect on μ_{min}. Therefore, the larger μ_{min} is, the better the worst-case velocity is. Intuitively, μ_{min} can be visualized as the smallest velocity on the manipulability polytope [89] with unit infinity-norm bounded input speeds (Figure 3.10). The algorithm and time complexity for computing μ_{min} will be given in a later section.

3.7.4.2 Worst-Case Error Index

The worst-case end effector error is the worst possible error in the position of the end effector given independently bounded joint errors. Similarly to μ_{min}, it is most intuitive to define the worst-case error index μ_{max} as:

$$\mu_{max} = \max_{\|\Delta\theta\|_\infty = 1} \|\Delta x\| = \max_{\|\Delta\theta\|_\infty = 1} \|J\Delta\theta\|_2 \tag{3.44}$$

Since $\dot{x} = J\dot{\theta}$, and $\Delta x \approx J\Delta\theta$ for small $\Delta\theta$, error and velocity are analogous for small errors. μ_{max} can then be derived as:

$$\mu_{max} = \max_{\|\dot{\theta}\|_\infty = 1} \|\dot{x}\| = \max_{\|\dot{\theta}\|_\infty = 1} \|J\dot{\theta}\|_2 \tag{3.45}$$

As with $\mu_{\min}$, decreasing the error in other directions does not improve the worst case error, and does not effect $\mu_{\max}$. Since $\mu_{\max}$ is the worst case error, the larger $\mu_{\max}$ is, the worse the worst-case error is. Intuitively, $\mu_{\max}$ can be visualized as largest velocity on the manipulability polytope given unit infinity-norm input speeds (Figure 3.10). The algorithm and time complexity to compute $\mu_{\max}$ will be given in a later section.

3.7.4.3 New Isotropy Index

As shown above, κ^{-1} is an isotropy index, though since it uses 2-norm input bounds, it is computing the isotropy of the manipulability ellipsoid and does not correspond to the realistic worst-case specifications represented by the manipulability polytope. Since the exact values of $\mu_{\min} = \frac{v_{\mathrm{wc}}}{v_{\mathrm{j}}}$ and $\mu_{\max} = \frac{e_{\mathrm{wc}}}{e_{\mathrm{j}}}$ for the manipulability polytope using infinity-norm input bounds have been determined, a new isotropy index ι can be defined using $\mu_{\min}$ and $\mu_{\max}$:

$$\iota = \frac{\mu_{\min}}{\mu_{\max}} = \frac{\min_{\|\dot{\theta}\|_{\infty}=1}\|J\dot{\theta}\|_{2}}{\max_{\|\dot{\theta}\|_{\infty}=1}\|J\dot{\theta}\|_{2}} \tag{3.46}$$

Similarly to the inverse condition number, when a robot is singular and cannot move in a certain direction, $\mu_{\min} = 0$, so $\iota = 0$. If the robot were fully isotropic, then the best and worst case velocities would be equal, meaning $\mu_{\min} = \mu_{\max}$, making $\iota = 1$.

3.7.5 Algorithms and analysis

3.7.5.1 The p, q-norm

Now that $\mu_{\min}$, $\mu_{\max}$, and ι have been defined, it must be considered how to actually compute them. One of the key problems with the inverse condition number was that it failed to apply the proper norms to actuator and end effector velocities. This can be remedied by examining the definition of the matrix norm. The definition of an induced matrix norm is given by:

$$\|A\|_{p} = \max_{x \neq 0} \frac{\|Ax\|_{p}}{\|x\|_{p}} \tag{3.47}$$

However, in this case a different p-norm must be used for the numerator than for the denominator. This construct already exists in matrix theory as the subordinate matrix norm, or p, q-norm. The p, q-norm of a matrix is defined as:

$$\|A\|_{p,q} = \max_{x \neq 0} \frac{\|Ax\|_q}{\|x\|_p} \tag{3.48}$$

A body of research exists on computing p, q-norms [90, 91], so it is desirable to express $\mu_{\min}$ and $\mu_{\max}$ in this form.

3.7.5.2 μ_{max} Algorithm

$\mu_{\max}$ is already close to the p, q-norm form, so it is trivial to express $\mu_{\max}$ as:

$$\mu_{\max} = \max_{\|\dot{\theta}\|_\infty = 1} \|J\dot{\theta}\|_2 = \max_{\dot{\theta} \neq 0} \frac{\|J\dot{\theta}\|_2}{\|\dot{\theta}\|_\infty} = \|J\|_{\infty,2} \tag{3.49}$$

μ_{max} is therefore the p, q-norm of J with $p = \infty, q = 2$. Computing or even approximating the p, q-norm of a matrix with $p > q$ has been shown to be NP-hard [90, 91], however in this case the size of J will usually be small so this computation is tractable. In the case of $p = \infty, q = 2$, it has been shown that the solution will always have the form $\dot{\theta} \in \{1, -1\}^n$ for $J_{n \times n}$. Since the sign of $\dot{\theta}$ does not affect the result, the sign of one element of $\dot{\theta}$ can be chosen arbitrarily, and then every possibility for the remaining values brute-force computed. This requires 2^{n-1} matrix-vector multiplications, each of which requires $O(n^2)$ multiply and add operations. This results in an overall time complexity of $O(n^2 2^n)$.

3.7.5.3 μ_{min} Algorithm

Computing $\mu_{\min}$ is similar to above. First it must be expressed in p, q-norm form.

$$\mu_{\min} = \min_{\|\dot{\theta}\|_\infty = 1} \|J\dot{\theta}\|_2 \tag{3.50}$$

Substitute $\dot{\theta} = J^{-1}\dot{x}$ to obtain

$$\mu_{\min} = \min_{\|J^{-1}\dot{x}\|_\infty = 1} \|JJ^{-1}\dot{x}\|_2 = \min_{\|J^{-1}\dot{x}\|_\infty = 1} \|\dot{x}\|_2 \tag{3.51}$$

Without loss of generality, define $\dot{x} = c\hat{x}$ where c is a positive constant and $\|\hat{x}\|_2 = 1$.

$$\mu_{\min} = \min_{\substack{\|J^{-1}c\hat{x}\|_\infty=1 \\ \|\hat{x}\|_2=1}} \|c\hat{x}\|_2 = \min_{\substack{c\|J^{-1}\hat{x}\|_\infty=1 \\ \|\hat{x}\|_2=1}} c\|\hat{x}\|_2 = \min_{\substack{c\|J^{-1}\hat{x}\|_\infty=1 \\ \|\hat{x}\|_2=1}} c \qquad (3.52)$$

Since $\mu_{\min}$ is the minimum value of c satisfying the constraints, substitute $\mu_{\min}$ into the first constraint equation:

$$\mu_{\min}\|J^{-1}\hat{x}\|_\infty = 1 \qquad (3.53)$$

$$\mu_{\min} = \frac{1}{\|J^{-1}\hat{x}\|_\infty} \qquad (3.54)$$

Again, since $\mu_{\min}$ is the minimum value of c satisfying the constraints, $\|J^{-1}\hat{x}\|_\infty$ must be maximized, retaining the $\|\hat{x}\|_2 = 1$ constraint.

$$\mu_{\min} = \frac{1}{\max_{\|\hat{x}\|_2=1}\|J^{-1}\hat{x}\|_\infty} = \frac{1}{\max_{\hat{x}\neq0}\frac{\|J^{-1}\hat{x}\|_\infty}{\|\hat{x}\|_2}} = \frac{1}{\|J^{-1}\|_{2,\infty}} \qquad (3.55)$$

$\mu_{\min}$ is therefore the reciprocal of the p,q-norm of J^{-1} with $p = 2, q = \infty$. It was reported by [90, 91] that any p,q-norm with $q = \infty$ can be solved in polynomial time. In the case of $p = 2, q = \infty$, this can be done by evaluating:

$$\mu_{\min} = \frac{1}{\max_{1<i<n}\|J_i^{-1}\|_2} \qquad (3.56)$$

Where J_i^{-1} is the ith row of J^{-1}. This requires taking the 2-norm of n vectors of size $1 \times n$, which takes $O(n^2)$ time.

3.7.5.4   Isotropy Index ι Expression

The full isotropy index can then be expressed as:

$$\iota = \frac{\mu_{\min}}{\mu_{\max}} = \frac{1}{\|J^{-1}\|_{2,\infty}\|J\|_{\infty,2}} \qquad (3.57)$$

3.7.6   Extension to force indices

v_{wc} and e_{wc} are closely related to f_{wc} by the well-known equation:

$$\tau = J^\mathsf{T}f \qquad (3.58)$$

Where $\boldsymbol{\tau}$ represents the joint torques, $\boldsymbol{f}$ represents the end effector forces, and $\boldsymbol{J}^{\mathrm{T}}$ is the transpose of the Jacobian. This is analogous to the equation:

$$\dot{\boldsymbol{\theta}} = \boldsymbol{J}^{-1}\dot{\boldsymbol{x}} \tag{3.59}$$

Where $\boldsymbol{\tau}$ and $\dot{\boldsymbol{\theta}}$ both represent joint values which require the ∞-norm, $\boldsymbol{f}$ and $\dot{\boldsymbol{x}}$ both represent end effector values which require the 2-norm, and $\boldsymbol{J}^{\mathrm{T}}$ and $\boldsymbol{J}^{-1}$ represent the relation between these values. To apply the indices for kinematics to force, simply substitute $\boldsymbol{J}^{\mathrm{T}}$ for $\boldsymbol{J}^{-1}$ to obtain:

$$\mu_{\max}^{\mathrm{f}} = \max_{\|\boldsymbol{\tau}\|_\infty=1}\|\mathbf{f}\|_2 = \max_{\|\boldsymbol{\tau}\|_\infty=1}\|\boldsymbol{J}^{-\mathrm{T}}\boldsymbol{\tau}\|_2 = \|\boldsymbol{J}^{-\mathrm{T}}\|_{\infty,2} \tag{3.60}$$

$$\mu_{\min}^{\mathrm{f}} = \min_{\|\boldsymbol{\tau}\|_\infty=1}\|\mathbf{f}\|_2 = \min_{\|\boldsymbol{\tau}\|_\infty=1}\|\boldsymbol{J}^{-\mathrm{T}}\boldsymbol{\tau}\|_2 = \frac{1}{\|\boldsymbol{J}^{\mathrm{T}}\|_{2,\infty}} \tag{3.61}$$

$$\iota^{\mathrm{f}} = \frac{\mu_{\min}^{\mathrm{f}}}{\mu_{\max}^{\mathrm{f}}} = \frac{1}{\|\boldsymbol{J}^{\mathrm{T}}\|_{2,\infty}\|\boldsymbol{J}^{-\mathrm{T}}\|_{\infty,2}} \tag{3.62}$$

From the definitions above, $\mu_{\max}^{\mathrm{f}}$ represents the maximum possible end effector force given unit joint torques. This is useful for determining a bound on the force a robot can exert, as well as quantifying the maximum possible error in output force. $\mu_{\min}^{\mathrm{f}}$ represents the minimum output force that can be obtained with unit joint torques, which quantifies how "weak" the robot can be in the worst case. ι^{f} represents force isotropy, quantifying how different the maximum and minimum possible output forces are, given unit joint torques.

3.7.7 Invariance and implications

Though these results appear analogous to the conventional results using κ^{-1}, there are some significant differences. Since the 2-norm of a matrix is invariant under transposition, and $\boldsymbol{J}$ and $\boldsymbol{J}^{-1}$ appear symmetrically in κ^{-1}, it follows that κ^{-1} is invariant under both transposition and inversion of $\boldsymbol{J}$. However, these results do not necessarily extend to when p, q-norms are used. Since $\boldsymbol{J}^{-1}$ and $\boldsymbol{J}$ no longer appear symmetrically in ι and ι^{f}, neither ι nor ι^{f} is generally invariant to inversion. Since the $\infty, 2$-norm and $2, \infty$-

norm both use the ∞-norm in their definitions, which is not generally invariant to transposition, they are also not generally invariant to transposition. ι and ι^f are therefore distinct unless $\boldsymbol{J}$ is unitary. This leads to the interesting result that the force and kinematic design problems must be considered independently when using realistic independent joint bounds and worst-case specifications.

3.7.8 Extension to global performance indices

The most common approach to Global Conditioning Indices (GCI) has been to average local performance indices such as κ^{-1} over the robot's workspace W [86, 87].

$$GCI = \frac{\int_W \kappa^{-1} dW}{\int_W dW} \tag{3.63}$$

Though this can give an intuitive feeling for how "well" the robot performs in its workspace, this approach has serious drawbacks. Intuitively, if there are a few configurations in the workspace where the local index is poor, but elsewhere the index is good, then the average will look good, even though the robot will perform poorly in some configurations. For system such as general purpose industrial robots where workspace utilization is not known a priori, GCI may be reasonable as an overall evaluation of performance, but for systems where failure is costly and workspace utilization is well understood, such as purpose-built medical or aerospace robots, this approach is not suitable. A more useful measure of global performance for specification-based design in these cases would be to use the worst case performance of the local index over the workspace. Since ι is a local worst-case value, a global index can be computed by sampling the workspace and finding the overall worst case value of ι. The Worst-case Global Index for isotropy (WGI_ι), analogous to the GCI above, can be defined as:

$$WGI_\iota = \min_W \iota \tag{3.64}$$

Similar global indices can be defined for μ_{min}, μ_{max}, and the force indices as well.

3.7.9 Discussion

Performance indices based on 2-norm joint constraints and average values over the workspace have their uses, but application of these to problems involving realistic independent joint bounds and worst-case specifications can lead to unsatisfactory results. Despite this, no viable alternative indices have yet been developed for specification-based design and evaluation. Worst-case p, q-norm indices can directly address these concerns, while also providing intuitive insights into robot performance. $\mu_{\min}$ and $\mu_{\max}$ are directly related to the worst-case velocity and error in a given configuration with realistic independent joint velocity/error bounds. $\iota = \frac{\mu_{\min}}{\mu_{\max}}$ quantifies the true kinematic isotropy of a robot in a given configuration, and provides an excellent objective function for optimizing competing error and velocity specifications or velocity isotropy. These indices also extend naturally to design and analysis problems with force specifications. The WGI further extends p, q-norm indices to global worst-case performance over the whole workspace. The literature is replete with design and optimization problems which would benefit from these indices even without further enhancement, including [65, 92, 93] and many more.

In terms of numerical performance, p, q-norm indices present no special challenges. Comparing (3.39) and (3.57), the main difference between computing ι and κ^{-1} is whether 2-norms or $\infty, 2$ and $2, \infty$-norms are used. The $\infty, 2$ and $2, \infty$-norms require nothing more than vector matrix multiplication to compute. The only potential numerical problem lies in computing $\mathbf{J}^{-1}$, but this is no different than for κ^{-1}. Additionally, all of the p, q-norm indices are simple enough to be easily implemented with only a few lines of code in $MATLAB$.

One potential drawback of the p, q-norm indices is that some require solving NP-hard problems. For large scale problems, such as long snake robots with many joints, or applications like analysis of protein folding, this could indeed be a concern, however for most realistic robots which generally have fewer than seven joints, a simple brute-force computational approach is very practical. To illustrate this, Figure 3.12, which required the indices to be evaluated 69,696 times, was generated in under 1 second on a 2.2 GHz Core i7 processor.

The utility of the p, q-norm family of indices can be demonstrated through the optimization and evaluation of the REMS. The REMS is designed to be cooperatively controlled, meaning the surgeon and

robot hold the surgical tool together, and the robot senses the surgeon's intent through a force sensor. Uniform velocity and error performance over the workspace is crucial for cooperatively controlled robots, particularly for surgical applications. Non-uniform performance can result in unexpected motion and serious manipulation errors, making isotropy the driving specification for this system.

The REMS uses a linear delta mechanism for a 3-dof translation stage. Due to the mechanical range of motion limits inherent in this design, the mobile platform is constrained to a cylindrical workspace defined by the three linear stages. The diameters of the base and mobile platform of the delta mechanism and the distance between the parallel legs have already been determined by mechanical and application constraints, leaving the length of the parallel legs as the only free parameter left for optimization. The highest performing linear actuators within size and cost limits are capable of up to $v_j = 200$ mm/s with a repeatability of $e_j = +/- 5$ μm, and a maximum force of $f_j = 136$ N. The required specifications for the delta robot of the REMS alone over its whole workspace are $v_{spec} > 100$ mm/s, $e_{spec} < 17$ μm, and $f_{spec} > 50$ N.

The importance of uniform performance in cooperatively controlled surgical robots means that the primary objective is to find the leg length maximizing kinematic isotropy. As discussed above, though m and κ^{-1} are often used as isotropy measures, their reliance on 2-norm joint bounds renders them unable to quantify true isotropy when realistic independent joint bounds are used. Since the REMS needs to be maximally isotropic over the whole workspace, global indices based on averages such as GCI are inappropriate. Since it combines true isotropy with worst case performance, WGI_ι is the most appropriate objective function for this application. Figure 3.11 shows WGI_ι as a function of leg length. The optimal worst-case isotropy occurs at a leg length of 174 mm. If the GCI is used along with ι, the optimal average-case isotropy occurs at a leg length of 164 mm. If the GCI is used along with κ^{-1}, the optimal average-case isotropy occurs at a leg length of 150 mm. This shows how conventional indices consistently overestimate the isotropy of mechanisms, and can result in significant differences in optimal parameters ($p_l = 150\ mm$ vs. $p_l = 174\ mm$).
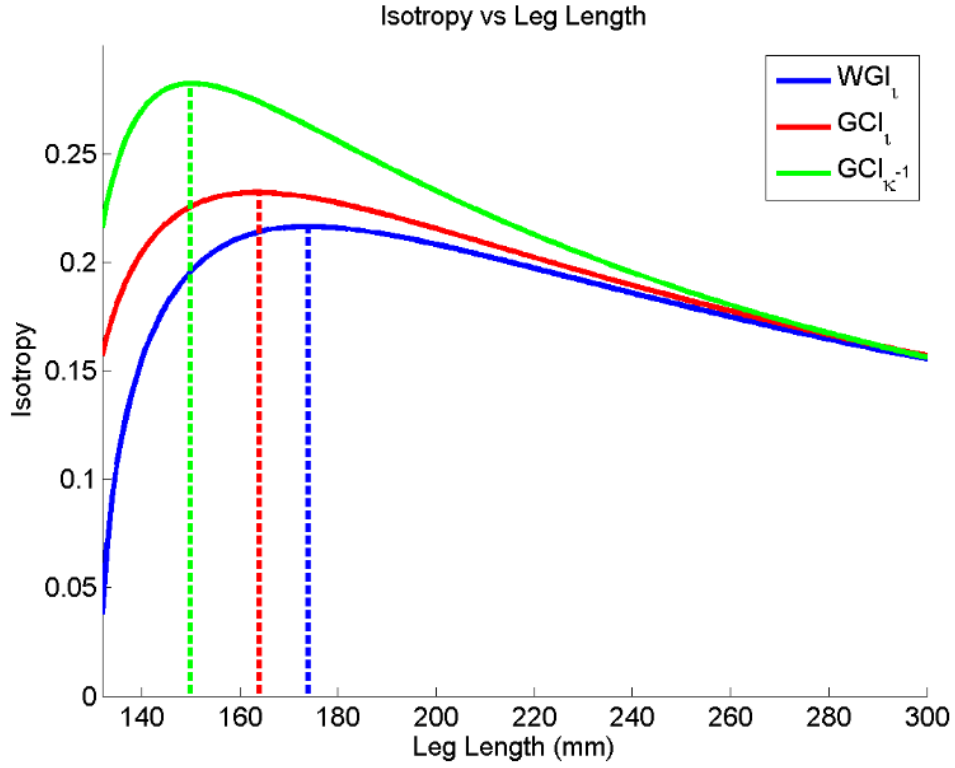
Figure 3.11: Comparison of WGI_ι, GCI_ι, and $GCI_{\kappa^{-1}}$.

The optimal leg lengths for the different indices are 174 mm for WGI_ι, 164 mm for GCI_ι, and 150 mm

for $GCI_{\kappa^{-1}}$.

Now that the optimal leg length has been found $WGI_{\mu_{\min}}$, $WGI_{\mu_{\max}}$, and $WGI_{\mu_{\min}^f}$ can be calculated

to check if the other specifications are met. Figure 3.12 shows ι, $\mu_{\min}$, $\mu_{\max}$, and $\mu_{\min}^f$ evaluated over the

workspace. Since the Jacobian of the linear delta robot is invariant in the z direction, every xy plane slice

through the workspace is identical when using Jacobian-based indices. Using these WGI index values, the

joint actuator specs, and (3.42), the global worst-case performance of the robot can be calculated as $v_{\mathrm{Gwc}} =$

130 mm/s, $e_{\mathrm{Gwc}} = 15$ μm, and $f_{\mathrm{Gwc}} = 82.6$ N, which are well within specifications.
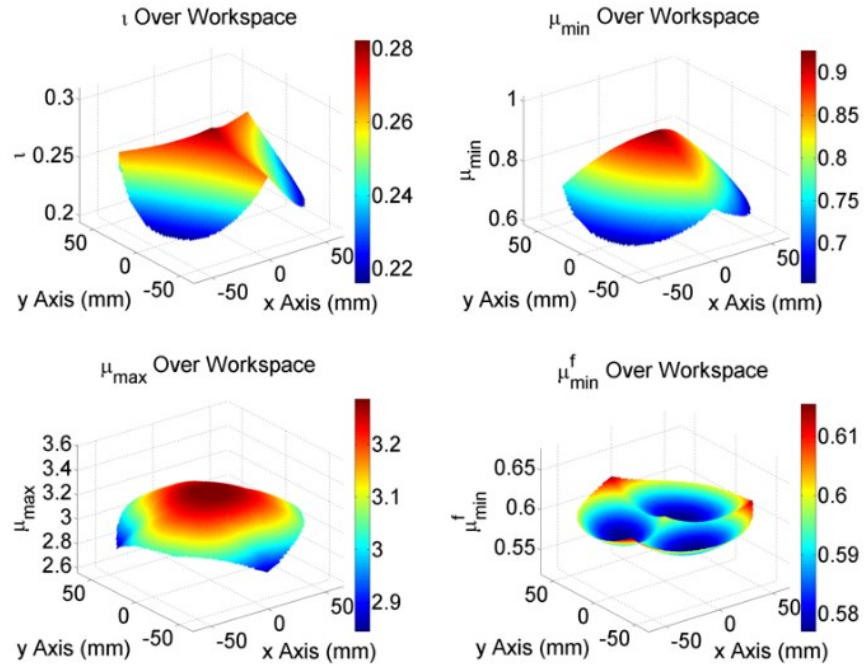
Figure 3.12: p, q-norm indices plotted over the REMS workspace.

3.8 Roll and Tilt Kinematic Optimization

Next, the parameters of the roll and tilt mechanisms must be optimized, which was done in collaboration with Alex He. These include h_r, the distance from the mobile platform to the axis of rotation of the roll joint, h_a, the distance from the axis of rotation of the roll joint to the arm, l_a, the length of the arm from the roll joint to the tilt joint, l_t, the distance from the tilt axis to the tool axis. Not all of these parameters effect the kinematic performance of the REMS, but some, such as h_r need to be tuned to ensure mechanical clearance and form-factor. Larger values of h_r provide clearance between the roll mechanism and the delta mechanism. However, ideally h_r would be as short as possible to avoid unnecessary leverage on the delta mechanism. To fit these constraints, h_r was chosen to be 51 mm, which provides the necessary clearance with a small safety margin.

Next, h_a and l_t must be chosen to optimize the kinematic performance of the roll and tilt joints. The main performance metrics for the roll and tilt joints are:

- The Required Translational Motion (RTM) of the delta mechanism required to enforce an RCM. For this analysis, an RCM located 40 mm down the tool shaft from the level of the tilt joint was used.

- The Total Rotary Motion (TRM) possible for each joint without collision with the patient. Collision with the patient is defined as a part of the robot crossing a horizontal plane through the RCM point.

- The amount of space the mechanisms occupy near the operating site. This can be quantified using the Environment occupation ratio (EOR). Since all of the ENT surgeries discussed require an approximately 40 mm diameter or less operating area the EOR is defined as the ratio of the occupied area S_P to the area of the circle S_C when the mechanism is projected onto a plane perpendicular to the tool shaft within a 40 mm diameter circle (Figure 3.13).
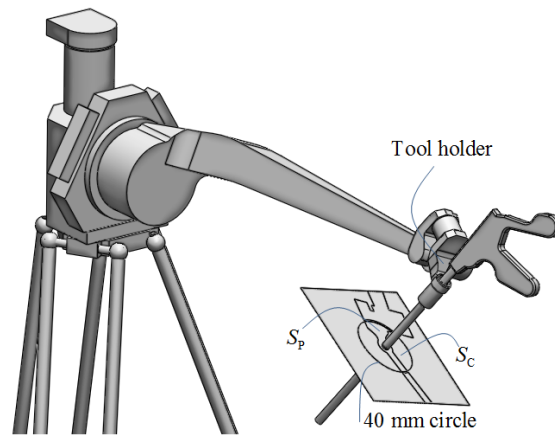
Figure 3.13: Environment Occupation Ratio (EOR)

Table 2.1 shows the 5 possible kinematic configurations of the rotary arm. C1 through C4 can be attained by varying the values of h_a and l_t, whereas C5 consists of a qualitatively distinct mechanical RCM mechanism.

Table 3.3: Kinematic Configurations for Rotary Arm

C1		$h_a = 0$ $l_t \neq 0$
C2		$h_a \neq 0$ $l_t \neq 0$
C3		$h_a = 0$ $l_t = 0$
C4		$h_a \neq 0$ $l_t = 0$
C5	Mechanical RCM	N/A

For this study, the values of h_a and l_t were chosen from $h_a \in \{0 \text{ mm}, 25 \text{ mm}\}$ and $l_t \in \{0 \text{ mm}, 25 \text{ mm}\}$. 25 mm was used because it fits within the mechanical and fabrication constraints of the design. These values can be further optimized in a future design iteration. Each configuration can now be evaluated according to each of the performance criteria as shown in Table 3.4. Based on these results, C2 is the best configuration since it has the best or intermediate values for each metric, whereas every other configuration has the worst value in one of the metrics. This results in choosing h_a and l_t to be $h_a = 25 \text{ mm}$, $l_t = 25 \text{ mm}$.

Table 3.4: RTM, TRM, and EOR for each configuration.

	C1	C2	C3	C4	C5
RTM for 20º Roll and 20º Tilt Motion [mm]	46.74	36.06	40.56	31.19	17.15
TRM Roll [º]	±50	>±70	±61	>±70	>±70
TRM Tilt [º]	±56	±56	±56	±56	±45
EOR	0.225	0.225	0.613	0.613	0.247

Finally, the length of the arm, l_a, can be determined. The main constraint for l_a is that the arm must be long enough to reach to the center of the bed when the robot is at the bedside. The standard width of an operating bed is 20" (~500 mm), so the arm must be a minimum of half this length (250 mm). It is also necessary to account for the width of the robot base, mostly determined by $r_b = 95.3 \; mm$, as well as $l_t = 25 \text{ mm}$, as well as a safety margin of an additional 50 mm. The required length of the arm can then be computed as:

$$250 \text{ mm} + r_b - l_t + 50 \text{ mm} = 370.3 \text{ mm} \qquad (3.65)$$

Based on this result, l_a was chosen to be 371 mm.

3.9 Phantom Mockup Validation

In order to validate the evaluation and analysis results, a prototype of the resulting optimal configuration, C2, was built using rapid prototyping methods. The wrist mechanism was composed of a laser cut acrylic arm with a 3D printed tilt joint and tool holder. The kinematic parameters of this wrist

mechanism were modified according to the analysis results. The wrist mechanism was then mounted on the rotary stage of the roll joint of JHU Eye Robot 1 (ER1) to form a 6 DOF robot as shown in Figure 3.14. In this configuration, the 3 DOF XYZ stage from the ER1 mimics the 3 DOF linear delta in the current design. The rotary stage of the ER1 provides the roll DOF in the wrist mechanism. Those four DOF can be driven using a joystick connected to ER1. The position of each DOF could also be recorded though the control interface of ER1, however, the tilt DOF of this prototype was left passive for simplicity. The 3D printed tool holder also provides a passive tool rotation DOF.
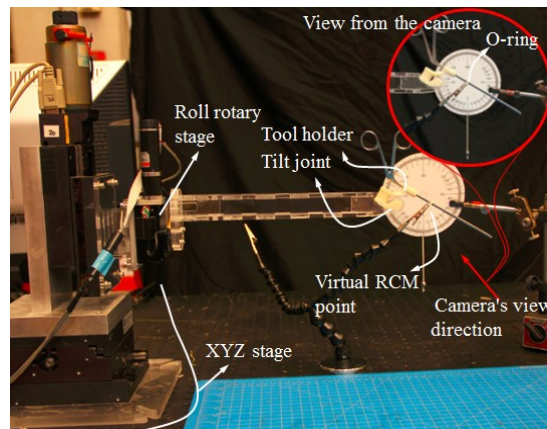
Figure 3.14: RTM verification experiment.

The goal of the first experiment was to verify the RTM required to implement a virtual RCM. As shown in Fig. 10, the positions of the XYZ DOF and angle of the roll DOF can be obtained directly from the control interface. A protractor was placed behind the tilt joint and a camera was mounted at the front of the robot to form a recording system for the tilt DOF. In the view from the camera, the virtual RCM point was coincident with the center of the protractor. A plastic O-ring was held at the virtual RCM point to indicate the position of this point.

The tilt DOF was rotated through a set of angles varying from -60º to +60º. The Roll DOF was fixed at 0º. Then the 3 DOF XYZ stage was manipulated in order to insure that the incision point on the tool is coincident with the virtual RCM point. The required stage motion is equal to the RTM. The experimental RTM and the calculated RTM from the above analysis can be compared with each other in Figure 3.15.
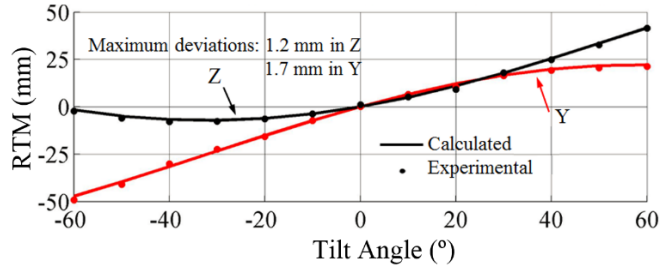
Figure 3.15: Experimental RTM verification results.

The RTM in the X direction was zero since the roll stage was left at 0 degrees for this experiment. The maximum error between the experimental and calculated RTM was only 2 mm.

Next, in order to further verify the feasibility of the design, the prototype was set up simulating three different OHNS surgeries using a rubber airway model. The setup for sinus surgery is shown in Figure 3.16 a). The robot arm enters the operating area from the top of the head of the model to hold the surgical tool. The initial angles of the roll and tilt DOF are -15 and -40 degrees from vertical respectively. The initial angles vary according to the location of the robot and posture of the patient's head. Exploration of the phantom using this setup showed that the previously determined +/-20 degree active range of motion is enough to cover the operating area.

Figure 3.16 b) illustrates the environment occupation near the surgical tool and the compatibility of this setup with additional tools. It can be seen that the right hand of the operator holds the instrument together with the robot. Another hand held tool is inserted though the left side of the nostril. Having $l_t \neq 0$ keeps the bulky mechanical structure of the robot out of the operating area and significantly reduces the possibility of instrument interference.
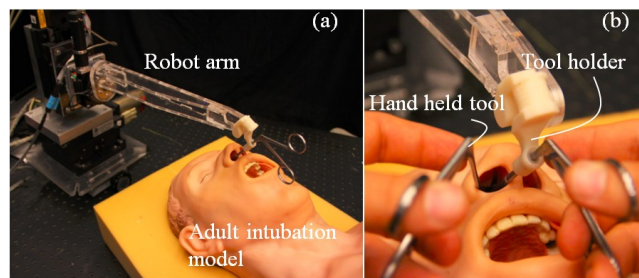
Figure 3.16: Sinus surgery mockup.

The setup for laryngeal surgery is presented in Figure 3.17 a). In this setup, the robot arm approached the operating area from left side of the patient's head to allow left handed operation. An additional hand-

held tool was also used in the right hand. The robot could have also been placed on the right side for a right hand operation. This feature allows the surgeon to switch hands if needed when performing laryngeal surgery. The roll and tilt angles in this setup are -50º and +10º from vertical. The active range of motion after the robot was initially positioned with the instrument in the laryngoscope was verified to be less than +/- 20 degrees. It was also verified that the tools are constrained to be approximately parallel to each other.

The environment around the operating area, as well as the field of view, were verified to be largely unobstructed by the robot or the tool holder in Figure 3.17 b). The unobstructed operating area also prevented tool interference.
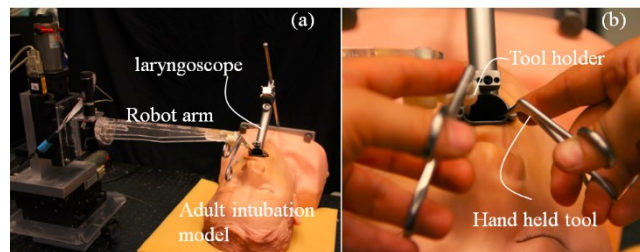
Figure 3.17: Laryngeal surgery setup.

Setup of the robot for middle ear surgery is shown in Figure 3.18. The intubation model was placed on its left side, simulating a right side cochlear implant. The robot was placed in front the model's chest. The operator manipulates the tool right-handed with the assistance of the robot. The simulated operation shows the restraints on the tool range of motion are much less than for the other two surgeries. The initial angles of the wrist DOF are also smaller than for the other two surgeries, since the tool is near vertical. The active range of motion required of each wrist DOF was small since much of the required movements was achieved with translation alone.
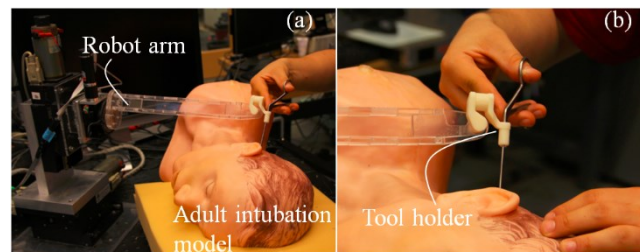
Figure 3.18: Middle ear surgery setup.

In each simulation, the robot configuration, range of motion, and space occupied near the tool were verified by the clinical collaborators to be reasonable for each surgery type.

113

3.10 Mechanical Implementation
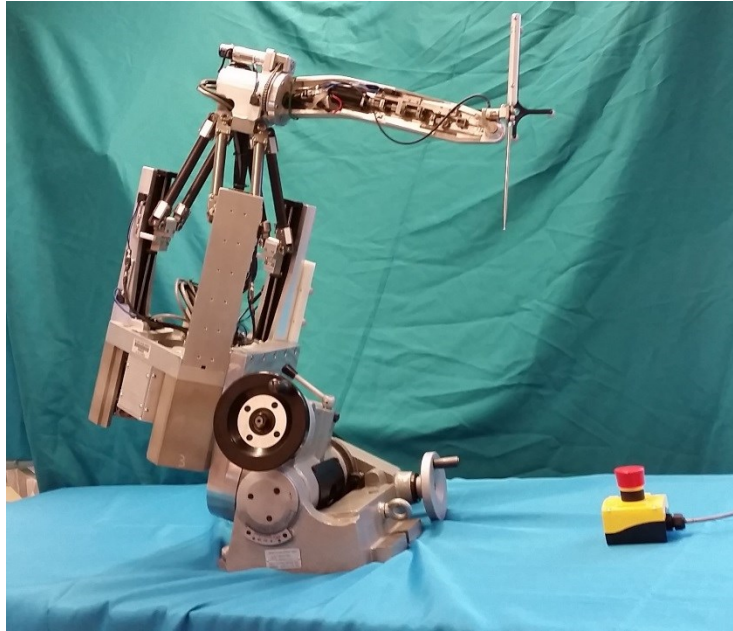
Figure 3.19: REMS Overview

3.10.1 Theoretical design goals

The first step in implementation is to determine rough design goals for each system component so that component selection and evaluation can begin. For each of the active joints, resolution, repeatability, and stiffness are considered.

3.10.1.1 Resolution

Resolution refers to the minimum incremental movement the robot can physically produce. It is mainly determined by the control unit, especially the encoders. It is also determined by the drive characteristics and the specific kinematic structure. The main factor we considered in this analysis is the fluctuation of encoders since motors can oscillate around the command position in a servo feedback control system.

Since encoder error is the main determinant of resolution, this section will focus on deriving an upper bound on the error of each joint in order to achieve a specified end effector error. First, define

$$\Delta x = J\Delta\theta \tag{3.66}$$

114

Where $\Delta\boldsymbol{\theta}$ is the vector of joint angle errors, and $\Delta\boldsymbol{x}$ is the vector of workspace errors of the instrument tip, and $\boldsymbol{J}$ is the Jacobian of the robot for the instrument tip. Since $\boldsymbol{J}$ changes over the workspace of the robot, it will be computed in the home position in this section, and over the whole workspace in later sections. When using $\boldsymbol{J}$, it is important to make sure the units are consistent and not to mix rotations and translations. Since the linear delta stage uses translations as inputs, the corresponding part of $\boldsymbol{J}$ must be scaled by the pitch of the ball screws used to implement it (here assumed to be 2 mm / 2π rad), to convert the input unit into radians and keep $\boldsymbol{J}$ consistent with input units of radians and output units of mm.

Since making joints more precise adds to the expense and complexity of the robot, it is desirable to find the joints responsible for the most error and focus on making those more precise. This can be done by computing the error contribution for each joint:

$$\|\Delta\boldsymbol{x}_i\|_2 = \|\boldsymbol{J}_i\Delta\theta_i\|_2 = |\Delta\theta_i|\|\boldsymbol{J}_i\|_2 \tag{3.67}$$

Where $\Delta\boldsymbol{x}_i$ is the end effector error due to the ith joint, $\Delta\theta_i$ is the ith joint error, and $\boldsymbol{J}_i$ is the ith column of $\boldsymbol{J}$. In order to equalize the contributions of each joint, let:

$$\varepsilon = |\Delta\theta_i|\|\boldsymbol{J}_i\|_2 \ \forall i \tag{3.68}$$

Then solve for $\Delta\theta_i$.

$$\Delta\theta_i = \pm\frac{\varepsilon}{\|\boldsymbol{J}_i\|_2} \tag{3.69}$$

Though this method determines the relative weighting of the desired errors of each joint, summing these results to reach an estimate total error will generally result in a significant overestimate, since the errors will likely not point in the same direction. Instead, a tighter bound can be computed by expanding (3.66) as follows:

$$\|\Delta\boldsymbol{x}\|_2 = \left\|\sum_{i=1}^{5}\boldsymbol{J}_i\,\Delta\theta_i\right\|_2 \tag{3.70}$$

Then substitute (3.69) into (3.71) and compute $\Delta x_{\max} = \max(\|\Delta\boldsymbol{x}\|_2)$, the worst case value of $\|\Delta\boldsymbol{x}\|_2$:

$$\Delta x_{\max} = \varepsilon\max_{\pm}\left\|\sum_{i=1}^{5}\pm\frac{\boldsymbol{J}_i}{\|\boldsymbol{J}_i\|_2}\right\|_2 \tag{3.72}$$

115

This can be solved by brute-force computing the sum for every combination of ± signs and selecting the maximum result. Since $\Delta x_{\max} = 25$ μm is known from the requirements, ε can be solved for as:

$$\varepsilon = \frac{\Delta x_{\max}}{\max_{\pm}\left\|\sum_{i=1}^{5} \pm \frac{J_i}{\|J_i\|_2}\right\|_2} \tag{3.73}$$

And $|\Delta \theta_i|$ can be solved for using (3.69) as:

$$|\Delta \theta_i| = \frac{\Delta x_{\max}}{\max_{\pm}\left\|\sum_{i=1}^{5} \pm J_i\right\|_2} \tag{3.74}$$

Using this result, the desired values of $|\Delta \theta_i|$ can be computed (Table 3.5).

Table 3.5: Desired joint resolution error bounds.

Joint	Delta 1	Delta 2	Delta 3	Roll	Tilt
$\|\Delta\boldsymbol{\theta}_i\|$ $(e^{-4}$ **rad**)	113.17	113.17	113.17	0.80	0.57

From this, it is clear that workspace resolution errors are most sensitive to the roll and tilt joints since these have by far the tightest error bounds.

3.10.1.2 Repeatability

Repeatability specifies the ability of the robot to return to the same location in a repetitive motion. The factors influencing repeatability include joint resolutions, which were computed in the previous section, and any backlash in the transmission system. The mechanical design must be optimized to minimize backlash through the use of preloaded bearings and backlash-free transmissions, but a small amount of backlash and hysteresis will inevitably still be present. Though the system does not have an independent repeatability requirement, repeatability affects unloaded accuracy, for which the design requirement is 1.0 mm of error over the workspace.

3.10.1.3 Stiffness

The structure and joint stiffnesses were considered in the design of the REMS, however only joint stiffness is discussed here since structural stiffness can be optimized by simply strengthening the robot's

frame. The influence of joint stiffness can be analyzed similarly to the previous joint error analysis. The calculation results are show in Table 3.6.

Table 3.6: Desired joint stiffness error bounds.

Joint	Delta 1	Delta 2	Delta 3	Roll	Tilt
$|\Delta\theta_i|$ (e^{-4} rad)	4527	4527	4527	32	23

In this calculation, the target compliance of the tool tip is 1.0 mm at the tip of the 100 mm long instrument shaft under the full operating load (5 N applied on a 100 mm tool handle). As before, displacement error due to compliance is by far most sensitive to the roll and tilt joints.

3.10.1.4 Velocity

For the delta stage, the goal is to determine what the required joint speeds v_j are for $v_{wc} = 100$ mm/s. $WGI_{\mu_{min}}$ can be used to determine this as follows:

$$v_j = \frac{v_{wc}}{WGI_{\mu_{min}}} = \frac{100 \text{ mm/s}}{.65} = 154 \text{ mm/s} \tag{3.75}$$

Computing the required motor speed for a 2 mm/rev ball screw results in:

$$154 \frac{\text{mm}}{\text{s}} \cdot \frac{1 \text{ rev}}{2 \text{ mm}} \cdot \frac{60 \text{ s}}{1 \text{ min}} = 4620 \text{ rpm} \tag{3.76}$$

For the roll and tilt stages, the required rotational velocity is 60 degrees per second, which is approximately 1 radian per second.

3.10.1.5 Force

Since the mobile platform plus the arm and rotary stages weigh approximately 2 kg, this must be added to the required 5 N operating force. $WGI_{\mu_{min}^f}$ can be used to determine the required joint forces f_j are for $f_{wc} = 5 \text{ N} + 9.8 \frac{m}{s^2} \cdot 2 \text{ kg}$.

$$f_j = \frac{f_{wc}}{WGI_{\mu_{min}^f}} = \frac{25 \text{ N}}{.69} = 36.2 \text{ N} \tag{3.77}$$

For the roll and tilt joints to be capable of producing 5 N of force at the end of a 100 mm length instrument handle, the required torque can be computed as follows:

$$\tau = 5 \text{ N} \cdot 100 \text{ mm} = 500 \text{ mNm} \tag{3.78}$$

3.10.2 Delta Mechanism Implementation

The primary components of the REMS delta mechanism include a custom machined aluminum base, ball screw linear stages (MCM03015P02K, NSK, Inc.) with custom machined aluminum supports, custom made carbon fiber tube parallelogram legs, custom made universal joints with preloaded bearings, a custom machined mobile platform, linear stage motors (3257G024, Micromo, Inc.) with 1024 pules per revolution encoders, custom made aluminum motor covers, and a custom made hexagonal shielded aluminum electronics enclose (Figure 3.20). The electronics enclosure serves as a breakout box for all of the system's wiring, as well as housing the force sensor interrogator board (9105-NETAOEM, ATI. Inc.). Each linear stage has forward and reverse limit switches (Figure 3.21). Next, the specifications of the components used in this design can be used to determine if the system should meet specifications.
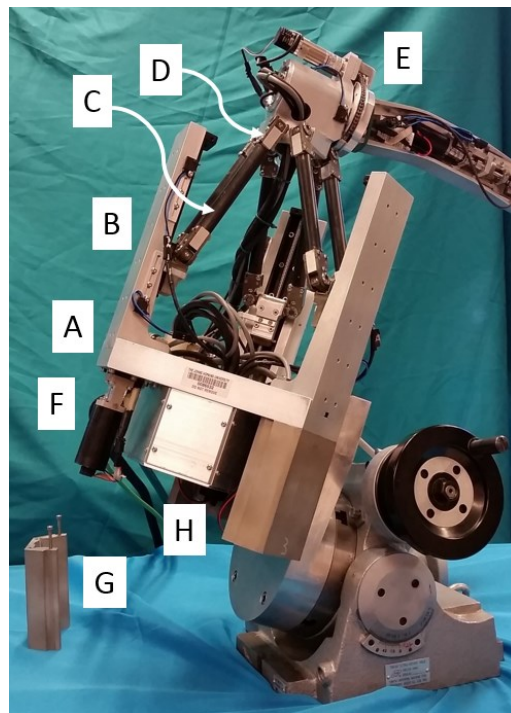
Figure 3.20: Delta mechanism implementation.

A) Base B) Linear stage and support C) Parallelogram leg D) Universal joint E) Mobile platform F) Linear stage motor G) Motor cover H) Shielded electronics enclosure.
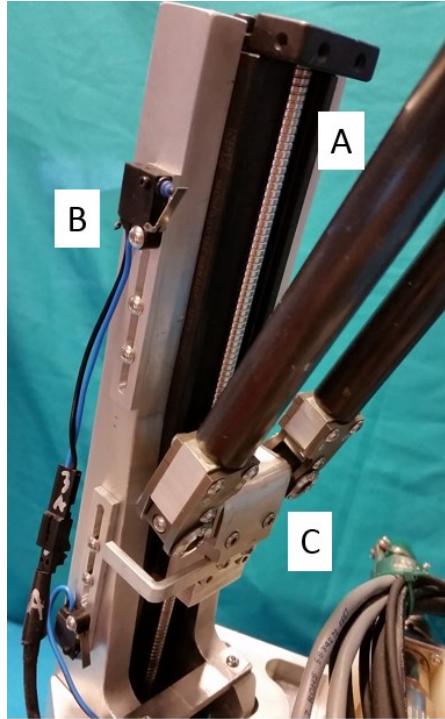
Figure 3.21: Linear stage.

A) Ball screw B) Limit switch on adjustable slider C) Parallelogram leg attachment block with limit switch lever

3.10.2.1 Resolution

Based on the analysis from Table 3.5, the goal resolution for each linear stage is:

$$\frac{113.7\mathrm{e}-4\ \mathrm{rad}}{\mathrm{inc}} \cdot \frac{2\ \mathrm{mm}}{2\pi\ \mathrm{rad}} = \frac{.0036\ \mathrm{mm}}{\mathrm{inc}} \tag{3.79}$$

Since 1024 pulse per revolution encoders were used, the actual resolution is 4 times greater that this since each pulse results in 4 counts. However, it is generally not reasonable to assume that a motor can be controlled to within 1 count, so it is assumed that the actual resolution increment (inc) is 1/1024 of a revolution to allow +/-4 counts for control errors. The resolution of each linear stage of the delta mechanism can be computed as:

$$\frac{1\ \mathrm{rev}}{1024\ \mathrm{inc}} \cdot \frac{2\ \mathrm{mm}}{1\ \mathrm{rev}} = \frac{1\ \mathrm{mm}}{512\ \mathrm{inc}} \approx \frac{.002\ \mathrm{mm}}{1\ \mathrm{inc}} \tag{3.80}$$

This is well within the specification.

3.10.2.2 Repeatability

The ball screw stages are rated to have a repeatability of .003 mm. Since no gearheads were used on the motors, and zero backlash shaft couplings were used to couple the motor to the stage, there are no other theoretical contributors to repeatability errors for each linear stage apart from this and the resolution.

3.10.2.3 Stiffness

The stiffness of the delta mechanism can be broken down into two parts, joint stiffness and structural stiffness. Since the ball screw stages have very high stiffness compared to the forces applied to the system, their stiffness is likely to be overwhelmed by structural compliance. Though it is possible to model structural compliance in delta mechanisms [66], this process is more complex and time consuming than simply building a prototype and evaluating the stiffness experimentally. Therefore, no theoretical stiffness evaluation was conducted.

3.10.2.4 Velocity

The motors used for the delta mechanism are capable of up to 5900 rpm, which exceeds the previously computed requirement of 4620 rpm.

3.10.2.5 Force

It was previously calculated that each linear stage must be capable of applying 36.2 N of force. In addition to this, the motor and linear stage both have friction effects to consider. According to its data sheet, the dynamic friction torque for the linear stages is 17 mNm, and the motor friction torque is 4.8 mNm. These can be used to solve for the required motor torque as follows:

$$\tau = \frac{2 \text{ mm}}{2 \pi} 36.2\text{N} + 17 \text{ mNm} + 4.8 \text{ mNm} = 33.3 \text{ mNm} \tag{3.81}$$

The rated torque of the motor is 70 mNm, so this is well within specification.

3.10.3 Rotary Arm Implementation

The detailed design and implementation of the rotary arm was mostly the work of Alex He under my supervision. My main contributions are the overall design, some of the fabrication, and some later revisions to the design. The implementation of the rotary arm is shown in Figure 3.22. The main components are the roll stage, arm, tilt stage, force sensor, and tool holder. In order to meet performance as well as size and weight requirements, both the roll and tilt stages incorporate complex, multi-stage transmission systems.
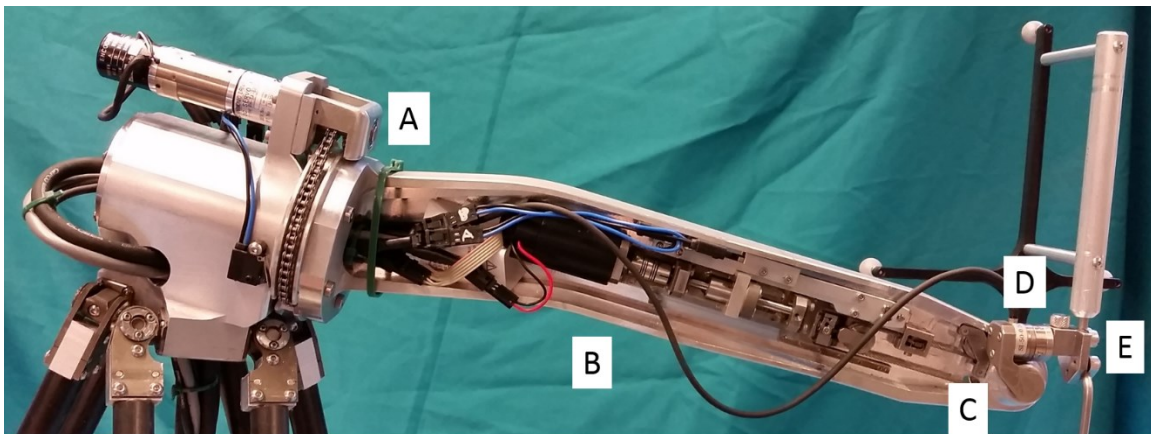
Figure 3.22: Rotary arm.

A) Roll joint B) Arm C) Tilt joint D) Force sensor E) Tool holder

3.10.4 Roll Joint Implementation

The roll joint consists of a DC servo motor with a harmonic drive gearhead and a 500 pulse per revolution encoder (RH5A8002E050AO, Harmonic Drive LLC. Peabody, MA), a 12 tooth chain sprocket (A 6X 7M1412, SDP-SI Inc. New Hyde Park NY 11040), a precision roller chain (A 6Y 7MM140, SDP-SI Inc. New Hyde Park NY 11040), and a custom machined chain pulley (Figure 3.23). Limit switches are mounted on each side of the roll stage which are triggered by adjustable tabs mounted on the chain pulley. Access holes enable wiring to pass up through the bottom of the mobile platform to both the roll stage, and a hollow shaft enables wiring to pass through the roll joint from the back in order to reach the tilt stage.
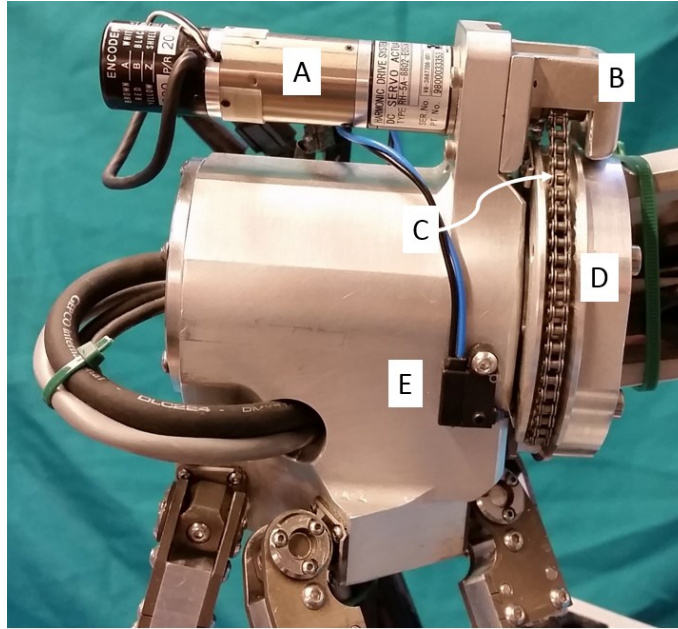
Figure 3.23: Roll joint.

A) Roll joint motor B) Motor sprocket C) Chain D) Roll Joint wheel E) Limit switch

The original design was to use a cable system rather than a chain, but due to the difficulty of manufacturing a cable pulley capable of winding 6 turns of a cable, as well as the limited reduction ratio possible due to the bend radius of the cable, the chain mechanism was used instead. In order to reduce backlash and aid in tensioning, the chain only interfaces with a sprocket on the motor size. On the joint side, the chain is split and each end is independently attached to the chain pulley. The chain can be tensioned by tightening tensioning screws on the chain pulley. This somewhat unusual configuration has several major advantages:

- Backlash is less than it would be in a system with two sprockets. In this configuration, there is no backlash between the chain and the pulley, and any backlash between the chain and the sprocket is reduced by the reduction ratio (~5.4:1).

- Tensioning is simple since no additional idlers are required and the motor and joint axes do not need to move relative to each other to tension the mechanism.

- Fabrication is simpler than for a cable mechanism, since to complex multi-turn pulleys are required.

122

- Stiffness is better than it would be for a comparable cable mechanism with similar reduction, since there are no bend radius constraints for the chain going around the sprocket (pitch diameter 14.48 mm), whereas a cable would need to be quite thin in order to handle a bend radius under 8 mm.

In order to attain sufficient reduction while maintaining a stiff, low-backlash design, a 50:1 reduction harmonic gearhead was used on the roll motor rather than a conventional planetary gearhead.

3.10.4.1 Resolution

The theoretical resolution of this design can be determined from the resolution of the encoder and the reduction of the transmission. As before, it is assumed that one resolution increment involves controlling the motor to within +/- 4 encoder counts. The reduction of the gearhead is 50:1, and the reduction of the chain mechanism is 5.4:1.

$$\frac{1 \text{ rev}}{500 \text{ inc}} \cdot \frac{2\pi \text{ rad}}{1 \text{ rev}} \cdot \frac{1}{50} \cdot \frac{1}{5.4} = 0.47\mathrm{e}-4 \text{ rad} \qquad (3.82)$$

This is well below the desired 0.8e-4 radians per increment computed in Table 3.5.

3.10.4.2 Repeatability

Though there is no independent repeatability requirement, it is still important to consider repeatability since it affects unloaded accuracy. The primary sources of repeatability errors in the roll mechanism are errors due to resolution, hysteresis in the harmonic drive gearhead, and backlash in the chain. Unfortunately, no specifications for backlash were given for the chain, so it is not possible to include this in the computation without empirically verifying the chain's performance. As for the harmonic drive gearhead, it is rated to have less than 3 arc-min of hysteresis, which when combined with the resolution, results in a repeatability of:

$$3 \text{ arc} - \min \cdot \frac{0.0003 \text{ rad}}{\text{arc} - \min} \cdot \frac{1}{5.4} + 0.47\mathrm{e}-4 \text{ rad} = 2.14\mathrm{e}-4 \text{ rad} \qquad (3.83)$$

3.10.4.3 Stiffness

The main contributors to the stiffness of the roll joint are the stiffness of the harmonic drive gearhead and the stiffness of the chain. According to its data sheet, the deflection of the harmonic drive actuator in

response to a 500 mNm torque reduced by a ratio of 5.4:1 is 16.1e-4 rad at the gearhead, which when reduced by 5.4:1 results in a roll joint deflection of 2.98e-4 rad at the roll joint. The chain deflection can be computed from the data sheet for a 150 mm length of chain as .005 mm. For an approximately 40 mm pulley radius and a 100 mm long instrument, the total chain deflection can be computed as:

$$\Delta l = \frac{.005 \text{ mm}}{40 \text{ mm}} \cdot 100 \text{ mm} = .0125 \text{ mm} \tag{3.84}$$

Finally, the total deflection of the tilt joint in radians can be computed by combining the chain result and the gearhead result as follows:

$$\frac{.0125 \, mm}{100 \, mm} + 2.98e - 4 \text{ rad} = 4.23e - 4 \text{ rad} \tag{3.85}$$

This is well below the desired deflection of 32e-4 rad computed in Table 3.6.

3.10.4.4 Velocity

The roll motor is rated for 4500 rpm, and when combined with the 50:1 gearhead reduction and 5.4:1 chain reduction, the final output speed can be computed as follows:

$$4500 \text{ rpm} \cdot \frac{1 \text{ min}}{60 \text{ sec}} \cdot \frac{2\pi \text{ rad}}{1 \text{ rev}} \cdot \frac{1}{50} \cdot \frac{1}{5.4} = 1.75 \text{ rad/s} \tag{3.86}$$

The requirement was 1 rad/s, so the motor speed is sufficient.

3.10.4.5 Force

According to its datasheet, the rated torque of the motor and gearhead is 400 mNm. The friction of the chain and roll joint bearings are dependent on the details of how the system was tensioned, so it is not possible to include these here without determining them empirically. Combined with the 5.4:1 chain reduction, the potential output torque of the roll joint can then be computed as:

$$400 \text{ mNm} \cdot 5.4 = 2.16 \text{ Nm} \tag{3.87}$$

The requirement was 0.5 Nm, so the output torque is sufficient and should be more than enough to make up for any friction effects.

3.10.5 Arm and Tilt Joint Implementation

The arm and tilt mechanism are composed of several major parts. The custom machined aluminum arm also acts as a partial enclosure for the tilt mechanism components. The tilt mechanism consists of a DC servo motor with a 1024 pulse per revolution encoder (2642W024CRIE2-1024 Micromo Inc. Evergreen, FL, USA), directly coupled to a custom translation stage made using a 0.5 mm / revolution pitch ball screw (1412.XXX/0,5.5.52.72 P5P, August Steinmeyer GmBH, Albstadt, Germany), which drives a cable mechanism linking to the tilt axis pulley (Figure 3.24). The stainless steel cables used were 1.6 mm in diameter (SN2065, Carl Stahl Sava Industries, Inc., Riverdale, NJ).
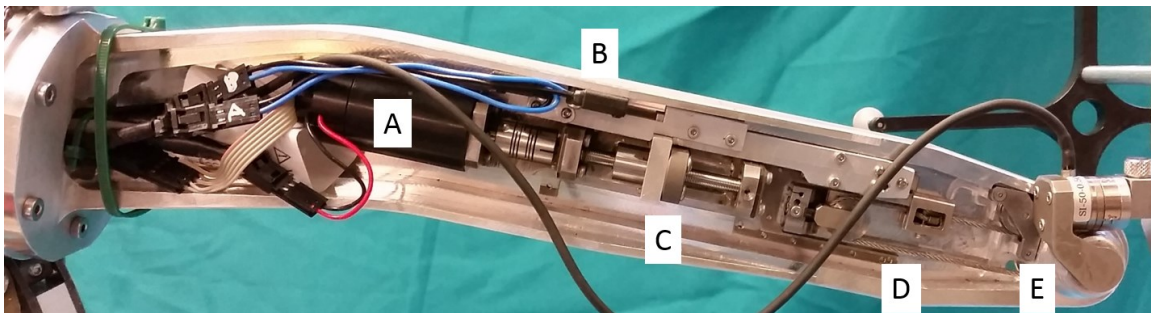
Figure 3.24: Arm and tilt mechanism.

A) Motor B) Limit switch C) Ball screw D) Cable mechanism E) Pulley and tilt arm

The main factors influencing the design of the arm were form factor and stiffness. Since the arm and tilt mechanisms are closer to the operating area than any of the robot components, compactness is critical. One of the most challenging aspects of the design is how to transmit torque to the tilt joint and meet stiffness requirements while fitting into this tight form factor. One way to do this would be to orient the tilt motor so that it is parallel with the tilt axis and located near the roll stage, transmitting torque to the tilt joint via a cable or chain mechanism. If a harmonic gearhead were used, it would provide enough reduction for sufficient resolution and torque, but the stiffness would still be a major issue. It would be difficult to implement a distal reduction after the harmonic drive, so stiffness of the gearhead would translate directly into the stiffness of the tilt joint. Also, any chain or cable mechanism long enough to reach from near the roll joint to the tilt joint would have poor stiffness due to its length. Additionally, the tilt mechanism is very close to the operating area, so pulley larger in diameter than 20 mm could not be used, making it difficult to use stiff cables or chains.

Because of these issues, a different approach was taken. The tilt motor was mounted axially aligned with the arm, which allows it to fit into the arm's form factor while also not requiring it to be very distal from the tilt joint. The main challenge of this design is how to transmit the motion of the motor to the tilt joint when their axes are perpendicular. Conventional approaches for changing the axis of rotation of a transmission like worm or miter gears are not suitable because of their substantial backlash. Ball screws, however, can perform a similar function while providing high stiffness and low backlash. The main challenge when using a ball screw is how to transform its linear output back into a rotary output with the correct rotation axis. This was achieved by using the ball screw to drive a linear stage which attaches to a cable going around a pulley system. For added stiffness, two cables were used in parallel. Though relatively thin 1.6 mm diameter cables had to be used in order to fit the 20 mm pulley diameter, their length is short, so the stiffness of the mechanism is not significantly compromised. The cable mechanism can be tightened by turning a screw which pulls on the idler pulley.

3.10.5.1 Resolution

The main factors affecting the resolution of the tilt joint are the encoder resolution and the reduction of the transmission, particularly the 0.5 mm/revolution pitch ball screw and 10 mm radius pulley. As before, it is assumed that the motors can be controlled to within +/- 4 encoder counts. The resolution can then be computed as:

$$\frac{1 \text{ rev}}{1024 \text{ inc}} \cdot \frac{0.5 \text{ mm}}{1 \text{ rev}} \cdot \frac{1 \text{ rad}}{10 \text{ mm}} = .49\text{e} - 4 \text{ rad} \tag{3.88}$$

The desired resolution from Table 3.5 was 0.75e-4 rad, so the resolution requirement is met.

3.10.5.2 Repeatability

Since no chains or gearheads are used in the tilt transmission system, and the ball screw has no specification for repeatability, the repeatability is theoretically only limited by the resolution. In practice, however, other effects such as hysteresis in the cable mechanism and backlash in the ball screw and linear stage will likely be present. The effect of these will have to be determined empirically in a later section.

3.10.5.3 Stiffness

The stiffness of the tilt mechanism is primarily determined by the stiffness of cable since the stiffness of the ball screw and other components are comparatively much larger. With 500 mNm of torque applied to the tilt axis, the force on the cable can be computed as:

$$\frac{500 \text{ mNm}}{10 \text{ mm}} = 50 \text{ N} \tag{3.89}$$

Since there are two cables, the force on each cable is 25 N. From the cable datasheet, 25N on an 80 mm cable length results in .016 mm of deflection. The deflection of the tilt joint in radians can then be computed as:

$$\frac{.016 \, mm}{10 \, mm} = 16e - 4 \, rad \tag{3.90}$$

This is within the desired 23e-4 rad from Table 3.6.

3.10.5.4 Velocity

From the datasheet, the tilt motor is capable of 6400 rpm. Using this and the transmission reduction, the maximum tilt joint speed can be computed as follows:

$$\frac{6400 \text{ rev}}{1 \text{ min}} \cdot \frac{1 \text{ min}}{60 \text{ sec}} \cdot \frac{0.5 \text{ mm}}{1 \text{ rev}} \cdot \frac{1 \text{ rad}}{10 \text{ mm}} = 5.33 \text{ rad/s} \tag{3.91}$$

This is significantly greater than the requirement of 1 rad/s.

3.10.5.5 Force

The motor is capable of 28 mNm of torque from its datasheet. The ball screw and motor result in a combined friction torque of 17 mNm (from their respective datasheets). Using the 0.5 mm pitch ball screw and the 10 mm tilt axis pulley, the output torque of the tilt mechanism can then be computed as:

$$(28 \text{ mNm} - 17 \text{ mNm}) \cdot \frac{2 \cdot \pi \cdot 10 \text{ mm}}{0.5 \text{ mm}} = 1.4 \text{ Nm} \tag{3.92}$$

This exceeds the required 0.5 Nm.

3.11 Overall Theoretical Validation

Now that the theoretical performance of each component is known for this implementation, the theoretical performance of the entire system can be calculated. Since the force and velocity requirements were already separate for each axis, there is no need to try to compute overall performance for these. Therefore this analysis will only be performed for resolution, repeatability, and stiffness.

3.11.1 Overall Theoretical Resolution

The REMS has many symmetries that can be exploited in order to speed up the calculation of overall theoretical resolution over the whole workspace, these include:

- The Jacobian of the delta mechanism is invariant in the z direction, so it only needs to be evaluated in the x-y plane.

- The Jacobian of the delta mechanism is symmetric about the x axis, so only one side of the y axis needs to be evaluated.

- The Jacobian of the roll/tilt stage is symmetric about roll = 0, so only one side of roll values needs to be evaluated.

Applying these symmetries, the worst-case resolution over the workspace at the tip of a 100 mm length instrument was 0.011 mm, which exceeds the required value of 0.025 mm. Figure 3.25 shows the resolution evaluated over the translational and rotational workspaces.
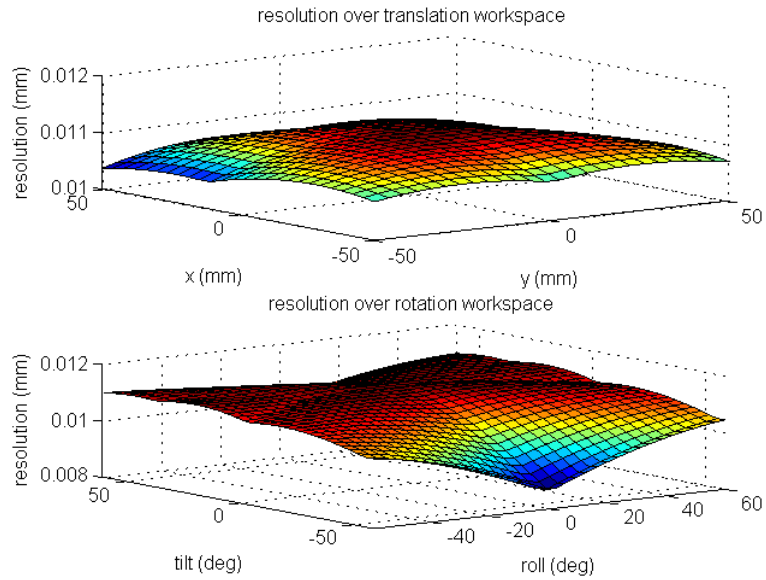
Figure 3.25: Resolution over workspace.

3.11.2 Overall Theoretical Repeatability

The theoretical repeatability over the workspace can be computed using the same methods as for resolution but with the theoretical repeatability values for each axis. The worst case value for repeatability was 0.033 mm. Figure 3.26 shows repeatability over the translational and rotational workspaces. Though these repeatability values can give a lower bound for the repeatability that can be expected, there are many unmodeled effects that this analysis cannot capture, such as hysteresis and backlash in components that were not listed in their datasheets.
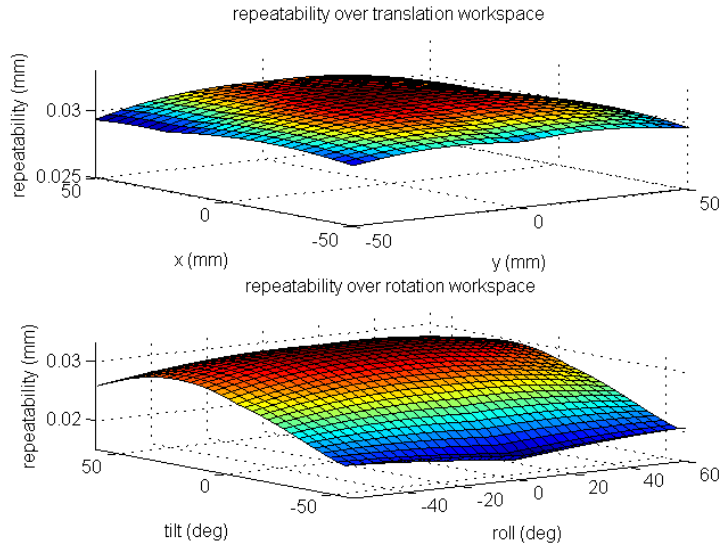
Figure 3.26: Repeatability over workspace.

3.11.3 Overall Theoretical Stiffness

Since there were no theoretical stiffness estimates for the delta mechanism, only the theoretical stiffness of the rotary axes can be used. The deflection values are measured at the tip of a 100 mm long instrument for a 5 N force applied at the end of a 100 mm instrument shaft. The worst case value was 0.138 mm, which is well within the 1.0 mm requirement. Figure 3.27 shows the deflection over the rotary workspace. This analysis is only modeling joint stiffnesses for which values can be theoretically computed, so it is expected that structural stiffness and unmodeled joint stiffnesses will be present in the actual design. These values are intended to be a lower bound.
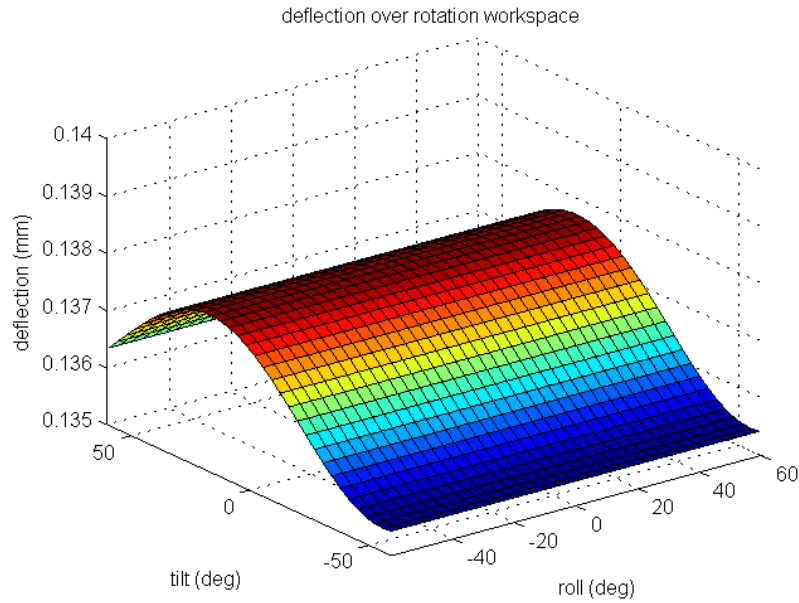
Figure 3.27: Deflection over workspace.

3.12 Force Sensor and Tool Holders

3.12.1 Force Sensor

The REMS uses a 6 degree of freedom force/torque sensor (Nano 17, ATI, Inc. Apex, NC 27539 USA) which integrates with an Ethernet enabled interrogator (NET F/T OEM, ATI, Inc. Apex, NC, USA). The force sensor is mounted at the end of the tilt arm (Figure 3.28). This specific force sensor was chosen because of its compact form factor and its force and torque ranges (5N, 500 mNm), which are well matched for surgical applications. The Ethernet interrogator was used rather than a cheaper analog digital converter (ADC) because similar force sensors with ADCs had been used previously with the JHU steady hand robots and encountered noise issues. The Ethernet interrogator has integrated hardware filtering to resolve issues with both mechanical and electrical noise. This force sensor also has several weaknesses, particularly its inability to work in environments with water or chemicals, and relatively low stiffness and breaking strength.
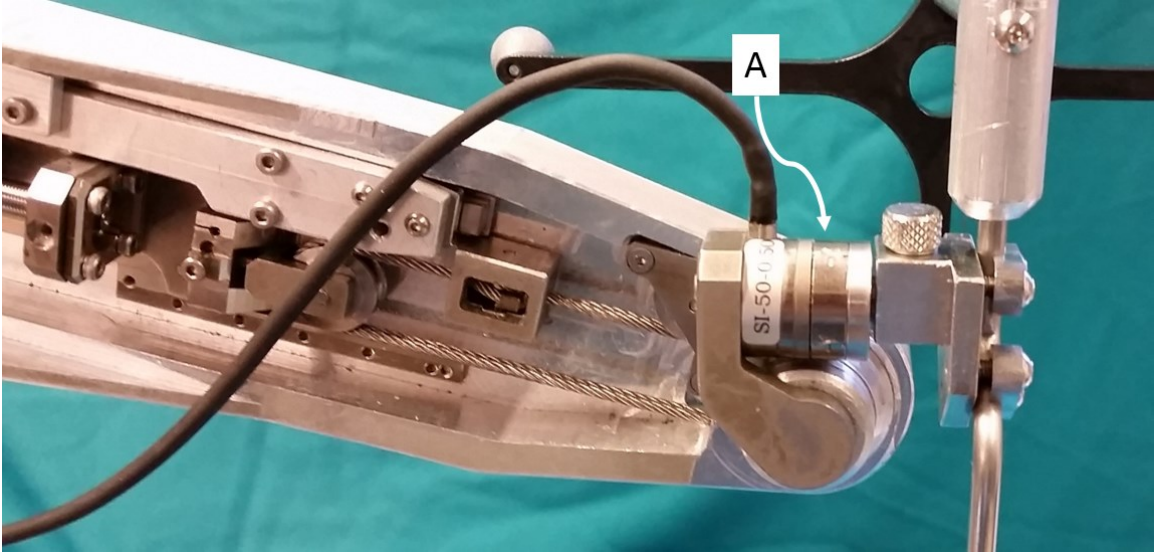
Figure 3.28: Force Sensor.

3.12.2 Basic Tool Holder

The basic tool holder attaches onto the force sensor and enables the REMS to hold instruments which do not need axial rotation (Figure 3.29). This tool holder uses a simple screw clamp to hold instruments in place, and is designed to accommodate up to 2 mm diameter instrument shafts. One key feature of the basic tool holder is the ability to hold standard surgical instruments without modification.
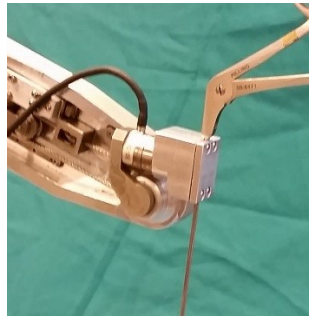
Figure 3.29: Basic tool holder.

3.12.3 Passive Rotation Tool Holder

The passive rotation tool holder is more sophisticated than the basic tool holder and enables passive tool rotation as well as quick release from the REMS (Figure 3.30). The instrument is held in the tool holder with screw driven clamps, but the clamps are supported by ball bearings which allow the instrument

to rotate axially about its shaft. The tension on the ball bearings can also be adjusted to eliminate backlash and adjust the friction force resisting rotation of the instrument. The quick release functionality is implemented using a separate mounting plate that mounts on the force sensor. The tool holder locates repeatably on this plate vial a screw lock and locating pins. This enables the tool holder to be disengaged from the REMS in seconds by loosening the screw lock. Crucially, this tool holder is also capable of working with unmodified surgical instruments with 2.0 mm diameter shafts. One of the more difficult aspects of the design was keeping the form factor small while keeping the stiffness high. In order to maximize stiffness, durability, and chemical resistance, the tool holder was made from 304 stainless steel.
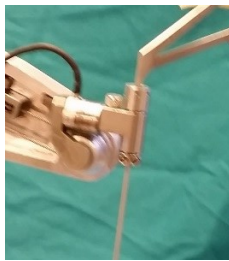
Figure 3.30: Passive rotation tool holder.

3.12.4 Sinus Tool Holder

The sinus tool holder was designed to hold probe instruments for sinus surgery (Figure 3.31). These instruments differ significantly from the small diameter instruments used in the previous tool holders, with shaft diameters up to 4.0 mm. This tool holder uses the same quick release mechanism as the passive rotation tool holder, but does not implement instrument rotation. The instrument is rigidly held in the tool holder by two screw clamps. The tool holder was designed to work primarily with tracked sinus probe instruments which incorporate an S-bend in their shafts to keep the handle offset and out of the way of other instruments.

Figure 3.31: Sinus tool holder.

3.13 Passive Mount

As discussed previously, adjustability to different operating angles is key to many OHNS surgeries. However, preceding JHU steady hand robots had no way to passively adjust the orientation of the robot. One of the difficulties with providing the functionality is the wide range of adjustability required (0-45 degrees about the Y axis, and +/- 45 degrees about the X axis), and the significant weight of the whole REMS system (~ 11 kg). To provide this functionality, a custom ball and socket based passive arm system was designed, however this approach quickly ran into several difficulties. When performing experiments, it is very useful to be able to set up the robot repeatably, and ball and socket joints have no way of easily achieving this. Also, without a highly complex gravity counterbalance system, when a ball and socket joint is loosened, the entire weight of the robot would need to be supported and moved. Because of these issues, the ball and socket mount design was scrapped.

Instead, an off-the-shelf TSK 160 tilting rotary table (Yantai Universal Machine Tool Accessory Group Co. LTD. PRC) was used for the passive mount. This rotary table was intended for use with milling machines, and can support over 50 kg of load with extremely high stiffness. In addition, the two rotational degrees of freedom are both screw driven, so even when the table is unlocked, it is not necessary to manually support the weight of the REMS. Both rotational degrees of freedom can also be precisely positioned using the dials on the hand wheels. Mounting the REMS on the rotary table requires only a simple custom mounting plate. Though this solution works well for lab experiments, it also has several

drawbacks, including the exceedingly heavy weight of the rotary table (over 40 kg) and its steel and cast iron construction, providing no rust or chemical resistance.
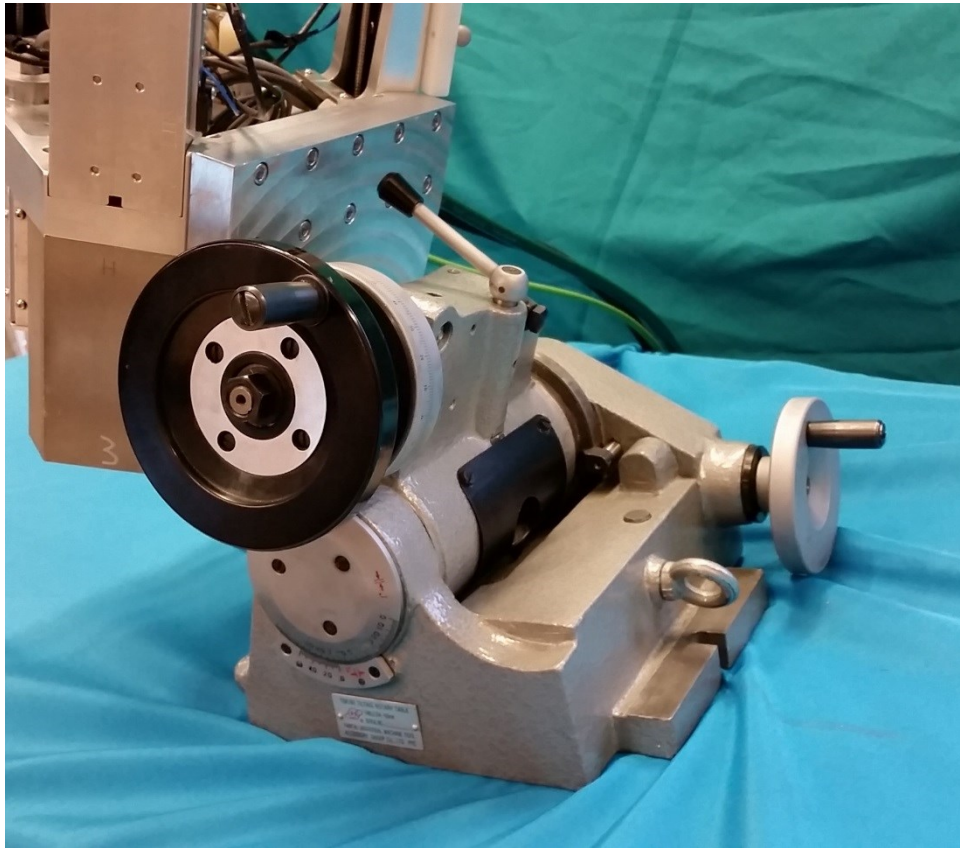
Figure 3.32: Passive mount.

3.14 Electronics

Most of the electrical components of the REMS not housed in the shielded enclosure on the robot's base are housed in a separate electronics enclosure (Figure 3.33). This enclosure consists of an off-the-shelf NEMA enclosure which has been modified with a panel for custom cabling and connectors. The REMS also includes a foot pedal for modulating control gains, and an emergency stop button for safety.
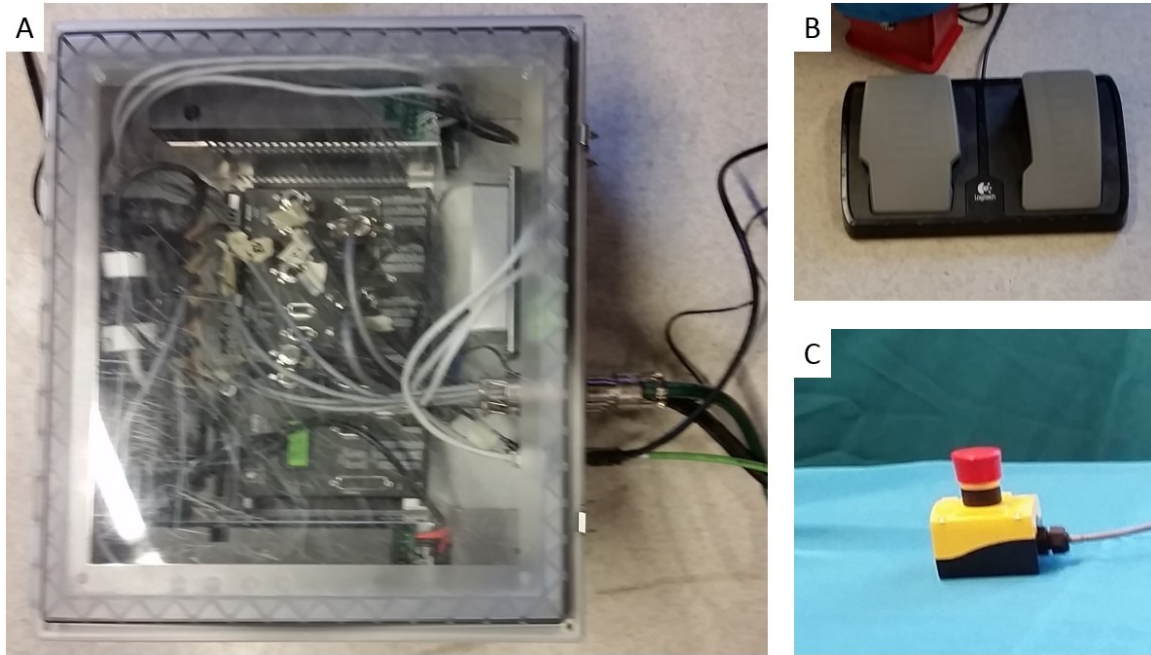
Figure 3.33: Electronics enclosure and components.

A) Electronics enclosure B) Foot pedal C) Emergency stop button

The electrical system is based on an 8 axis motor controller with integrated amplifiers (DMC-4080(MO,ISCNTL)-C012-I000-I000-D3040-D3040, Galil Motion Control Inc. Rocklin, California) (Figure 3.34). The motor controller communicates with a PC via Ethernet. The motors are powered by two 24 V DC power supplies which supply the integrated 500 W PWM amplifiers in the motor controller. Since the coreless DC motors used in the REMS have very low inductance, it was necessary to add a 2 mH inductor in series with each motor to prevent heating from shoot-through current. The motor controller also has analog to digital conversion, which is how the analog foot pedal values are digitized. The electronics enclosure also includes an Ethernet switch which enables one PC to communicate with both the motor control and the force sensor's Ethernet interrogator simultaneously.

The wiring in the REMS attempts to minimize the number of wires needed by using custom cables with large circular connectors to go between the electronics enclosure and the robot. Grounding and shielding were also carefully considered in the design of the electrical system to prevent noise from interfering with encoder or other signals, and shielded cables are used wherever possible. All of the connectors used in the REMS are latching, to prevent them from working loose over time.
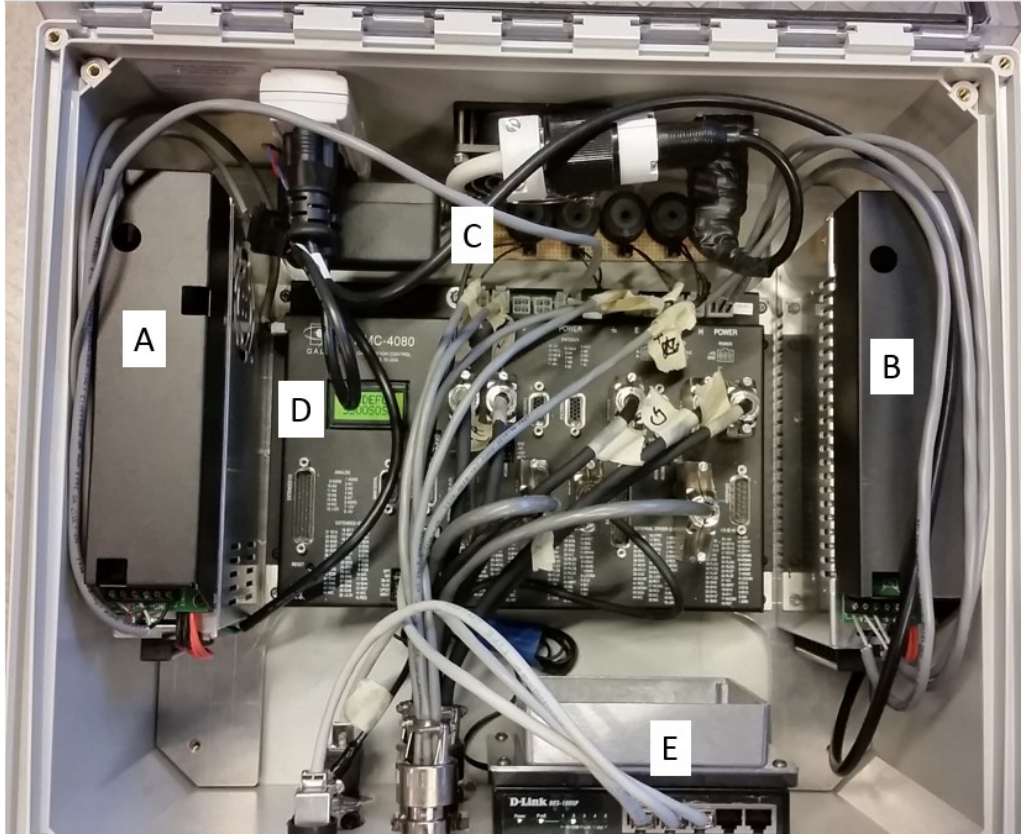
Figure 3.34: Electronics enclosure interior.

A and B) AC/DC converters C) Inductor board D) Motor controller E) Ethernet switch

3.15 Software

3.15.1 Overview

I participated in the high level design and debugging of the REMS software, but I did not write any of it directly, so this software section will be a high level overview without implementation details. Most of the detailed software design and implementation was done by Preetham Chalasani (then a MSE student in Computer Science at JHU) and Marcin Balicki (CS postdoc). The REMS software runs on a PC running Ubuntu and is implemented in C++ using the CISST libraries (http://github.com/jhu-cisst) [94]. It is significantly inspired by the software system for the JHU Eye Robots [33]. My contributions are primarily the design of the control and virtual fixture algorithms.

The control software for the REMS resides in two main locations, the C++ code on the PC, and the motor controller code. The motor controller handles low-level control, such as the PID gains for each motor, and the overall control mode. The PID gains for each motor were determined using the auto-tune function in GalilTools, the proprietary software that interfaces with the motor controller. The REMS uses the velocity control mode because this mode is the easiest to use with admittance control. In this mode, the PC sends the motor controller velocity commands (as opposed to relative or absolute position commands) at each time step. The motor controller servo loop runs at 1000 Hz, but the PC can only handle running the high level control loop at 200 Hz.

One of the main challenges in implementing a cooperatively controlled system is ensuring that the output is intuitive and predictable for the user. This generally involves a tradeoff between stability and responsiveness. If the control gains are low and the force sensor input is heavily filtered, the system will be very stable (not vibrate or run away) but it will exhibit undesired behavior such as sluggishness, or even worse, inertia. If the control gains are high and the force sensor input is lightly filtered, the system will be very responsive with minimal sluggishness or inertia, but it will exhibit undesired behavior such as vibration, oscillations, and jerky movements. Either of these extremes makes the response of the system difficult to predict and control, so control gains and filter cutoff frequencies must be carefully tuned to avoid these undesired effects.

One issue that was encountered early in development was vibrations when the robot was hold long, thin surgical instruments, such as laryngeal forceps. These instruments tended to resonate at around 20 Hz, making them difficult to control. Through empirical testing, it was determined that a cutoff frequency of 8 Hz for the force sensor inputs was sufficient to remove these vibrations without making the robot too sluggish.

3.15.2 Optimization Based Admittance Control

The basic control framework is based on the work of [95], [96], which combines admittance control with an optimization framework for handling constraints and virtual fixtures. The optimization framework solves linear optimization problems with objective functions of the form:

$$\underset{x}{\text{argmin}}(\|Ax - b\|) \tag{3.93}$$

With constraints of the form:

$$Cx \le d$$
$$x_{min} \le x \le x_{max} \tag{3.94}$$

This approach works by using incremental position control and framing the problem of finding what incremental joint positions should be in the next time step as a linear optimization problem of the above form. First, define the relationship between incremental workspace position and incremental joint position using the Jacobian:

$$\Delta x = J\Delta q \tag{3.95}$$

Where:

$$\Delta x = \begin{bmatrix} \Delta x \\ \Delta y \\ \Delta z \\ \Delta roll \\ \Delta tilt \end{bmatrix}, \Delta q = \begin{bmatrix} \Delta l_1 \\ \Delta l_2 \\ \Delta l_3 \\ \Delta roll \\ \Delta tilt \end{bmatrix} \tag{3.96}$$

Admittance control can then be implemented using an objective function:

$$\underset{\Delta q}{\text{argmin}}(\|Gf - J\Delta q\|) \tag{3.97}$$

Where G is the matrix of admittance gains:

$$G = \begin{bmatrix} g_{1,1} & 0 & 0 & 0 & 0 \\ 0 & g_{2,2} & 0 & 0 & 0 \\ 0 & 0 & g_{3,3} & 0 & 0 \\ 0 & 0 & 0 & g_{4,4} & 0 \\ 0 & 0 & 0 & 0 & g_{5,5} \end{bmatrix} \tag{3.98}$$

And f is the vector of forces and torques from the force sensor:

$$f = \begin{bmatrix} f_x \\ f_y \\ f_z \\ \tau_{roll} \\ \tau_{tilt} \end{bmatrix} \tag{3.99}$$

Essentially, the optimizer is trying to compute the Δq which will bring the error between the desired incremental position ($\Delta x_{desired} = Gf$), and the next incremental positon of the robot ($\Delta x_{next} = J\Delta q$) to zero. One issue with this approach is that it is assuming the robot can be treated as quasi-

static so that the optimization can be fully solved in each time-step. However, the closed loop system is likely to be unstable if the optimizer attempts to remove all error in one time step Δt. Instead, we will define a longer time step Δt_{opt} that is a multiple of Δt, which will act as the time over which the optimizer will attempt to reduce error to zero.

$$\Delta t_{opt} = m_{opt}\Delta t \tag{3.100}$$

Where $m_{opt} \geq 1$ is this scale factor.

For maximum dynamic range, the gain matrix $\boldsymbol{G}$ should be set so that the maximum allowable force/torque on the force sensor results in the maximum allowable velocity. This can be done as follows:

$$g_{i,i} = p * m_i^f \frac{\dot{x}_i^{max} \Delta t_{opt}}{f_i^{max}} \tag{3.101}$$

Where $\dot{x}_i^{max}$ is the maximum allowable velocity for the ith workspace degree of freedom, f_i^{max} is the maximum allowable force/torque for the ith force sensor input, p is the gain of the foot pedal, which has been normalized to be 0 when the pedal is not pressed, and 1 when it is fully pressed, and m_i^f is a scale factor which can be used to adjust the relative sensitivity of each axis.

Once $\Delta \boldsymbol{q}$ has been computed by the optimization framework, it can then be converted from an incremental joint position into a velocity as follows:

$$\dot{\boldsymbol{q}} = \frac{\Delta \boldsymbol{q}}{\Delta t_{opt}} \tag{3.102}$$

An additional complication that can arise is the way the acceleration profile of the motion of each axis is handled by the motor controller. If all axes do not accelerate to reach their desired velocity at the same time, the motion will not be coordinated and some axes will reach their desired velocity while the others are still accelerating, which can result in undesired motions and even vibration and instability in extreme cases. In order to compensate for this, the acceleration of each axis should be scaled so that all the axes will reach their desired velocity at the same time. This can be done by computing the desired velocity change vector:

$$\Delta \dot{\boldsymbol{q}} = \dot{\boldsymbol{q}} - \dot{\boldsymbol{q}}_c \tag{3.103}$$

Where $\dot{q}$ is the desired joint velocity, $\dot{q}_c$ is the current joint velocity, and $\Delta\dot{q}$ is the desired velocity change vector. Next, compute:

$$r = \Delta\dot{q}./a_{lim} \qquad (3.104)$$

Where a_{lim} is the vector of acceleration limits of each axis, r is the ratio between the desired velocity change and acceleration limit of each axis, and "./" signifies element-wise division. Let i be the index of the axis with the largest value of r. Finally, form the desired acceleration vector a by scaling $\Delta\dot{q}$ as follows:

$$a = \frac{a_i}{\Delta\dot{q}_i}\Delta\dot{q} \qquad (3.105)$$

Since the accelerations remain proportional to the desired velocity changes, this will ensure that motions stay coordinated, and since one axis is always accelerating at its limit, responsiveness is maximized. The acceleration and velocity values, a and $\dot{q}$ can then be sent to the motor controller for execution. This basic admittance control scheme can then be augmented using enhanced objectives and constraints to implement more complex constraints and virtual fixtures.

3.15.3 Constraints

[96] describes how to implement soft constraints which include a forbidden region that cannot be entered under any circumstances, as well as a boundary region which slows down the robot before the forbidden region is reached. This construct is ideally suited to handling joint and workspace limits which risk being overshot because of inertia. Joint space position limits can be implemented as constraints as follows. First, compute the distance from the current joint position q to the lower and upper joint limits q_l and q_u.

$$\begin{aligned} \Delta q_l &= q_l - q \\ \Delta q_u &= q_u - q \end{aligned} \qquad (3.106)$$

Next, incorporate these into a soft constraint as follows:

$$\begin{aligned} \Delta q_l &\leq \Delta q + s \\ \Delta q - s &\leq \Delta q_u \\ 0 &\leq s \leq s_b \end{aligned} \qquad (3.107)$$

Where $\boldsymbol{s}$ is a vector of slack variables, and $\boldsymbol{s}_b$ is the size of the slow-down boundary region.

Joint space velocity limits can be implemented by adding the following constraints to the optimization:

$$\dot{\boldsymbol{q}}_{min}\Delta t_{opt} \leq \Delta \boldsymbol{q} \leq \dot{\boldsymbol{q}}_{max}\Delta t_{opt} \tag{3.108}$$

Where $\dot{\boldsymbol{q}}_{min}$ and $\dot{\boldsymbol{q}}_{max}$ are the minimum and maximum allowable joint velocities.

Workspace velocity limits can be implemented similarly:

$$\dot{\boldsymbol{x}}_{min}\Delta t_{opt} < \boldsymbol{J}\Delta \boldsymbol{q} < \dot{\boldsymbol{x}}_{max}\Delta t_{opt} \tag{3.109}$$

Where $\dot{\boldsymbol{x}}_{min}$ and $\dot{\boldsymbol{x}}_{max}$ are the minimum and maximum allowable workspace velocities.

Finally, workspace position limits can be added by using planes to define limits. For each plane, compute the vector from the current position to the plane:

$$\Delta \boldsymbol{x}_p = \boldsymbol{x} - \boldsymbol{x}_p \tag{3.110}$$

Where $\Delta \boldsymbol{x}_p$ is the vector from the current position to the closest point on the plane, $\boldsymbol{x}$ is the current position, and $\boldsymbol{x}_p$ is the closest point on the plane to $\boldsymbol{x}$. Next, use the normal vector of the plane (pointing toward the allowed region) $\boldsymbol{n}_p$ to form the constraint:

$$0 \leq \boldsymbol{n}_p \cdot \left(\Delta \boldsymbol{x}_p + \boldsymbol{J}\Delta \boldsymbol{q}\right) + s \\ 0 \leq s \leq s_p \tag{3.111}$$

Where s is a slack variable, and s_p is the size of the slow-down region. Finally, all slack variables must be added to the objective function as follows:

$$\underset{\Delta \boldsymbol{q}}{\operatorname{argmin}}(\|O(\Delta \boldsymbol{q}) + k(s)^2\|) \tag{3.112}$$

Where $O(\Delta \boldsymbol{q})$ is the other objectives, and k is a constant used to set the priority of the constraint the slack variable s corresponds to.

3.15.4 Objectives

Though [96] describes implementing behaviors like RCM points as constraints, this approach can introduce substantial complexity for many REMS use cases. The main drawback to this approach is the need to implement every constraint as linear inequalities. To illustrate this, [96] implements an RCM constraint by creating a polygon approximation of a sphere and uses inward facing inequality constraints to keep the robot inside. This can require hundreds of constraints. This complexity only gets worse as more complex constraints are used. In the case of the REMS, the most complex constraint required is a path constraint, which requires the robot to travel along a specified sequence of configurations. The path is encoded as a sequence of configurations, and for points between the path points, linear interpolation is used. Encoding an arbitrary path like this using inequality constraints would require creating a mesh envelope likely involving thousands of constraints. Because of this, REMS behaviors more complex than simple joint and workspace limits are implemented as objectives. The basic approach is to perturb the current configuration in the direction of the user's force input, then find the closest point on the path to this perturbed configuration and use this is the goal for the objective.

One significant complication of configuration objectives is that they can mix rotational and translational degrees of freedom. When both orientation and position constraints are present, there must be some way for the optimizer to compare the relative importance of position and orientation errors. In the case of the REMS, this can be done simply by transforming orientation errors into position errors by using the length the instrument shaft h_t. Therefore, given a point on a path constraint $\boldsymbol{p}_i$ defined as:

$$\boldsymbol{p}_i = \begin{bmatrix} x_i \\ y_i \\ z_i \\ roll_i \\ tilt_i \end{bmatrix} \tag{3.113}$$

Where roll and tilt are in radians. A normalized point $\boldsymbol{pn}_i$ can be defined as:

$$\boldsymbol{pn}_i = \begin{bmatrix} x_i \\ y_i \\ z_i \\ roll_i * h_t \\ tilt_i * h_t \end{bmatrix} \tag{3.114}$$

143

Similarly, the current configuration of the robot:

$$x = \begin{bmatrix} x \\ y \\ z \\ roll \\ tilt \end{bmatrix} \tag{3.115}$$

And the current force/torque vector:

$$f = \begin{bmatrix} f_x \\ f_y \\ f_z \\ \tau_{roll} \\ \tau_{tilt} \end{bmatrix} \tag{3.116}$$

Can also be normalized as:

$$xn = \begin{bmatrix} x \\ y \\ z \\ roll * h_t \\ tilt * h_t \end{bmatrix}$$

And:

$$fn = \begin{bmatrix} f_x \\ f_y \\ f_z \\ \tau_{roll}/h_t \\ \tau_{tilt}/h_t \end{bmatrix}$$

The next step is, given the normalized current configuration and the normalized force, to compute the desired configuration d. However, we don't want the system to be capable of skipping over large parts of the path when large forces are applied, so we must limit the distance the desired configuration is from the current configuration. This can be done by:

$$d = xn + g * fn \tag{3.117}$$

Where the constant g scales fn such that the maximum force output maps to the desired maximum displacement. For the REMS, $g = 1/5$ such that the force sensor maximum of 5 N maps to 1 mm of displacement. Then we can compute the closest configuration to the desired configuration on the path constraint. Assuming that the path constraint consists of a sequence of points connected by line segments, for each line segment, we compute the closest point on the segment to d as follows:

$$t = \frac{(d - a_i) \cdot (b_i - a_i)}{\|b_i - a_i\|} \tag{3.118}$$

144

$$cp_i = a_i + (b_i - a_i) * t$$

Where a_i, and b_i are the end points of the ith line segment, t is the parameterized distance along the line segment, and cp_i is the closest point to d on the ith line segment. We can then repeat this for every line segment to determine the closest point on the path. Though it would theoretically be more efficient to use a k-d tree or some other more sophisticated space partitioning data structure to find the closest line segments to d, in practice this brute force approach is both simpler and faster for short paths. cp, the overall closest point on the path to d can then be computed as the cp_i closest to d.

Now that the closest point has been found, we can form the objective function:

$$\underset{\Delta q}{\mathrm{argmin}}\left(\left\|(1-h)*(Gf - J_{handle}\Delta q) + h*(g_{con}*(cp - xn) - J_{tip}\Delta q)\right\|\right) \tag{3.119}$$

Where h is the hardness of the objective and should vary from 0 (pure admittance control) to 1 (maximally hard path constraint), J_{handle} is the Jacobian at the instrument handle, J_{tip} is the Jacobian at the tool tip, and g_{con} is the constraint gain which controls how quickly the system will attempt to meet the constraint. g_{con} should be tuned with $h = 1$.

Intuitively, if $h = 0$, the objective function reduces to:

$$\underset{\Delta q}{\mathrm{argmin}}(\left\|(Gf - J_{handle}\Delta q)\right\|) \tag{3.120}$$

Which is just a normal admittance control objective function. If $h = 1$, the objective function reduces to:

$$\underset{\Delta q}{\mathrm{argmin}}\left(\left\|g_{con}*(cp - xn) - J_{tip}\Delta q\right\|\right) \tag{3.121}$$

Which is a pure path constraint which will only allow incremental movements resulting in configurations on the path.

Simpler objectives such as an RCM point are a special case of a path where the path consists of one point with no orientation constraints. The objective function in this case would be:

$$\underset{\Delta q}{\mathrm{argmin}}(\left\|(1-h)*(Gf - J_{handle}\Delta q) + h*(g_{con}*(cp^t - xn^t) - J_{RCM}\Delta q)\right\|) \tag{3.122}$$

Where cp^t is the RCM point in the workspace, xn^t is the position of the RCM point on the instrument, and roll and tilt are set to 0 in both. J_{RCM} is the Jacobian at the RCM point on the instrument, again with the roll and tilt components set to 0.

To implement an RCM point that includes axial translation of the instrument, only a slight modification must be made to the standard RCM point objective. Rather than xn^t being the position of the fixed RCM point on the instrument, it is instead the closest point on the instrument to the RCM point after the RCM point has been shifted by $-Gf$, and J_{RCM} is the Jacobian at xn^t.

3.16 Conclusions and Future Work

3.16.1 Chapter Summary

This chapter presented the design and development of the REMS, including hardware and software design and implementation, and theoretical analysis methods. First, requirements were derived by analyzing common representative surgical procedures in the ear, nose, and throat. Based on these requirements and analysis of prior steady-hand controlled robots, a design concept for the REMS was derived, which emphasizes minimizing the mass of the moving parts of the robot, minimal interference with conventional surgical techniques, and easy reconfigurability. The performance of the mechanical design was then optimized using custom developed performance indices, and components were chosen based on analysis to ensure requirements for each were met. The final design was then analyzed to ensure all requirements for the whole system were met. The design was then implemented and realized as a functional prototype. Software was then developed to provide both basic steady hand control and more advanced virtual fixture control.

3.16.2 Conclusions

This chapter has shown that the current version of the REMS is at least theoretically capable of providing all of the required functionality. The validation of this functionality is presented in the next chapter. In addition to the REMS results, the novel optimization and evaluation methods developed as part of this work have broader applications in robotics as a whole. The p-q norm indices in particular have the

potential to fill a need for specification-based performance indices that has remained unmet since the beginning of performance index work over 30 years ago.

3.16.3 Future Work

The current REMS prototype is well enough developed to demonstrate technical feasibility, however this prototype was not designed for clinical use. The next step in bringing the REMS into clinical use is to choose an initial target procedure (such as sinus surgery) and design a clinical version of the REMS optimized for that procedure. Ideally this next prototype would be capable of receiving an FDA investigational device exemption (IDE) and performing operations in patients. Additional things to consider in an IDE capable prototype are draping and cleaning, safety features such as redundant sensing and software safety interlocks, optimization of ergonomics for setup and use, development of tool holders and an instrument set, detailed development of a REMS version of the target procedure, and development of a mobile cart for transporting, positioning, and securing the REMS to the operating table.

Another direction of future work is to develop additional procedures for the REMS beyond the ones considered here. These could include such diverse areas as neurosurgery in the spine or brain, precision insertion of needles or probes into tissue such as for biopsy and ablation, and open microsurgical tasks, such as precision suturing of small nerves or blood vessels. There may also be additional non-medical applications, such as industrial or research applications using a REMS-like system for precision work such as soldering or preparing biological specimens.

In addition to the REMS future work, the performance index results also have significant potential for future expansion. The current limitations on redundancy and mixed degrees of freedom can potentially be relaxed using the p-q norm framework to provide indices for general specification-based design.

3.17 Contributions

- Requirements and specifications for instrument manipulation in OHNS [55].
- A novel design concept and mechanical design for a microsurgery robot for general purpose OHNS [55], [56].

- A novel design optimization method for specification-based design of parallel robots [57].

- A functional prototype demonstrating the feasibility of the design concept and mechanical design, and the validity of the design optimization [58].

Chapter 4   REMS Calibration and Validation

4.1 Resolution, Repeatability, and Stiffness Validation

4.1.1 Methods

In order to verify whether the REMS meets the technical requirements described in Table 3.1, a series of technical evaluations were performed. These evaluations specifically focus on evaluating the resolution, repeatability, and stiffness of the REMS. The calibration of the REMS and evaluation of accuracy will be done in section 4.2.

4.1.1.1 Resolution

The setup for the resolution evaluation is shown in Figure 4.1, left. The robot was started in its home position, with delta stage in the center of its workspace with the stiff steel evaluation tool oriented vertically. For each DOF (x, y, z, roll, and tilt), a 0.001 mm resolution dial indicator on a stiff passive arm was aligned with the motion direction and zeroed. The DOF was then commanded to move 1000 encoder counts in reverse, then 1000 counts forward, eliminating backlash in the forward direction. The DOF was then commanded to move forward by decreasing numbers of encoder counts until the dial indicator did not show a change. The incremental distance corresponding to the smallest number of counts for which the indicator changed was recorded. Each measurement was performed five times to ensure consistency and the worst-case value computed.
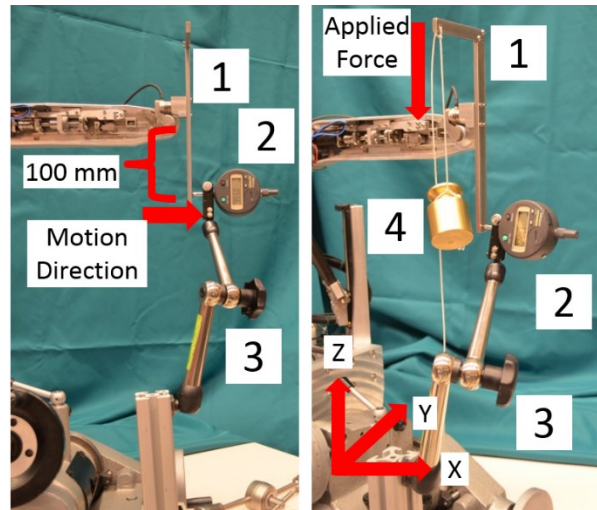
Figure 4.1: REMS evaluation setups.

Left: Resolution and Repeatability setup 1) Evaluation tool 2) Indicator dial 3) Dial support arm Right: Stiffness setup 4) 500g weight

4.1.1.2 Repeatability

In order to capture workspace repeatability including backlash, the robot was initially positioned in its home position with the dial indicator aligned with the direction of motion of the DOF being tested. The indicator was zeroed, then the DOF was moved 1000 encoder counts forward, then 1000 counts in reverse and the indicator value recorded. The DOF was then moved 1000 counts in reverse, then forward and the indicator value recorded. This process was repeated 5 times for each DOF to ensure consistency, and the worst-case difference between indicator readings for motion in the forward and reverse directions was computed for each DOF.

In this application, only the Cartesian position of the tool tip is relevant, so errors in the orientation of the tool are only significant in how they affect the Cartesian position of the tool tip. Also, because of the way the surgical tools are held, it is difficult to apply significant pure torques to the tool handle, making these irrelevant for this case. Therefore, the stiffness evaluation focuses on only linear forces applied to the tool handle, and linear displacements at the tool tip.

4.1.1.3 Stiffness

Figure 4.1, right shows the setup for the stiffness evaluation. The stiffness was also evaluated with the robot in its home position. A 500g weight on a string with a low-friction pulley was used to apply a force to the tool handle in the x, y, and z directions, at the location where a standard tool is typically held. For each of these force directions, the deflection at the tool tip (100 mm below the tilt joint) was measured in the x, y, and z directions using the same dial indicator. Five measurements were taken for each deflection to ensure consistency, and the average was computed and used as the value of that deflection. The results were then used to form a compliance matrix to compute the worst-case possible deflection as follows. Let $\delta_{i,j}$ represent the deflection in the i direction resulting for a force in the j direction, and let f be the magnitude of the force applied. The compliance matrix C can then be formed as below.

$$C = \begin{bmatrix} \dfrac{\delta_{x,x}}{f} & \dfrac{\delta_{x,y}}{f} & \dfrac{\delta_{x,z}}{f} \\ \dfrac{\delta_{y,x}}{f} & \dfrac{\delta_{y,y}}{f} & \dfrac{\delta_{y,z}}{f} \\ \dfrac{\delta_{z,x}}{f} & \dfrac{\delta_{z,y}}{f} & \dfrac{\delta_{z,z}}{f} \end{bmatrix} \tag{4.1}$$

Since the forces involved are small compared to the stiffness and scale of the structure, it is reasonable to assume linear compliances. By finding the largest singular value of this compliance matrix, the worst-case deflection for a given force magnitude can be computed. Also, since the force sensor is mechanically in series between the robot and the tool holder, its stiffness will impact the stiffness of the overall system. The stiffness of the force sensor can be found from its data sheet (F/T Transducer Installation and Operation Manual, ATI Inc. Apex, NC, USA). The force sensor has very high linear stiffness for the forces applied, but relatively low torsional stiffness. It is therefore useful to compute a second compliance matrix for the force sensor to determine its contribution to the total deflection and thus whether a stiffer force sensor should be used in a future design iteration.

4.1.2 Results

Table 4.1 shows the resolution and repeatability results.

Table 4.1: Resolution and Repeatability at Tool Tip

Degree of Freedom	Resolution (mm)	Repeatability (mm)
X	0.003	0.077
Y	0.003	0.069
Z	0.002	0.018
Roll	0.005	0.099
Tilt	0.004	0.173
Worst-Case Total	0.011	0.302

Table 4.2 shows the stiffness evaluation results.

Table 4.2: Average Deflections at Tool Tip.

	X Force	Y Force	Z Force
X Deflection (mm)	-0.610	0.020	0.287
Y Deflection (mm)	0.120	0.350	-0.242
Z Deflection (mm)	-0.250	-0.017	0.453

Using the force magnitude of 500 grams force, the resulting compliance matrix was calculated in mm/N.

$$C_{\text{total}} = \begin{bmatrix} -0.125 & 0.004 & 0.059 \\ 0.025 & 0.072 & -0.050 \\ -0.051 & -0.004 & 0.093 \end{bmatrix} \tag{4.2}$$

The worst-case deflection was then computed by finding the largest singular value σ_{max} of the compliance matrix and multiplying by the force magnitude $f = 500$ grams-force.

$$\sigma_{\text{max}}(C_{\text{total}}) \cdot f = \frac{0.175 \text{ mm}}{\text{N}} \cdot 4.89 \text{ N} = 0.855 \text{ mm} \tag{4.3}$$

The worst-case deflection of the entire system was therefore 0.855 mm for a 500 gram force load. However, for the purposes of future design iterations, it is useful to know the individual contributions of the robot and the force sensor to this deflection. Using the kinematics of the tool, the torsional stiffnesses from the force sensor data sheet, and the force magnitudes and directions, the above method can be repeated for the force sensor alone, resulting in a force sensor compliance matrix (transformed into the tip frame) C_{sensor}.

$$C_{\text{sensor}} = \begin{bmatrix} -0.040 & 0.000 & 0.011 \\ 0.006 & -0.023 & -0.019 \\ -0.007 & 0.000 & 0.002 \end{bmatrix} \tag{4.4}$$

The compliance matrix of the robot alone, C_{robot}, can then be computed as:

$$C_{\text{robot}} = C_{\text{total}} - C_{\text{sensor}} \tag{4.5}$$

The worst-case deflection due to the robot alone was then:

$$\sigma_{\max}(C_{\text{robot}}) \cdot f = \frac{0.142 \text{ mm}}{\text{N}} \cdot 4.89 \text{ N} = 0.693 \text{ mm} \tag{4.6}$$

4.1.3 Discussion

The worst-case resolution of the tool tip in Cartesian space was 0.011 mm, which is well within the 0.025 mm requirement, as expected based on the previous analysis. The worst-case repeatability at the tool mounting plate was 0.105 mm, which is typical of comparable industrial robots. The worst-case repeatability at the tip of the 100 mm long tool in Cartesian space was 0.302 mm. Most of this is backlash from the tilt joint's cable mechanism, which has not yet been optimally tuned, and can be improved in the future.

The worst-case deflection at the tip of the 100 mm length tool with 500 grams force applied to the tool handle was 0.855 mm including the force sensor and 0.693 mm excluding it, and was mostly in the X direction. Since the force sensor itself contributes significantly to the overall deflection, a stiffer sensor will be used in a future design iteration. Most of the deflection of the robot itself was from the cable mechanism of the tilt joint (which resulted in the X direction deflection), and rotational deflection of the mobile platform of the delta stage, both of which could be improved with relatively simple design changes.

Overall, the worst-case error at the tip of the 100 mm length tool, including resolution, repeatability, and stiffness errors, was 1.167 mm. However, if the error due to the force sensor is eliminated, the total error is 1.005 mm. Since this was only a preliminary technical analysis, only the performance in the home configuration was analyzed, however, this is very representative of the configurations which will be commonly used. This work did not include analysis of dynamic effects (friction, hysteresis, and tracking accuracy) because the intended surgical applications are very low speed and can be treated as quasi-static.

4.2   Calibration and Accuracy

Now that positioning errors from resolution, repeatability, and compliance for the REMS are well understood, overall accuracy can be evaluated. However, before attempting to measure overall accuracy, the REMS must be calibrated to correct kinematic errors resulting from machining tolerances and errors in zeroing joints. Two main approaches were considered for calibrating the REMS, active ground truth, and passive ground truth. Active ground truth methods involve using an active system such as an optical tracker to observe the REMS moving, and then compare this ground truth to the estimate from the REMS kinematics to determine kinematic errors. Passive ground truth methods involve using the REMS itself to measure position data while interacting with a passive device, such as a precision machined pivot calibration plate. Since the pivot locations on the plate are known relative to each other with high precision, this can be used as a ground truth when compared to the REMS position measurements. Since the active methods are more direct and provide richer data, this was the approach that was used first.

To provide ground truth data, an NDI Polaris optical tracker (Norther Digital Inc. Waterloo, Ontario, Canada) was used. This tracker uses passive marker spheres with an IR reflective coating. A custom instrument for the REMS incorporating these spheres was produced for these evaluations. A reference body with tracker spheres was also attached to the robot base. Figure 4.2 shows the setup for the tracker validation.
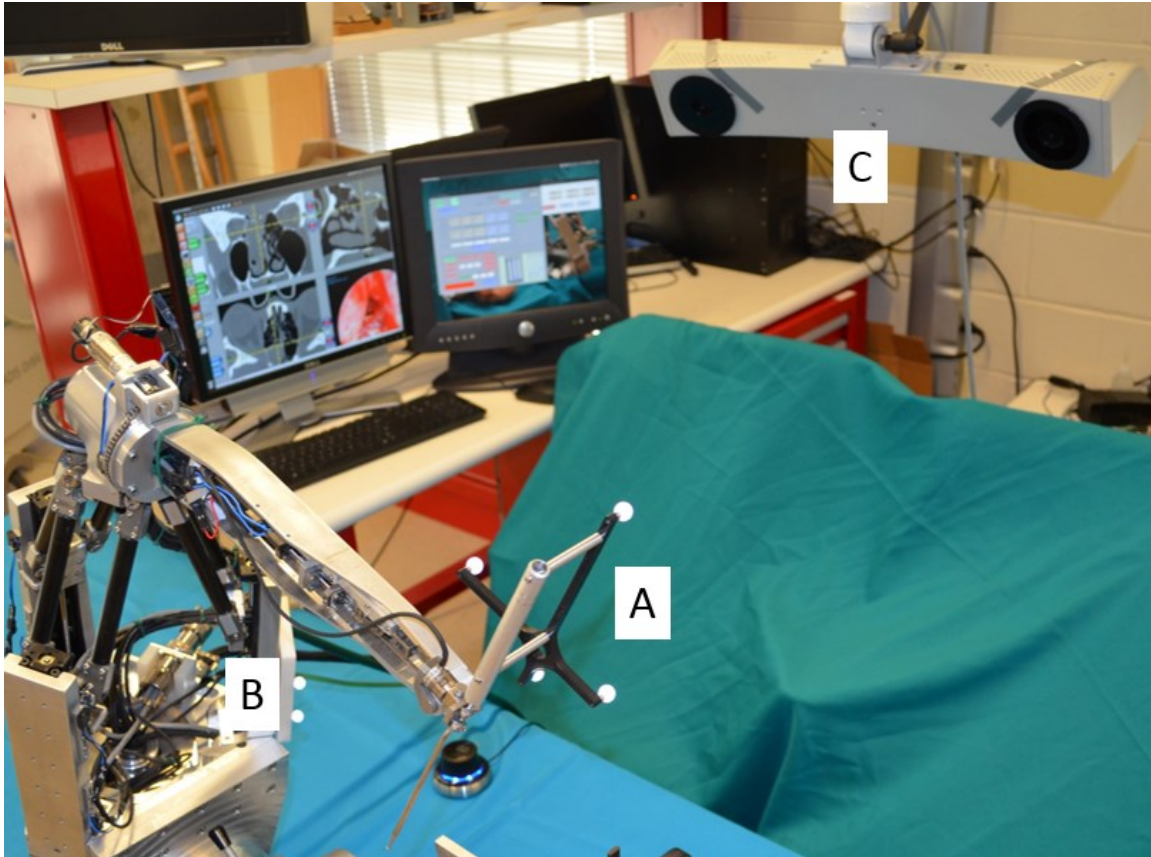
Figure 4.2: REMS Polaris calibration setup.

A) Instrument with marker spheres B) Reference body C) Tracker

Since the delta mechanism and rotary joints can be easily decoupled from each other, the measurements can be taken in two stages, one in which only the delta mechanism moves over its workspace, and one in which only the rotary joints move over their workspaces. First, the delta mechanism was moved to 414 sample locations covering its workspace and both the robot and tracker position estimates were recorded. The rotary joints were kept fixed. Figure 4.3 shows the results of this data collection. These results show a distinct distribution of errors which vary in both magnitude and direction uniformly along a single axis. Interestingly, the axis along which the errors vary is not aligned with the kinematics of the robot in any way, and is instead aligned with the tracker's vertical axis. This leads to the conclusion that most of this error is in fact due to tracker distortion rather than anything in the REMS.

Additionally, the maximum rotational error observed during this data collection was .0068 rad according to the tracker. If there were 0.3 mm error for each sphere on the tool body and the reference body

(which is what is expected according to the Polaris specifications), then we would expect .008 rad of rotation error (since both bodies are about 150 mm from sphere to sphere). This means that the observed rotation error is within the noise range of the tracker. If this rotation were instead caused by the delta stage distorting, we would expect it to result in 2.2 mm of translation error (due to the ~400 mm long robot arm) in the worst case, but the max translation error is actually about 1.2 mm. Attempts to account for these errors through optimizing the kinematic parameters of the REMS also did not produce useful results. These results all confirm that the rotation error observed is mostly due to tracker distortion, indicating that the Polaris is not sufficiently accurate to be used for REMS calibration, since it appears that the Polaris distortion errors dominate errors caused by the REMS.
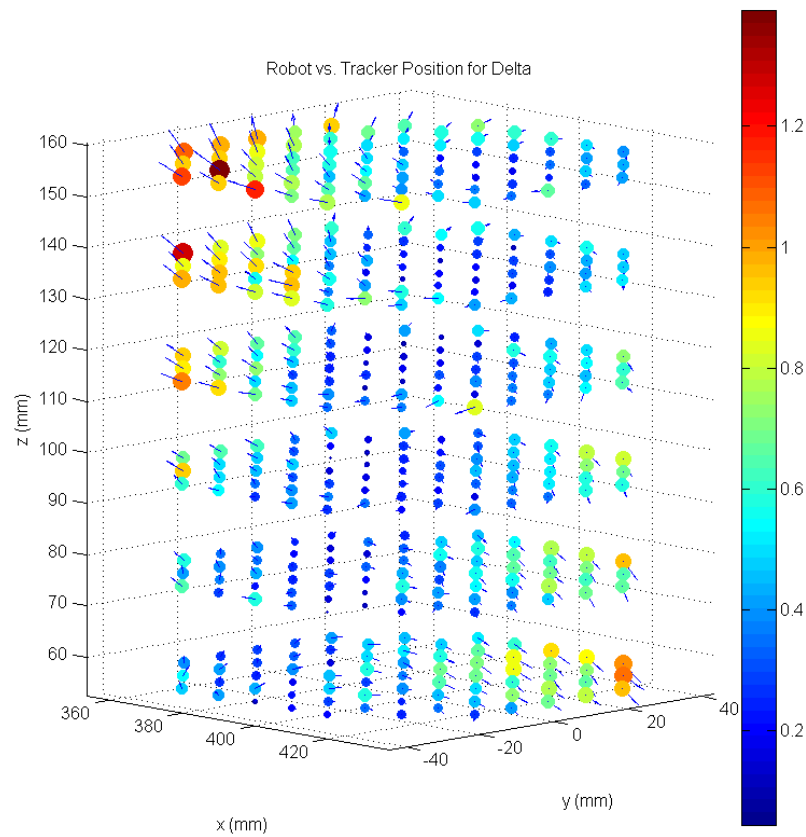
Figure 4.3: Robot vs. tracker position data for delta mechanism.

The color of each point indicates the magnitude of the error between the robot and tracker estimates of the point location (scale is in mm). The blue arrows indicate both the magnitude and direction of this error.

Since the Polaris proved to be insufficiently accurate for this application, a passive ground truth consisting of a precisely-machined pivot calibration plate was constructed to make a second attempt at calibration (Figure 4.4). This plate consists of 9 numbered divots spaced in a square at 50 mm intervals. The plate accuracy is +/- 0.05 mm. The end of the REMS tracked tool was precisely machined as a 3 mm ball in order to aid in pivot calibration. One difficulty with this approach is that there are many unknowns, including all of the REMS kinematic parameters, as well as the tool tip offset. In order to have sufficient data to solve for all of these parameters, 7 configurations were recorded at different pivot angles in each divot, resulting in 63 total data points. This data was then used to simultaneously optimize both the kinematic parameters of the REMS and the tool tip offset. In order to collect this data, the robot was hand-guided into each configuration using the admittance control mode. Alignment of the ball tip in the divots was verified by visual and tactile inspection.
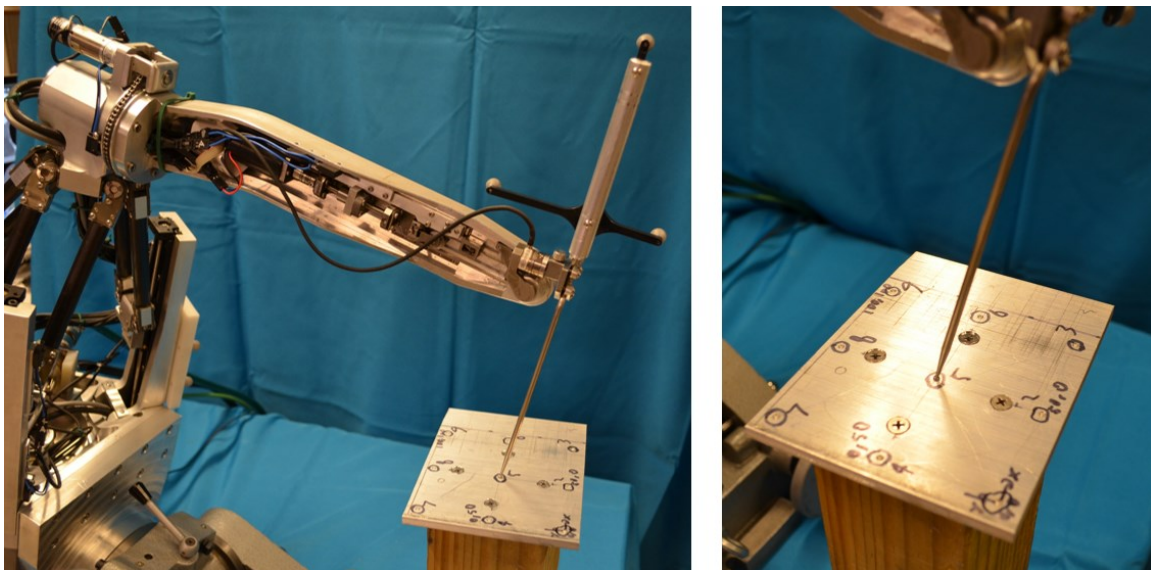
Figure 4.4: Pivot calibration plate.

One key decision in this type of analysis is how to choose which kinematic parameters to optimize. If all possible errors were considered for every component of the REMS, this would result in an extremely complex model with hundreds or thousands of variables which would require an enormous amount of data in order to prevent over-fitting. Because of this, a useful approach is to add parameters to the optimization one by one in order of likely importance until either the error stops improving, or obviously non-physical over-fit results emerge. In the case of the REMS, the most useful parameters were found to be:

- The three parameters for the tool tip offset relative to the tool holder plate.

  o This is the normal pivot calibration parameters.

- The zero value of the roll axis.

  o There is no precise zero defined in the hardware, so it must be defined through calibration.

- The zero values of two of the delta linear stages.

  o Since the linear delta mechanism is kinematically invariant in the z direction, it is redundant to adjust the zero position of all 3 stages, so adjusting two stages is sufficient.

- The scale of the roll joint.

  o Though the roll stage does use a chain, it also relies on a non-toothed pulley. Small errors in the pulley diameter can introduce errors in the scale of the roll axis which must be calibrated for.

- The scale of the tilt joint.

  o The tilt stage also relies on a pulley, so pulley diameter errors must be calibrated for.

Other parameters that were considered and found to be unuseful include:

- The zero value of the tilt.

  o This is redundant with the tool tip position parameters.

- Errors in the angle of the tilt axis.

  o Adjusting these parameters did not reduce the error.

- Error in the offset from the roll axis to the tilt axis.

  o Adjusting this parameter did not reduce the error.

- Errors in the angle of the roll axis.

  o Adjusting these parameters did not reduce the error.

- Errors in the position of the delta linear stages.

  o Adjusting these parameters resulted in obviously non-physical over-fitting.

- Errors in the length of the parallelograms of the delta mechanism.

  o Adjusting these parameters resulted in obviously non-physical over-fitting.

The results of the calibration are shown in Table 4.3. The optimization was done using lsqnonlin() in MATLAB. The objective function in lsqnonlin() first took in the above kinematic parameters, and used the forward kinematics to compute the tool tip position for every configuration. This was then rigidly registered to the known divot positions using Arun's method. The errors between the computed tip positions and the registered divot positions was then returned. lsqnonlin() works by minimizing the square of the errors returned by the objective function, so this algorithm has the effect of minimizing the squared error between the kinematically computed tip position estimates and the registered divot positions.

Table 4.3: Calibration Results

Parameter	Value
Tip Offset X	17.91 mm
Tip Offset Y	-19.55 mm
Tip Offset Z	-162.06 mm
Roll Offset	-602 counts
Roll Scale	0.9734
Tilt Scale	1.0006
Delta Leg 1 Offset	4675 counts
Delta Leg 2 Offset	-720 counts

Using these adjusted parameters, the tool tip location of the REMS were computed and registered to the known locations of the divots on the pivot calibration plate. The errors between the computed tool tip locations and the divot locations were then computed (Figure 4.5). The mean error was 0.32 mm with a standard deviation of 0.17 mm. The maximum error was 0.75 mm, which is within 3 standard deviations of the mean, so it is likely not an outlier. The errors did not have a clear pattern in either the workspace or the joint space. This may mean that some of the errors were from sources independent of the robot's kinematics, such as errors from positioning the ball tip in the divots, as well as backlash and stiffness.
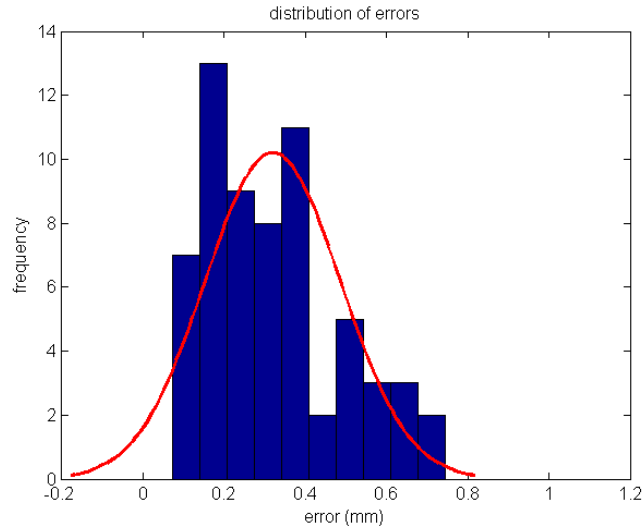
Figure 4.5: Calibration error distribution.

After calibration, an evaluation was conducted to evaluate the accuracy of the REMS in a realistic scenario using an artificial phantom design to simulate a hypothetical REMS sinus surgery (Figure 4.6). The phantom consists of a plastic skull with seven aluminum registration screws embedded in the front of the skull, and six test screws embedded inside the nose. An artificial plastic nose was added to the skull to better simulate the constrained environment of sinus surgery. This phantom was then CT scanned in order to quantify the screw locations. The CT scan resolution was 1.0 mm. The locations of the heads of the screws were then manually segmented using 3D Slicer 4.0 (Figure 4.7). After the CT scan, the head was fixed in an aluminum head holder using plywood screws. The head holder was then clamped to the table to prevent motion relative to the REMS during experiments.
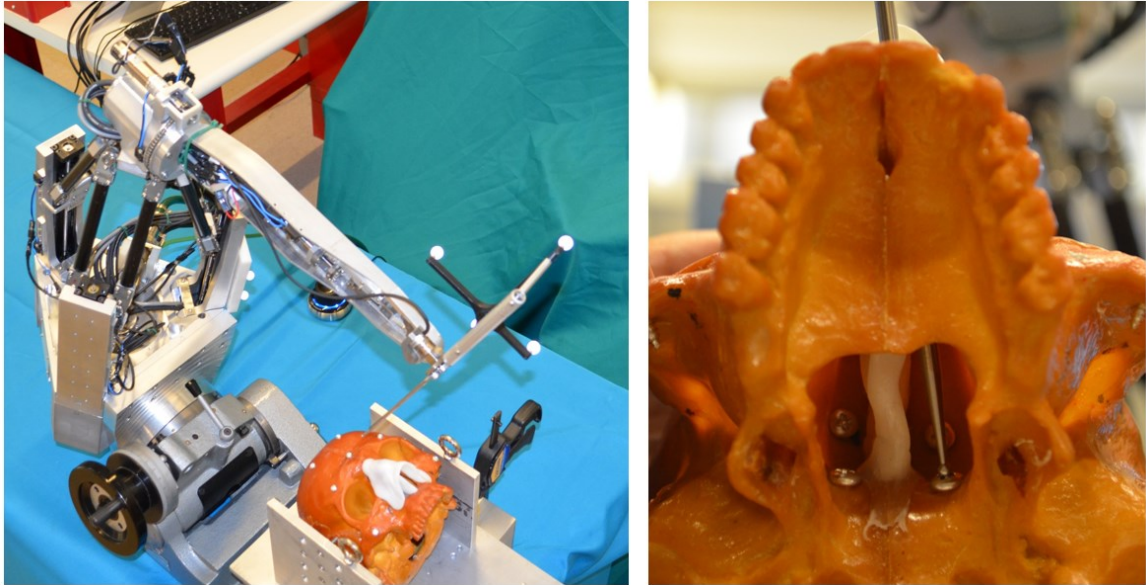
Figure 4.6: Sinus phantom.
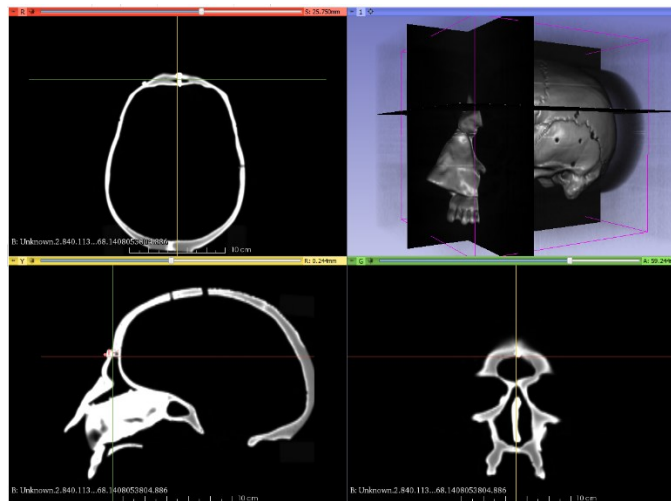
Figure 4.7: Sinus phantom CT segmentation.

The realistic accuracy of the REMS system combined with the registration procedure was then evaluated by locating the 7 outer registration screws with the instrument tip using the REMS, and then registering these points to the segmented screw locations from the CT scan. As before, the REMS was hand-guided to position the ball tip in each screw head using admittance control mode, with manual visual and tactile verification. The max registration error was 0.88 mm with a mean of 0.25 mm and a standard deviation of 0.30 mm. The REMS was then used to locate the 6 test screws located inside the nose, and the REMS estimate was compared to the CT estimate. The max error for the test points was 1.53 mm with a

mean of 0.87 mm and a standard deviation of 0.42 mm. This evaluation has many possible sources of error, including CT error, segmentation error, registration error, error in locating the instrument tip in the screw heads, REMS errors, motion between the REMS and the phantom during the experiment, and warping of the phantom since the CT scan caused by temperature or mechanical load (such as mounting the head into the head holder).

After the calibration and evaluation, it was discovered that the REMS loses 1 to 2 mm of accuracy if the tool holder with the ball tip probe instrument is detached and reattached to the REMS. The likely cause of this is that the tool holder does not re-locate precisely. Because of this, to achieve optimal accuracy, it is necessary to do a simple pivot calibration after the instrument is detached and reattached in order to re-estimate the tool tip offset. The values typically vary by no more than 1-2 mm, which is consistent with slight variations in the angle of the tool holder reattaching to the tool plate.

Additionally, in order for the REMS to be have full navigation capability, not only the location of the tool tip, but also the entire tool shaft must be known in order to avoid collisions between the shaft and tissue. To calibrate the tool shaft, an additional calibration fixture was created (Figure 4.8). This fixture consists of a piece of 90 degree angle aluminum stock fixed to a rigid mount which can be clamped to the table. The tool shaft is then inserted into the corner of the stock, and slid up and down along the angle stock for the full range of motion of the REMS. This approach was preferable to other approaches such as inserting the shaft into a precision drilled hole because of safety. If anything goes wrong during the calibration, the instrument can easily be removed from the fixture, which would be more difficult if the instrument was inserted into a tight tolerance hole.
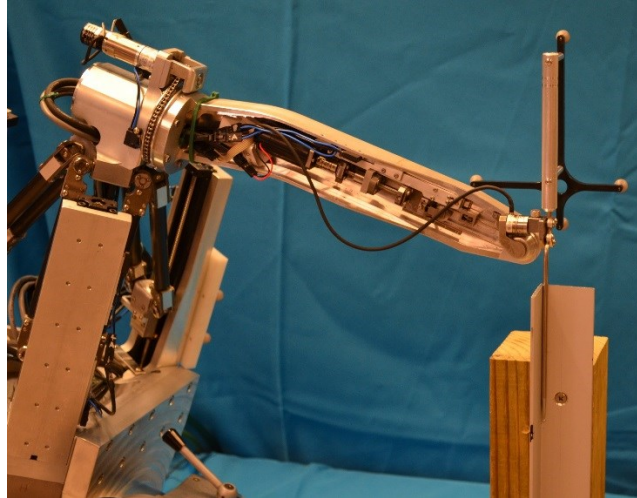
Figure 4.8: Tool axis calibration fixture.

4.3 Laryngeal Validation Studies

4.3.1 Precision Augmentation Validation

I designed the experimental protocol and setup for this experiment, and ran the data collection. Dr. Lee Akst and Dr. Paulette Pacheco-Lopez (Johns Hopkins Hospital OHNS Physicians) provided clinical guidance and support for this experiment. Marcin Balicki (then a JHU CS PhD Student) and Preetham Chalasani (then a JHU CS Masters Student) assisted with software support and data collection.

4.3.1.1 Methods

The study is summarized below. See [60] for the full IRB protocol.

The precision augmentation evaluation was designed to test surgical precision by performing a task resembling needle insertion in microlaryngeal phonosurgery. The goal of the task was to precisely touch targets with laryngeal surgical instrument as quickly as possible. A testing phantom was constructed from several layers: a foam base, a conductive aluminum foil layer, an insulating rubber layer, and a perforated aluminum plate (Figure 4.9). The holes in the perforated plate were grouped by size into three clusters of 2 mm, 1.5 mm and 1.2 mm diameter holes.
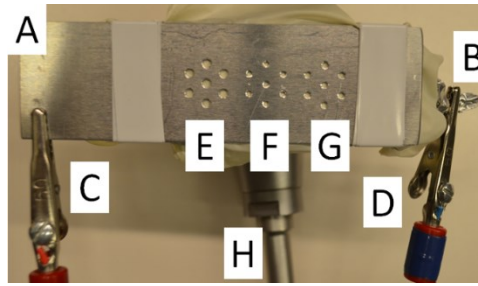
Figure 4.9 Testing Phantom.

A) Perforated aluminum plate B) Foil layer C) Failure electrode D) Success electrode E) 2.0 mm holes F) 1.2 mm holes G) 1.5 mm holes H) Passive support stand

A test instrument was also constructed by fixing a 0.4 mm diameter needle onto the end of a standard 25 cm long microlaryngeal forceps and attaching it to the robot's tool holder. This results in clearances of 1.6 mm, 1.1 mm, and 0.8 mm. These sizes were chosen because they are on the scale of the anatomy for phonosurgery, and our preliminary evaluation showed that approximately 1.1 mm is the smallest that is feasible by hand, even for a skilled surgeon. Electrical leads were connected to the tool, foil, and plate, such that any contact between the needle and the plate, or the needle and the foil could be detected as a short circuit.

Since this is a preliminary evaluation and the goal was to get a first impression of how different types of users respond to the robot, three subjects participated in the study, a laryngeal surgeon, a surgical fellow, and a novice. The subjects were instructed to insert the needle through the hole as quickly as possible without touching the plate. Each subject was asked to start with the needle over the center hole starting with the 2 mm diameter cluster. The subjects were then told a random hole to insert the needle through. If the needle touched the plate, a buzzer would sound indicating a failure. If the needle was inserted through the hole touching the foil without touching the plate, then a different buzzer would sound indicating a success. Once the attempt was completed as a success or failure, the subject returned the needle to the starting position over the center hole of the cluster before beginning to reach for the next hole. Holes were assigned in random order. After a brief unmeasured period to allow for familiarization with robot operation, testing began. Each subject performed the task with each cluster of holes, for a total of 18 attempts per subject with the robot. The tool was then removed from the robot and the subjects repeated the task manually, using the robot arm as a tool rest to parallel real operating conditions but without use of the robot otherwise, resulting

164

in 18 manual attempts per subject. Figure 4.10 shows an attempt with the robot. All kinematics, time, success/fail, pedal, and force data during the robotic experiments were logged by the software system.

Figure 4.10: Setup for the precision augmentation evaluation.

4.3.1.2   Results

The results of the precision augmentation evaluation can be split into three main parts, accuracy, time, and force. Table 4.4 summarizes the accuracy results. Table 4.5 summarizes the average time per successful result in seconds. Failures were not counted in the total time estimate. Since there was no force recording for manual attempts, Table 4.6 only shows force data for robotic attempts. Torques in the force data were measured about the force/torque sensor.

Table 4.4: Successes out of 6 attempts for hole size, surgical skill, and robot/manual.

	Robot				**Manual**			
Hole Size (mm)	*2.0*	*1.5*	*1.2*	*All*	*2.0*	*1.5*	*1.2*	*All*
Surgeon	4	5	6	15	4	4	1	9
Fellow	6	6	6	18	2	0	1	3
Novice	6	5	5	16	1	0	2	3

Table 4.5: Average time in seconds per successful attempt.

Hole Size (mm)	Robot				Manual			
	2.0	*1.5*	*1.2*	*All*	*2.0*	*1.5*	*1.2*	*All*
Surgeon	4.2	11.5	9.3	8.2	6.2	5.6	6.0	5.9
Fellow	8.4	7.3	15.8	10.5	8.6	N/A	9.4	8.8
Novice	9.6	7.8	7.1	8.3	9.2	N/A	10.7	9.9

Table 4.6: Maximum and average torque applied to tool holder

	Surgeon	Fellow	Novice
Average Torque (N-mm)	61	84.0	80.2
Maximum Torque (N-mm)	173	384	296.5
Average Force (N)	1.6	2.6	2.0
Maximum Force (N)	4.8	11.9	6.8

4.3.1.3 **Discussion**

Due to ergonomics limitations of the setup, it is possible that the surgeon and fellow could not perform as well as they would in a real operation. However, accepting this limitation, the subjects, taken together, completed 28% of attempts successfully manually, and 91% with the robot, which is a striking improvement. In order to determine the statistical significance of this result, a one tailed z-test was used to compare these two population proportions. This gave a z score of 6.585, which corresponds to a p-value < 0.01, showing that the result is statistically significant. The effect size is so large that the improvement of each user individually from manual to robotic across all hole sizes is statistically significant $p < 0.05$, and the improvement of each hole size individually across all users from manual to robotic is also statistically significant $p < 0.01$. Though the number of subjects is small, each subject did a total of 36 insertions, so even though outliers and learning curve effects are likely present in the data, the p-values show that it is very unlikely the robotic performance improvements are by chance, which is the main goal of this preliminary evaluation.

The average time per success was 7.0 seconds manually vs. 9.0 seconds with the robot, which is very likely worth the significantly improved precision. However, due to the small number of successful manual trials, this result is not statistically significant. Also, since the surgeon and fellow were already skilled in manual surgery, their robotic performance should improve given more training time.

The force results also yielded valuable insights into the performance of the system. The surgeon exerted by far the least maximum and average force and torque, never exceeding the 500 gram force handle load predicted above. However, the novice and the fellow both exceeded this limit. The subjective feedback indicates that the surgeon tended to have the pedal down further than the fellow or novice, meaning that less force was needed on the tool handle for a desired velocity. Also, since there was no warning for either workspace limits of force sensor saturation, this could have led to many of the higher forces exerted. In light of these results, auditory tones were added to alert the user when force or workspace limits were reached. However, since the average force of all the users was far below 500 grams force, it is likely that trained users with appropriate warnings could use the robot effectively with much less force, reducing fatigue and increasing precision. Additionally, since the robot is using a naïve admittance controller without any specific tuning, a more advanced control method should further reduce the operating force. Future work will include a more sophisticated and clinically relevant evaluation with a larger number of subjects.

4.3.1.4 Conclusions

The results of the precision augmentation evaluation are very encouraging. Even with a 25 cm long tool providing a large lever arm to amplify tremor, the robot significantly improved surgical precision over manual operation across all users, with only a small increase in operation time. These results show that manipulation tasks with these tools with a clearance of less than 1 mm that are infeasible by hand even for a skilled surgeon become feasible using the robot. That a statistically significant result was obtained from such a small scale study shows that the effect size is quite large. Subjective feedback from the surgeon and fellow was also very encouraging, despite the ergonomic limitations of the setup. Simple ergonomic changes to the robot and experimental setup, such as a microscope lens with a longer focal distance, and warnings for force and workspace limits will also be added for future experiments.

4.3.2 Laryngeal Precision Motion Study

I designed the experimental protocol and setup for this experiment, and ran the data collection. Dr. Lee Akst (JHH OHNS Physician) provided clinical guidance and support for this experiment. Marcin Balicki (then a JHU CS PhD Student) and Preetham Chalasani (then a JHU CS Masters Student) assisted with software support and data collection. Fumbeya Marungo (JHU CS PhD Student) assisted with data reduction and analysis.

4.3.2.1 Methods

The goal of this study was to expand on the results of the precision augmentation study by using a richer, more realistic task with a larger number of subjects. In order to more closely resemble microlaryngeal phonosurgery, a new task was designed involving precisely moving a realistic surgical instrument through a target at the end of a laryngoscope. Significant effort was made to replicate the ergonomics of the OR environment, including a similar microscope with the correct 400 mm focal distance lens, correct chair height with functionally equivalent arm rests, and correct angle and positioning of the target, instrument, laryngoscope, robot, microscope, and user. An endoscopic camera was also fixed viewing the end of the laryngoscope from the outside in order to capture video data of each participant's performance. Figure 4.11 shows the experimental setup.
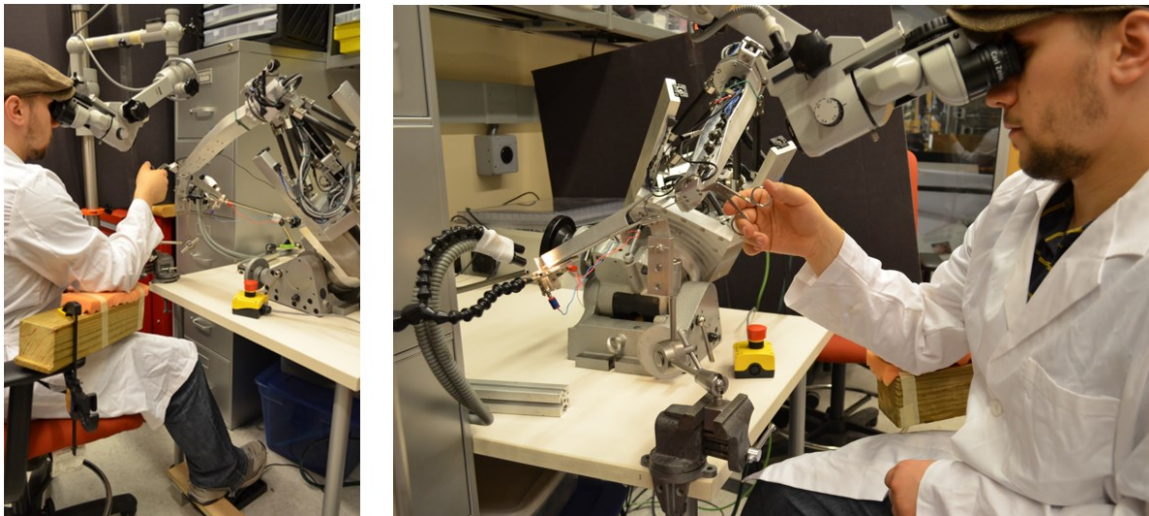
Figure 4.11: Setup for laryngeal precision motion study.

The instrument used is a 25 cm laryngeal forceps with the tip modified to hold a 0.4 mm diameter needle. The targets consist of aluminum plates with spiral grooves cut into them (Figure 4.12). The objective for the user is to start with the instrument tip in the center of the spiral and maneuver the instrument around to the other end of the spiral without letting the instrument touch the sides. Since the instrument and target are both electrically conductive, any contact between the instrument and the target can be detected through electrical conductivity. At the end of the spiral, another small plate was mounted but insulated from the main target. This second plate signals when the end of the spiral has been successfully reached. Electrodes are alligator clipped onto these two plates, with the ground connected to the instrument. Four different sizes of spiral targets were used with four different spiral widths: 1.2 mm, 1.5 mm, 2 mm, and 2.5 mm (Figure 4.13).

When operating manually, surgeons tend to use the corner of the laryngoscope where the instrument enters it as a fulcrum to help improve precision and keep the instrument handle out of the microscope view. In order to simulate this natural rotation center when the robot was used, a remote center of motion constraint was set up so that the robot would naturally rotate the instrument about its insertion point into the laryngoscope. This was necessary to prevent extraneous forces from the instrument touching the laryngoscope from interfering in the robot control. Insertion and removal of the instrument along its shaft was not altered.
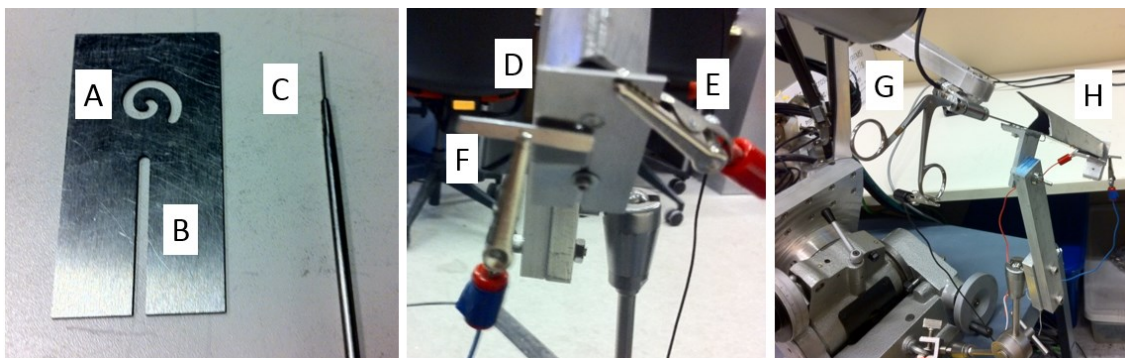
Figure 4.12: Targets and electrodes precision motion study.

Left) Target and instrument A) slot instrument must be navigated through B) mounting slot C) instrument tip. Center) Target mounted on training laryngoscope D) target E) failure electrode F) success electrode. Right) Target and training laryngoscope mounted for robotically assistance G) laryngeal instrument H) training laryngoscope.
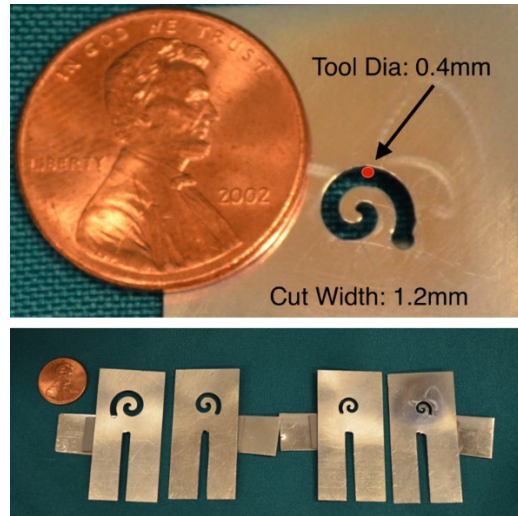
Figure 4.13: Spiral targets.

Ten surgeons, fellows, and residents from the Johns Hopkins Department of OHNS were recruited for this experiment. After consent was obtained, each participant was given hands-on training with the REMS and instruction about the goals of the experiment to ensure the study procedures were understood. Participants were asked to navigate the instrument from the center to the end of the spiral as quickly as possible but without touching the sides. If the instrument contacted the spiral, a buzzer sounded to indicate so. When the end of the spiral was reached, a different buzzer sounded to indicate that the trial was over. The 2.5 mm spiral was used first for training so that the users could become familiar with the task. These trials were not recorded. Once the users felt comfortable with the study, they performed 5 trials each with the 2 mm, 1.5 mm, and 1.2 mm spiral targets. The orientation of each spiral was reversed compared to the previous one in order to keep users from becoming accustomed to moving in the same direction on each trial. In order to prevent fatigue and learning curve effects from contaminating the results, the study was conducted in two blocks, a robot first block, and a manual first block. The robot first block completed the study with the robot first, then repeated it manually, and the manual first block did the reverse. The assignment of participants to blocks was randomized. The total time contacting the spiral (fail time) and total overall time (total time) were recorded for each trial. Participants were also asked to fill out a short anonymous questionnaire at the end in order to obtain more information about their background as well as their feedback about the REMS and the study as a whole.

170

4.3.2.2 Results

Though 10 participants were enrolled, the first participant's data could not be used since the experimental procedure was amended based on his/her feedback, resulting in usable data for 9 participants (numbered 1-9). Since it is not possible to have a fail time or total time of less than 0, the data are highly skewed, preventing any assumptions of normality. Because of this, a distribution free bootstrapping method with 1000 repetitions was used to calculate confidence intervals. Figure 4.14 shows the average fail time results of all participants together. Figure 4.15 shows the average fail time results of each participant individually. Figure 4.16 shows the average total time results for all participants together. Figure 4.17 shows the average total time results for each participant individually. Table 4.7 shows the results of the questionnaires.
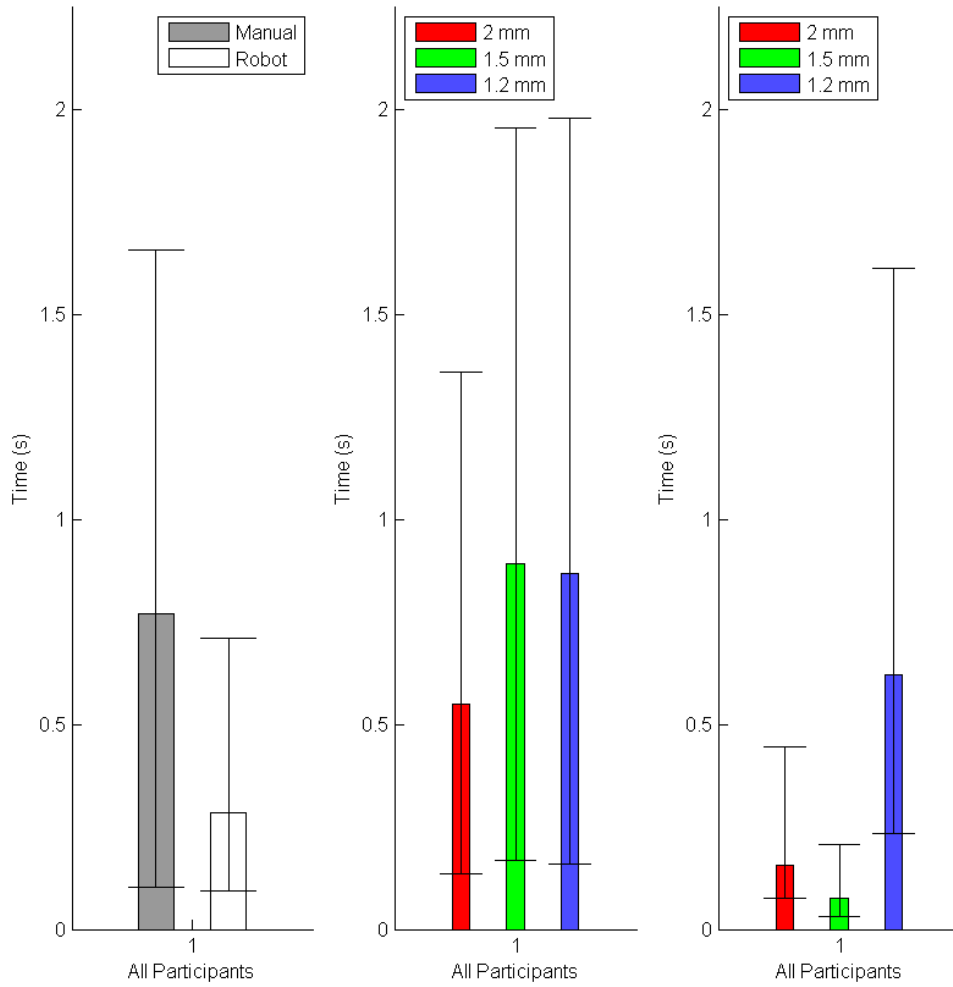
Figure 4.14: Average fail time for all participants with 95% confidence intervals.
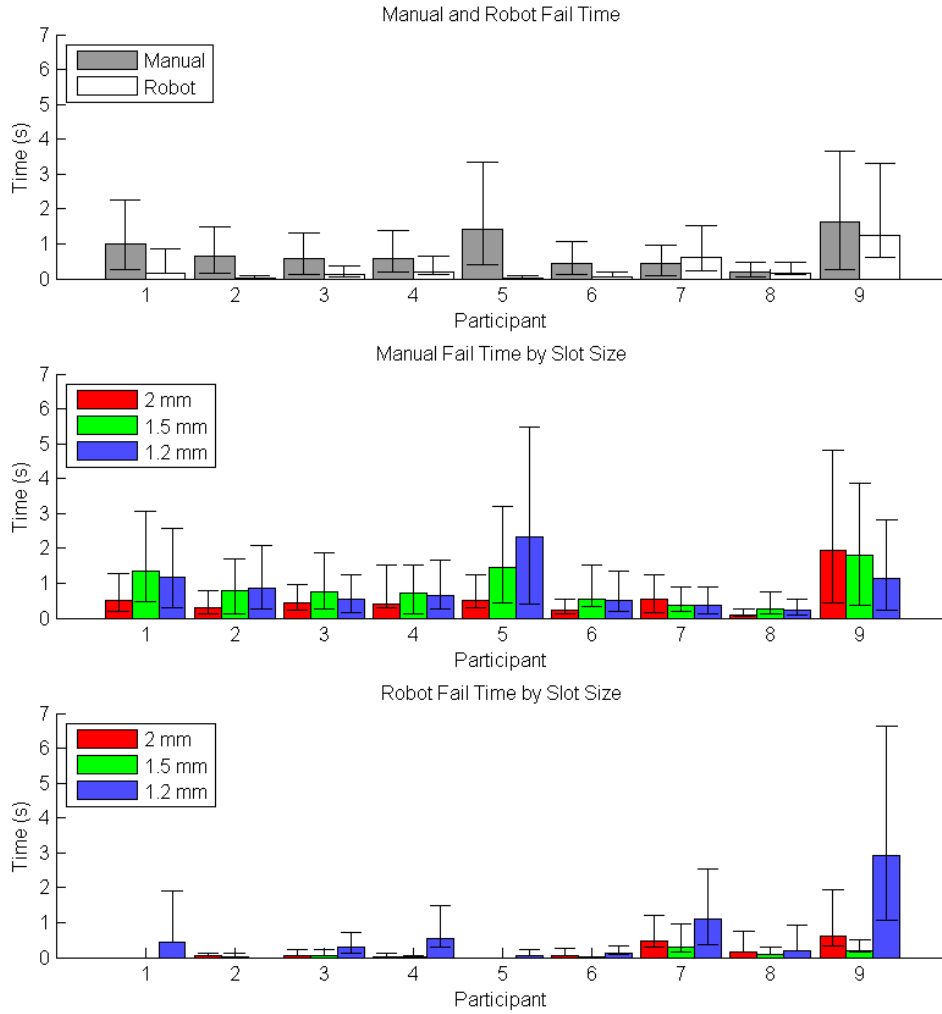
Figure 4.15: Average fail time for each participant with 95% confidence intervals.
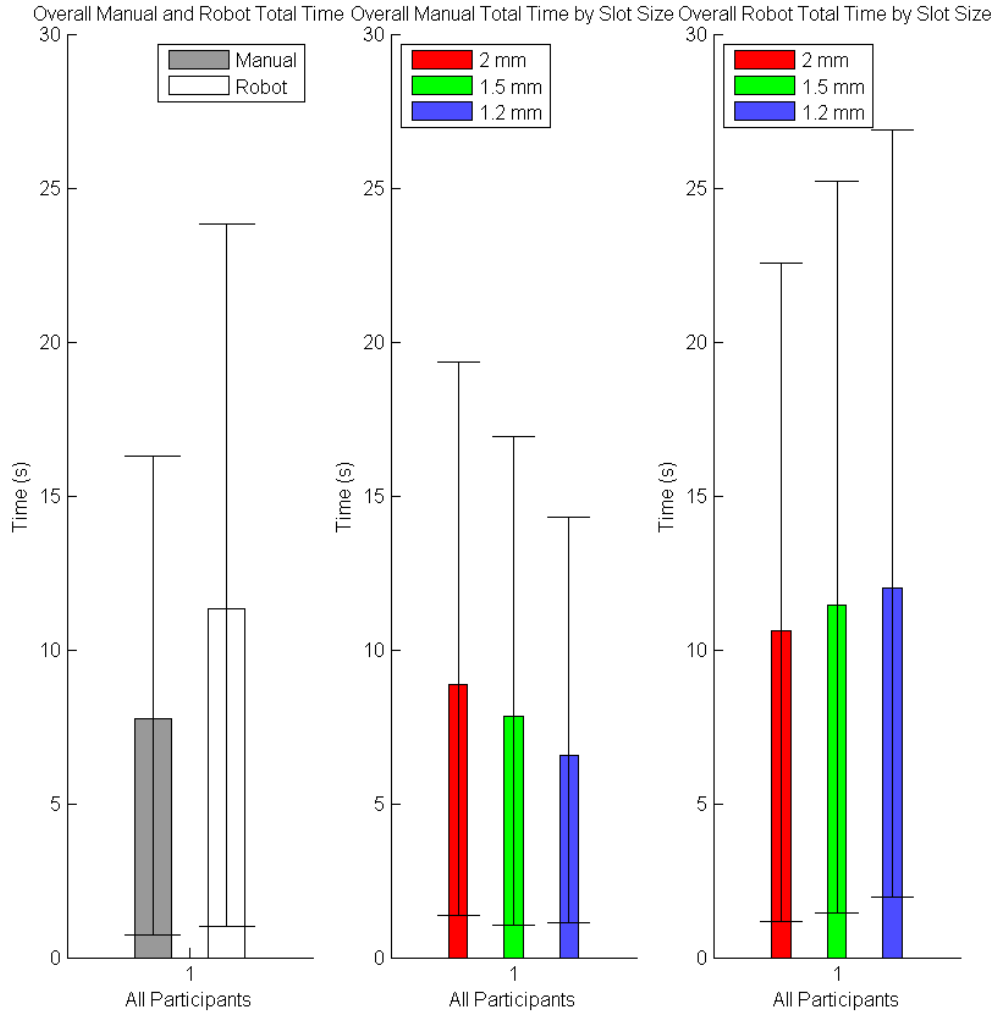
Figure 4.16: Average total time for all participants with 95% confidence intervals.
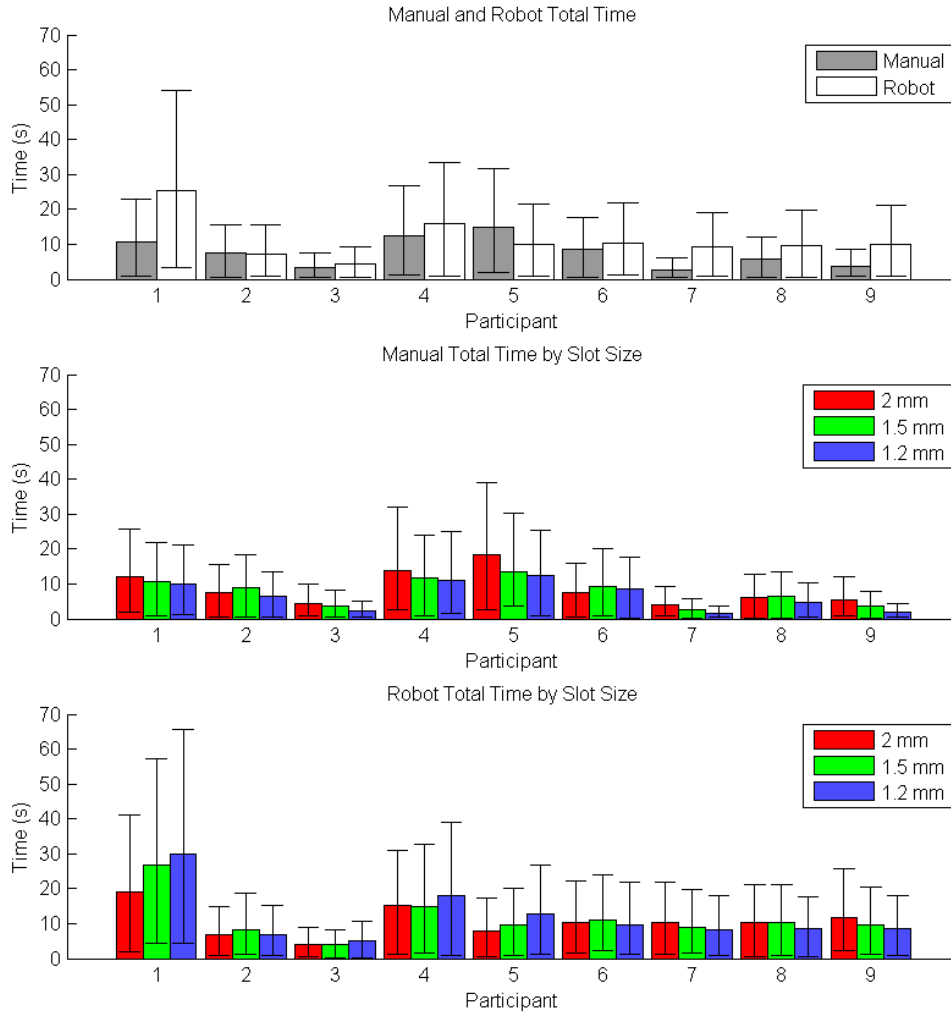
Figure 4.17: Average total time for each participant with 95% confidence intervals.

Table 4.7: Questionnaire Results

Experience is quantified by: 1 = Medical student, 2 = Junior resident, 3 = Senior resident, 4 = Fellow, 5 = Attending <5 years, 6 = Attending 6-10 years, 7 = Attending >10 years.

Specialty is quantified by: L = Laryngology, HN = Head and Neck, O = Other. Residents and below do not have a specialty yet.

Other data quantified by: 1-5 Likert scale or self-evident binary value.

Participant	1	2	3	4	5	6	7	8	9
Manual or Robot First	M	R	M	R	M	R	M	R	M
Experience	6	6	4	2	3	6	3	7	7
Specialty	L	L	L	N/A	N/A	HN	N/A	HN	O

Left or Right Handed	R	R	R	R	R	R	R	R	R
Used Robot Before	Y	Y	N	N	Y	Y	Y	Y	N
Experiment Fair Representation	4	5	4	3	5	5	3	3	3
Skill without Robot	2	3	3	3	2	2	2	2	3
Skill with Robot	5	5	5	4	5	5	3	4	4
Robot Ease of Use	5	5	4	3	5	4	3	4	4
Robot Aid in Real Use	5	5	5	4	5	4	4	5	5
Better if Bimanual?	Y	Y	Y	Y	Y	Y	Y	Y	Y
Would use it clinically?	Y	Y	Y	Y	Y	Y	Y	Y	Y

4.3.2.3   Discussion

Based on the questionnaire data, the experience level of the participants varied broadly from junior residents to senior attending physicians. A broad range of OHNS specialties was also represented, with laryngeal, head and neck, and others participating. There does not seem to be any significant difference in performance whether the task was done robotically or manually first, or whether the participant had used a surgical robot before. According to the survey results, the spiral navigation task was not perfect, but was a reasonable representation of skills used in these types of surgeries, with all ratings from 3-5 on a scale of 1-5. It was also clear that the task was difficult without the robot, with ratings of manual skill at the task from 2-3. It is also clear that the robot improved subjective assessment of skill at the task, with ratings of 3-5. The robot was generally easy to use with ratings of 3-5. Participants also agreed that the robot would be able to aid in the treatment of patients with ratings of 4-5. All participants agreed that the robot would be most helpful if it were bimanual, and that they would use it clinically if it were available.

The REMS reduced average fail time across all participants by 63% (95% CI [44%, 75%]) compared to manual results. Breaking down these results by slot size doesn't produce many significant results since the confidence intervals are so large due to inter subject variability and small sample size, however it is at least clear that the REMS results for every slot size have a lower mean than the manual results, though this is only statistically significant for the 2 mm and 1.5 mm slot sizes.

Breaking down the same results for each participant individually produces some interesting results (Figure 4.15). The REMS improved average fail time in 8 out of 9 participants (6 of which are statistically significant), ranging from an amazing 99% (95% CI [96%, 100%]) reduction in average fail time for participant 5, to a -45% (95% CI [-150%, 10%]) reduction (45% increase) in average fail time for participant 7. The combination of dramatic variation between participants with significant consistency within some participants seems to indicate that for this task the REMS works better for some people than for others. It is desirable to determine what factors influence how well the participants could use REMS, however, the questionnaire data from Table 4.7 for participants 5 and 7 are almost identical. The only difference is in their opinion of how well the experiment represents clinical practice, and how easy and effective the REMS was. Interestingly, participants 1, 2, 3, 4, and 6 all show relatively similar results despite the significant differences in their questionnaire data. Participant 8 is unique in that his/her manual performance is substantially better than the other participants (which is not surprising for a senior attending who frequently performs microsurgery), making it difficult for the REMS to provide much assistance. Participant 9 is also unique since he/she is the only participant who is an attending but not a laryngeal or head and neck specialist. This explains why his/her manual performance is worse than the other participants, since this type of microsurgery is not typically part of his/her normal workload. In spite of this, the REMS did improve participant 9's performance, though not by a significant amount.

A similar analysis for the average total amount of time taken per trial (Figure 4.16) reveals that the REMS resulted in an overall 46% (95% CI [32%, 65%]) increase in time taken. Breaking this data down by slot size reveals a potentially interesting trend. Participants took more time for smaller slot sizes with the REMS, but actually took less time for smaller slots manually, though these results are not statistically significant due to significant inter-subject variability. This correlates well with the subjective feedback from some of the participants who reported that they intentionally go faster in situations where accuracy is poor in order to avoid causing additional damage by spending more time in inaccurate contact with the tissue. Breaking this data down for each participant individually (Figure 4.17) reveals that most participants were slower with the REMS (7 out of 9), but the variability both between and within participants was substantial.

Though the REMS and the experiment overall were generally well received, there were also some drawbacks. The sample size of the participants was smaller than desired, largely due to the limited number of potential participants and the difficulty in scheduling. In addition to this, the variability between the participants is significant, with many experience levels and specialties represented. These factors combine to make it difficult to draw many strong conclusions other than overall results. Another key weakness is the lack of a standardized training protocol for the REMS. Each participant was given a basic explanation and then told to try out the task and the REMS until they were comfortable. Participants rarely used more than 5 minutes for this familiarization. Also, though it is not apparent from the data, there was subjective evidence of significant learning curve effects where participants seemed to understand the task and the REMS better over time. A more rigorous training protocol might have improved performance and reduced variability. Another minor drawback is that the spirals of different widths were not the same length, with the narrower spirals being shorter. This was intentional to prevent the participants from getting acclimated to the same spiral shape over time, but it also had the potential effect of interfering with some of the time results.

4.3.3 Laryngeal Cadaver Study

I designed the experimental protocol and setup for this experiment, and ran the data collection. Dr. Lee Akst (Johns Hopkins Hospital OHNS Physician) provided clinical guidance and support for this experiment. Marcin Balicki (then a JHU CS postdoc) assisted with software support and data collection.

4.3.3.1 Methods

The laryngeal precision motion study showed how the REMS can improve technical performance in an artificial surgical task. The next step was to demonstrate the feasibility of using the REMS in a realistic surgical environment. The goal of this study was to demonstrate the precision enhancing capabilities of the REMS in a human cadaver model of microlaryngeal phonosurgery. One human cadaver head fixed in phenol was used in this study. The head had been preserved for over a year when the study was conducted, so some of the tissues were stiff and unrealistic, however the vocal folds were still in good condition. The REMS was draped with a large plastic bag and positioned on the operating table. The head was rested on a plastic draped aluminum tray and suspended in place with a laryngoscope attached to a passive arm which

was clamped to the table. A surgical microscope with a 400 mm lens was used to visualize the vocal folds through the laryngoscope. A video camera adapter was used so that images could be recorded from the right eye of the microscope. In order to better simulate operating room ergonomics, custom arm rests were attached to both arms of the operator's chair. An unmodified right-facing curved alligator forceps was attached to the REMS using the rotation preserving tool holder. An elastic band was wrapped around the instrument handle to enable it to stay closed when not being held. The friction of the axial rotation of the instrument in the tool holder was tuned so that the instrument was easily movable but would not move under the influence of gravity or small tissue forces when released. Figure 4.18 shows the setup.

Figure 4.18: REMS microlaryngeal phonosurgery cadaver setup.

Since this was a preliminary study to demonstrate the utility of the REMS in this realistic environment, the main method of data collection was photographs and videos taken through the microscope and with a handheld camera showing how the REMS could be used. The important REMS functionalities to record included:

- Grabbing tissue precisely using only a few teeth on the forceps.
- Holding tissue still hands-free.

4.3.3.2   Results

The REMS was used by a laryngeal surgical specialist to grab and retract tissue on the right vocal fold (Figure 4.19). The REMS significantly reduced hand tremor and improved control compared to manual operation, enabling carefully targeted movements. Using the REMS, it was possible to precisely grab tissue using only the tip of the alligator forceps, reducing tissue damage. The tissue was then retracted and held in place using the REMS. Figure 4.20 shows the REMS holding tissue retracted hands-free while another manual instrument was being used to operate on the vocal fold.
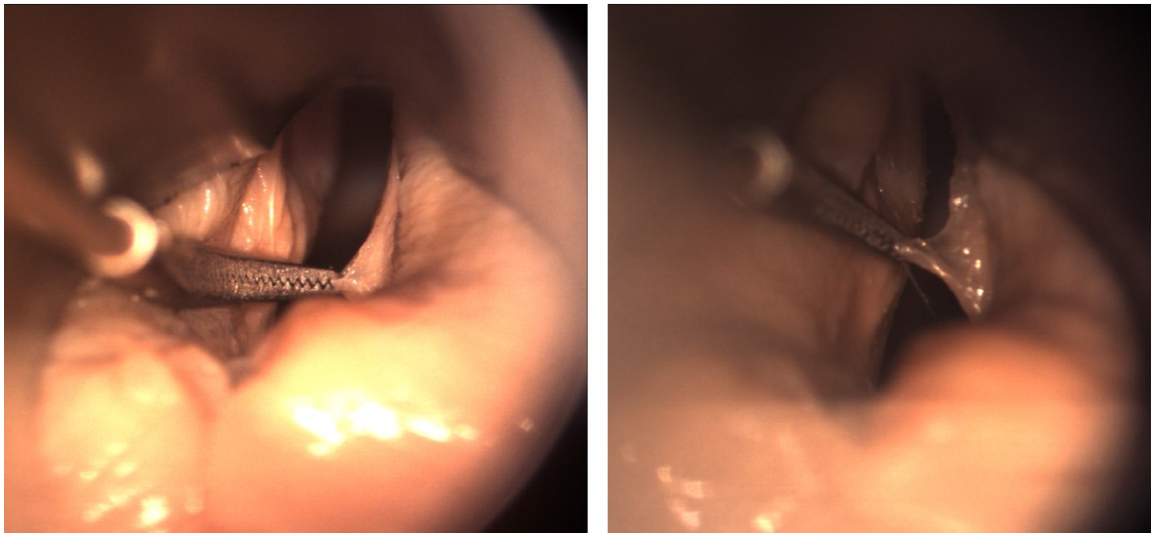
Figure 4.19: Holding vocal fold tissue with REMS.

Left: Grabbing tissue precisely with only two forceps teeth. Right: Retracting and holding tissue still using the REMS.

Figure 4.20: Hands-free tissue holding with REMS.

4.3.3.3 Discussion

First, this study has shown that the REMS has sufficient technical capability to be used in a realistic environment, including the ability to operate while covered with plastic drapes, sufficient range of motion and speed, sufficient passive adjustability, and sufficient compactness to not obstruct the microscope view. The basic tremor cancellation and precision enhancement capabilities of the REMS were also demonstrated. In addition to these basic capabilities, it was also shown that even this early-stage REMS prototype can provide stable, hands-free tissue retraction. These capabilities have the potential to significantly impact microlaryngeal phonosurgery, where minimizing damage to healthy vocal fold tissue is the key indicator of surgical success. Grabbing vocal fold tissue in a precise, targeted way using only a few teeth on the forceps is considered a very advanced technique when operating manually, whereas with the REMS it is easily achieved even by less-skilled users. This ability to hold tissue retracted hands-free with high stability is unprecedented in microlaryngeal phonosurgery. This capability is very advantageous to surgeons, since rather than having to carefully balance the tremor and inaccuracy of two hands simultaneously, it enables them to focus only on the operating instrument while the retracting instrument is

handled by the REMS. Additionally, if a second REMS were used, both instruments could be robotically manipulated, further enhancing surgical precision.

4.4 Microvascular Suturing Feasibility Study

In order to show that the precision enhancement capabilities of the REMS have diverse applications beyond microlaryngeal phonosurgery, a microvascular suturing feasibility study was conducted. My contributions included designing and fabricating the surgical instrument, as well as assisting in the experiment design and execution. Marcin Balicki (JHU CS postdoc) did most of the software work, and Dr. Richmon (JHH OHNS physician) and Allen Feng (JHH OHNS medical student) did most of the protocol design.

4.4.1.1 Methods

The goal of this study was to demonstrate the basic feasibility of using the REMS for high-precision open suturing in an ex-vivo chicken model. A food-grade chicken thigh was acquired from a grocery store, and dissected to reveal the femoral vein. The vein was bisected using surgical scissors. A curved titanium ENT micro forceps was modified and mounted into the REMS rotation-preserving tool holder (Figure 4.21). Visualization was provided by a surgical microscope with a 200 mm lens.

Figure 4.21: REMS with suturing instrument.

Using this attachment, the REMS was then used along with a manually controlled vein spreader to pass sutures through two vein ends, and this was compared to doing the same task manually (Figure 4.22). Two participants attempted to suture the vein, one senior medical student with training in microvascular suturing, and one novice. Since this was a preliminary study to determine if a larger study should be conducted for this application, the primary data collected were subjective feedback, video, and photographs.
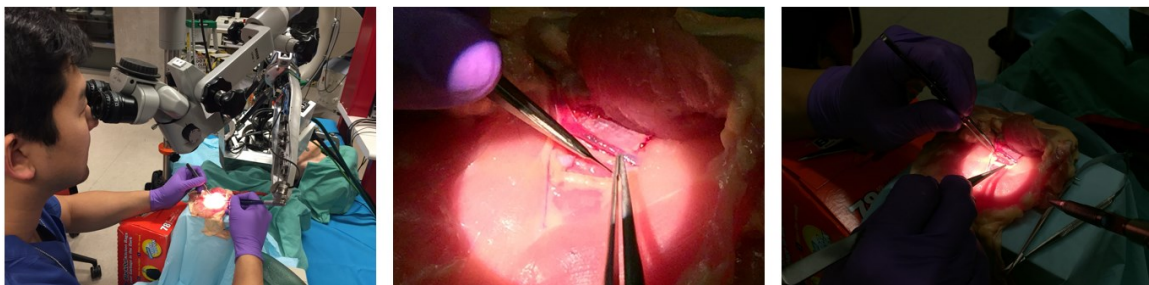
Figure 4.22: Microvascular Suturing

Left: Suturing with the REMS Middle: Suturing with the REMS close-up Right: Manual Suturing.

4.4.1.2 Results

The vein was between 2 and 3 mm in diameter, making manual suturing difficult because of hand tremor (clearly visible under the microscope), making it particularly difficult to position the needle at the correct position and angle to form the suture. Tearing the needle out of the vein while attempting to pull it through was also observed. Using the REMS, hand tremor was eliminated (also clearly visible under the microscope), making needle placement much easier. However, since neither the instrument nor the REMS design or software were optimized for this procedure, there were some challenges in holding the needle with the forceps and tuning the control parameters. Hitting the REMS delta mechanism workspace limits was also a concern, since the instrument was not physically constrained by either equipment (such as a laryngoscope) or anatomy. In spite of these issues, both users agreed that they would rather use even the current un-optimized REMS for this procedure than attempt it manually.

4.4.1.3 Discussion

The tremor reduction attained by using the REMS was significant, and subjectively improved precision while reducing both mental and physical fatigue. The technical issues encountered using the REMS were relatively minor and should not be difficult to overcome with some further hardware and software development, including a better instrument design, and control software optimized for this task. Based on these results, it is likely that the REMS could be clinically useful for open micro-suturing, and further development and study should be carried out.

4.5   Sinus Navigation Feasibility Study

In order to demonstrate the navigation capabilities of the REMS, a sinus navigation feasibility study was conducted. My contributions included the study design, hardware design and implementation, and some high level software and control design, implementation, and debugging. Most of the software design, implementation, and debugging was done by Marcin Balicki. Algorithmic path generation was done by Narges Ahmidi, a graduate student in the JHU Department of Computer Science. Clinical support and guidance (especially on protocol development) was provided by Dr. Masaru Ishii (JHH OHNS physician).

4.5.1.1 Methods

The goal of this study was to demonstrate two key functionalities of the REMS, basic navigation and virtual fixtures. Basic navigation covers the same functionality as conventional navigation systems such as optical trackers. This includes the ability to register physical anatomy to a pre-operative CT scan, and show on the CT scan where the probe instrument is located in real time. In order to demonstrate this one human male cadaver head was equipped with aluminum registration screws and CT-scanned. The probe instrument on the REMS was then used to locate these screws. The REMS estimates and the manually segmented CT estimates were then registered using Arun's method. The CT scan and pointer instrument were then displayed visually using 3D Slicer [97] (www.slicer.org/) (Figure 4.23). The probe instrument was then inserted into the nose of the cadaver head and navigated to different anatomical targets, including the Eustachian tube. The instrument could be visualized in the nose using a conventional sinus endoscope and camera system. Figure 4.24 shows navigation in progress. The video feed from the endoscope and the graphical display in 3D Slicer were then compared to qualitatively verify the effectiveness of the registration and navigation.

Once the effectiveness of the registration and basic navigation were established, the study switched to evaluating virtual fixtures. Two methods of generating virtual fixtures were tried, manual and algorithmic. In manual fixture generation, the REMS was manually guided along a desired path, while the path was being recorded. In algorithmic generation, the CT scan was analyzed based on [98], and an optimal path was derived which minimized collisions between the instrument shaft and the tissue. Once paths were obtained, the REMS path constraints were then qualitatively evaluated.
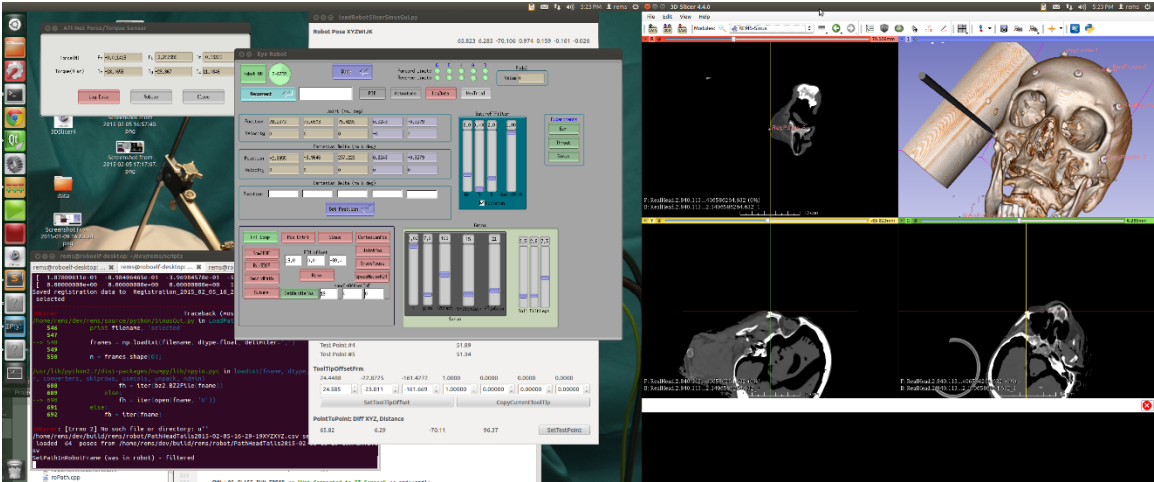
Figure 4.23: Top) REMS registration Bottom) 3D Slicer navigation
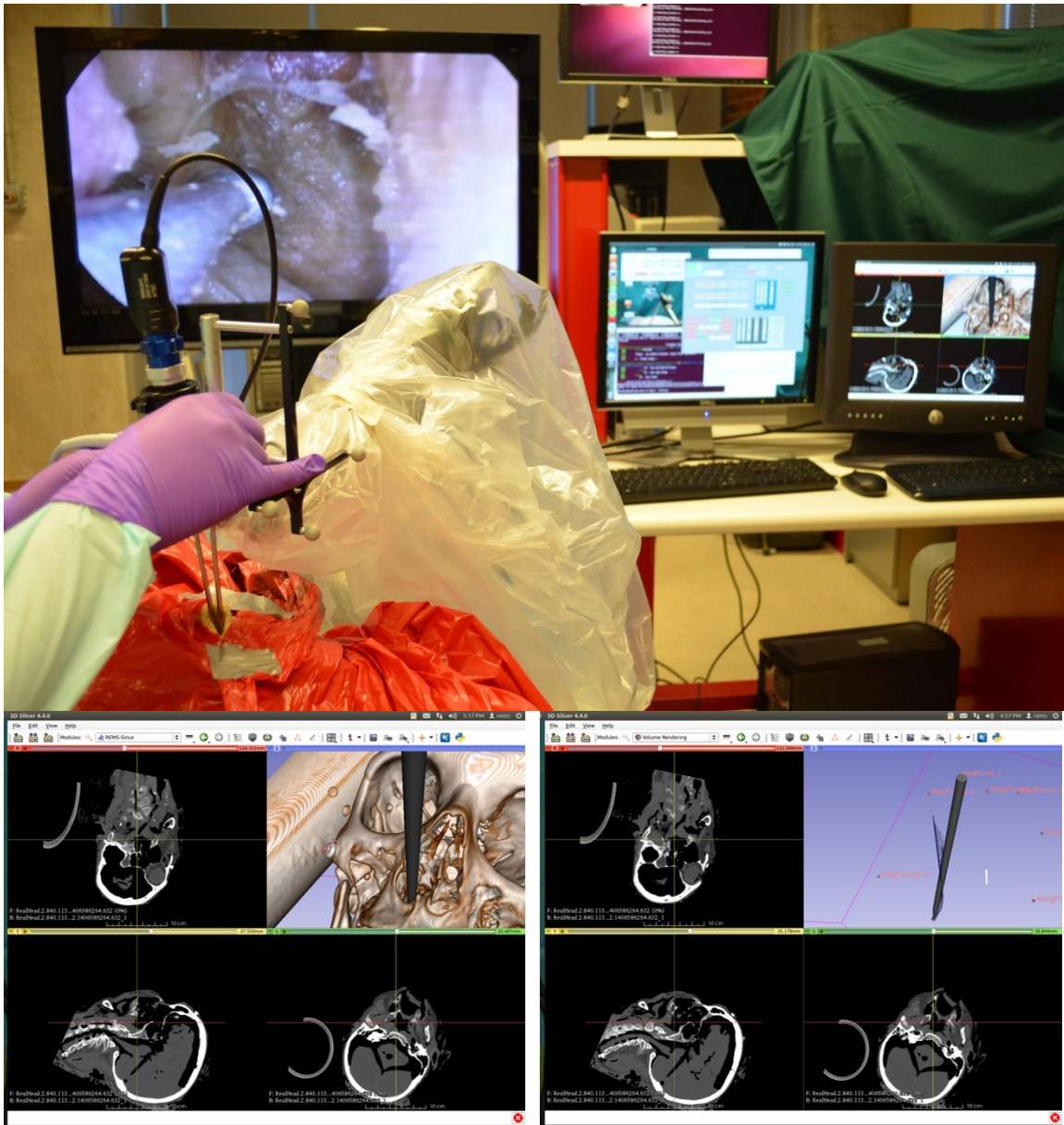
Figure 4.24: Sinus navigation using the REMS.

4.5.1.2   Results

The registration of the REMS to the CT scan used 5 screws, and resulted in an average registration error of 0.46 mm with a standard deviation of 0.22 mm, and a max deviation of 0.81 mm. The registration process was relatively fast, taking only a few minutes. The REMS probe tip was then used to touch structures visible in the CT scan (screws, anatomical features) to qualitatively check if the registration and navigation were sufficiently accurate. Figure 4.23 shows the REMS probe tip touching a screw on the head,

and Figure 4.24 shows the probe tip near the Eustachian tube, while the corresponding 3D Slicer images are displayed. Based on manual analysis by checking the coordinates in 3D Slicer, it was concluded that the registration and navigation likely had better than 1 mm accuracy over the region of interest in and around the head.

Next, manual path generation was evaluated. The REMS was navigated to the Eustachian tube while the path was recorded. However, when this path was used as a virtual fixture constraint with the REMS, some issues became apparent. Raw manual paths tend to contain non-smooth motions (e.g. square corners), which tend to feel awkward and unintuitive when replayed using the REMS. In order to fix this issue, the manually recorded paths were smoothed using a Savitzky-Golay filter. The smoothed path was significantly improved, enabling intuitive, realistic navigation. Figure 4.24 (bottom right) shows a recorded, filtered path in 3D Slicer, with a blue arrow representing the position and orientation of the path at each point along the path.

One key issue with virtual fixtures such as these is how to transition between being off the fixture and being on it. This was achieved by starting with the hardness of the feature (Equation (3.119) set to 0, which is equivalent to conventional admittance control. The hardness was then gradually turned up as the instrument got closer to the path, until the instrument was on the path and the hardness was set to 1 (its maximum value). Once on the path, different hardness were qualitatively evaluated to determine if soft virtual fixtures were feasible. Though the soft path constraints worked as expected, it was determined that in the future, a more sophisticated tube constraint should be evaluated, which would enable the probe to move freely within the tube, but prevent it from moving outside.

With the path hardness at maximum, the stiffness of the system was also evaluated. The instrument was manually pushed until the force sensor reading was 5 N (its maximum value) and the deflection of the tip was observed in the sinus using the endoscope. The deflection was not enough to result in collision between the probe tip and the sinus tissue, and was estimated to be on the order of +/- 1 mm, which is in line with the stiffness analysis for the REMS.

Due to difficulties segmenting the cadaver head CT volume, the algorithmic path could not be evaluated in the cadaver head as part of this study. Therefore, it was evaluated in the plastic phantom head from Figure 4.6. The unmodified algorithmic trajectories were found to be too non-smooth to work with the

REMS, though they produced excellent results for keeping the probe tip away from the sinus walls. After the algorithm parameters were tuned to optimize smoothness (particularly for orientation), the algorithmic trajectories were found to be highly effective for the REMS.

4.5.1.3 Discussion

These results are very encouraging, and have successfully demonstrated that the REMS is capable of both basic navigation and virtual fixtures. Even for the current preliminary version of the REMS, the navigation results appear to be superior to those for a conventional optical tracking system, though this will need to be quantitatively evaluated with more rigor in future work. The path recording also had the unexpected effect of making small errors in manual paths very apparent through tactile feedback. Non-smoothness and unnecessarily indirect paths became very apparent when using the REMS, which could replay path errors with sub-millimeter precision. This could potentially be a very useful feature for surgical training, which will be investigated in future work.

It was also determined that for the REMS to be broadly useful in sinus surgery, a 6th motorized degree of freedom would be necessary to enable control of axial rotation for curved instruments. This would also require significant enhancement of both the REMS control software, and the algorithmic path generation software in order to rigorously handle the added complexity of curved tools and a 3rd rotational degree of freedom. This is also left for future work.

4.6 Chapter Summary

This chapter presented the technical and functional validation of the REMS. First, a technical validation was done evaluating resolution, repeatability, stiffness, calibration, and accuracy. Once these technical requirements were met, a series of functional validations were performed in which the REMS was used to replicate important aspects of surgical procedures. Two laryngeal validations were performed in synthetic phantoms, one involving precision needle insertion, and the other precision instrument manipulation, both with successful results. Another laryngeal validation was performed with a realistic setup replicating microlaryngeal phonosurgery in a human cadaver model, which was also successful. A preliminary microvascular suturing validation was also performed using the REMS to suture a vein in an

ex-vivo chicken model. This study was too preliminary to draw significant conclusions, but it at least showed the feasibility of using the REMS for open micro suturing. Finally, a preliminary sinus navigation validation was conducted in a human cadaver model, successfully demonstrating the navigation capability of the REMS.

4.7 Conclusions

These results indicate that the REMS has the potential to be very effective in enhancing both surgical precision and navigation. The needle insertion and precision motion studies have both shown that the REMS improves surgical precision in laboratory tasks resembling laryngeal surgery, with only a moderate increase in operating time. The microlaryngeal phonosurgery cadaver study has shown that the REMS can be feasibly used in a more realistic environment, and can also act as a "3rd hand" which can hold tissue fixed. In addition to these precision results, the suturing study has also demonstrated that the REMS can feasibly be used for enhancing precision of more diverse tasks with different instrument types. The sinus navigation study, combined with the calibration and accuracy results, has demonstrated that the REMS can potentially achieve better accuracy than conventional optical trackers, while also providing advanced assistance and safety features.

4.8 Contributions

- Calibration of REMS and validation that it meets technical requirements [59].
- Study demonstrating improved surgical precision using REMS compared to manual operation in two phantom models of microlaryngeal phonosurgery [59].
- Demonstration of feasibility of robotic microlaryngeal phonosurgery in a human cadaver.
- Demonstration of feasibility of REMS for microvascular suturing in an ex-vivo chicken model.
- Demonstration of feasibility of navigation in sinus surgery using REMS in human cadaver.

Chapter 5   Chapter Summaries and Future Work

5.1 Chapter Summaries

5.1.1 Chapter 1 Introduction

Chapter 1 introduced OHNS in general as well as examples of specific conditions and surgical procedures that could benefit from robotic surgical assistance. These examples were used to distil general surgical challenges which can be addressed to improve surgical performance. Previous relevant commercial and research surgical robots were also surveyed and analyzed to determine the best approaches for assisting in OHNS. Based on this work, it was determined that there is significant overlap between the surgical challenges for different OHNS procedures, that it is reasonable for a small number of general systems to assist in broad classes of OHNS procedures, and that no current robotic systems address these needs.

5.1.2 Chapter 2 Robo-ELF Scope

Chapter 2 first analyzed the challenges involved in robotic flexible endoscope manipulation and derived a set of requirements. These requirements were validated using a proof of concept prototype which was qualitatively evaluated. These results were then used to build a full-scale prototype, the Robo-ELF Scope, which was validated and improved through two human cadaver studies. A human subjects study was designed and passed through 3 iterations of IRB, FDA, and CES review, as well as revisions by JHU Perioperative Services to make the system compatible with the hospital infrastructure. This resulted in a clinically usable version of the Robo-ELF Scope and approval of a human subjects study.

5.1.3 Chapter 3 REMS Design and Development

Chapter 3 derived the requirements for precision and navigation enhancement in OHNS based on the analysis from the introduction. Additional detailed prior work from the JHU Steady Hand Robots was also analyzed. Based on these results, a concept design of the REMS was created. The kinematic design of the REMS was then analyzed and optimized in detail. Novel optimization techniques for parallel robots were also derived. The design was then analyzed to ensure that it should be capable of meeting requirements. A functional prototype was then build based on this design, and software and control algorithms were then derived. The final result was a functional REMS prototype theoretically capable of meeting requirements.

5.1.4 Chapter 4 REMS Calibration and Validation

Chapter 4 validated the REMS prototype both technically and functionally. Technical performance such as resolution, repeatability, and accuracy were confirmed to meet requirements. Functional evaluation included two validations of robotic microlaryngeal phonosurgery using phantom models, and one using a human cadaver model, all with successful results. An ex-vivo animal feasibility validation using an ex-vivo chicken model was also conducted with successful results. Finally, a robotic sinus surgery feasibility validation in a human cadaver model was conducted, with successful results.

5.2 Robo-ELF Future Work

5.2.1 Technical Development

Once the Robo-ELF has been validated in a human subjects study, validating the robotic flexible endoscope manipulation concept, one logical next step would be to build a second version of the Robo-ELF Scope using the knowledge gained from the first one. This could include substantial miniaturization, and the introduction of some disposable parts in order to improve the draping and cleaning procedures. Advances in 3d printing technology, including printing laser sintered biologically compatible nylon, could make prototyping a second version much quicker and cheaper than the for the previous version.

Another possible next step is the introduction of advanced features, particularly involving the user interface and visualization. This could include advanced user interfaces such as a touch screen that enables users to simply tap the screen where they want the Robo-ELF Scope to look or move. It may also be worthwhile to investigate gesture interfaces, which could make the user interface more intuitive, as well as improve hygiene since there would be no need to make physical contact with a user interface during operation. Advanced visualization features could include things like robotically assisted 3d reconstruction which uses the robot's motion to reconstruct 3d images from the monoscopic endoscope data. It could also be possible to use the Robo-ELF Scope to pass an OCT fiber through the working channel of the scope and hold it still, enabling precise OCT imaging of desired anatomical targets. It would also be possible to develop other applications for the current Robo-ELF Scope or future versions, such as robotically assisted flexible endoscopy for pulmonology, gastrointestinal applications, or sinus surgery.

Finally, it may also be feasible to use the Robo-ELF Scope for more advanced surgical behaviors. These could include robotically assisted biopsy and laser ablation with instruments passed through the working channel of the endoscope.

5.2.2 Future Validation Studies

The obvious next step for validation would be to finish the currently planned human subjects study. See [60] for the full FDA submission and IRB protocol for this study. Once this is complete, subsequent validation studies could include more advanced validations of the current Robo-ELF Scope, including using it for more involved procedures rather than pure endoscopy. Another possibility would be to perform validation studies for future iterations of the Robo-ELF Scope, or for advanced features as discussed above.

5.3 REMS Future Work

5.3.1 Technical Development

The obvious next step for the REMS would be to implement all of the suggested design changes from the previous sections, including:

- Redundant position sensing for all active degrees of freedom.

- More rigorous calibration and control, including a fully developed system model.

- Improvements to the tilt mechanism to improve stiffness and repeatability.

- A larger force sensor to improve durability and stiffness.

- Improvements to the delta mechanism to enhance stiffness, manufacturability, and range of motion.

- Development of a motorized tool holder providing a 6th active degree of freedom.

- Development of a true quick-release tool holder.

- Enhancement of the instrument set to include specialized instruments which fully take advantage of robotic manipulation, particularly for suturing and sinus applications.

Another set of next steps would be to implement novel behaviors using the REMS. These could include:

- Using the REMS to manipulate rigid endoscopes

- Integrating the REMS with a miniaturized version of the Robo-ELF Scope to enable greater control of flexible endoscopes.

- Advanced registration using a stereo camera or structured light to enable rapid, accurate registration of the robot to the patient's head.

- Development of advanced navigation features for sinus surgery, including:

  o Semi-automated segmentation-based surgical planning.

  o Semi-automated operation, such as high level commands to ablate certain structures.

  o Integration with computer vision to enable more accurate registration.

Finally, another set of next steps could include development of REMS applications for other surgical procedures. These could include:

- Neurosurgical procedures such as suturing nerves, craniotomy, and spine surgery.

- Needle insertion/ablation procedures such as for cancer treatment or precision injections.

- Otology applications such as stapes footplate fenestration, middle ear surgery, and drilling cochleostomies.

- Plastic surgery applications such as precision suturing of tissue and anastomosis of small vessels.

194

- Dental applications such as drilling for implants or crowns.

5.3.2 Future Validation Studies

Three future validation studies are currently planned for the REMS.

5.3.2.1 Sinus

A sinus surgery study has also already been planned for the REMS. A JHU IRB protocol has already been approved. A brief summary of this study is given below. See [60] for the full IRB protocol for this study.

Previous work has shown that expert sinus surgeons tend to use very similar tool trajectories, implying that there is a single optimal solution to many sinus navigation problems. It has also been shown that surgical skill can be assessed by quantitatively comparing tool trajectories to expert trajectories [98]. This study seeks to combine these methods with the REMS to provide real-time data-driven force feedback to experts, as well as novice trainees learning sinus surgery with a human cadaveric head.

The goal of this research is to determine whether robotic surgical assistance improves surgical skill compared to unaided surgery. The surgical task for this evaluation will be navigating a tracked instrument to contact anatomical targets in the sinuses of a cadaver head. First, an expert group will perform the task to determine a baseline and gather data on how the robot affects expert surgeons. Then 20 novice participants will be divided into two randomized groups. The first group will be trained using the standard training method. The second group will be trained using the robotic training method. Both groups will then be assessed using a standard assessment method to determine whether robotic surgical assistance increases surgical skill, and whether these benefits of robotic training are retained even when operating conventionally.

The primary objective of this study is to objectively assess whether robotic sinus surgery results in an improvement in surgical skill compared to conventional surgery. A secondary objective of this study is to objectively determine whether skill improvement gained from robotic sinus surgery training is retained when operating manually. Another secondary objective of this study is to examine the difference between experts operating manually and with the robot, including subjective feedback. Another secondary objective

of this study is to examine whether robotically enforced safety barriers can prevent tissue damage even with novice users.

Hypotheses:

- Hypothesis 1: robotic sinus surgery results in improved surgical skill compared to conventional surgery.

- Hypothesis 2: Skill improvement gained from robotic sinus surgery training is retained when operating manually.

- Hypothesis 3: Robotic sinus surgery reduces hand tremor in experts compared to conventional surgery.

- Hypothesis 4: Robotically enforced safety barriers prevent tissue damage even for novice users.

5.3.2.2 Otology

A study using the REMS to perform stapes footplate fenestration has already been planned. A JHU IRB protocol has already been approved. A brief summary of this study is given below. See [60] for the full IRB protocol for this study.

The goal of this research is to evaluate whether the Robotic Ear Nose and Throat Microsurgery System (REMS), a novel surgical robot being developed at JHU, can improve surgical precision in a model of Laser Stapes Footplate Fenestration (LSFF) over conventional manual methods. This study will involve recruiting surgeons, fellows, and residents from Johns Hopkins Hospital who are trained in LSFF. Participants will perform a simulation of LSFF on a synthetic phantom both conventionally and with the REMS. The phantoms will be analyzed to determine if the REMS was able to improve surgical precision over conventional manual operating methods. No identifiable information from the participants will be kept except for the consent form, and no information will be kept linking participants to their experimental results.

Hypothesis: Fewer laser shots will be needed to ablate a correct size/shape fenestration when using the REMS vs. operating manually. Fenestration shape and size will be closer to specifications when using the REMS than when operating manually.

5.3.2.3 Microvascular Suturing

A microvascular suturing study has also already been planned for the REMS. A JHU IRB protocol has already been approved. A brief summary of this study is given below. See [60] for the full IRB protocol for this study.

The goal of this research is to determine whether a new robotic surgical system developed at JHU can improve surgical precision in a simulated suturing task in ex-vivo animal tissue. Participants will be surgeons, fellows, residents, and medical students from Johns Hopkins Hospital and School of Medicine who have had surgical training. Participants will be asked to perform the simulated surgical task manually, and with robotic assistance in a randomized order. The robot data, video data of the operating field (not showing the participant's face) and phantom/tissue results will be analyzed to determine if robotic assistance has improved surgical precision. No identifiable data will be kept for any of the participants except for the consent forms.

The primary objectives of this study are:

- To conduct an initial user study to determine if robotic system with custom microvascular needle drivers improves efficiency in simulated microvascular surgical techniques using a chicken thigh model.

- Evaluate use of robotic system in simulated microvascular surgical tasks for individuals with no training in microvascular surgery (but who have received general training in suturing) compared to trained microvascular surgeons.

Hypotheses:

- Hypothesis 1: The REMS improves efficiency in simulated microvascular surgical techniques using a chicken thigh model.

- Hypothesis 2: The REMS improves surgical performance more for less experienced users vs trained surgeons.

References

[1] P. Plinkert and H. Lowenheim, "Trends and perspectives in minimally invasive surgery in otorhinelaryngology-head and neck surgery," *Laryncoscope,* vol. 107, pp. 1483-1489, 1997.

[2] C. Brockmann, "Perception Space-The Final Frontier," *PLoS Biol,* vol. 3, no. 4, p. e137, 2005.

[3] NIDCD Information Clearinghouse, "Cochlear Implants," NIH Publication No. 11-4798, Bethesda, MD, 2014.

[4] D. L. Hamilos, "Chronic rhinosinusitis: epidemiology and medical management," *The Journal of Allergy and Clinical Immunology,* vol. 128, no. 4, pp. 693-707, 2011.

[5] N. Battacharyya, "Ambulatory Sinus and Nasal Surgery in the United States: Demographics and Perioperative Outcomes," *The Laryngoscope,* vol. 120, no. 3, pp. 635-638, 2010.

[6] M. Rubinstein and W. Armstrong, "Transoral laser microsurgery for laryngeal cancer: A primer and review of laser dosimetry," *Lasers Med Sci,* vol. 26, no. 1, pp. 113-124, 2011.

[7] R. Taylor, "A Perspective on Medical Robotics," *Proceedings of the IEEE,* vol. 94, no. 9, pp. 1652-1664, 2006.

[8] G. Weinstein, B. O'Malley, S. Desai and H. Quon, "Transoral robotic surgery: does the ends justify the means?," *Current Opinion in Otolaryngology & Head and Neck Surgery,* vol. 17, pp. 126-131, 2009.

[9] H. Lee, M. Yun, J. Bahk, H. Park, Y. Jeon and S. Lee, "Rupture of endotracheal tube cuff during robot-assisted endoscopic thyroidectomy," *Korean Journal of Anesthesiology,* vol. 59, no. 6, pp. 416-419, 2010.

[10] S. Gidaro, M. Buscarini, E. Ruiz, M. Stark and A. Labruzzo, "Telelap Alf-X: a novel telesurgical system for the 21st century," *Surg Technol Int.,* vol. 22, no. Dec, pp. 20-25, 2012.

[11] M. J. Lum, D. C. Friedman, G. Sankaranarayanan, H. King, K. Fodero, R. Leuschke and M. Sinanan, "The RAVEN: Design and validation of a telesurgery system," *Int. J. Robot. Res.,* vol. 9, no. 28, pp. 1183-1197, 2009.

[12] B. Hagag, R. Abovitz, H. Kang, B. Schmitz and M. Conditt, "RIO: Robotic-arm interactive orthopedic system MAKOplasty: user interactive haptic orthopedic robotics," in *Surgical Robotics*, Springer US, 2011, pp. 219-246.

[13] W. Bargar, A. Bauer and M. Borner, "Primary and revision total hip replacement using the Robodoc (R) system," *Clinical orthopaedics and related research,* vol. 354, pp. 82-91, 1998.

[14] J. Smith, P. Riches and P. Rowe, "Accuracy of a freehand sculpting tool for unicondylar knee replacement," *The International Journal of Medical Robotics and Computer Assisted Surgery,* vol. 10, no. 2, pp. 162-169, 2013.

[15] L. Joskowicz, R. Shamir, Z. Israel, Y. Shoshan and M. Shoham, "Renaissance robotic system for

keyhole cranial neurosurgery: in-vitro accuracy study," in *Proceedings of the Simposio Mexicano en Ciruga Asistida por Computadora y Procesamiento de Imgenes Mdicas*, 2011.

[16] M. Lefranc, C. Capel, A. Purvot-Occean, A. Fichten, C. Desenclos, P. Toussaint, D. Le Gars and J. Peltier, "Lefranc, Michel, et al. "Frameless robotic stereotactic biopsies: a consecutive series of 100 cases," *Journal of neurosurgery,* pp. 1-11, 2011.

[17] K. Abhinav, S. Prakash and D. Sanderman, "Use of robot-guided stereotactic placement of intracerebral electrodes for investigation of focal epilepsy: initial experience in the UK," *British journal of neurosurgery,* vol. 27, no. 5, pp. 704-705, 2013.

[18] S. Briot, C. Baradat, S. Guegan and V. Arakelian, "Contribution to the mechanical behavior improvement of the Robotic navigation device Surgiscope®," in *ASME 2007 International Design Engineering Technical Conferences and Computers and Information in Engineering Conference*, Las Vegas, 2007.

[19] F. Kiemeneij, M. Patterson, G. Amoroso, G. Laarman and T. Slagboom, "Use of the Stereotaxis Niobe® magnetic navigation system for percutaneous coronary intervention: Results from 350 consecutive patients," *Catheterization and Cardiovascular Interventions,* vol. 71, no. 4, pp. 510-516, 2008.

[20] K. Chun, B. Schmidt, B. Kokturk, R. Tilz, A. Furnakranz, M. Konstantinidou, E. Wissner, A. Metzner, F. Ouyang and K. Kuck, "Catheter ablation–new developments in robotics," *Herz Kardiovaskuläre Erkrankungen,* vol. 33, no. 8, pp. 586-589, 2008.

[21] E. Khan, M. Ejaz, W. Frumkin, A. Ng, S. Neelagaru, F. Abi-Samra, J. Lee, M. Giudici, ... and H. Calkins, "First experience with a novel robotic remote catheter system: Amigo™ mapping trial," *Journal of Interventional Cardiac Electrophysiology,* vol. 37, no. 2, pp. 121-129, 2013.

[22] S. Payal and M. Khashab, "New Platforms and Devices in Colonoscopy," *Gastroenterology Clinics of North America,* vol. 42, no. 3, pp. 671-688, 2013.

[23] P. Johnson, C. Serrano, M. Castro, R. Kuenzler, H. Choset, S. Tully and U. Duvvuri, "Demonstration of transoral surgery in cadaveric specimens with the medrobotics flex system," *The Laryngoscope,* vol. 123, no. 5, pp. 1168-1172, 2013.

[24] R. Bischoff, J. Kurth, G. Schreiber, R. Koeppe, A. Albu-Schaffer, A. Beyer, O. Eiberger, A. Haddadin, G. Grunwald and G. Hirzinger, "The KUKA-DLR Lightweight Robot arm - a new referene platform for robotics research and manufacturing," in *Robotics (ISR), 2010 41st International Symposium on and 2010 6th German Conference on Robotics (ROBOTIK)*, Munich, Germany, 2010.

[25] O. Weede, H. Monnich, B. Muller and H. Worn, "An Intelligent and Autonomous Endoscopic Guidance System for Minimally Invasive Surgery," in *IEEE ICRA*, Shanghai, China, 2011.

[26] G. Mylonas, P. Giataganas, M. Chaudrey, V. Vitiello, A. Darzi and G. Yang, "Autonomous eFAST Ultrasound Scanning by a Rbotic Manipulator using Learning from Demonstrations," in *IEEE IROS*, Tokyo, Japan, 2013.

[27] H. Monnich, H. Worn and D. Stein, "OP Sense - a robotic research platform for telemanipulated and automatic computer assisted surgery," in *IEEE International Workshop on Advanced Motion Control*, Sarajevo, Bosnia and Herzgovnia, 2012.

[28] R. Taylor, P. Jensen, L. Whitcomb, A. Barnes, R. Kumar and D. Stoianovici, "A steady-hand robotic system for microsurgical augmentation," *Int J Rob Res,* vol. 18, pp. 1201-1210, 1999.

[29] R. Taylor and D. Stoianovici, "Medical Robotics in Computer-Integrated Surgery," *IEEE TRANSACTIONS ON ROBOTICS AND AUTOMATION,* vol. 19, no. 5, pp. 765-781, 2003.

[30] S. Najarian, M. Fallahnezhad and E. Afshari, "Advances in medical robotic systems with specific applications," *Journal of Medical Engineering & Technology,* vol. 35, no. 1, pp. 19-33, 2011.

[31] R. H. Taylor, Computer-integrated surgery: technology and clinical applications, Cambridge: MIT Press, 1996.

[32] B. Mitchell, J. Koo, I. Iordachita, P. Kazanzedes, A. Kapoor, J. Handa, G. Hager and R. Taylor, "Development and application of a new steady-hand manipulator for retinal surgery," in *IEEE International Conference on Robotics and Automation*, Rome, Italy, 2007.

[33] A. Uneri, M. Balicki, J. Handa, P. Gehlbach, R. Taylor and I. Iordachita, "New steady-hand eye robot with micro-force sensing for vitreoretinal surgery," in *International Conference on Biomedical Robotics and Biomechanics*, Tokya, Japan, 2010.

[34] S. Wang, Q. Li and J. Ding, "Kinematic design for robot-assisted laryngeal surgery systems," in *IEEE Int. Conf. on Robotics and Automation*, Orlando, Florida, 2006.

[35] N. Simaan and R. Taylor, "A dexterous system for laryngeal surgery," in *IEEE Int. Conf. Robotics and Automation*, New Orleans, Louisiana, 2004.

[36] L. Kratchman, G. Blachon, T. Withrow, R. Balachandran, R. Labadie and R. Webster, "Toward automation of image-guided microstereotactic frames: a bone-attached parallel robot for percutaneous cochlear implantation," in *Robotics Science and Systems 2010: Workshop on Enabling Technologies*, Zaragoza, Spain, 2010.

[37] T. Maier, G. Strauss, M. Hofer, T. Kraus, A. Runge, R. Stenzel, J. Grumprecht, T. Berger, A. Deitz and T. Leuth, "A new microsurgical manipulator system for middle ear surgery," in *IEEE International Conference on Robotics and Automation*, Anchorage, Alaska, 2010.

[38] R. Reilink, S. Stramigioli and S. Misra, "Image-based flexible endoscope steering," in *IEEE/RSJ Intenational Conference on Intelligent Robotics and Systems*, Taipei, Taiwan, 2010.

[39] R. Eckl, J. Gumprecht, G. Strauss, M. Hofer, A. Dietz and T. Lueth, "Comparison of manual steering via joystick of a flexible rhino endoscope," in *32nd Annual International Conference of the IEEE EMBS*, Buenos Aires, Argentina, 2010.

[40] T. Kobayashi, S. Lemoine, A. Sugawara, T. Tsuchida, T. Gotoda, I. Oda, H. Ueda and T. Kakizoe, "A flexible endoscopic surgical system: first report on a conceptual design of the system validated by experiments," *Jpn J Clin Oncol,* vol. 35, no. 11, pp. 667-671, 2005.

[41] W. Shin, S. Kim and D. Kwon, "Development of a flexible-rigid endoscopic robot system for NOTES," in *Asia Conference on Computer Aided Surgery*, Taichun, Taiwan, 2009.

[42] S. Phee, S. Low, V. Huynh, A. Kencana, Z. Sun and K. Yang, "Master and slave transluminal endoscopic robot (MASTER) for natural orifice transluminal endoscopic surgery (NOTES)," in *31st Annual International Conference of the IEEE EMBS*, Minneapolis, 2009.

[43] D. Abbott, C. Becke, R. Rothstein and W. Peine, "Design of an endoluminal NOTES robotic system," in *IEEE/RSJ International Conference on Intelligent Robots and Systems*, San Diego, 2007.

[44] N. Suzuki, M. Hayashibe and A. Hattori, "Development of a downsized master-slave surgical robot system for intragastic surgery," in *ICRA Surgical Robotics Workshop*, Barcelona, 2005.

[45] C. Peters, K. Cleary and L. Haifeng, "Enhanced control of flexible endoscopes through human-machine interface". US Patent 13/608,487, 16 May 2013.

[46] R. Gervacio, F. Blanco, P. Ha, J. Califano and J. Saunders, "Transoral robotic surgery of the vocal cord," *J Laparoendosc Adv Surg Tech,* vol. 21, no. 2, pp. 157-159, 2011.

[47] P. Ceruse, B. Lallemant, S. Moriniere, S. Vergez, A. Benlyazid, A. Ramade, G. Buiret and Y. Mallet, "Transoral minimially invasive robotic surgery for carcinoma of the pharynx and the larynx: a new approach," *Anticancer Drugs,* vol. 22, no. 7, pp. 591-595, 2011.

[48] A. Hillel, A. Kapoor, N. Simaan, R. Taylor and P. Flint, "Applications of robotics for laryngeal surgery," *Otolaryngologic Clinics of North America,* vol. 41, no. 4, pp. 781-791, 2008.

[49] K. Olds, A. Hilel, E. Cha, M. Curry, L. Akst, J. Richmon and R. H. Taylor, "A Robotic Assistant for Trans-Oral Surgery: The Robotic Endo-Laryngeal Flexible (Robo-ELF) Scope," in *Hamlyn Symposium on Medical Robotics*, London, 2011.

[50] K. Olds, R. H. Taylor and J. Richmon, "Robotic system to augment endoscopes". US Patent US20120065470 A1, 14 Sept 2010.

[51] A. Nair, K. Olds and R. H. Taylor, "Endoscope manipulation adapter". US Patent US20130079711 A1, 25 Aug 2011.

[52] K. Olds, A. Hilel, E. Cha, M. Curry, L. Akst, R. H. Taylor and J. Richmon, "Robotic Endolaryngeal Flexible (Robo-ELF) Scope: A Preclinical Feasibility Study," *The Laryngoscope,* vol. 121, no. 11, pp. 2371-4, 2011.

[53] K. Olds, A. Hillel, J. Kriss, A. Nair, H. Kim, E. Cha, M. Curry, L. Akst, R. Yung, J. Richmon and R. H. Taylor, "A Robotic Assistant for Trans-Oral Surgery: The Robotic Endo-Laryngeal Flexible (Robo-ELF) Scope," *Journal of Robotic Surgery,* vol. 6, no. 1, pp. 13-18, 2011.

[54] K. Olds, L. Akst, R. Taylor and J. Richmon, "Assessment of the robotic endolaryngeal flexible (Robo-ELF) scope by novice users," in *8th International Conference on Head and Neck Cancer*, San Francisco, California, 2012.

[55] C. He, K. Olds, L. Akst, W. Chen, M. Ishii, I. Iordachita and R. Taylor, "Evaluation, Optimization, and Verification of the Wrist Mechanism of a New Cooperatively Controlled Bimanual ENT Microsurgery Robot," in *ASME IMECE*, Houston, Texas, 2012.

[56] K. Olds and R. H. Taylor, "Steady hand micromanipulation robot". US Patent US20130131867 A1, 4 Nov 2011.

[57] K. Olds, "Global Indices for Kinematic and Force Transmission Performance in Parallel Robots," *IEEE Transactions on Robotics,* vol. (In Press), 2015.

[58] C. He, K. Olds, I. Iordachita and R. Taylor, "A new ENT microsurgery robot: error analysis and

implementation," in *IEEE ICRA*, Karlsruhe, 2013.

[59] K. Olds, P. Chalasani, P. Lopez, I. Iordachita, L. Akst and R. H. Taylor, "Preliminary Evaluation of a New Microsurgical Robotic System for Head and Neck Surgery," in *IEEE IROS*, Chicago, 2014.

[60] K. Olds, "CIIS Wiki," 5 March 2015. [Online]. Available: https://ciis.lcsr.jhu.edu/dokuwiki/doku.php?id=research.rems&#other_links.

[61] R. Taylor, P. Jensen, L. Whitcomb, A. Barnes, R. Kumar, D. Stoianovici, P. Gupta, Z. Wang, E. deJuan and L. Kavoussi, "A Steady-Hand Robotic System for Microsurgical Augmentation," *Int. J. Robot. Res.,* vol. 18, no. 12, pp. 1201-1210, 1999.

[62] X. He, D. Roppenecker, D. Gierlach, M. Balicki, K. Olds, P. Gehlbach, J. Handa, R. Taylor and I. Iordachita, "Toward Clinically Applicable Steady-Hand Eye Robot for Vitreoretinal Surgery," in *ASME IMECE*, Houston, Texas, 2012.

[63] R. H. Taylor, B. Mittelstadt, H. Paul, W. Hanson, P. Kazanzides, J. Zuhars, B. Williamson, B. Musits, E. Glassman and W. Bargar, "an image-directed robotic system for precise orthopaedic surgery," *Robotics and Automation, IEEE Transactions on,* vol. 10, no. 3, pp. 261-275, 1994.

[64] R. Clavel, "Device for the Movement and Positioning of an Element in Space". Ecublems, Switzerland Patent 4,976,582, 11 Dec. 1990.

[65] X. Liu, J. Wang, K. Oh and J. Kim, "A New Approach to the Design of a DELTA Robot with a Desired Workspace," *J. Intell. Robot. Sys.,* vol. 39, no. 2, pp. 209-225, 2004.

[66] D. Deblaise, X. Hernot and P. Maurine, "A Systematic Analytical Method for PKM Stiffness Matrix Calculation," in *IEEE ICRA*, Orlando, Florida, 2006.

[67] J. Merlet, "Jacobian, Manipulability, Condition Number, and Accuracy of Parallel Robots," *J. Mech. Design,* vol. 128, no. 1, pp. 199-206, 2006.

[68] K. Salisbury and J. Craig, "Articulated Hands, Force Control, and Kinematic Issues," *Int. J. Robot. Res.,* vol. 1, no. 1, pp. 4-17, 1982.

[69] T. Yoshikawa, "Manipulability of Robotic Mechanisms," *Int. J. Robot. Res.,* vol. 4, no. 2, pp. 3-9, 1985.

[70] J. Angeles and C. Lopez-Cajun, "Kinematic Isotropy and the Conditioning Index of Serial Robotic Manipulators," *Int. J. Robot. Res.,* vol. 11, no. 6, pp. 560-571, 1992.

[71] C. Gosselin, "The Optimum Design of Robotic Manipulators Using Dexterity Indices," *Robot. Auton. Sys.,* vol. 9, no. 4, pp. 213-226, 1992.

[72] A. Fattah and A. Hasan Ghasemi, "Isotropic Design of Spatial Parallel Manipulators," *Int. J. Robot. Res.,* vol. 21, no. 9, pp. 811-824, 2002.

[73] S. Kim and J. Ryu, "New Dimensionally Homogeneous Jacobian Matrix Formulation by Three End-Effector Points for Optimal Design of Parallel Manipulators," *IEEE Trans. Robot. Autom.,* vol. 19, no. 4, pp. 731-736, 2003.

[74] G. Pond and J. Carretero, "Formulating Jacobian Matrices for the Dexterity Analysis of Parallel

Manipulators," *Mech. Mach. Theory,* vol. 41, no. 12, pp. 1505-1519, 2006.

[75] R. Mayogra and J. Carrera, "A Manipulator Performance Index Based on the Jacobian Rate of Change: A Motion Planning Analysis," in *IEEE ICRA*, Orlando, Florida, 2006.

[76] G. Boschetti and A. Trevisani, "Direction Selective Performance Indexes for Parallel Manipulators," in *1st Joint Int. Conf. Multibody System Dynamics*, Lappeenranta, Finland, 2010.

[77] T. Huang, H. Lui and D. Chetwynd, "Generalized Jacobian Analysis of Lower Mobility Manipulators," *Mech. Mach. Theory,* vol. 46, no. 6, pp. 831-844, 2011.

[78] G. Boschetti, R. Rosa and A. Trevisani, "Parallel Robot Translational Performance Evaluation Through Direction-Selective Index," *J. Robot.,* vol. 2011, pp. 1-14, 2011.

[79] P. Cardou, S. Bouchard and C. Gosselin, "Kinematic Sensitivity Indices for Dimensionally Nonhomogeneous Jacobian Matrices," *IEEE Trans. Robot.,* vol. 26, no. 1, pp. 166-173, 2010.

[80] C. Wu, X. Liu and J. Wang, "Force Transmission Analysis of Spherical 5R Parallel Manipulators," in *ASME/IFToMM Int. Conf. Reconfigurable Mech. and Robots*, London, UK, 2009.

[81] J. Wang, C. Wu and X. Liu, "Performance Evaluation of Parallel Manipulators: Motion/Force Transmissibility and its Index," *Mech. Mach. Theory,* vol. 45, no. 10, pp. 1462-1476, 2010.

[82] J. Chen and L. Chao, "Positioning Error Analysis for Robotic Manipulators with All Rotary Joints," *IEEE J. Robot. Autom.,* vol. 3, no. 6, pp. 539-545, 1987.

[83] J. Merlet, "Computing the Worst Case Accuracy of a PKM Over a Workspace or Trajectory," in *5th Chemnitz Parallel Kinematics Seminar*, Chemnitz, Germany, 2006.

[84] S. Briot and I. Bonev, "Accuracy Analysis of 3-DOF Planar Parallel Robots," *Mech. Mach. Theory,* vol. 43, no. 4, pp. 445-458, 2008.

[85] A. Yu, I. Bonev and P. Zsombor-Murray, "Geometric Approach to the Accuracy Analysis of a class of 3-DOF Planar Parallel Robots," *Mech. Mach. Theory,* vol. 43, no. 3, pp. 364-375, 2008.

[86] C. Gosselin, "Kinematic Analysis Optimization and Programming of Parallel Robotic Manipulators," in *PhD Thesis, McGill University, Department of Mechanical Engineering*, Montreal, Canada, 1988.

[87] H. Pham and I. Chen, "Optimal Synthesis for Manipulability of Parallel Flexure Mechanisms," in *Proc. 11th World Congr. Mech. Mach. Science*, Tianjin, China, 2003.

[88] E. Staffetti, H. Bruyninckx and J. De Schutter, "On the Invariance of Manipulability Indices," in *Advances in Robot Kinematics: Theory and Applications*, Dordecht, The Netherlands, Kluwer Academic Publishers, 2002, pp. 57-66.

[89] J. Lee, "A Study on the Manipulability Measures for Robot Manipulators," in *IEEE IROS*, Grenoble, France, 1997.

[90] D. Steinberg, "Computation of Matrix Norms with Application to Robust Optimization," in *Master's Thesis, Isreali Institute of Technology, Department of Inustrial Engineering and Management*, Haifa, Israel, 2005.

[91] J. Hendrickx and A. Olishevsky, "Matrix p-Norms are NP-Hard to Approximate if p is not 1, 2, or infinity," *Soc. Ind. Appl. Mathematics J. Matrix Anal. Applicat.,* vol. 31, no. 5, pp. 1-12, 2010.

[92] R. Stamper, L. Tsai and G. Walsh, "Optimization of a Three DOF Translational Platform for Well-Conditioned Workspace," in *IEEE ICRA*, Albuquerque, New Mexico, 1997.

[93] F. Gao, X. Liu and W. Gruver, "Performance Evaluation of Two-Degree-of-Freedom Planar Parallel Robots," *Mech. Mach. Theory,* vol. 33, no. 6, pp. 661-668, 1998.

[94] M. Y. Jung, M. Balicki, A. Deguet, R. Taylor and P. Kazanzides, "Lessons learned from the development of component-based medical robot systems," *J. of Software Engineering for Robotics (JOSER),* vol. 5, no. 2, pp. 25-41, 2014.

[95] J. Funda, R. H. Taylor, K. Gruben and D. LaRose, "Optimal motion control for teleoperated surgical robots," in *SPIE*, Boston, 1993.

[96] A. Kapoor, "Motion Constrained Control of Robots for Dexterous Surgical Tasks," in *Ph.D. thesis in Computer Science, Johns Hopkins University*, Baltimore, 2007.

[97] A. Fedorov et al., "3D Slicer as an Image Computing Platform for the Quantitative Imaging Network," *Magn Reson Imaging,* vol. 30, no. 9, pp. 1323-41, 2012.

[98] N. Ahmidi, G. Hager, L. Ishii, G. Gallia and M. Ishii, "Robotic Path Planning for Surgeon Skill Evaluation in Minimally-Invasive Sinus Surgery," in *Medical Image Computing and Computer Assisted Intervention (MICCAI)*, Berlin, Germany, 2012.

Curriculum Vitae

Kevin Olds   Born 3/14/85, Danvers, MA

Educational History:

Ph.D. expected   2015   Biomedical Engineering   Johns Hopkins School of Medicine

                                  Advisor: Russell H. Taylor PhD

B.E.   2008   Engineering Sciences   Dartmouth College

B.A.   2007   Engineering Sciences   Dartmouth College

Other Professional Experience:

Robotics Consultant   2012-2015   The Kata Project, Brain, Learning, Animation, and Movement
     Laboratory, Johns Hopkins School of Medicine

Robotics Specialist   2008   Greenland Inland Traverse 2008, National Science Foundation
     and Army Corps of Engineers Cold Regions Research and Engineering Laboratory

Research Internship   2007   Visiting Summer Scholars Program, Robotics Institute
     Medical Instrumentation Lab, Carnegie Mellon University

Academic or other honors:

2011   Best Paper Runner-Up   Hamlyn Symposium

2007   Member   Phi Beta Kappa Society

2007   Magna Cum Laude   Dartmouth College

2007   High Honors in the Engineering Major Dartmouth College

2007   Officer   Tau Beta Pi, NH Beta

Publications:

K. Olds, "Global Indices for Kinematic and Force Transmission Performance in Parallel Robots" IEEE
     Transactions on Robotics (In Press).

K. Olds, P. Chalasani, P. Lopez, I. Iordachita, L. Akst, R. H. Taylor, "Preliminary Evaluation of a New
     Microsurgical Robotic System for Head and Neck Surgery" IEEE International Conference on
     Intelligent Robotics and Systems (IROS) 2014.

C. He, **K. Olds**, I. Iordachita, R. H. Taylor, "A New ENT Microsurgery Robot: Error Analysis and
     Implementation" IEEE International Conference on Robotics and Automation (ICRA) May 2013.

S. Sunshine, M. Balicki, X. He, **K. Olds**, J. Kang, P. Gehlbach, R. Taylor, I. Iordachita, J. Handa, "A force-
     sensing microsurgical instrument that detects forces below human tactile sensation" Retina, vol
     33, issue 1. Jan. 2013.

C. He, **K. Olds**, L. M. Akst, W. W. Chien, M. Ishii, I. Iordachita, and R. H. Taylor, "Evaluation,
     Optimization, and Verification of the Wrist Mechanism of a New Cooperatively Controlled

Bimanual ENT Microsurgery Robot," In Proceedings of ASME International Mechanical Engineering Congress & Exposition, IMECE2012, Houston, Texas, USA, Nov. 2012.

X. He, D. Roppenecker, D. Gierlach, M. Balicki, **K. Olds**, P. Gehlbach, J. Handa, R. Taylor, I. Iordachita, "Toward Clinically Applicable Steady-Hand Eye Robot for Vitreoretinal Surgery" In Proceedings of ASME International Mechanical Engineering Congress & Exposition, IMECE2012, Houston, Texas, USA, Nov. 2012.

K. Olds, L. Akst, R. H. Taylor, J. Richmon, "Assessment of the Robotic Endolaryngeal Flexible (Robo-ELF) Scope by Novice Users" 8th International Conference on Head and Neck Cancer. July 2012.

K. Olds, A. Hillel, J. Kriss, A. Nair, H. Kim, E. Cha, M. Curry, L. Akst, R. Yung, J. Richmon, RH. Taylor, "A Robotic Assistant for Trans-Oral Surgery: The Robotic Endo-Laryngeal Flexible (Robo-ELF) Scope" Journal of Robotic Surgery. Dec. 2011.

K. Olds, A. Hillel, E. Cha, M. Curry, L. Akst, RH. Taylor, J. Richmon, "Robotic Endolaryngeal Flexible (Robo-ELF) Scope: A Preclinical Feasibility Study" The Laryngoscope, vol 121, issue 11. Oct. 2011.

K. Olds, A. Hillel, E. Cha, M. Curry, L. Akst, J. Richmon, RH. Taylor, "A Robotic Assistant for Trans-Oral Surgery: The Robotic Endo-Laryngeal Flexible (Robo-ELF) Scope" Hamlyn Symposium on Medical Robotics. June 2011.

Patents and patent applications (currently published):

K. Olds, R. Taylor, "Steady Hand Micromanipulation Robot," U.S. Patent 13/669,176, Dec. 16, 2014.

K. Olds, R. Taylor, "Rotation Preserving Quick Connect Device," U.S. Patent Application 14/299,082, Dec. 11, 2014.

A. Nair, **K. Olds**, R. Taylor, "Endoscope Manipulation Adapter," U.S. Patent Application 13/595,643, Mar. 28, 2013.

K. Olds, R. Taylor, J. Richmon, "Robotic System to Augment Endoscopes," U.S. Patent Application 13/232,617, Mar. 15, 2012.

Service and leadership while at Hopkins:

2012   Instructor, "A Survey of Medical Technology", Johns Hopkins University

2010   Teaching Assistant, "BME Freshman Modeling and Design", Johns Hopkins University